Neuroelectronic and Nanophotonic Devices Based on Nanocoaxial Arrays

Author: Jeffrey R. Naughton

Neuroelectronic and Nanophotonic Devices Based on Nanocoaxial Arrays

Jeffrey R. Naughton

A dissertation

submitted to the Faculty of

the department of Physics

in partial fulfillment

of the requirements for the degree of

Doctor of Philosophy

Boston College
Morrissey College of Arts and Sciences
Graduate School

August 2017

Neuroelectronic and Nanophotonic Devices Based on Nanocoaxial Arrays

Jeffrey R. Naughton

Advisor: Prof. Michael J. Naughton Ph.D.
Dr. Michael J. Burns Ph.D.
Prof. Jan R. Engelbrecht Ph.D.
Prof. Tom C. Chiles Ph.D.
Prof. John P. Christianson Ph.D.

Abstract

Recent progress in the study of the brain has been greatly facilitated by the development of new measurement tools capable of minimally-invasive, robust coupling to neuronal assemblies. Two prominent examples are the microelectrode array, which enables electrical signals from large numbers of neurons to be detected and spatiotemporally correlated, and optogenetics, which enables the electrical activity of cells to be controlled with light. In the former case, high spatial density is desirable but, as electrode arrays evolve toward higher density and thus smaller pitch, electrical crosstalk increases. In the latter, finer control over light input is desirable, to enable improved studies of neuroelectronic pathways emanating from specific cell stimulation. Herein, we introduce a coaxial electrode architecture that is uniquely suited to address these issues, as it can simultaneously be utilized as an optical waveguide and a shielded electrode in dense arrays.

Table of Contents

List of figures

Acknowledgements

To all the members of my thesis committee: Michael Naughton, Michael Burns, Jan Engelbrecht, Tom Chiles, and John Christianson, I would like to extend my profound thanks for your guidance throughout my thesis. I have benefited greatly from your support and advice, both scientifically and professionally.

I'd like to start by personally thanking my thesis advisor, and Uncle, Michael Naughton. When I visited you as an undergraduate, your love of Physics and desire to understand the natural world inspired me to do the same. I am extremely grateful that in my first year at Boston College, I was given the chance to attend your Quantum Mechanics lecture and marveled at your ability to relate a topic so seemingly esoteric. After having worked in your lab, the force with which you would explode through the lab doors to question what work was being done, has left an indelible mark on my auditory cortex. One of my profound joys was to compare a finalized presentation with the iteration that I thought couldn't possibly be improved. I leave Boston College, with zero excuses for not putting together a proper presentation. It was extraordinarily humbling to work with you throughout this project and I take with me a great wealth of knowledge to lead me throughout my career. All of the sacrifices that you made on my behalf did not go unnoticed, and my gratitude goes beyond words, especially English ones… *go raibh mile maith agat.*

To my advisor Michael Burns, thank you for sharing your vast experience as it pertained to my thesis, the other projects I was involved in, as well as my personal career. Without you the streamlining and documentation of our fabrication processes might never have happened. I am especially thankful for your ability to quickly

diagnose a problem as well as come up with numerous solutions, often an overlooked step in problem-solving. Most importantly, thank you for your patience.

I am eternally grateful to Stephen Shepard of the nanofabrication facility at Boston College. You were instrumental in my photolithography and PVD training, and my thesis work would not have been possible without your mentorship. I sincerely enjoyed learning from you and my long hours in the clean room were much more enjoyable because of you. Furthermore, I appreciate your lenience in letting me use clean room equipment during my (ab)normal working hours as well as your patience in reminding me to fill out the log books.

I would like to thank all of the members of Naughton lab throughout my time at Boston College. It has been a privilege interacting with all of you and I sincerely appreciate all the support you gave me. For those who have not finished, I have every confidence you will do great things in your Ph.D. Personally, I would like to thank Binod Rizal for introducing me to his work on using the nanocoaxial architecture as a sensing element, which set the foundation for my own work, and for passing on his unparalleled skills in micro/ nanofabrication. Spending countless hours in the clean room with you was invaluable in the development of my skills as a graduate student. I will always share a special bond with you given our experience with pain and frustration: the twin pillars of the nanocoaxial fabrication process. To Fan Ye, thank you for your patience in entertaining the myriad questions I posed to you and for your physics expertise, from which I've benefited greatly. It was incredibly humbling working next to you and I look forward to reading about your research work in the future. To Aaron Rose and Nate Nesbitt, thank you for stimulating conversation and

brainstorming on a variety of topics, physics and otherwise. Aaron, you were instrumental in performing optics simulations and I dare not think of the time and anxiety cost I would have endured if you weren't there. Nate, thanks for elucidating the intricacies of chemistry, electrode dynamics, and being a strong foundation to bounce ideas off of. To Juan Merlo and Yitzi Calm, thank you for holding my hand as I dipped my toe into the world of nanoscale optics. Juan, thank you for enduring the long hours teaching me how to use the NSOM and showing incredible restraint when I broke 2 tips. I'm forever indebted to you for this and all the technical support you gave me throughout my thesis. Yitzi, thank you for the lucid explanations, analytical eloquence, and unrelenting encouragement. To Luke D'Imperio, you've been an immense help by indulging my ideas and bringing a sobering reality to them when necessary. I look forward to seeing the progress you make with the neurosensing platform. Thank you to Chaobin Yang for helpful advice with fabrication techniques and sharing the clean room space.

To the members of the Biology and Psychology departments, whom I worked with throughout my time at Boston College. My Advisor, Tom Chiles, thank you for your advice and stories as well as pushing myself and the project forward when it seemed we weren't making progress. Tim Connolly, thank you for your support in growing and monitoring the cells used throughout my thesis. I am extremely humbled by your selflessness in taking time away from your classes to help me. I hope the number of experiments we discussed, come to fruition and I wish we had more time and resources so that I could've had a part in them. Special thanks to Juan Varela, for his patience while sharing his knowledge of electrophysiology with me. You were a

much needed light as I wandered around in the darkness. To my advisor, John Christianson, thank you for all your help in framing our work with a neuro-scope. You were instrumental in getting our first paper published and our work displayed at SFN, which was a much needed introduction to the field.

I would like to thank Kevin Lukas, Claire Watts and Dusty for making life outside of academia not only possible, but mandatory. Kevin and Dusty, the March Meeting really isn't the same when either of you is not in attendance. Special thanks go to Matt Gochan, for helpful advice and setting the bar for TAs.

Additionally, I'd like to thank the staff members of the Boston College Physics office: Nancy, Sile, and Jane. You were always there in a time of crises and also when I simply needed a light moment to get me through the day.

Finally, to my Family, I'm dedicating this dissertation to all of you for more reasons that I can list. Allow me to be honest for a moment and say that throughout my time at Boston College I held hands with doubt and shame. Wandering through the unknown can be terrifying and distractions abound. However, you were always there and always encouraging. I hope my work herein makes you proud and proves worthy of the sacrifices you made along the way. I love all of you.

Chapter 1: Introduction

A major goal of neurophysiology is to understand how ensembles of neurons generate, store and recall representations of the physical world, and coordinate responses to its changing environment. To understand these fundamental capacities, neuroscientists investigate the electrical activity of individual and networks of neurons to correlate patterns of activity to specific behaviors or cognitions. To this end, some of the goals of neural device development are to increase biocompatibility; to increase the recording scale, i.e. ability to record and stimulate tens to hundreds or thousands, or more of individual neurons simultaneously without compromising cell viability; to increase the duration of electronic coupling to neurons over extended periods of time (hours to days to months); and to better dissociate the many neurophysiological events (action potentials, excitatory/inhibitory postsynaptic potentials, *etc*.) that occur in a neural circuit. Since the first tools in the 1940's, many years of device development and refinement have produced state-of-the-art tools capable of measuring action potentials (APs) originating from multiple neurons, as well as tracking propagation of APs[1,2,3]. One such tool is the microelectrode array (MEA), which is highly scalable and able to be utilized in a multiplex assay, the type necessary to study ensembles of neurons[4].

Well-characterized and commercially-available microelectrode arrays fall under two categories: *in vitro* arrays, consisting of planar metal microelectrodes[5], and *in vivo* arrays, which can vary from 2D (Michigan array[6,7]) and 3D (Utah array[8]) structures to flexible polymer devices[9], with electrode separations from several tens to hundreds of microns. In considering ways to further advance extracellular recording, one approach is to decrease the scale of the recording element from the micro- to the nanoscale (including

smaller than the neurons themselves). Next generation versions of MEAs[10] include nanowire electrode arrays[11], field effect transistor arrays[12,13], novel structure arrays[14] and nanopillar arrays[15,16]. In some cases, such technologies have brought the electrode pitch down to the 20 micron range[17,18].

Although recent advances have reduced electrode scale and pitch, a prevailing problem in extracellular recording from neuronal networks is the ability to identify the individual neurons from the local field potentials (LFPs) recorded by one or more adjacent electrodes, a process known as spike sorting. Even with high density MEAs, synchronous discharges of similar waveforms from multiple neurons equidistant from a recording site make spike sorting difficult[19]. Complexities in neuronal firing modes, neuronal morphology and other intrinsic properties all complicate the identification of individual neurons based on the recorded extracellular field potential waveforms[1,20]. The development of validated spike sorting algorithms and a desire for standardization has been previously discussed, yet the process depends on subjective standards and time-consuming offline data analysis[20,21]. The need for spike sorting is a direct result of the phenomenon of electrical crosstalk, wherein an electrical signal sourced near one electrode is also sensed by one or more neighboring electrodes. Crosstalk makes spatiotemporal identification of a signal source difficult, even with offline spike sorting. Unfortunately, reducing the pitch and scale of conventional electrodes has only magnified the problems associated with crosstalk.

Another possibility for electrode development is the integration of optical components with electrodes, producing devices called “optrodes”. Optrodes[22] enable electric field sensing and delivery simultaneous to local light sensing and delivery, and so

provide a closed-circuit interface to light-sensitive proteins and light-emitting biosensors such as channel rhodopsins and genetically-encoded calcium indicators, respectively (e.g., optogenetics). These advances in bioengineering now permit actuation and sensing of individual or groups of neurons depending upon their phenotype and anatomy, among other factors (see Refs. 23, 24 for reviews). Thus, optogenetic tools overcome a limit of conventional extracellular recording from neuronal networks, which do not permit precise electrical actuation of a specific cell type within an assembly of multiple neuronal types[25]. As such, hybridization of optical and electrical elements into optrode arrays can help in the progression of traditional MEA technology for use with the emerging field of optogenetics[26,27,28]. Nonetheless, the technical issues of electrical crosstalk in MEAs, and local light delivery in optogenetics, have not been fully resolved, such that new approaches are needed to facilitate the targeting of specific cell types within a neuronal assembly.

The goal of the research described in this dissertation has been the development of a shielded electrode architecture that can both reduce crosstalk and integrate an optical element. In this thesis, we provide proof of principle that a multiplexed nanoscale coaxial optrode can lead to a next generation of optrode neurointerfaces capable of very high spatial resolution electrical sensing and local optical stimulation. In Chapter 2, we provide a historical background of electrophysiology and optogenetics, as well as discuss the structure and function of neurons. We conclude Chapter 2 by discussing the virtue of locally shielding neural probes through simulations and preliminary experiments. Chapter 3 provides a proof of concept study by using coaxial nanoelectrode arrays (cNEA) to extracellularly record from leech neuronal assemblies. In Chapter 4, we introduce the

coaxial microelectrode array (cMEA) for preliminary use as an optrode in optogenetic studies using Human Embryonic Kidney (HEK-293) cells transfected with a Channelrhodopsin protein. When used as an optrode, light is propagated through the core of the coaxial structure in both the cNEA and cMEA. Chapter 5 discusses the optical throughput of metal-coated (Au and Cr) cylindrical structures in an effort to characterize the ability of our devices for use an optrode. In Chapter 6, we start by discussing the phenomenon of crosstalk, introduce and provide a background on spike sorting (a method for dealing with crosstalk), and conclude by discussing two experiments comparing crosstalk suppression in unshielded and locally shielded electrodes. Chapter 7 concludes the thesis and also provides prospects of future work to be done.

One important note on the details of device fabrication: each Chapter contains a similar, but unique architecture centered around the coaxial geometry (excluding Chapter 5, where the device does not contain an outer shield). Because of this, instead of having a separate Chapter on device fabrication, the particular fabrication steps of the device used in a particular experiment have been included each Chapter.

Chapter 2: Background

2.1 Neuron: structure, function, models

The building block of the human sensory system, broadly divided into the central nervous system and the peripheral nervous system, is the nerve cell, or neuron. The structure of a neuron includes a cell-body known as the soma, which contains the nucleus, a network of short branches known as dendrites, and a separate branch (typically longer) known as the axon (Figure 2.1)[29]. The main function of a neuron is to receive, interpret, and send messages in the form of an electrical impulse called an action potential. The dendrites and other areas of the cell receive this pulse at specialized junctions known as synapses. In the brain alone, there are roughly one hundred million neurons and each neuron contains input junctions from roughly ten thousand synapses. The incoming signals from synapses can be excitatory (which lead to an action potential) or inhibitory (suppresses action potential generation). When an action potential is generated in the soma (mainly the axon hillock), the signal travels down the axon, which is covered with an insulating material called myelin that helps conduct the signal by containing the signal within the axon (mitigating any current leakage). Neurons can range from 4 to 100 microns in diameter, while the axon length and cross section are quite variable and can range from 1 to 1000 mm in length and 1 to 20 μm in diameter. The information passing through the axon is transmitted from the first neuron (pre-synaptic cell) to a target neuron (post-synaptic cell) via chemical messengers called neurotransmitters at pre-synaptic terminals. The neurotransmitters travel across the synaptic cleft (a roughly 50 nm gap between pre- and post-synaptic terminals), and bind to the membrane receptors of the post-synaptic

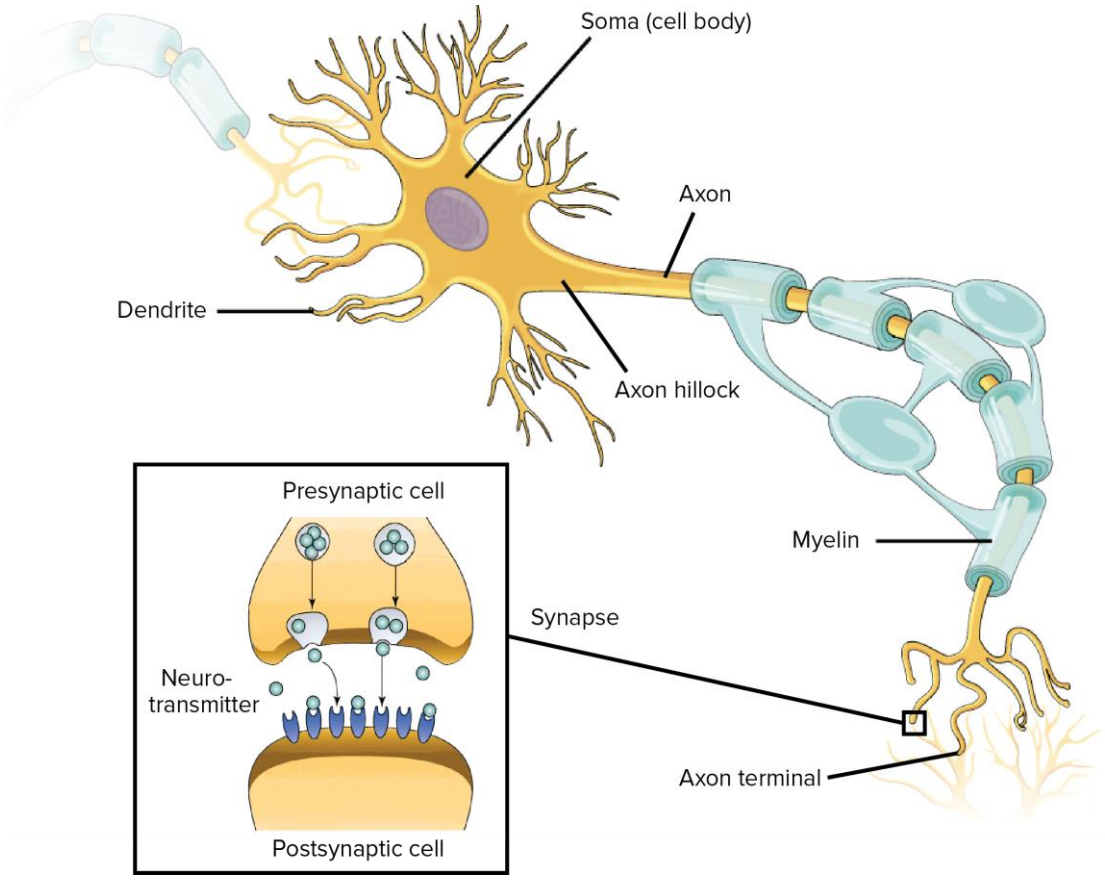

Figure 2.1 Structure of a neuron. The neuron is comprised of a dendritic tree, a soma, and axon. The axon terminal (collection of synapses) connects to the dendritic trees of other neurons and the inset in the lower left gives an overview of the synapse structure. Image is from Reference 29.

Table 1: Ion concentration inside and outside neurons			
Ion	Extracellular concentration (mM)	Intracellular concentration (mM)	Ratio outside/inside
Na^+	145	12	12
K^+	4	155	0.026
Cl^-	120	4	30
Organic anions (A^-)	—	100	

Table 2.1 Resting ion concentrations inside and outside a neuron. The extracellular and intracellular ion concentrations of important ion species for cell behavior. These are the concentration values when the cell is in equilibrium or "at rest". Ratio values give sense of direction of ion flow, as a value of less than 1 represents a gradient pointing from inside to outside the cell.

cell, and the signal is propagated as either an excitatory post-synaptic potential or an inhibitory post-synaptic potential. Both of these inputs will perturb the resting potential (a potential difference between the interior and exterior of the cell that is maintained when the cell is in equilibrium) of the cell and either cause or prevent an action potential.

Action potentials are able to occur (and thus cells are able to communicate) due to there being a potential difference between the inside and outside of a cell. This potential difference arises from differences in ion concentrations inside and outside the lipid bilayer cell membrane (typical ion concentrations shown in Table 2.1). The lipid bilayer is roughly 10 nm in thickness and can be modeled as a parallel plate capacitor with a capacitance per unit area of ~ 1 $\mu F/cm^2$ using typical values for the dielectric constant and length[30]. Embedded within the cell membrane are tunnel like structures (proteins) called ion channels that allow specific ions to pass through the cell membrane (Figure 2.2)[31]. These proteins span the cell membrane and have three states: open, closed, and inactive. As previously mentioned, the "resting membrane" potential is caused by a non-equilibrium of ion flow through ion channels, as some channels need to be activated

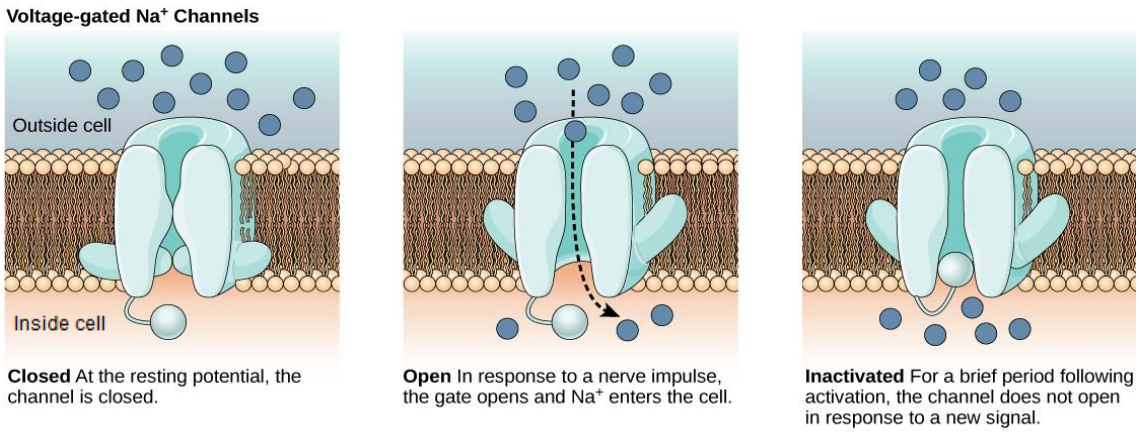

Figure 2.2 Structure of ion channels. Proteins embedded in the cell lipid bilayer that span the cell membrane, called ion channels, allow specific ions to travel into or out of the cell. Ion channel "gates" have open, closed and inactive states. The gates shown above are actuated by voltage changes. Image is from Reference 29.

(through a perturbation in the local environment) in order to undergo a conformal change and thus allow the passage of ions. We can model the movement of ions as a two-compartment system (inside and outside) separated by a selectively permeable membrane allowing diffusion of one ion species, but not of another. The change in flux due to the diffusion of ions is governed by the following equation:

$$f_{diff} = -D\nabla C \tag{1}$$

where D is the diffusion constant and C is the concentration. Thus, the equation represents the flow of ions down a concentration gradient. This flow of ions will result in an accumulation of excess positive charges inside one of the compartments and thus a potential difference V_m (also written as Φ) across the membrane. An electric field of strength $E = V_m/d$, where d is the lipid bilayer thickness, will be directed from inside to outside. This electric field will impose a force on the ions and thereby causing a change in flux due to a drift velocity given by the following equation:

$$f_{drift} = -\mu_n C \frac{Z_n}{|Z_n|} \nabla\Phi \tag{2}$$

where μ_n is the ion mobility, C is the concentration, Z_n is the ion valence and $\nabla\Phi$ is the electric field. Once equilibrium is reached the total flux across the membrane is zero, leaving us with the following drift-diffusion relation:

$$f_{diff} + f_{drift} = 0 = -D\nabla C(x) \; - \mu_n C \frac{Z_n}{|Z_n|} \nabla\Phi \tag{3}$$

to which we can apply Einstein's equation connecting μ_n and D:

$$D = \frac{\mu_n RT}{|Z_n|F} \tag{4}$$

where R is the gas constant (8.315 j/mol. K), T is the absolute temperature, Z_n is the valence number, and F is Faraday's constant (96,487 C/ mole). Multiplying by FZ_n

(number of charges carried by each mole), we get the current density (typically around 2 pA/cm^2) in a form similar to the Nernst-Planck equation:

$$J_n = -\left(\mu_n RT \frac{Z_n}{|Z_n|}\nabla C + \mu_n |Z_n| CF \nabla \Phi\right) \tag{5}$$

The first term on the right-hand side of equation (5) is the current due to diffusion and the second is that due to drift. From equation (5), it is a straightforward calculation to find the resting (equilibrium) transmembrane potential, defined as $\Phi_{in} - \Phi_{out}$, assuming the ion concentration only varies in the direction perpendicular to the membrane (which I will call *x*):

$$J_n = 0 = -DFZ_n\left(\nabla C + \frac{Z_n CF}{RT}\nabla \Phi\right)$$

$$\rightarrow \quad \frac{dC}{dx} = -\frac{Z_n CF}{RT}\frac{d\Phi}{dx}$$

$$ln\left(\frac{[C]_{in}}{[C]_{out}}\right) = -\frac{Z_n F}{RT}\{\Phi_{in} - \Phi_{out}\}$$

$$\Phi_{in} - \Phi_{out} = -\frac{RT}{Z_n F} ln\left(\frac{[C]_{in}}{[C]_{out}}\right) \tag{6}$$

Equation (6), known as the Nernst potential, can be calculated for each ion species separately, given the concentration values in Table 2.1. Notice that because the ratio for K^+ is less than one this will reverse the polarity of the transmembrane potential and therefore K^+ ions flow in a different direction than Na^+ and Cl^- ions. Typical resting potentials of neurons are in the −70 to −100 mV range. An action potential is a brief reversal of this membrane potential (Figure 3, lower left region) and is an all or nothing event. Input, in the form of neurotransmitters, arrives at the postsynaptic cell and alters the permeability for specific ion species, causing an electric field and a current along the interior of the cell. If a threshold potential is reached (Figure 2.3, region a) the cell is

depolarized until a peak potential is reached (Figure 2.3, region b), after which, the cell begins to "reset" its membrane potential back to the resting value. Repolarization is achieved by closing Na^+ and opening K^+ channels, causing the membrane potential to once again become negative. The diffusion of the K^+ ions out of the cell due to voltage-gated channels opening causes a hyperpolarization of the cell (Figure 2.3, region c) and a Na+ /K+ transporter channel called the Na/K pump restores the resting membrane potential.

The action potential is transferred along an axon in the form of a solitary wave of depolarization followed by a repolarization. The membrane potential provides the energy needed to propagate the pulse, driving the wave through a potential change, which in turn triggers the neighboring region of the cell, allowing the action potential to travel with undiminished amplitude. Using a simple model of a collection of dipole current sources and sinks, depending on the direction of the current, for the opening and closing of ion channels, can lead one to analytically computing the electric field in the extracellular medium and the extracellular potential. Starting from first principles, and dividing the neuron into N compartments, the extracellular potential due to neuronal activity is given by the following:

$$\Phi(r,t) = \frac{1}{4\pi\sigma}\sum_{n=1}^{N}\frac{I_n(t)}{|r-r_n|} \qquad (7)$$

where σ is the extracellular conductivity, $I_n(t)$ is the transmembrane current, and r_n is the position of the n^{th} channel. In general, the extracellular potential waveform is considered biphasic (Figure 2.4b,c) while the intracellular waveform shown in Figure 2.4a is labeled monophasic. The behavior of neurons is mostly described in terms of these (intra- and extracellular) potentials and currents as they are a representation of the

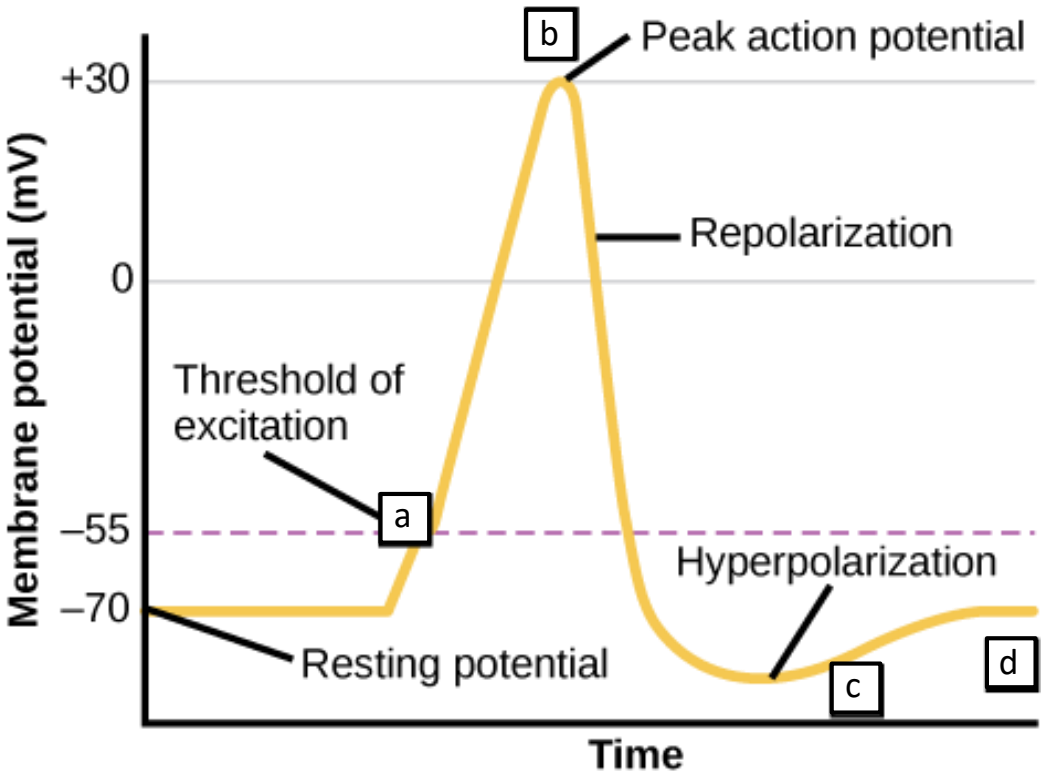

Figure 2.3 Intracellular action potential waveform and components. An action potential is a brief reversal of the membrane potential. Once a threshold potential is reach (a) the membrane potential rises to a peak amplitude (b) before repolarizing, hyperpolarizing (c) and returning to its original state (d). Image adapted from Reference 31.

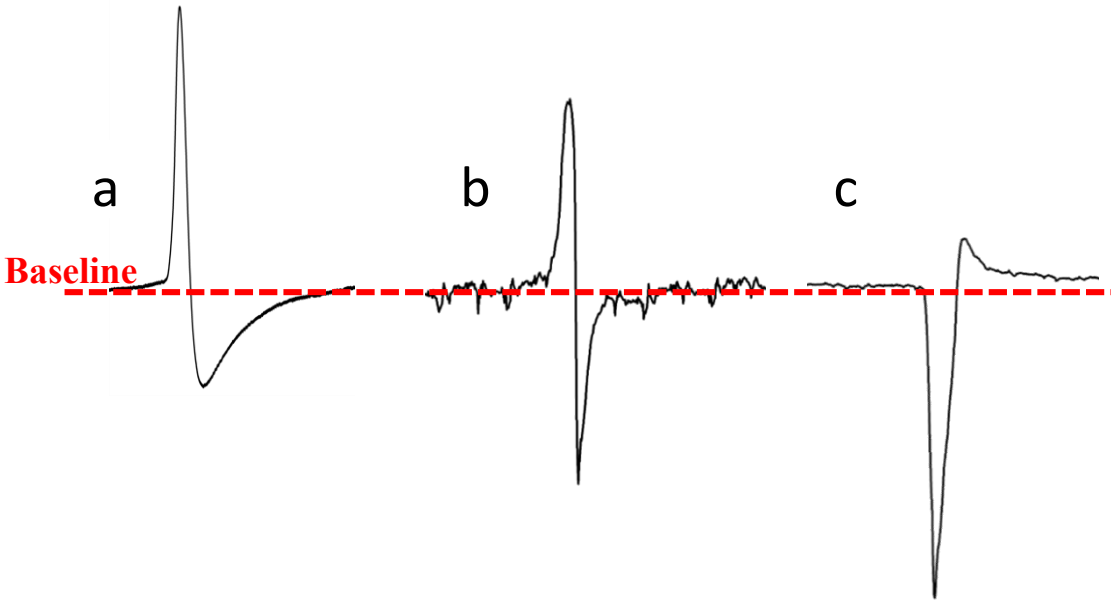

Figure 2.4 Intracellular and extracellular waveforms. Conventionally, the intracellular waveform shown in (a) is considered monophasic, while the extracellular waveforms shown in (b) and (c) are considered biphasic. These action potentials were taken from intra- and extracellular recordings of leech neuronal assemblies as will be discussed in chapter 2.

transmission of information. It is the dynamics of the intra- and extracellular potential that electrophysiologists measure and use to gain insight into the underpinnings of neurological behavior.

2.2 Electrophysiology: history, methods, current technology

Beginning with Cole and Marmont[32] using electrodes to probe the axons of the giant squid in 1947, the field of electrophysiology and the tools used therein have undergone a steady development. From the original device of a simple twisted pair of millimeter-scale electrodes, as well as similar electrodes used in pioneering experiments by Hodgkin and Huxley[33], the relationship between ionic currents and action potentials was discovered. Since then, the interplay between the electronic signals passed within neurons as well as throughout neural networks, and the correlation to behavior, has been a wide area of study. To gain access to those signals, many tools have been developed and can be broadly separated into two classes of measurement devices: intracellular and extracellular.

Measuring the current across the membrane of a single cell (to follow the change in membrane potential) by placing an electrode inside or attached to the cell membrane is known as intracellular recording. The standard tool for intracellular recording involves using a glass micropipette with a tip pulled to a diameter on the order of a micron and filled with an electrolyte solution of similar ionic composition to the intracellular fluid of the cell. Typically, a chlorided silver wire is placed within the micropipette and attached to a headstage amplifier to connect the electrolyte to a signal processing unit. Chlorided silver wires have a stable electrode potential and are non-polarizing (meaning current can easily pass through them) and are thus suitable for use in the field. The voltage measured by the electrode tip is compared to a reference electrode which usually consists of a mm^2 scale chlorided silver disc or pellet placed in the electrolyte bath far away from recording site. In general, all intracellular tools follow this simple description, however, the use of

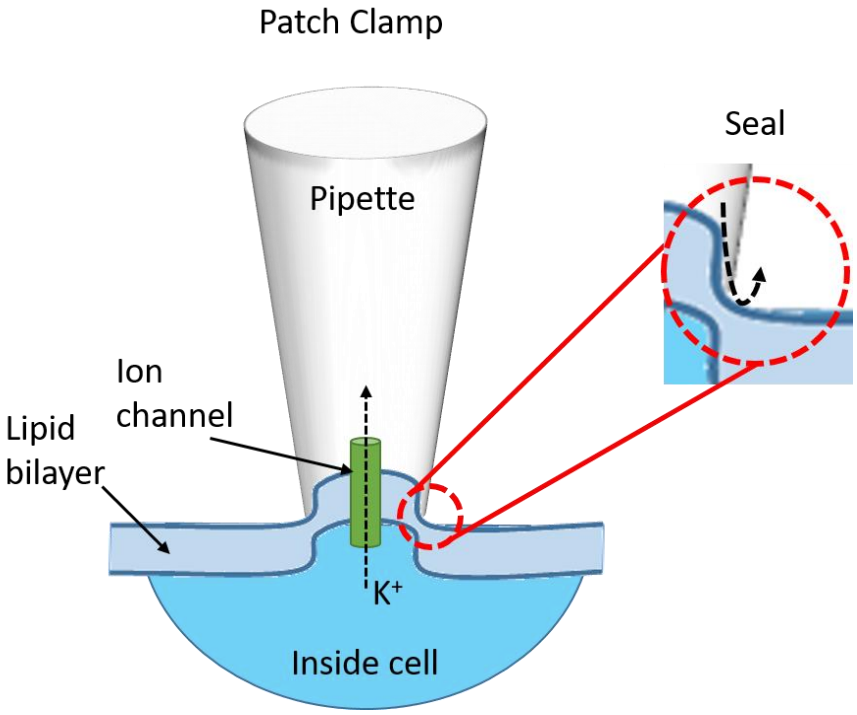

Figure 2.5 Patch clamp and seal. The patch clamp uses light suction to pull a piece of the membrane into the pipette tip. This creates a seal (red dashed circle) that blocks ion species from leaking out into the extracellular space (see inset in top right corner, black dashed line represents current path leaking into extracellular space).

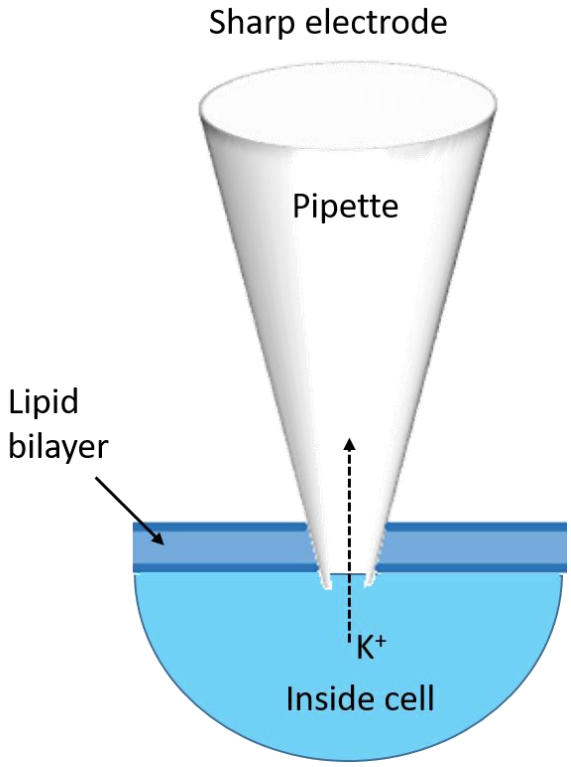

Figure 2.6 Sharp electrode technique. The sharp electrode measurement involves puncturing the cell membrane (lipid bilayer) of the cell to facilitate direct access to the inner cell.

the device can be broadly categorized into two similar, but separate techniques: patch clamp (including voltage and current clamp) and sharp electrode recording.

The "patch" technique involves bringing the tip of the micropipette into approximate contact with the cell membrane and using light suction to draw a section of the cell membrane into the pipette, creating a high resistance seal (Figure 2.5). This seal is very important to the integrity of the measurement, as a low seal resistance will cause a degradation in the signal[34]. This degradation occurs because the impedance of the path between the electrolyte solution in the pipette and the extracellular space is too low to stop a substantial amount of ions (representing the signal to be recorded) from leaking into the extracellular space. In sharp electrode recording, the tip of the pipette punctures the cell membrane as seen in Figure 2.6 (this is also known as whole cell-recording). For both techniques, the cell-type under interrogation determines the morphology of the pipette; some cells require a gradual taper to a 1-3 μm diameter tip, while others (such as tissue slices) require a blunt "bee-stinger" like tip[35]. The greatest utility of both intracellular techniques is that they represent a "ground-truth" measurement. In other words, the user knows with exact certainty which neuron is being interrogated. However, as each pipette is only capable of measuring a single neuron at one time, these tools are not ideal for studies that involve recording from a network that can contain tens to thousands of neurons.

One of the most ubiquitous tools in electrophysiology, used to record the electrical transients of neuronal activity stemming from an array of neurons, is the microelectrode array. The first-generation versions of this device generally consisted of a 2D array of flat cylindrical electrodes (usually platinum) surrounded by a dielectric

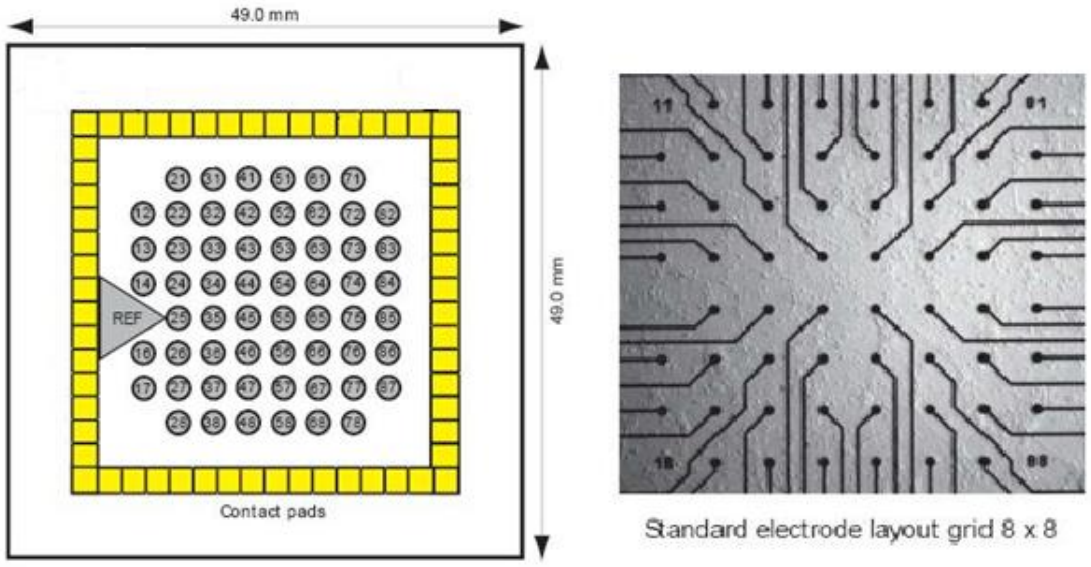

Figure 2.7 Standard MEA layout. The microelectrode array consists of an array of flat cylindrical electrodes with passivated address lines terminating in macro-contact pads. The figure above is from a commercially available 8x8 MEA (Image from Multichannel systems MEA brochure)

material, with address lines (passivated by a dielectric) extending away from the cylinders and terminating in a metal macro pad meant to connect to a pin-out amplifier system (see Figure 2.7 for schematic). The sensing areas ranged from 10s to 100s of microns in diameter and the inter-electrode distance was of the same scale. When used in *ex vivo* experiments, neurons are cultured on top of the device and stimulated (usually electrically) as each sensing element in the MEA extracellularly records an aggregate of the electrical response. As MEAs are sufficiently non-invasive (i.e. they don't pierce or attach to the cell wall), they are the ideal tool for recording cultured cells over time scales longer than that of intracellular recording (patch clamp and sharp electrodes are capable of recording for minutes to possibly over an hour). The second generation of multielectrode arrays moved the individual sensing elements into the single micron and nanoscale level. These devices include field effect transistors (FETs), nanowires, and some novel geometries such as Au mushroom electrodes. Although the sensing region is comprised of nanoscale structures, the pixel size of these devices remains in the tens of microns in scale.

Another regime in which MEA technology is implemented is that of *in vivo* studies where the device is implanted into the brain. Two of the most well-known extracellular MEA technologies for *in vivo* recording are the Michigan and Utah arrays (Figure 2.8). They are both silicon-based microelectrode arrays with a large number of recording sites and capable of implantation. The Michigan arrays are 2D silicon shanks (shown in Figure 2.8a) with recording sites along the center of the shanks. The Utah arrays have a 3D geometry consisting of 100 or more conductive silicon needles (electrodes). In the Utah arrays (Figure 2.8b), the sensing elements are only at the tips of

(a)

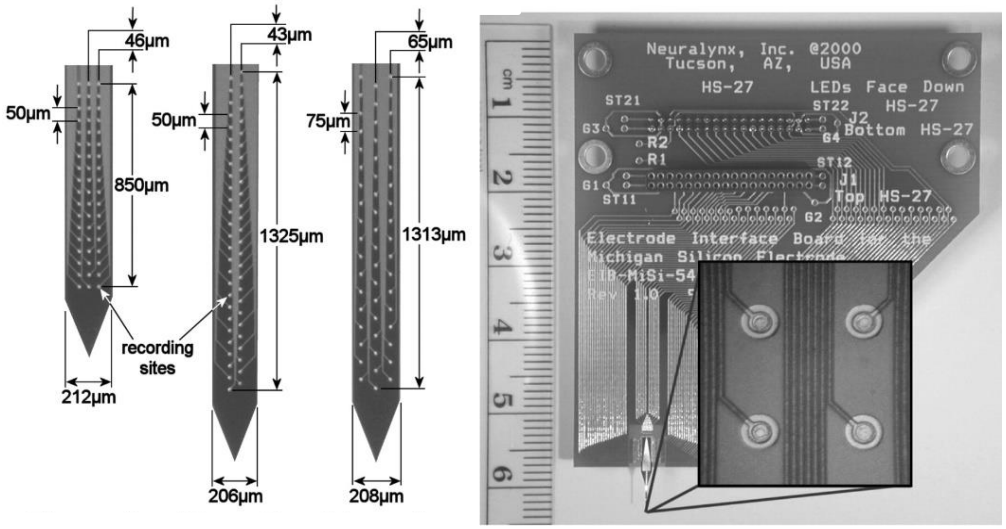

(b)

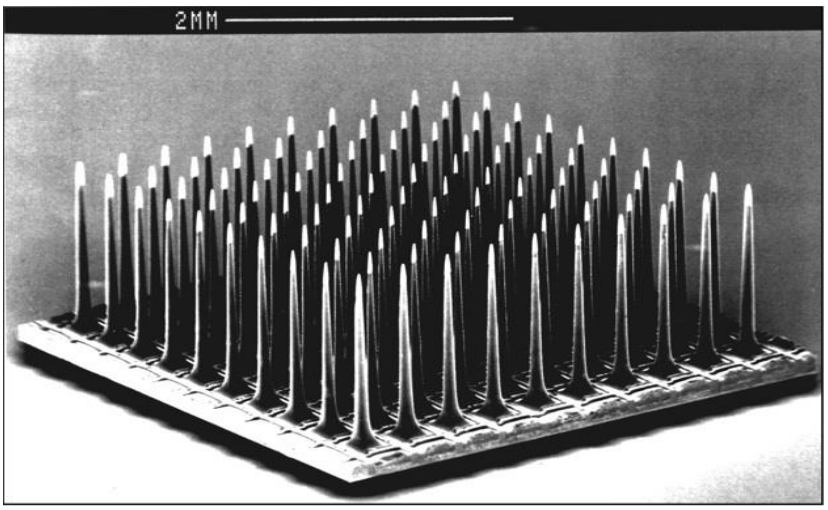

Figure 2.8 Michigan and Utah microelectrode arrays. Both the Michigan (a) and the Utah (b) arrays are used for *in vivo* assays. The Michigan array is considered a 2D device while the Utah array is considered a 3D device. Images from References 6-8.

the electrodes and therefore have a lower resolution than the Michigan arrays. Another advantage of the Michigan arrays is that they have more freedom in their design, whereas the Utah array comes with a set geometry with one exception: a second generation slanted architecture has been developed where the pointed electrodes have a descending height across 1 axis of the array (instead of having every electrode of the same height like in the Figure shown). One disadvantage to both of these tools, and silicon based implantation devices in general, is the difference in young's modulus between that of silicon and brain tissue (silicon has a much higher value). This difference greatly contributes to shear-induced inflammation, which then causes encapsulation tissue (astrocytes) to surround the device, thereby lowering its efficacy[36].

Both first and second generation MEA technologies hold a common theme between them: bare (unshielded) electrodes. While this allows higher signal to noise value (a highly desirable trait) when compared to shielded electrodes, it also has the added consequence of overlapping sensing regions (which we introduced earlier as crosstalk). The ability of the bare electrodes to capture more of the source signal is most likely due to a larger surface area of the recording electrode. However, shielded electrodes can use techniques such as nanostructering and a lower shield height to increase surface area (and therefore the S/N value) while also reducing crosstalk. Given that local field potentials and activity from action potentials can travel hundreds of microns, the bare electrode arrays must rely on spike sorting algorithms to try to discern the origin of a signal. The spatial dependence of neuronal activity and the intricacies of spike sorting will be discussed more fully in Chapter 6. In a worst case scenario, when bare electrodes are spaced in close proximity to one another, spatial resolution will be

lost to the point that an array of nanoscale sensing elements becomes an array of microscale sensing elements.

2.3 Optogenetics: history and current technology

As was mentioned in the introduction, a novel method for interrogating neurons that combines optics, genetics and bioengineering is called Optogenetics. It involves the use of light to control brain activity in a precise, targeted manner with opsin genes, which encode light-activated channel and pump regulators of transmembrane ion conductance[37]. A commonly held notion among neuroscientists is that the ability to manipulate individual components of the brain is a prerequisite for assembling a general theory of the mind[38]. Unfortunately, neither intra- nor extracellular electrical stimulation is capable of activating (or inactivating) all neurons of a single type, while leaving the rest unaltered. The utility of having cell-specific manipulation for activity mapping is realized by the ability to progress beyond passive observation of activity to observation coupled with insight into causal significance. This has occurred in preliminary studies using optogenetics in mapping circuits that are causally associated with disease-related phenomena such as anxiety[39],[40] depression[41], and fear memory[42].

Many of the tool families of optogenetics (see Figure 2.9 above) have the term "opsin" in their name because they are a derivative of opsin genes, which encode light-responsive proteins. This is achieved through the retinal molecule, required by all opsin proteins, and which acts as an antenna for photons. When retinol absorbs light, the photon energy allows the molecule to isomerize (change its location in the protein chain), which triggers a sequence of conformal changes in the protein. Opsin genes are divided into microbial opsins (also known as type I) and animal opsins (type II). The microbial opsin differs from the type II opsins in that it combines light absorption and ion flux into a single protein[43]. Beginning with Channelrhodopsin[44], in 2005, microbial opsins were

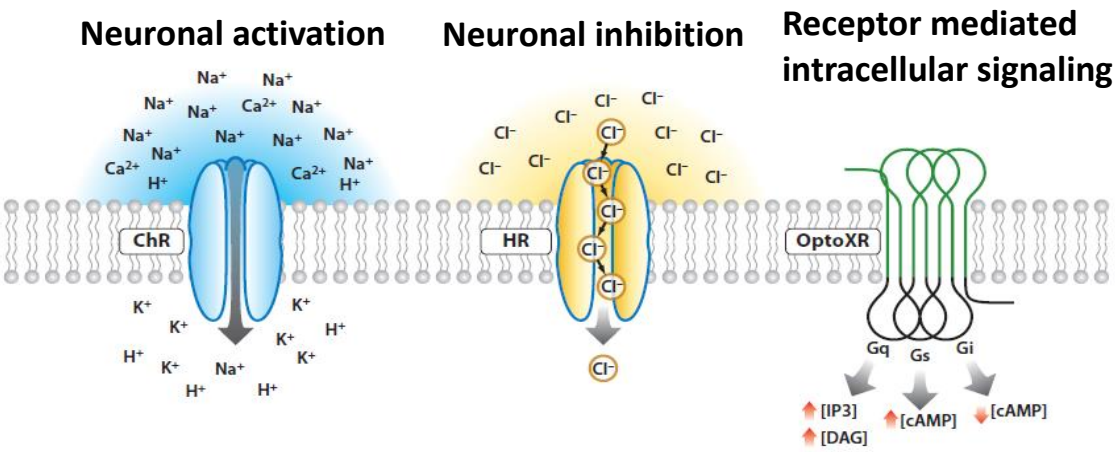

Figure 2.9 Optogenetic tools. Three types of optogenetic tools: Channelrhodopsin (left), Halorhodopsin (center), and rhodopsin-GPCR or G-protein coupled receptor (right). Upon illumination with blue light, Channelrhodopsins conduct inward currents of cations that depolarize the neuron, causing activation. Halorhodopsins, when illuminated with yellow light, conduct chloride ions into the cell, causing neuronal inhibition. OptoXRs respond to green light and activate intracellular signaling pathways like cAMP, which is used for transferring the effects of hormones like adrenaline and other molecules that cannot pass through the cell membrane, into cells. This figure was adapted from Reference 38.

introduced into hippocampal neurons helped in part by the serendipitous fact that sufficient retinal is present in mammalian brains (as well as other vertebrate tissues)[45]. Since then, the optogenetic toolbox has been greatly expanded to include a number of proteins activated by various wavelengths of light (red, in addition to higher spectral specificity in blue, yellow and green wavelengths)[38,46].

While optogenetics has given users unprecedented targeting of specific cell-types, the technology does have some drawbacks. Temporal precision can be problematic as some of the proteins have delayed channel closures or a long (10-12 ms) deactivation time constant, which impairs high speed spiking[47]. Another problem that we specifically address in this thesis (in Chapter 5) is the confinement of light to a specific region of a cell network. Most optogenetic studies involve the use of fiber optic cables to deliver light to the brain area of interest. This can become problematic when attempting to illuminate smaller and smaller regions of the brain. As mentioned above in the introduction, a coaxial structure facilitates local light delivery by confining the illumination area to the micro- and possibly nanoscale-sensing region. The principle of a single coaxial structure as an optrode was validated through the use of a tapered, metal-coated optical fiber for studies in non-human primates[48]. The next section of this thesis discusses local shielding through a coaxial electrode geometry and how this structure can address problems found in both electrophysiology and optogenetic tools.

2.4 Local shielding: coaxial structure, function, parameter space, simulations, reciprocity

This thesis deals with the development of an electrode geometry designed to overcome the perceived limitations of unshielded neural probes. The shielded electrode we have adapted has a coaxial architecture that consists of two concentric metals in a vertically-oriented cylindrical structure, separated by an electrically-insulating layer. The inner metal is a micro/nanowire that acts as a coax core, while the outer metal functions as a shield or faraday cage, in a manner similar to a macroscale radio frequency coaxial cable, such as that used for cable TV. As mentioned, crosstalk between pixels of conventional devices with high spatial resolution is a consequence of their unshielded nature; a shielded coaxial device can suppress this limitation, uniquely allowing increases in functional pixel density beyond extant technologies. Also similar to that macroscale coax is the micro- and nanoscale version's ability to propagate subwavelength electromagnetic radiation, including visible light[49,50]. Nanoscale coaxial arrays have been previously used[51] in a variety of biological[52], chemical[53,54], optical[29,30] and photovoltaic[55] devices, and the device presented herein is another implementation of that basic structure.

In order to tailor a coaxial multielectrode array for use in a particular assay, a number of parameters are considered. The most important parameter is thermal (Johnson–Nyquist) noise of the device since this determines the capability of the device to record the desired neuronal activity (if the internal noise of the device rises above the extracellular voltage of an action potential, the signal will be indiscernible). The Johnson–Nyquist noise is given by the following equation:

$$V_{cp} = \sqrt{4k_B T/C} \tag{8}$$

where k_B is Boltzmann's constant, T the absolute temperature, and C is the capacitance of the device. This equation is discussed in Chapter 3 and real numbers are given for the particular device in that study.

Figure 2.10 shows a point-contact model of the cell-coaxial electrode interface with an equivalent circuit of the cell-electrode junction. V_m is the membrane potential discussed previously, while C_m and R_m are the membrane capacitance and resistance respectively. There are typically given by the following equations:

$$C_m = c_{mem} A_{ce} \tag{9}$$

$$R_m = \frac{1}{g_{mem} A_{ce}} \tag{10}$$

c_{mem} and g_{mem} are the capacitance and conductance per unit area (typical values are 1 μF/cm^2 and 0.3 mS/cm^2, respectively), while A_{ce} is the cell-electrode attached area. The sealing resistance R_{seal} represents the resistance between the cleft and the surrounding solution and is directly proportional to ρ_s/d, the ratio of the resisitivity of the electrolyte solution (typically around 1 Ω·m) to the cell-electrode distance. Just like in patch clamp and sharp electrode experiments, a high R_{seal} is desirable, otherwise crosstalk can occur as current will leak into the extracellular space (and to other electrodes). One improvement 3D structures have over 2D planar electrodes is a higher sealing resistance through cell engulfment of the electrode[56]. To enhance this advantage some studies have been done to bio-functionalize electrodes in an effort to characterize[57] and promote engulfment[58]. However, as the inter-electrode spacing becomes smaller and smaller, the difficulty in maintaining a high R_{seal} increases.

From the point-contact model another important factor to be considered is R_e, the charge-transfer resistance, between the sensing electrode and the electrolyte solution.

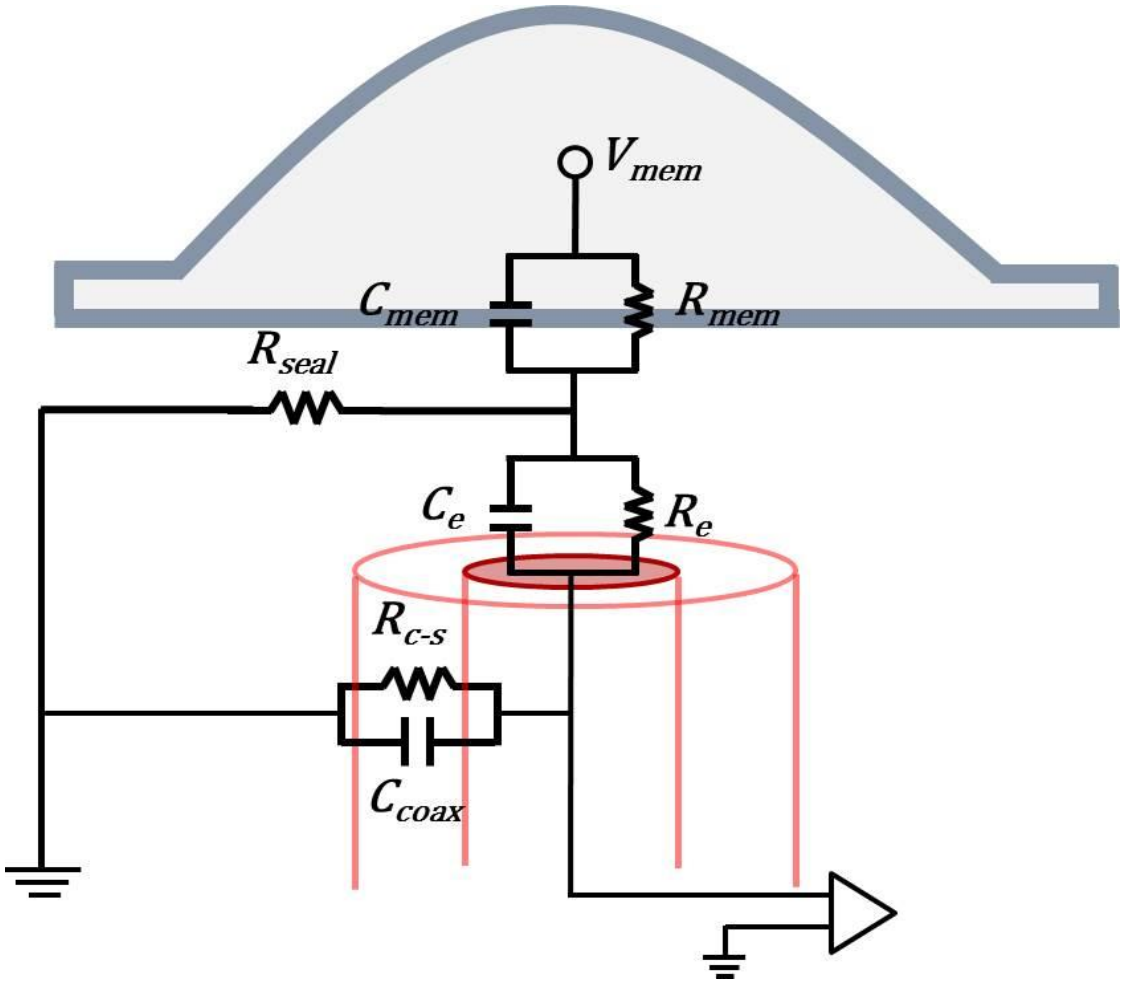

Figure 2.10 Point-Contact model of the cell-electrode interface. Equivalent circuit model of the cell-electrode environment. V_{mem}, C_{mem}, and R_{mem} are the membrane potential, capacitance, and resistance respectively. R_{seal} is the resistance between the cleft and the surrounding solution, similar to the sealing resistance in patch clamp and sharp electrode experiments. C_e is the double layer capacitance and R_e is the charge–transfer or electrode resistance. C_{coax} is the capacitance of the coaxial structure (plus stray capacitance from the end) and $R_{c\text{-}s}$ is the resistance between the core and shield layers.

This "electrode resistance" represents the faradic process where charges transfer between the core electrode and the electrolyte by means of oxidation-reduction reactions. During a faradic charge-transfer, this factor can be expressed as:

$$R_e = \left(\frac{k_B T}{zq}\right)\left(\frac{1}{J_0 A_{el}}\right) \qquad (11)$$

With z being the number of electrons involved in the reaction, J_0 is the exchange current density, and A_{el} is the electrode surface area. By inspecting the units, we can see this equation is essentially a version of ohm's law and therefore has been written with two terms on the right hand side of the equation, to mirror the fundamental equation: $R = V/I$. The denominator of the second term in the right hand side of (11) underscores the importance of the sensing electrode surface area, as it is indirectly related to the electrode resistance. In other words, the more surface area of a sensing element, the lower the charge-transfer resistance, and therefore, a larger fraction of the signal will be recorded. Later, we will show results from simulations which illustrate that increasing electrode surface area by lowering the outer metal of a coaxial electrode increases the sensing capability of the device.

The last term to be discussed is $R_{c\text{-}s}$, the resistance between the core and shield of the coax. This resistance is determined by the thickness and electric permittivity of the dielectric material between the core and shield. It is important for the core-shield resistance to be high (GΩ range) because a low value (below 1 kΩ) represents an electrical short between the two metal layers and therefore will lose the shielding effect of the outer metal. Furthermore, since the outer metal is set to ground, any signal originating from a cell sitting above the device will not be seen if the two metals are shorted.

In a preliminary effort to understand the environment around a coaxial electrode in close proximity to a neuron, a computational model was made using the finite element method (FEM) simulation software Quickfield. One of the limitations of this simulation software was that it was only capable of creating a two dimensional model. A 2D model was sufficient for simulating a single coaxial structure because we were able to create a pseudo 3D model by applying rotationally symmetric boundary conditions about the core axis (+z direction). However, when using an array of coaxial electrodes, the model remained 2D and the only boundary conditions we applied were ones on the domain sidewalls to make an infinite linear array of coaxes as well as Dirichlet boundary conditions (the potential, $\Phi = 0$ as $r \to \infty$). Figure 2.11 shows the equipotential lines emanating from inner metal electrodes, each biased at 1 mV and surrounded on each side by two electrodes, representing the outer (shielding) metal of a coaxial geometry, set to ground. In the model, the heights of the electrodes are 1500 nm (representing 100 % shielding) and the pitch of the array is 2000 nm. Since this was a preliminary simulation, with few inputs for material characteristics (i.e. no conductivity or permittivity input), it will not be discussed further, other than to note that the results do not deviate greatly from the more robust subsequent simulations.

A second, more robust, computational model of the coaxial device was made using the FEM simulation software COMSOL Multiphysics, with the intention to simulate the environment in which a neuron is in close proximity to multiple electrodes. This time, the model was 3D and realistic materials parameters taken from literature were employed. A hexagonal pattern of coaxial electrodes was placed in an electrolyte solution having the same electrical properties as the medium used in experiment, i.e. dielectric

constant ε ~ 80, electrical conductivity σ ~ 1.5 S/m. Although the detection of field potentials *in situ* is influenced by myriad factors including cell type, distance from electrode and the nature of the contact with electrodes, the purpose of this simulation was to find the amplitude of the potential at the recording electrode surface generated by a source (e.g. neuron spike) as a function of separation distance. Green-Lorentz reciprocity[59] reduces this problem to solving Poisson's equation for the scalar potential generated from the recording electrode as a voltage source. The simulations, shown in Fig. 2.12, were performed for non-shielded electrodes (Fig. 2.12a), coaxial electrodes with an outer shield electrode comprising 25% of the inner (recording) electrode height (Fig. 2.12b), and coaxial electrodes with a shield comprising 85% of the inner electrode height (Fig. 2.12c).

The device was modeled with the inner metal at a fixed potential (100 μV) and the outer metal at ground (reference), placed in a conducting solution. From the simulations, we were able to generate profiles of the recording field surrounding the electrodes. 2D cross-sections of the profiles are shown in Fig. 2.12 for microcoaxes having 5 μm core height and 10 μm array pitch. Keeping the core height constant, we simulated various shield heights (Fig. 2.12 b,c) and compared the results to the case of bare electrodes (i.e. no shield, Fig. 2.12a). It is clear that as the shield height becomes closer to that of the core, the recording field spatial localization improves. Comparing the overlapping profile regions in each of the regimes shown (bare electrode, 25% shield height, 85% shield height), it can be seen that the field near bare electrodes overlaps that of its neighbors, while this overlap is suppressed for shielded electrodes. In other words,

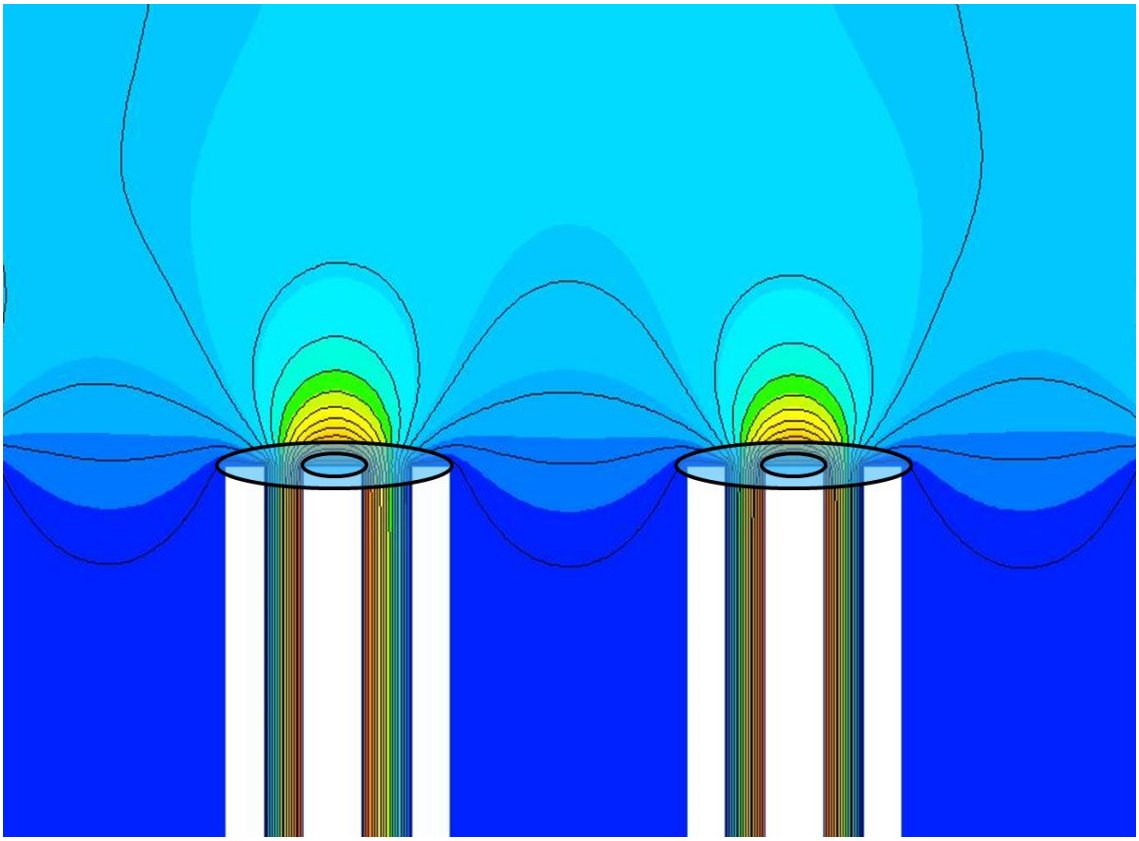

Figure 2.11 2D Quickfield simulation of electric potential profile from linear array of coaxes. Equipotential contours for infinite linear array of coaxial electrodes. 2D pseudo coaxial coaxial structure given by center (core) electrode surround on either side by shielding electrodes. Heights of electrodes are 1.5 μm and the array pitch is 2 μm. Core electrodes are biased at 1 mV while shields are set to ground. Top of coax added for guide.

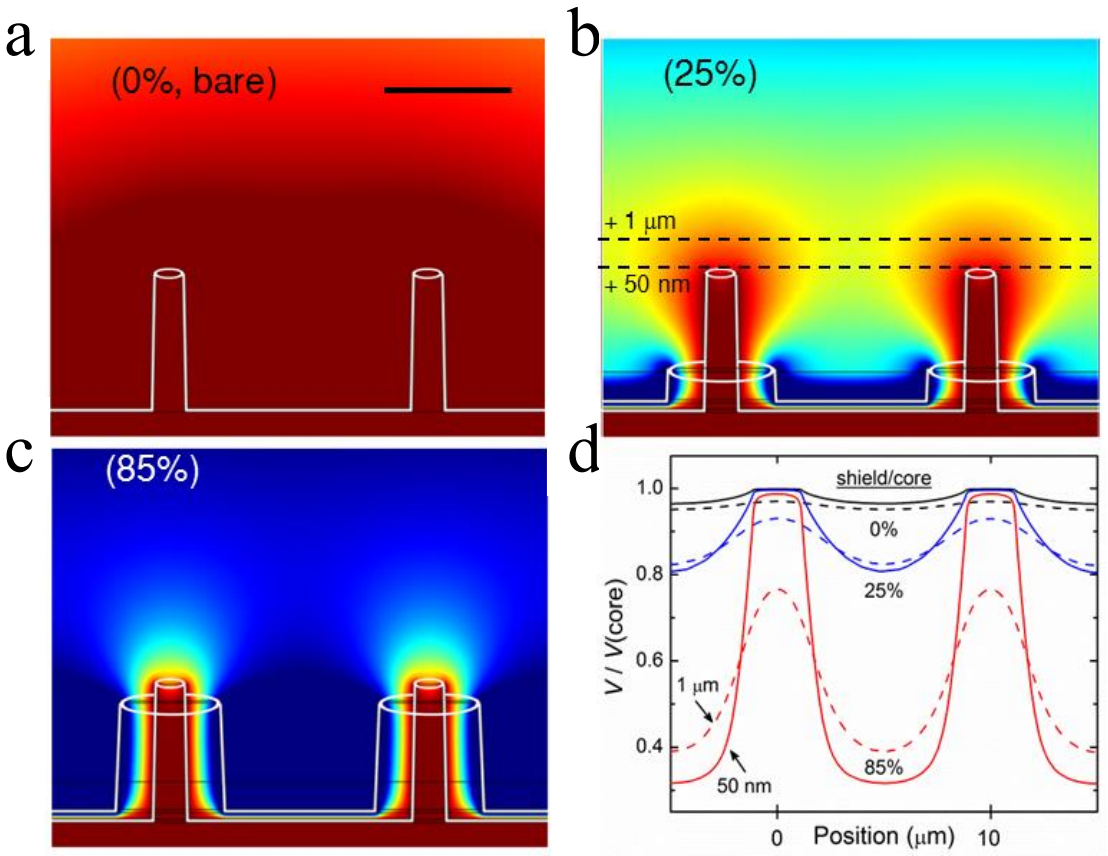

Figure 2.12 Simulation of electric potential profile. (a) Equipotential contours for bare (unshielded) electrodes, 5 µm tall and 10 µm apart, biased at 100 µV (ground at infinity). (b) Electrodes with grounded shield 25% the height of the biased core (1.25 µm). Scale bar: 5 µm. (c) Electrodes with grounded shield 85% the height of the biased core (4.25 µm). Dark red represents areas where > 95% of the signal from the point current source would be seen by the electrode while dark blue represents areas where < 20% of the signal would be seen. As the shield progresses in height, overlapping areas shrink and result in discretized electrodes, and thus lower electrical crosstalk. (d) Plots of electric potential for the three cases shown, plotted for two constant heights above the core tips, 50 nm and 1 µm, and scaled to the core potential, further demonstrating the virtue of the shielded architecture: bare electrodes only negligibly resolve the spatial variation of V, while the shielded coaxes in Fig. 2.12c show clear discrimination.

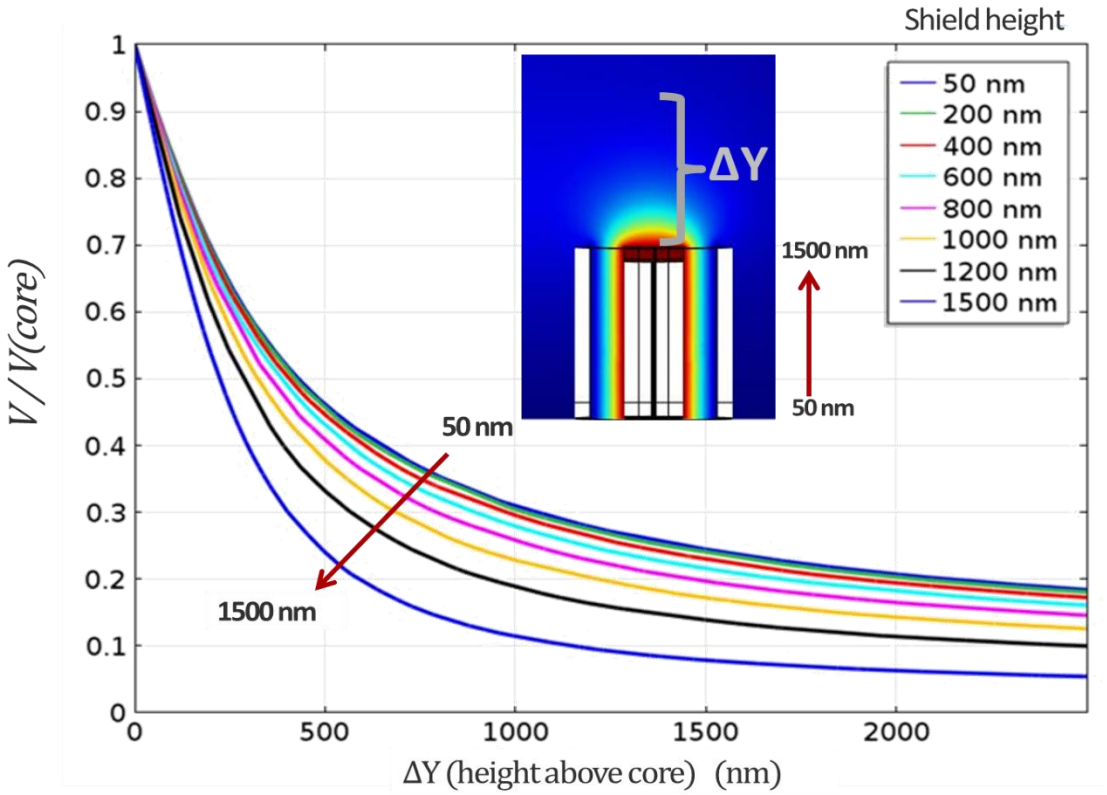

Figure 2.13 Simulation of different shield heights. The fractional voltage vs. height above the core electrode is plotted for various shield heights. Inset, shown in the upper center-right, is a 2D cross section of the model. Height of the core is 1500 nm and has been biased at 1 mV. Shield height starts at 50 nm (3% of core height) and is incrementally increased up to 1500 nm (100% of core height). Fractional voltage decreases with increasing shield height at all distances above the core electrode.

locally-shielded electrodes suppress electrical crosstalk. By approximating the proximity of an electrogenic cell to our electrode array to be 50 nm or more[60], we were able to obtain a range of shield heights appropriate for sensitive extracellular action potential recording and crosstalk suppression. The results of the simulations can be quantified by plotting the fraction of the electric potential of the core (e.g. 100 μV) that would be sensed certain distances from the core. Figure 2.12d shows calculations of this proportion, V/V(core), for two heights above the cores, 50 nm (solid lines) and 1 μm (dashed lines), for the three cases of Fig. 2.12a, b and c, plotted along a horizontal distance. At 50 nm height, V above a core (i.e. Position ~0 or 10 μm) and V between cores (Position ~5 μm) differ by only 3% for the bare electrodes, but by more than a factor of 3 for the 85% shielded coaxes. At 1 μm height, the bare electrodes differ by <2%, and the 85% shielded coaxes by ~100% (i.e. a factor of 2), for these positions. Similar simulations were done for smaller, nanoscale coaxes, with comparable results, confirming that the shielding discussed here improves pixel discretization at all scales.

As was mentioned in the point-contact model discussion, one method for increasing the purview or sensing area of the coaxial electrode is to lower the outer metal acting as an electromagnetic shield thereby increasing the surface area of the sensing (inner) electrode. Although this increases the crosstalk between sensing elements, simply having a local shield (even 10% the height of the core electrode) is an advantage over bare electrodes (in reference to crosstalk). In order to characterize this parameter, we computationally modeled the coaxial array in an effort to find the correlation of sensitivity and shield height. Figure 2.13 shows results from a COMSOL simulation of a single coaxial structure, biased to 100 μV with a 1.5 μm core height. An inset above the

data shows a 2D cross section of the model. This shows the fractional voltage sensed as a function of height above the core electrode for various shield heights, ranging from 50 nm to 1.5 μm). It is clear from the data the highest sensitivity occurs when the shield height is at its lowest (50 nm). In analyzing these data, it is important to consider the location of the cut line from where the data were extracted; in this case, it was perpendicular to the plane of top of the core electrode. From Figures 2.11-12 as well as the inset in 2.13, it is evident that the equipotential lines are not isotropic when there is a shield present, as the grounded outer electrode seems to have a slight squeezing effect on the equipotential lines. This is precisely the effect we desire in suppressing crosstalk, as the most favorable path for current in the extracellular space will be directly above the sensing electrode. A similar study to the one in Figure 2.13, one that also varied the angle of the data cut line, would show a sharp cut off in sensitivity at a given distance for low angles (taken from the plane of the top of the coax) when the shield is close to the height of the core. As the shield is lowered, this cut off would relax as the field would become more isotropic. In conclusion, lowering the shield is a compromise between gaining spatial sensitivity at high angles, or directly above the sensing electrode (good), while also increasing spatial sensitivity at low angles (leads to crosstalk).

Given the scale invariance of Maxwell's equations, which govern the electromagnetic environment at the cell-coaxial electrode interface, we built a macroscale model of the device to test its ability as a dielectric sensor. The program PCB express was used to create a PC board with a 10x10 array of concentric metal rings (representing the top of an open-ended coax) and a bud box was altered to function as a platform for the board (Figure 2.14). In this geometry, the stray capacitance of the concentric ring

structure is affected by any perturbation in the local dielectric environment (just like that of a nanoscale open-ended coax). BNC connectors were attached to the topside of the bud box and coaxial cable was used to attach the connector to the PC board. BNC cables were used to connect the board to a capacitance bridge, and the capacitance between the inner and outer ring of each node in the array was tested to create a baseline contour plot (Figure 2.15). The outer ring was grounded and the inner ring was left floating. Once this baseline capacitance was established, various materials were placed onto the board and the capacitance was re-measured for each of the 100 nodes. Figures 2.16 and 2.17 show the results of two experiments, the first in placing an object with a high dielectric constant (it was mostly water) in the middle of the board, while the second shows results from placing 2 objects of different dielectric constants ($\varepsilon\sim 8$ and $\varepsilon\sim 80$) on opposite corners of the board. From these figures, we see that not only does the board qualitatively sense where the object is (Figure 2.16), it quantitatively senses the different dielectric constants of the objects (Figure 2.17). From these results, we felt confident in the coaxial architecture's viability as a biological sensor. The next step was to build the device on a much smaller (micro- and nanoscale level) and to test it on neuronal assemblies.

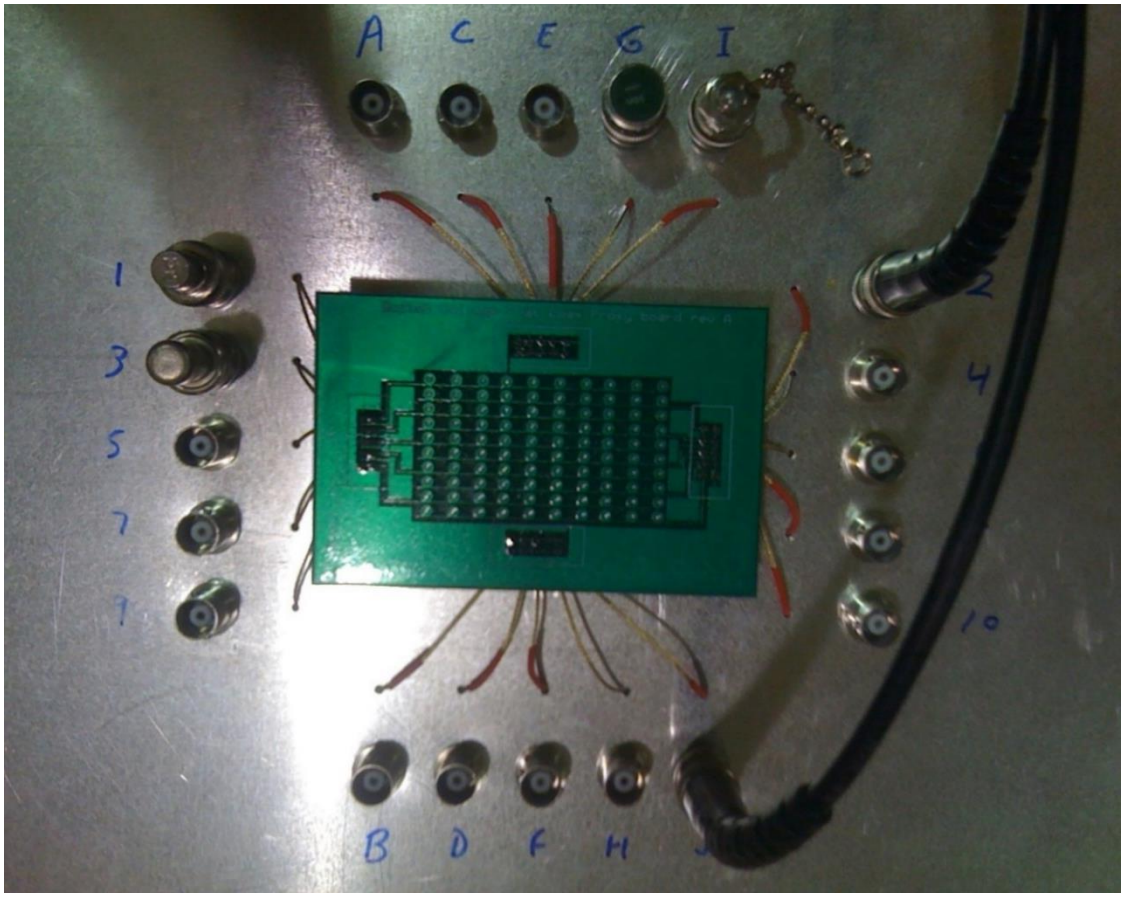

Figure 2.14 PC board of capacitor array and platform. A 10x10 capacitor array of concentric metal rings was attached to a bud box fabricated with BNC connectors around the exterior.

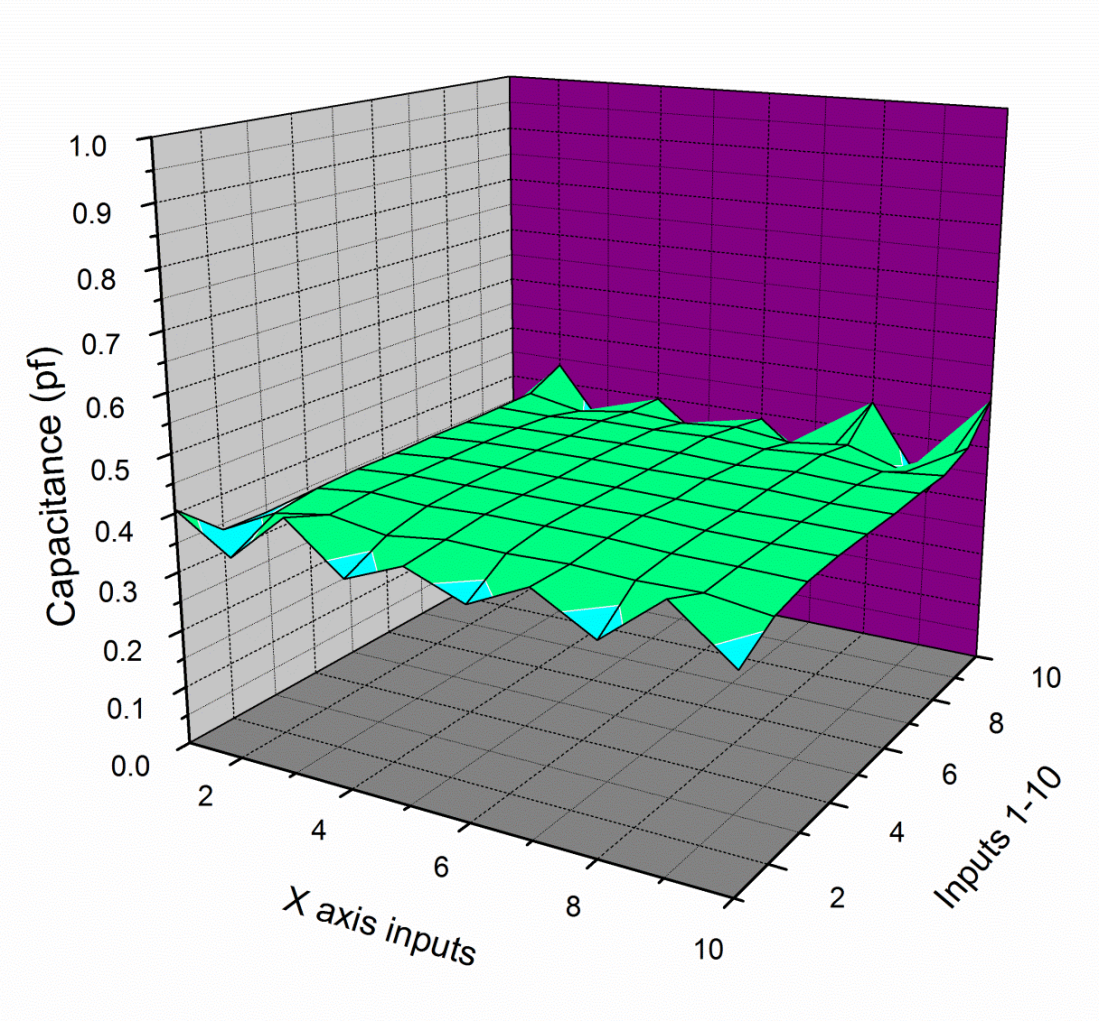

Figure 2.15 3D contour of baseline capacitance. Each node of a 10x10 array of capacitors was measure by a capacitance bridge to obtain a baseline capacitance for the board.

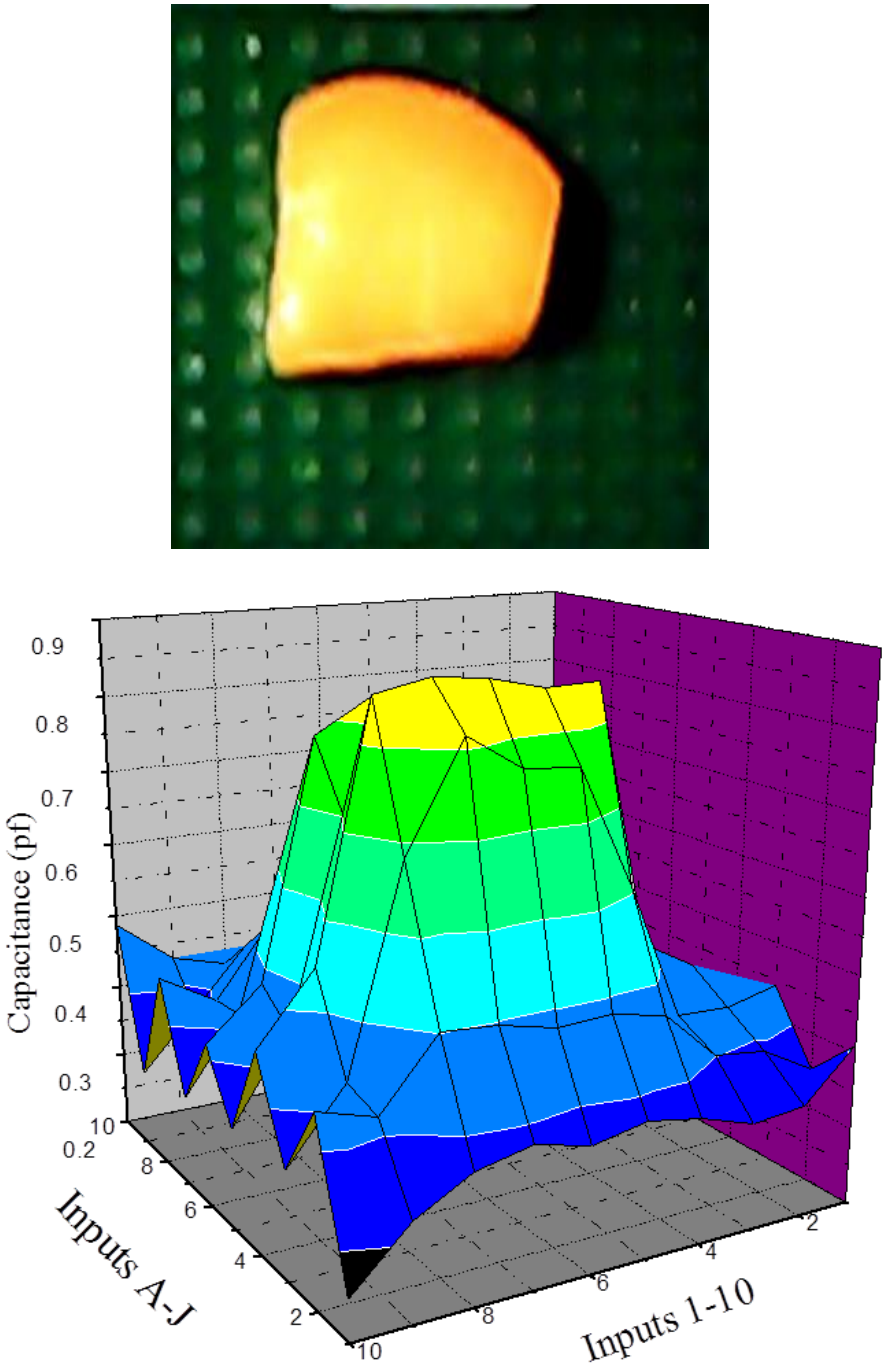

Figure 2.16 3D contour of change in capacitance. Object with dielectric strength ε~80 placed onto capacitor array and measured. Change in capacitance occurs where object is located.

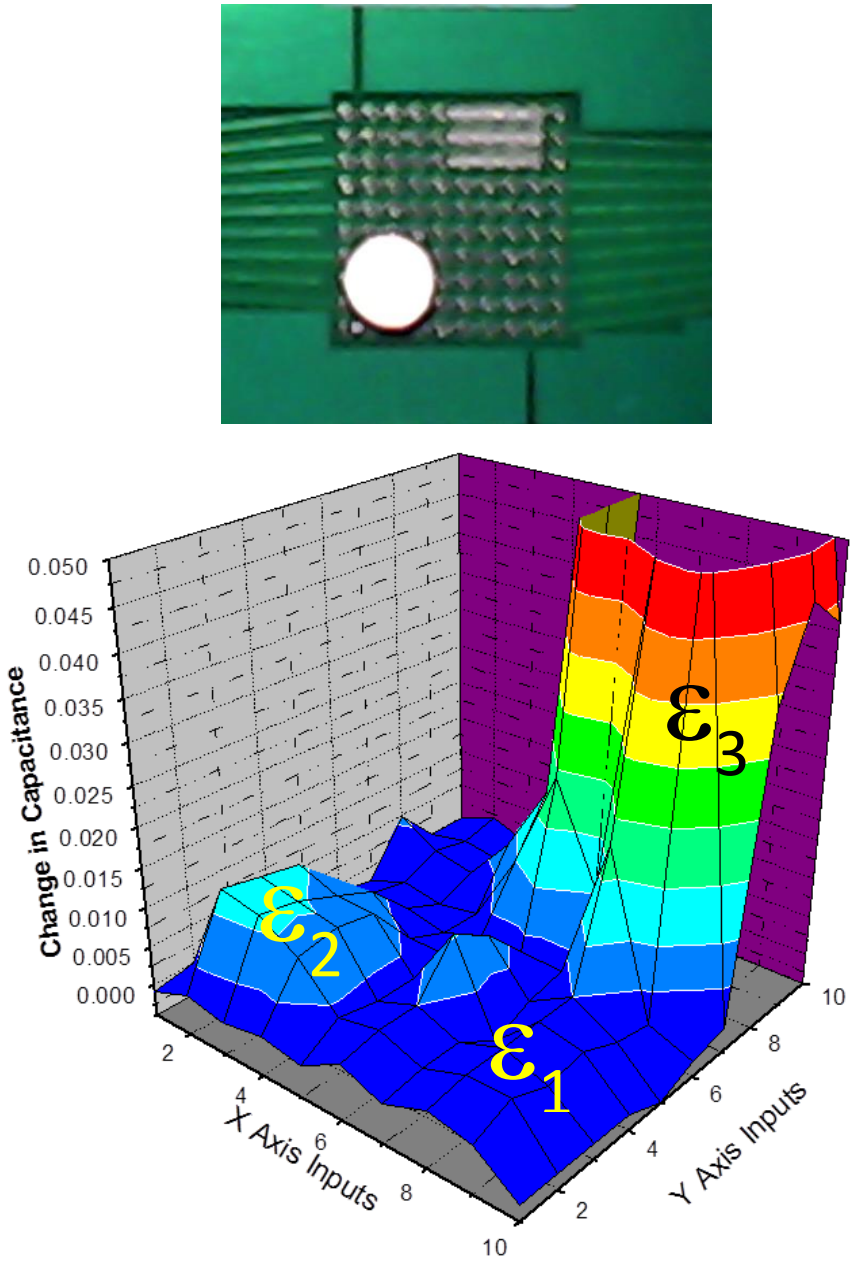

Figure 2.17 3D contour plot of change in capacitance. 2 objects with different dielectric constants ($\varepsilon_2 \sim 8$ and $\varepsilon_3 \sim 80$) placed onto the capacitor array. Plot shows clear location of objects as well as quantitative difference between dielectric strength of the objects.

2.5 References

[1] Buzsáki, G., Stark, E., Berényi, A., Khodagholy, D., Kipke, D. R., Yoon, E., et al. Tools for probing local circuits: high-density silicon probes combined with optogenetics. Neuron **86**, 92-105 (2015).

[2] Blanche, T. J., Spacek, M. A., Hetke, J. F., & Swindale, N. V. Polytrodes: high-density silicon electrode arrays for large-scale multiunit recording. J. Neurophysiol. **93**, 2987-3000 (2005).

[3] Bakkum, D. J., Frey, U., Radivojevic, M., Russell, T.L., Müller, J., Fiscella, et al. Tracking axonal action potential propagation on a high-density microelectrode array across hundreds of sites. Nat. Commun. **4**, 2181 (2013).

[4] Hierlemann, A., Frey, U., Hafizovic, S., & Heer, F. Growing cells atop microelectronic chips: interfacing electrogenic cells in vitro with CMOS-based microelectrode arrays. Proc. IEEE **99**, 252-284 (2011).

[5] Multichannel Systems MCS GmbH, Reutlingen Germany.

[6] Seymour, J. P., & Kipke, D. R. Neural probe design for reduced tissue encapsulation in CNS. Biomaterials **28**, 3594-3607 (2007).

[7] Najafi, K., & Wise. K.D. An implantable multielectrode array with on-chip signal processing. *IEEE* J. Solid-State Circuits **21**, 1035-1044 (1986).

[8] Maynard, E. M., Nordhausen, C.T., & Normann, R.A., The Utah intracortical electrode array: A recording structure for potential brain-computer interfaces. Electroen. Clin. Neuro. **102**, 228-239 (1997).

[9] Rodger, D. C., Fong, A.J., Li, W., Ameri, H., Ahuja, A.K., Gutierrez, C., et al. Flexible parylene-based multielectrode array technology for high-density neural stimulation and recording. Sens. Actuator B-Chem. **132**, 449-460 (2008).

[10] Spira, M.E. & Hai, A. Multi-electrode array technologies for neuroscience and cardiology. Nat. Nanotechnol. **8**, 83-94 (2013).

[11] Robinson, J. T., Jorgolli, M., Shalek, A. K., Yoon, M. H., Gertner, R. S., & Park, H. Vertical nanowire electrode arrays as a scalable platform for intracellular interfacing to neuronal circuits. Nat. Nanotechnol. **7**, 180-184 (2012).

[12] Duan, X., Gao, R., Xie, P., Cohen-Karni, T., Qing, Q., Choe, H.S., et al. Intracellular recordings of action potentials by an extracellular nanoscale field-effect transistor. Nat. Nanotechnol. **7**, 174-179 (2012).

[13] Voelker, M., & Fromherz, P. Signal transmission from individual mammalian nerve cell to field-effect transistor. Small **1**, 206-210 (2005).

[14] Hai, A., Dormann, A., Shappir, J., Yitzchaik, S., Bartic, C., Borghs, et al. Spine-shaped gold protrusions improve the adherence and electrical coupling of neurons with the surface of micro-electronic devices. J. R. Soc. Interface **6**, 1153-1165 (2009).

[15] Xie, C., Lin, Z., Hanson, L., Cui, Y., & Cui, B. Intracellular recording of action potentials by nanopillar electroporation. Nat. Nanotechnol. **7**, 185-190 (2012).

[16] Lin, Z. C., Xie, C., Osakada, Y., Cui, Y., & Cui, B. Iridium oxide nanotube electrodes for sensitive and prolonged intracellular measurement of action potentials. Nat. Commun. **5**, 3206 (2014).

[17] Frey, U., Heer, F., Pedron, R., Ballini, M., Müeller, J., Bakkum, D., et al. Switch-matrix-based high-density microelectrode array in CMOS technology. IEEE J. Solid-State Circuits **45**, 467-482 (2010).

[18] Hutzler, M., Lambacher, A., Eversmann, B., Jenkner, M., Thewes, R. & Fromherz, P. High-resolution multitransistor array recording of electrical field potentials in cultured brain slices. J. Neurophysiol. **96**, 1638-1645 (2006).

[19] Nadasdy, Z., Csicsvari, J., Penttonen, M., & Buzsáki, G. Extracellular recording and analysis of neuronal activity: from single cells to ensembles in Neuronal Ensembles: Strategies for Recording and Decoding, eds. Eichenbaum, H. & Davis, J. L. (New York, Wiley-Liss) (1998).

[20] Einevoll, G. T., Franke, F., Hagen, E., Pouzat, C., & Harris, K. D. Towards reliable spike-train recordings from thousands of neurons with multielectrodes. Curr. Op. Neurobio. **22**, 11-17 (2012).

[21] Obien, M. E. J., Deligkaris, K., Bullmann, T., Bakkum, D. J., & Frey, U. Revealing neuronal function through microelectrode array recordings. Front. Neurosci. **8**, 423 (2014).

[22] Zhang, J., Laiwalla, F., Kim, J.A., Urabe, H., Van Wagenen, R., Song, Y.K., et al. Integrated device for optical stimulation and spatiotemporal electrical recording of neural activity in light-sensitized brain tissue. J. Neur. Eng. **6**, 055007 (2009).

[23] Boyden, E. S., Zhang, F., Bamberg, E., Nagel, G., & Deisseroth, K. Millisecond-timescale, genetically targeted optical control of neural activity. Nat. Neurosci. **8**, 1263-1268 (2005).

[24] Deisseroth, K. Controlling the brain with light. Sci. Amer. **303**, 48-55 (2010).

[25] Butovas, S., & Schwarz, C. Spatiotemporal effects of microstimulation in rat neocortex: a parametric study using multielectrode recordings. J. Neurophysiol. **90**, 3024-3039 (2003).

[26] Zhang, J., Laiwalla, F., Kim, J.A., Urabe, H., Van Wagenen, R., Song, Y.K., et al. Integrated device for optical stimulation and spatiotemporal electrical recording of neural activity in light-sensitized brain tissue. J. Neur. Eng. **6**, 055007 (2009).

[27] Kim, T.I., McCall, J.G., Jung, Y.H., Huang, X., Siuda, E.R., Li, Y., et al. Injectable, cellular-scale optoelectronics with applications for wireless optogenetics. Science **340**, 211-216 (2013)

[28] Wu, F., Stark, E., Ku, P.C., Wise, K.D., Buzsáki, G. and Yoon, E., Monolithically integrated μLEDs on silicon neural probes for high-resolution optogenetic studies in behaving animals. Neuron **88**, 1136-1148 (2015).

[29] OpenStax College. Neurons and Glial Cells, OpenStax-CNX Web site. http://legacy.cnx.org/content/m44747/1.4/, May 27, 2016

[30] Hobbie, R. K. Intermediate physics for medicine and biology. 3rd edition. (American Institute of Physics, New York) (1997)

[31] OpenStax College. How Neurons Communicate, OpenStax-CNX Web site. http://cnx.org/contents/185cbf87-c72e-48f5-b51e-f14f21b5eabd@10.8, Mar 23, 2016

[32] Cole, K. S. Dynamic electrical characteristics of the squid axon membrane. Arch. des Sci. Physiol. **3**, 253-258 (1949).

[33] Hodgkin, A. L., Huxley, A. F., & Katz, B. Measurement of current-voltage relations in the membrane of the giant axon of Loligo. J. of Physiol. **116**, 424-448 (1952).

[34] Sherman-Gold, R. The axon guide for electrophysiology & biophysics: Laboratory techniques. Axon Instruments, (1993).

[35] Oesterle, A. "P-1000 & P-97 Pipette Cookbook." (2011).

[36] Biran, R., Martin, D. C., & Tresco, P. A. The brain tissue response to implanted silicon microelectrode arrays is increased when the device is tethered to the skull. J. Biomed. Mat. Res. Part A **82**, 169-178 (2007).

[37] Alivisatos, A. Paul, et al. Nanotools for neuroscience and brain activity mapping. ACS Nano 7, 1850-1866 (2013).

[38] Fenno, L., Yizhar, O., & Deisseroth, K. The development and application of optogenetics. Annu. Rev. Neurosci. **34**, 389-412 (2011).

[39] Tye, K. M., & Deisseroth, K. Optogenetic investigation of neural circuits underlying brain disease in animal models. Nat. Rev. Neurosci. **13**, 251-266 (2012).

[40] Allsop, S. A., Vander Weele, C. M., Wichmann, R., & Tye, K. M. Optogenetic insights on the relationship between anxiety-related behaviors and social deficits. Front. Behav. Neurosci. **8**, 241 (2014).

[41] Tye, Kay M., et al. Dopamine neurons modulate neural encoding and expression of depression-related behaviour. Nature **493** 537-541 (2013).

[42] Liu, X., Ramirez, S., Pang, P. T., Puryear, C. B., Govindarajan, A., Deisseroth, K., & Tonegawa, S. Optogenetic stimulation of a hippocampal engram activates fear memory recall. Nature **484**, 381-385 (2012).

[43] Oesterhelt, D., & Stoeckenius, W. Rhodopsin-like protein from the purple membrane of Halobacterium halobium. Nature **233**, 149-152 (1971).

[44] Boyden, E. S., Zhang, F., Bamberg, E., Nagel, G., & Deisseroth, K. Millisecond-timescale, genetically targeted optical control of neural activity. Nat. Neurosci. **8**, 1263-1268 (2005).

[45] Deisseroth, K., Feng, G., Majewska, A. K., Miesenböck, G., Ting, A., & Schnitzer, M. J. Next-generation optical technologies for illuminating genetically targeted brain circuits. J. Neurosci. **26**, 10380-10386 (2006).

[46] Zhang, Feng, et al. The microbial opsin family of optogenetic tools. Cell **147**, 1446-1457 (2011).

[47] Gradinaru, V., Thompson, K. R., Zhang, F., Mogri, M., Kay, K., Schneider, M. B., & Deisseroth, K. Targeting and readout strategies for fast optical neural control in vitro and in vivo. J Neurosci. **27**, 14231-14238 (2007).

[48] Ozden, I., Wang, J., Lu, Y., May, T., Lee, J., Goo, W., et al. A coaxial optrode as multifunction write-read probe for optogenetic studies in non-human primates. J. Neurosci. Meth. **219**, 142-154 (2013).

[49] Rybczynski, J., Kempa, K., Herczynski, A., Wang, Y., Naughton, M.J., Ren, Z.F., Huang, et al. Subwavelength transmission line for visible light. Appl. Phys. Lett. **90**, 021104 (2007).

[50] Merlo, J. M., Ye, F., Rizal, B., Burns, M.J. and Naughton, M.J. Near-field observation of light propagation in nanocoax waveguides. Optics Expr. **22**, 14148-14154 (2014).

[51] Rizal, B., Merlo, J. M., Burns, M. J., Chiles, T. C., & Naughton, M. J. Nanocoaxes for optical and electronic devices. Analyst **140**, 39-58 (2015).

[52] Archibald, M.M., Rizal, B., Connolly, T., Burns, M.J., Naughton, M.J. & Chiles, T.C. A nanocoaxial-based electrochemical sensor for the detection of cholera toxin. Biosens. and Bioelect. **74**, 406-410 (2015).

[53] Zhao, H., Rizal, B., McMahon, G., Wang, H., Dhakal, P., Kirkpatrick, T., et al. Ultrasensitive chemical detection using a nanocoax sensor. ACS Nano **6**, 3171-3178 (2012).

[54] Rizal, B., Archibald, M.M., Connolly, T., Shepard, S., Burns, M.J., Chiles, T.C. et al. Nanocoax-based electrochemical sensor. Analyst. Chem. **85**, 10040-10044 (2013).

[55] Naughton, M. J., Kempa, K., Ren, Z.F., Gao, Y., Rybczynski, J., Argenti, N., et al. Efficient nanocoax‐based solar cells. Phys. Stat. Sol. (RRL) **4**, 181-183 (2010).

[56] Hai, A., Shappir, J., & Spira, M. E. Long-term, multisite, parallel, in-cell recording and stimulation by an array of extracellular microelectrodes. J. Neurophysio. **104**, 559-568 (2010).

[57] Santoro, Francesca, et al. Interfacing electrogenic cells with 3D nanoelectrodes: position, shape, and size matter. ACS nano **8**, 6713-6723 (2014).

[58] Hai, A., Shappir, J., & Spira, M. E. In-cell recordings by extracellular microelectrodes. Nat. Meth. **7**, 200-202 (2010).

[59] Lorentz H. A. het theorema van Poynting over energie in het electromagnetisch veld eneen paar algemeene stellingen over de voorplanting van het licht, Vers. Konig. Akad. Wetensch. **4**, 176 (1896).

[60] Fromherz, P. Neuroelectronic interfacing with semiconductor chips in Nanoelectronics and Information Technology, Waser, R., ed. (Berlin, Wiley-VCH Verlag). 783-810 (2003).

Chapter 3: Proof of concept using coaxial nanoelectrode arrays and Hirudo Medicinalis

3.1 Introduction

To test the utility of the coaxial multielectrode array as an extracellular sensing device, a suitable biological paradigm (*i.e*. electrogenic cell-type) had to be chosen. The ideal candidate should satisfy the following criteria: (1) large in surface area (at least 20 μm in diameter) (2) magnitude of extracellular action potential on the order of 100 μV or greater and (3) fire spontaneously (*i.e.* not requiring chemical or electrical stimulis for action potential generation). The medicinal leech proved to be an ideal model for testing a multielectrode extracellular device, as it satisfied all 3 requirements, and facilitated the use of the device in passive extracellular recording.

The medicinal leech or *Hirudo Medicinalis* has been used for medicinal applications and basic research since the days of ancient Greece and India[1]. This invertebrate animal was studied extensively by anatomists in the 19th century for its simple model of a nervous system; it has 21 body ganglia segments arranged in a linear fashion along its central axis (Figure 3.1), each containing around 400 neurons[2] (Figure 3.2). The neuron cell bodies range from 10 μm to 60 μm in diameter and are arranged in 6 groups within the ganglia called packets. The ganglia are joined by 2 lateral connectives that contain bundles of nerve fibers and a thin connective called the Faivre's nerve. A fibrous sheath covers the nerve cord and must be removed prior to recording, as this dielectric material acts to insulate the electric signals traveling along the main axis. In the 1960s, neurophysiology techniques were applied to the leech nervous system and it was demonstrated that the physiological interactions of the leech individual neurons were

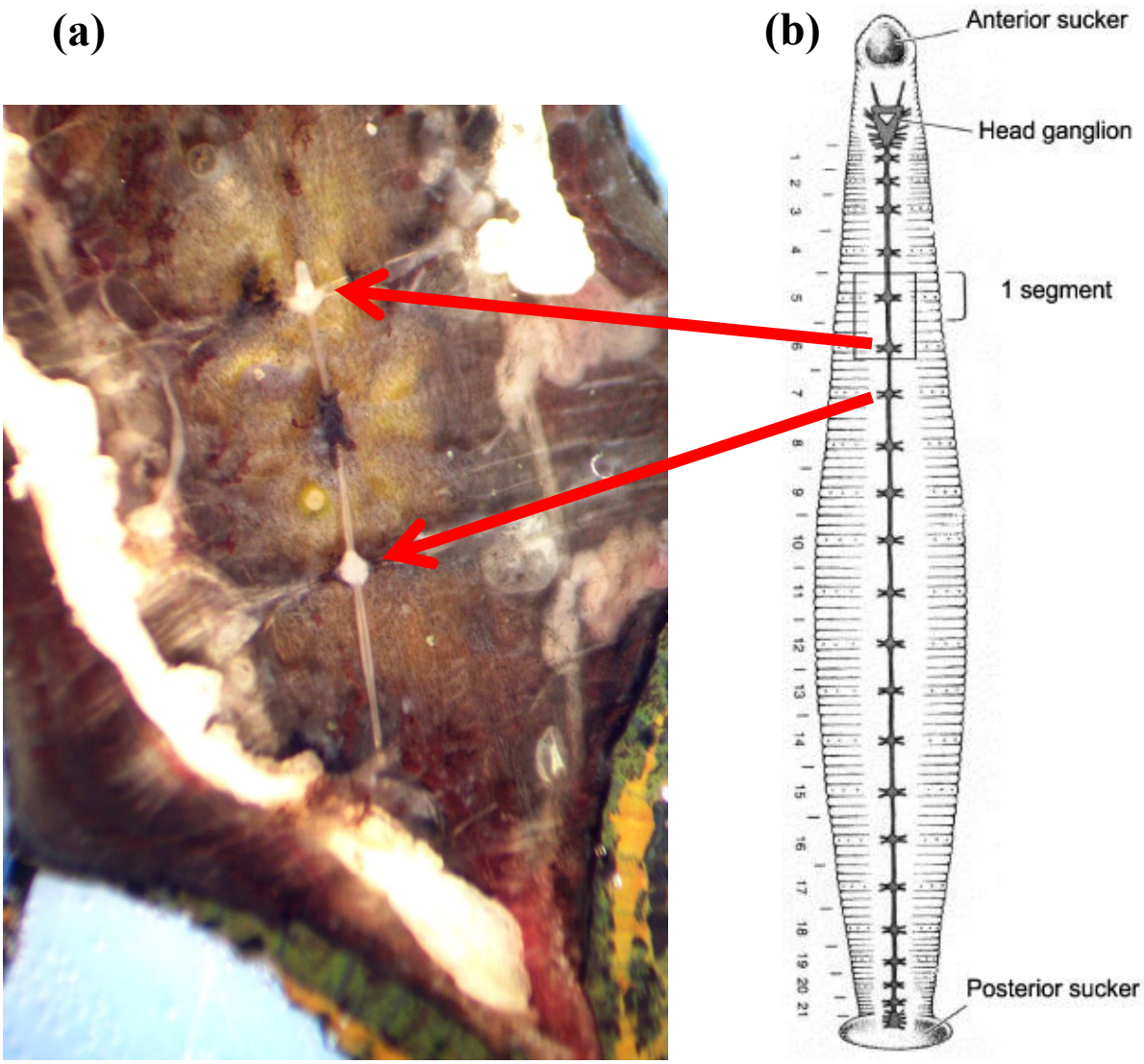

Figure 3.1 Leech anatomy. (a) Partially dissected leech with de-sheathed nerve cord showing two ganglion sacs to be extracted for extracellular recording. (b) Schematic of leech nerve cord anatomy with 21 ganglion sac segments (Reference 2).

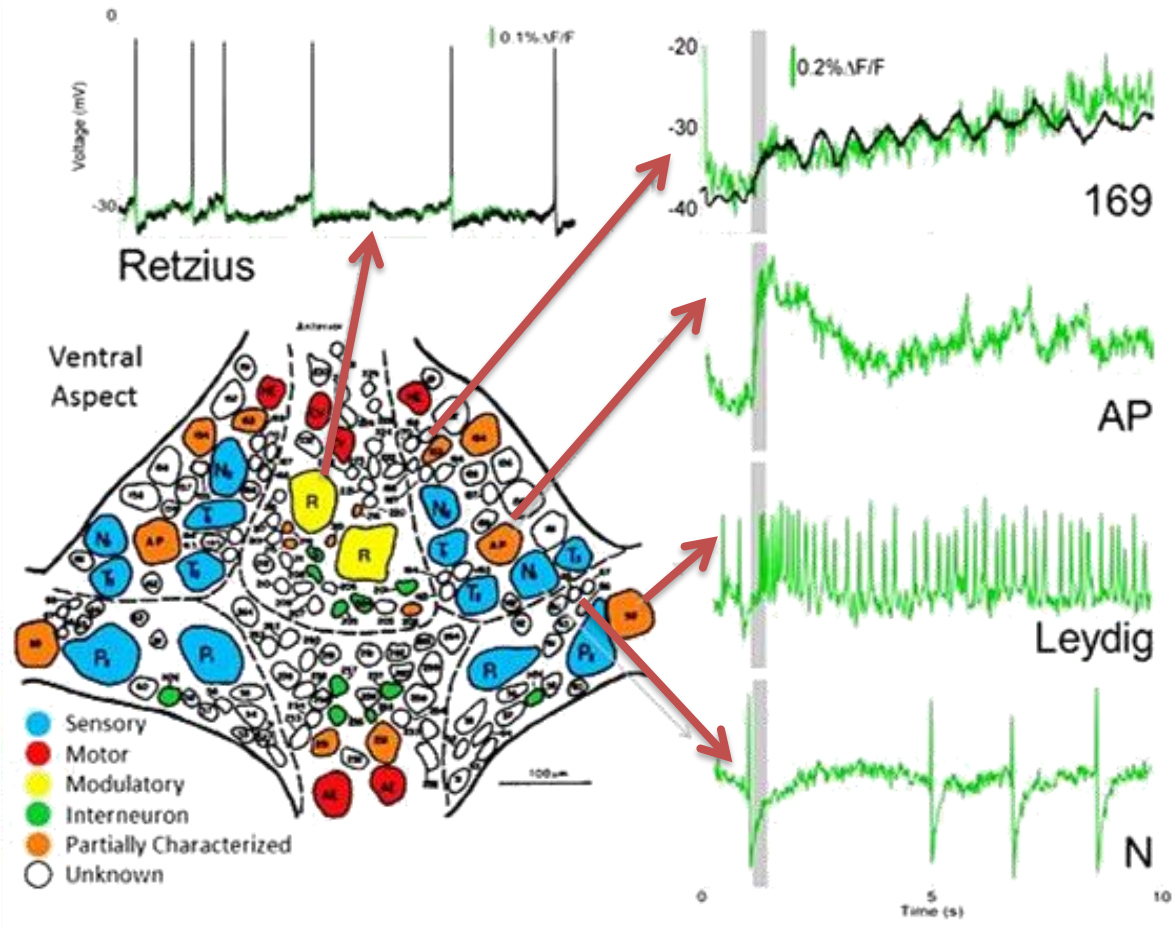

Figure 3.2 Atlas of cells contained within leech ganglion sac. Atlas of ganglion sac shown with waveform of various cell-types.

identified by morphological appearance and the diagnosis was confirmed by intracellular recordings[3]. Waveform traces of these cell types as well as the Retzius cell type can be found throughout the literature and, along with the ganglion atlas found in Figure 3.2, were used as a reference to confirm direct coupling during intracellular recordings[2].

The definitive resource for Leech biology is the book titled "Neurobiology of the Leech" written by Muller, Nicholls, and Stent (see Reference 2). It is a compilation of experimental research work with every type of leech and covers history, biology, and structure of the leech nervous system. Using the experimental guidelines provided in the appendices of this book as well as a brief 2-day lesson from Dr. Daniel Wagenaar (currently a research professor at Caltech) on the intricacies of leech dissection, we were able to obtain an overview of leech neurophysiology. We then set out to test the viability of the cells contained within an extracted leech ganglion sac by intracellularly recording from various cell types using the sharp electrode technique described in the Chapter 2. Once we familiarized ourselves with ganglion extraction and intracellular recording, we moved to extracellularly record from a de-sheathed leech ganglion using our coaxial nanoelectrode array (cNEA), the fabrication of which is described below. After obtaining initial results, we made an attempt to record from 2 different cell assemblies that had been laid across 2 different cNEAs separated by 5 mm. Afterwards, we added some new techniques to bring the extracted ganglion into closer proximity with the cNEA and made extracellular recordings of multiple waveforms.

3.2 Leech ganglion extraction process

In order to record electrical transients using leech neurons dissected from a live (anesthetized) specimen of the medicinal leech, the sheath covering the ganglion sac of interest had to be removed. Initially this was crudely done using a boom microscope with a 20x objective and leaving the entire leech body and ganglion sac in the tray. Given the diameter of the ganglion sac (roughly 1 mm) and the thickness of the sheath covering the sac (micron scale), a higher objective was needed to facilitate a higher yield in successful dissection. After many attempts and some initial experiments, we moved to using a stereo microscope with a 40x objective and extracted the ganglion sac from the leech body. The extraction was resquired due to the fact that the dissection tray was too large to fit underneath the stereo microscope objectives. This new microscope as well as extra fine tweezers and spring scissors greatly helped the success rate of the extraction process.

The leech was anesthetized by placement in a 5:1 H_20:C_2H_6O solution for approximately 10 min and afterwards, pinned to a dissection tray while submerged in a phosphate buffered saline (PBS) solution. The 3 main dangers during dissection are drying out, overheating, and bursting the ganglia. To avoid the first two problems, the solution was flushed approximately every 10 minutes and some frozen PBS (kept in a freezer prior to dissection) was placed into the solution as well. The two ends of the leech (tail and head) were initially pinned to the tray at low tension (in reference to the skin) and then moved further and further apart (increasing the length of the pinned leech) until there was sufficient tension in the skin. This occurred when the leech was stretched to roughly 10 cm. A long incision was made on the dorsal (top) side of the specimen and the

skin was pinned to the side, opening the interior of the leech. Various muscle tissues were then removed in order to expose the nerve cord (Figure 3.3). Starting with the 4th ganglion from the head, the nerve cord was isolated by removing the dark brown coating tissue, known as the stocking, as well as the underlying skin. For pinning purposes used later, it was important to leave a small amount of stocking near the sidewall connectives. The stocking and underlying skin removal process was continued until the 18th ganglion (head and tail ganglion were left unexposed for pinning purposes); leaving 14 exposed ganglion sacs. For the next part (myelin sheath removal) only the final 10 ganglion sacs were chosen as the previous ganglia contain the heart interneurons that not of interest for this particular set of experiments. The process for accessing the leech neuronal assembly used in all experiments was the same up to this point; however, there were various ways in which we tried to remove the myelin sheath.

In our initial attempts the myelin sheath coating each individual ganglion sac was removed in the large dissection tray with the leech nerve cord still intact. The boom microscope was centered over a particular ganglion sac and the lighting from a goose-neck fiber optic illuminator was manipulated so the light would hit the sac at a low angle. This helped reveal the coating. A fine tip scalpel (0.15 mm thickness) was then used to cut along the outside of the sac by dragging the tip of the scalpel. This was rarely successful and did not leave a clean cut most of the time (the neurons could be seen to be spilling out of the sac post-dissection). After some initial experiments using this method, we moved to a more robust process: ganglion extraction.

In the ganglion extraction process, an individual ganglion sac was selected and

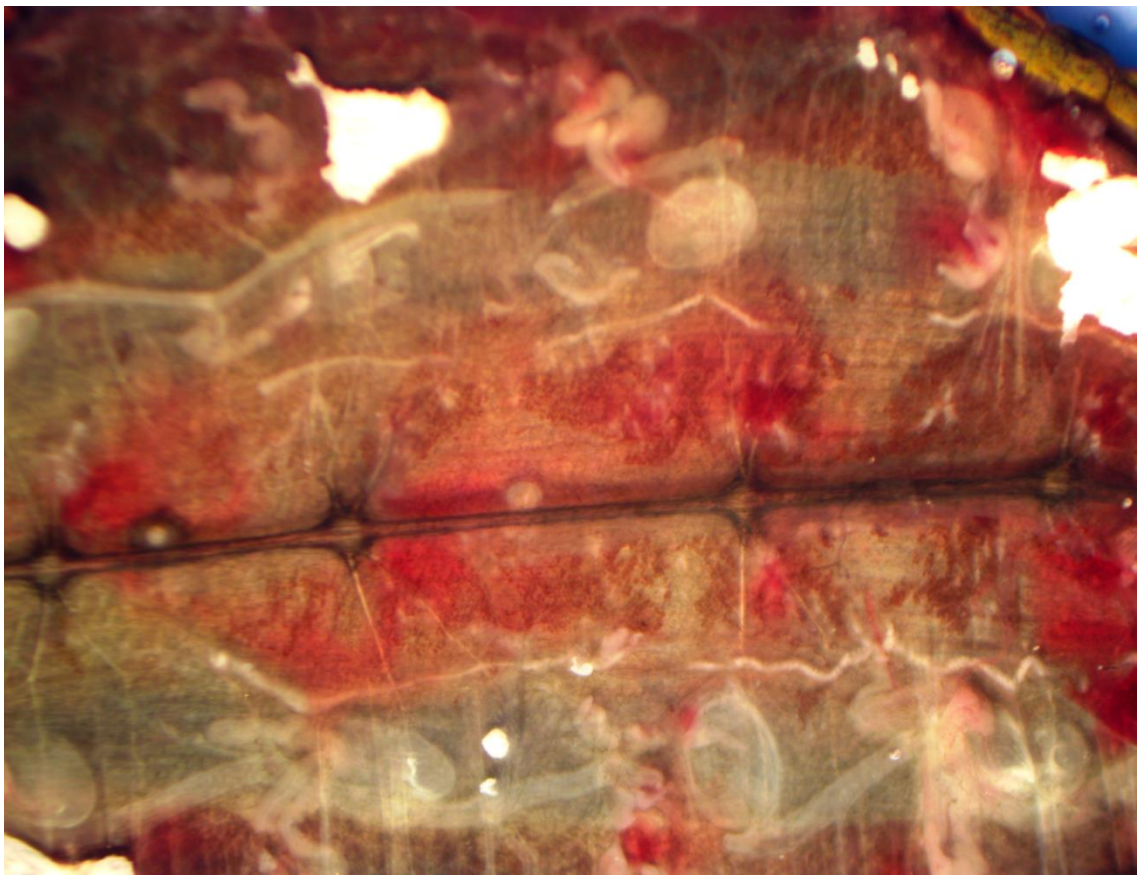

Figure 3.3 Central nerve cord of leech. Partially dissected leech is shown to view the central nerve cord containing the 21 ganglion sacs (4 seen here).

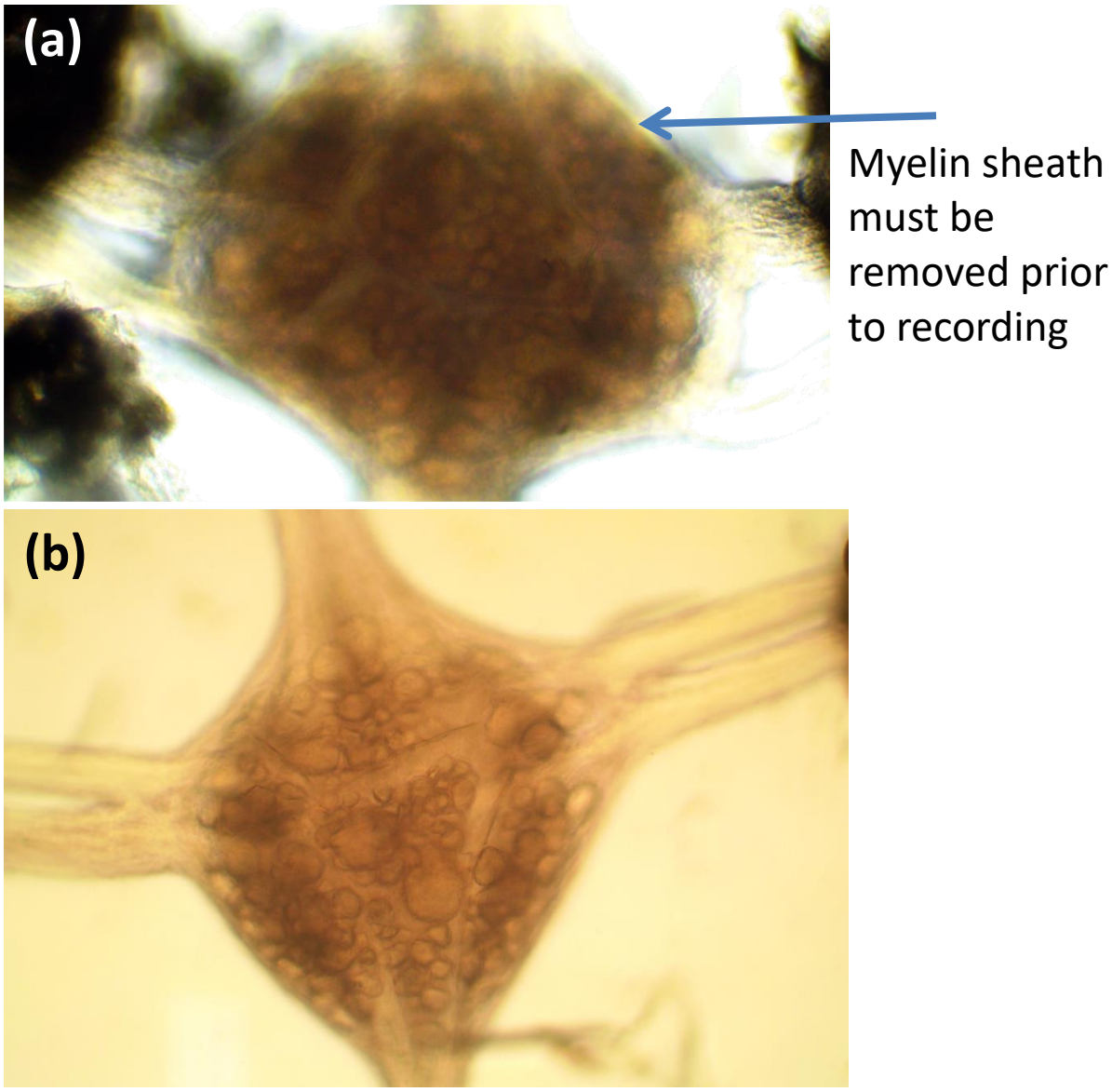

Figure 3.4 Microscopic image of ganglion sac. Dorsal (top) and ventral (bottom) side of ganglion sac containing neurons of the Leech is shown. Retzius cells are clearly visible as they are the two large cells in the center of the sac.

removed from the nerve cord and placed into a smaller PDMS dissection petri dish (3.75 cm diameter) filled with the same buffer solution as the large dissection tray. Again, dehydration and overheating were avoided by changing the solution every 5 minutes (smaller dish therefore shorter flushing time was needed) and adding frozen PBS shavings to the solution. The sac was removed by first cutting the side wall connectives (each containing a small amount of stocking coating) and then the connectives along the main nerve cord. A pin (0.0015 inch diameter platinum wire) was placed in each of the four connectives and they were pulled apart so that there was sufficient tension in the ganglion sac (Figure 3.4). The light was then focused at an upward angle to the cells and a micro-scalpel as well as dissection scissors were used to remove the sheath. Ganglia were dissected and recorded intracellularly one at a time as the sharp electrode recordings were made right in the PDMS petri dish used for dissection. We found that after roughly 3 hours of experiments, the neurons stopped firing and were therefore no longer viable. The leech was then euthanized by being placed into the anesthetizing solution for approximately 30 minutes.

3.3 Coaxial Nanoelectrode Array Design and Fabrication

The first generation of the coaxial nanoelectrode array was constructed using a pre-fabricated 2.0x1.0 cm hexagonal patterned Si pillar (2 μm tall with variable pitch) array centrally located on a 3.0x1.6 cm Si substrate (these were fabricated by contract from Benchmark Corp.). The substrate was initially put through a standard piranha etch process (substrate placed in a 3:1 H_2SO_4: H_2O_2 solution heated to 150^0C for 30 minutes) and rinsed thoroughly with deionized (DI) water to ensure any stray/ unwanted organics were removed. A standard hard-contact photolithography method with Shipley S1813 photoresist (PR) was used to generate the desired pattern of the bottom layer metal (inner metal of coax). While there were many different versions (differentiated by metal patterns) of the cNEA device (see Appendix B), the common theme was an array of individually addressed sensing regions containing a number of coaxes wired in parallel. The sensing region diameter was kept constant for each version or "chip"; and varied from 1 mm down to 50 μm, all individually addressed. The data shown from subsequent extracellular recording are from a cNEA with a sensing region diameter of 50 μm which, given the 1.3 μm HCP pitch, corresponds to roughly 1,300 coaxes.

Prior to coating the substrate with S1813 PR, an additional lift-off resist (LOR) type LOR3A (MicroChem Corp.) photoresist layer was spun on to aid in the subsequent lift off process. A physical vapor deposition (sputter) process was used to deposit the bottom layer metal consisting of 10 nm Ti and 120 nm Au onto the PR coated substrate and a standard lift-off process followed. The adhesion promoting Ti layer is needed as Au does not readily bond with the Si substrate. It should also be noted that Au could be

substituted for any other biocompatible metal, however one has to account for the corrosive nature of a selected metal, as it will be submerged in an ionic biological media over long time scales (hours to weeks). LOR3A cannot be removed with acetone (common reagent used during lift-off) and therefore a combination of sonication + Michrochem Remover PG + Microposit 165 stripper was used. The sample was then thoroughly rinsed in DI water and blow-dried with N_2. 180 nm of Al_2O_3 was then deposited using atomic layer deposition (ALD). This dielectric layer coated the entire substrate as no available PR would survive the high temperatures necessary during ALD (substrate temperature set to 200^0C during deposition). A similar photolithographic process was then used for patterning the top (outer) metal and the same PVD process was used to deposit 120nm Cr. Given the width of the sensor pad address lines (< 50 μm), it is impractical to wirebond directly to them and instead we created macro size (2.25 mm^2) electrode regions evenly distributed along the edge of the substrate. To do this, we masked the substrate with S1813 PR and performed a standard chemical wet etch using Transetch-N (Transene Inc.) as an Al_2O_3 etchant to open the intended bottom layer macro electrode regions. We found that heating the Transetch-N solution during the etch process (as suggested by Transene Inc.) had corrosive effects on our PR mask and corrupted our pattern. Therefore, the etching solution was left at room temperature, resulting in etch rate of 20 nm/h; a significantly lower etch rate than what is listed by the manufacturer for the heated rate (12 nm/min).

The final step in fabrication was to expose the center conductor of the coax which was initially done by chemical mechanical polishing. To prepare for this process, which we call decapitation, the substrate was coated with an SU8 PR layer for structural

stabilization. The polymer was spun onto the substrate, soft baked at 65^0C and 90^0C for 5 min each, UV exposed (365 nm i-line) for 90s, and put through a multi-step hard baking process. This consisted of baking in 2 min intervals, starting at 65^0C, and incrementally (30 degrees) increasing the temperature until reaching 210^0C. The sample was left to bake at this temperature (210^0C) for 45 min and an incremental cool down process followed (identical to the incremental heating process). After cooling, the sample was then mounted onto a holder and placed (facedown) in a wafer polisher, which had been coated with a MasterPrep® Polishing suspension (0.05 μm: water [20-45%] + aluminum oxide [5-23%] + propylene glycol [5-35%] + hydroxyethyl cellulose [1-12%]). The typical polishing time was 120 minutes. Placement of the substrate in the center of the holder was critical. Even a slight deviation from the center of the holder would cause the polishing to become uneven to the point of erasing address lines and/or macro electrode pads. Another consequence of the polishing process was a lack of depth uniformity. This stemmed from the non-uniform nature of the spin-on process used to coat the substrate with SU8. The polymer was thicker in the middle of the substrate causing a longer "decapitation time" than required for the pillars located on the edge of the array. The result: border pillars were left with the inner metal only coating the side walls, as the "cap" (metal coating the top of the pillar) had been polished away. This flaw along with the capricious nature of the polishing time required for decapitation necessitated a move to the extended core process described in Appendix A.

Shorting (inter-electrode DC resistance being less than 1 kΩ) between the inner electrodes (bottom layer metal) became an issue with the first generation cNEAs, probably due to the substrate unknowingly being doped-Si instead of c-Si. While this was

never explicitly confirmed (*i.e.* through x-ray diffraction) the substrate was placed on a hot plate and the DC resistance was measured at various temperatures. As the temperature was increased, the DC resistance decreased, leading one to believe the shorting was through the dielectric Si substrate. At high temperatures extrinsic semiconductors behave like intrinsic semiconductors and their resistivity decreases exponentially with temperature. Had the shorting been through the metal regions touching, the initial resistance would have been smaller (on the order of 1-10 Ω), and the subsequent resistance would have increased with temperature. To avoid crosstalk between electrodes, new samples were made with an initial 20 nm ALD Al_2O_3 layer deposited over the entire substrate. While there were still occasionally samples with shorted bottom electrodes, this new step increased the over yield of working cNEA chips from less than 50% to over 75%. The second generation cNEAs were made using the nano-imprint lithography process described earlier to fabricate a 2.0x1.0 cm array (a replica of the Si pillar array) comprised of SU-8 polymer nanopillars on Si as a starting substrate. Having a 2 μm thick SU8 layer between the bottom contacts and the Si substrate removed the possibility of shorting through the substrate. Images of completed cNEAs can be seen in Figure 3.5. Once the extended-core process was the finished the cNEA was then tested for inter-electrode shorting as well as capacitance and impedance values.

Many neurophysiological phenomena occur within the 0.1 – 10 kHz frequency band and, therefore, a low impedance value within this range is desired[4]. The cNEA device compares favorably to similar devices found in the literature, as well as commercial microelectrode arrays, with a measured impedance of $|Z| = 1.5 \pm 0.7$ kΩ) at

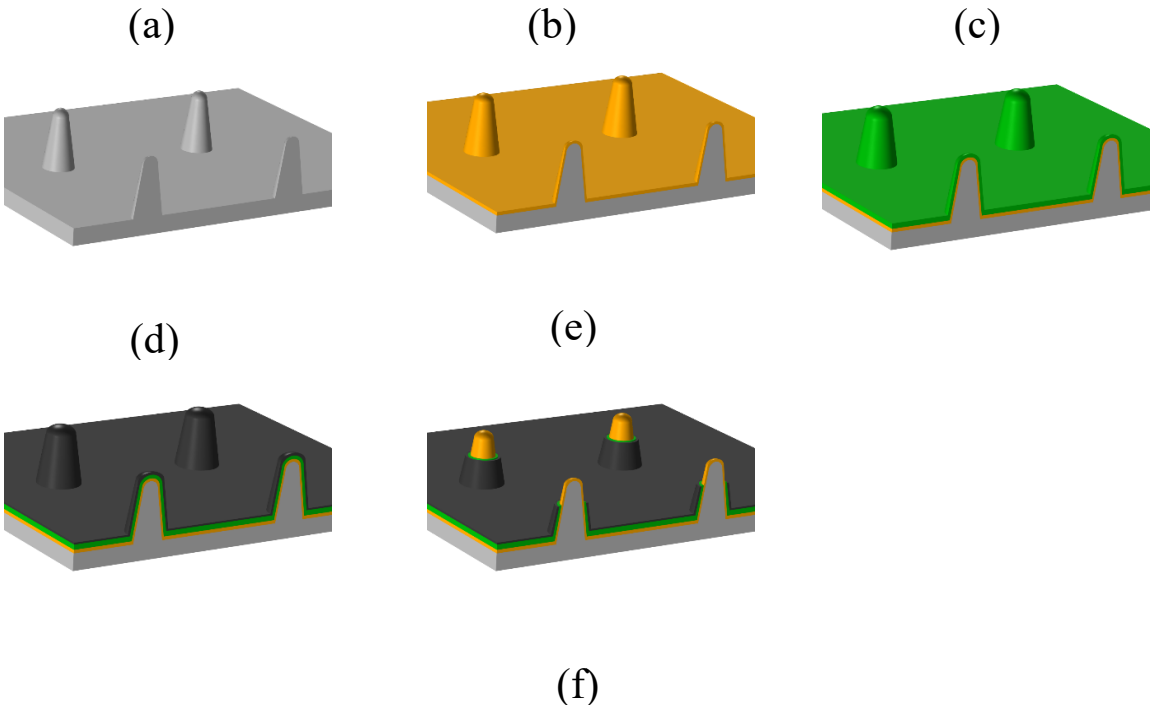

Figure 3.5 Fabrication process and cNEA devices. Fabrication process: (a) Si substrate pre-fabricated by Benchmark Corp. (b) Au sputter deposition. (c) Alumina ALD deposition (d) Cr sputter deposition. (e) Extended core photolithography + wet etch process to lower outer metal and alumina layer. (f) Microscopic images of completed samples. One device shows plastic well attached to contain electrolyte solution (third image in from the left).

(a)

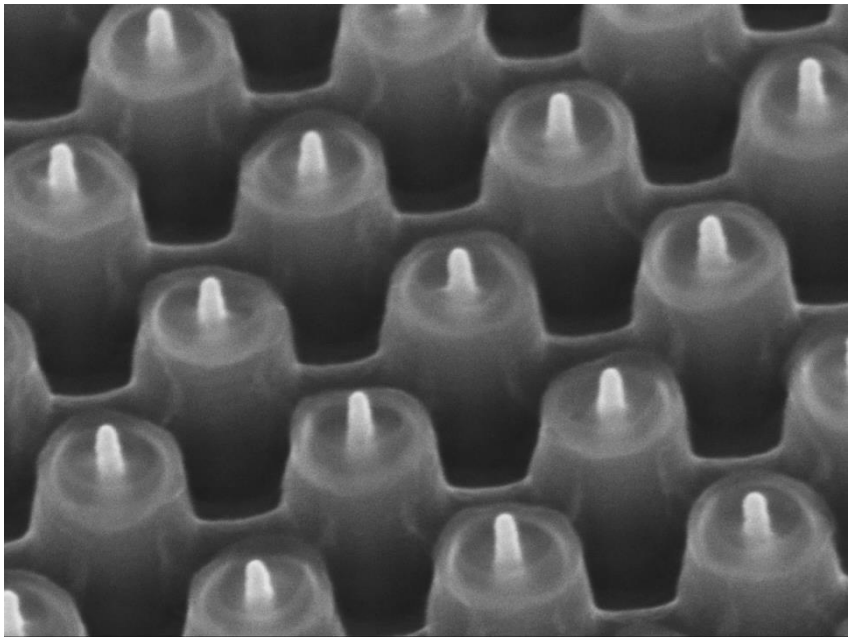

(b) (c)

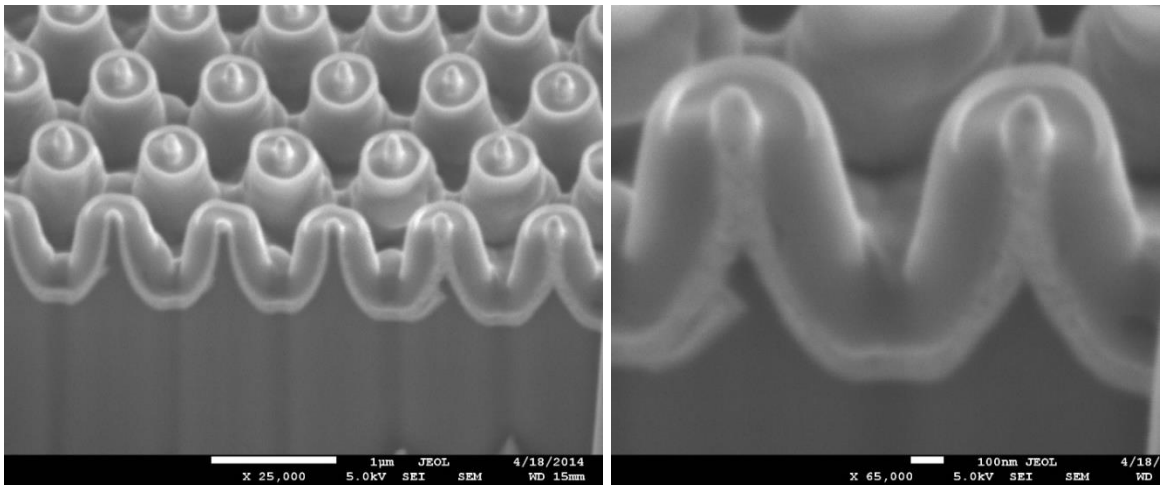

Figure 3.6 SEM of cNEA. (a) SEM of extended core coax structure used for the cNEA device. (b) and (c) show results from FIB cross section of a cNEA (post-use) device to show coaxial structure.

1 kHz. The capacitance of an individual coaxial structure is determined by its geometry and is described by equation 1. Here L is the length of the coax, while b and a are the outer and inner (respectively) radius of the metals used.

$$C = \frac{2\pi\varepsilon_0 L}{ln(b/a)} \qquad (1)$$

The intrinsic RMS thermal noise of our capacitive device, known as the Johnson-Nyquist noise, is given below in equation 2 where k_B is known as Boltzmann's constant (1.38 x 10^{-23} J/K), T the absolute temperature (K), R the resistance (Ω), and B the bandwidth over which the noise is measured (Hz).

$$V_{th} = \sqrt{4k_B TRB} \qquad (2)$$

Here we can substitute $B = 1/4RC$ as this is the thermal noise bandwidth (due to the filtering done by the sensor's resistance and capacitance) and we are left with equation 3. Using the capacitance calculated earlier (multiplied by the number of coaxes in an individual sensing region) and other known parameter values we found the thermal noise associated with our device should be roughly 6 μV over a bandwidth of 1-10 kHz; lower than any electrical activity we intended to record.

$$V_{cp} = \sqrt{4k_B T/C} \qquad (3)$$
$$= 6.42\ x\ 10^{-6}\ V$$

The figure of merit of any biological sensing device is the peak–peak noise level with the requirement that the magnitude must be lower than that of the signal to be recorded. For most biological systems the range is 10 μV to 100 mV. The fabricated cNEA satisfied

this requirement with a typical noise level of 10-20 μV before any filtering techniques were implemented. This left a signal to noise ratio of roughly 10:1.

3.4 Extracellular recording of leech neurons

Prior to extracellularly recording from the dissected leech ganglia, sharp electrode measurements were taken to ensure the cells contained within an individual ganglion sac remained viable post-dissection. A platform was made so that the small PDMS ganglia dissection dish could be fixed to the stereo-microscope stage with 360-degree rotation capability. A hydraulic micromanipulator was used to move a headstage, connected to a Multiclamp 700B amplifier, with a pulled pipette (see electrophysiology section in background chapter) at the end of it. The de-sheathed ganglion sac was focused in the center of a computer screen and the end of the pipette was moved into frame. A neuron was selected and the end of the pipette would be brought into slight contact with it. To puncture the cell membrane, either the "buzz" feature (small current injection) of the Multiclamp software, or a light tap on the end of the headstage was used. Figures 3.7a, b, and d show various waveforms captured through intracellular recordings of T, Retzius, and N cells respectively[2,3] while Figures 3.7c and e show magnified Retzius and N cell action potentials. Although leech neurons can fire autonomously (thus a reason for their selection as an assay), we wanted to test the intracellular response to a chemical stimulus should we decide to use such a trigger in subsequent extracellular recordings. For this experiment we chose to perfuse a high K^+ solution into the original PBS solution. As seen in Figure 3.8, a high firing rate occurred for a prolonged period of time that had a monotonic decrease in firing amplitude and slight decrease in firing rate towards the end

of the recording. The decrease in action potential amplitude and rate is most likely due to cell death, as we were unable to illicit a response from the cell after one minute of high K^+ perfusion. Upon confirming cell viability post-dissection and getting an idea of allowable recording time before cell death, we moved

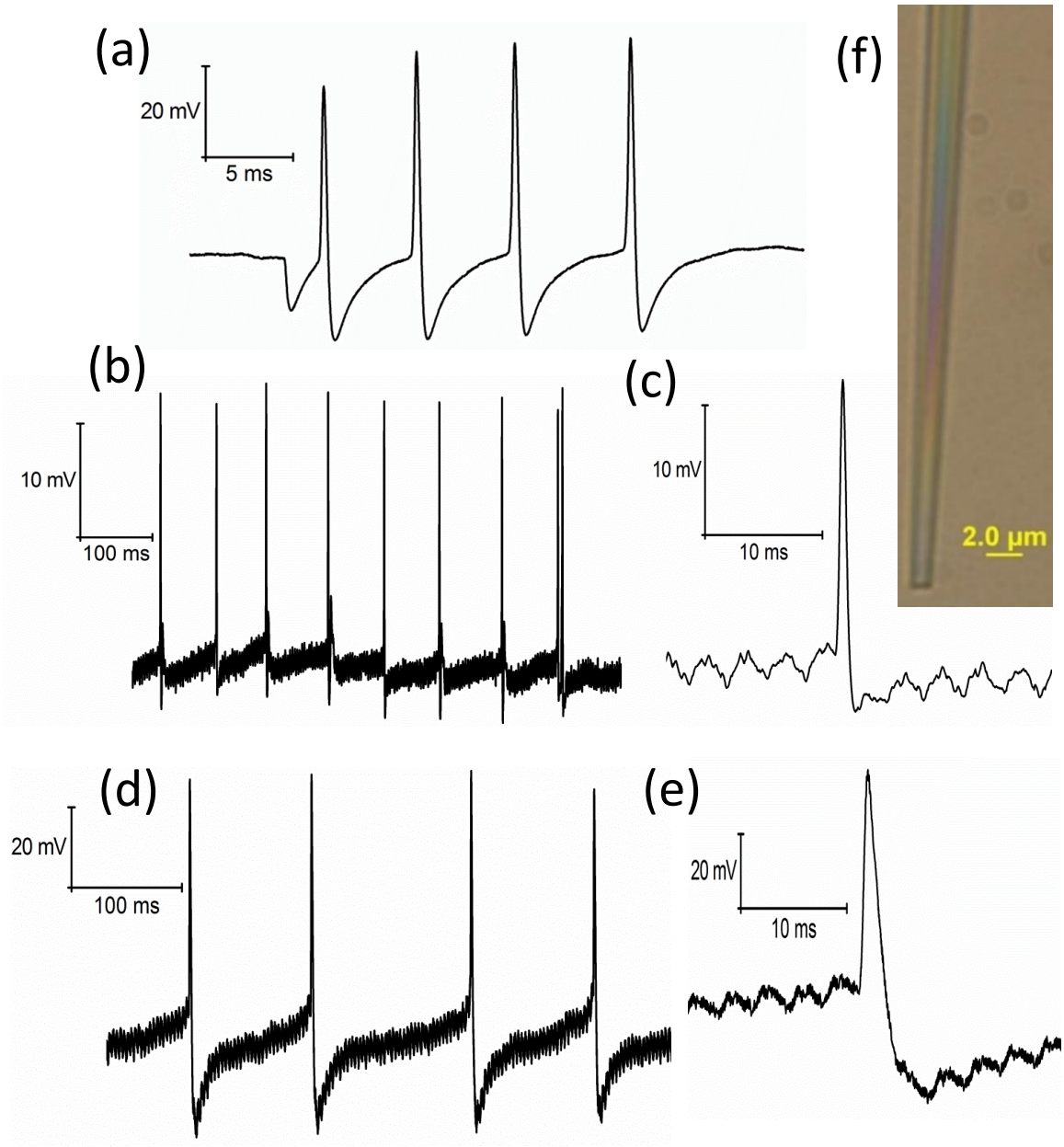

Figure 3.7 Sharp electrode recordings of leech neurons. Leech neurons recording intracellularly using sharp electrode technique. (a) T cell action potential train. (b) Retzius action potential train. (b) Magnification of the Retzius cell action potential from train seen in (b). (d) N-cell (nociceptive) action potential train. (e) Magnification of N-cell action potential to show waveform difference (compared to T and Retzius cells). (f) Microscopic image of pipette used during intracellular recording.

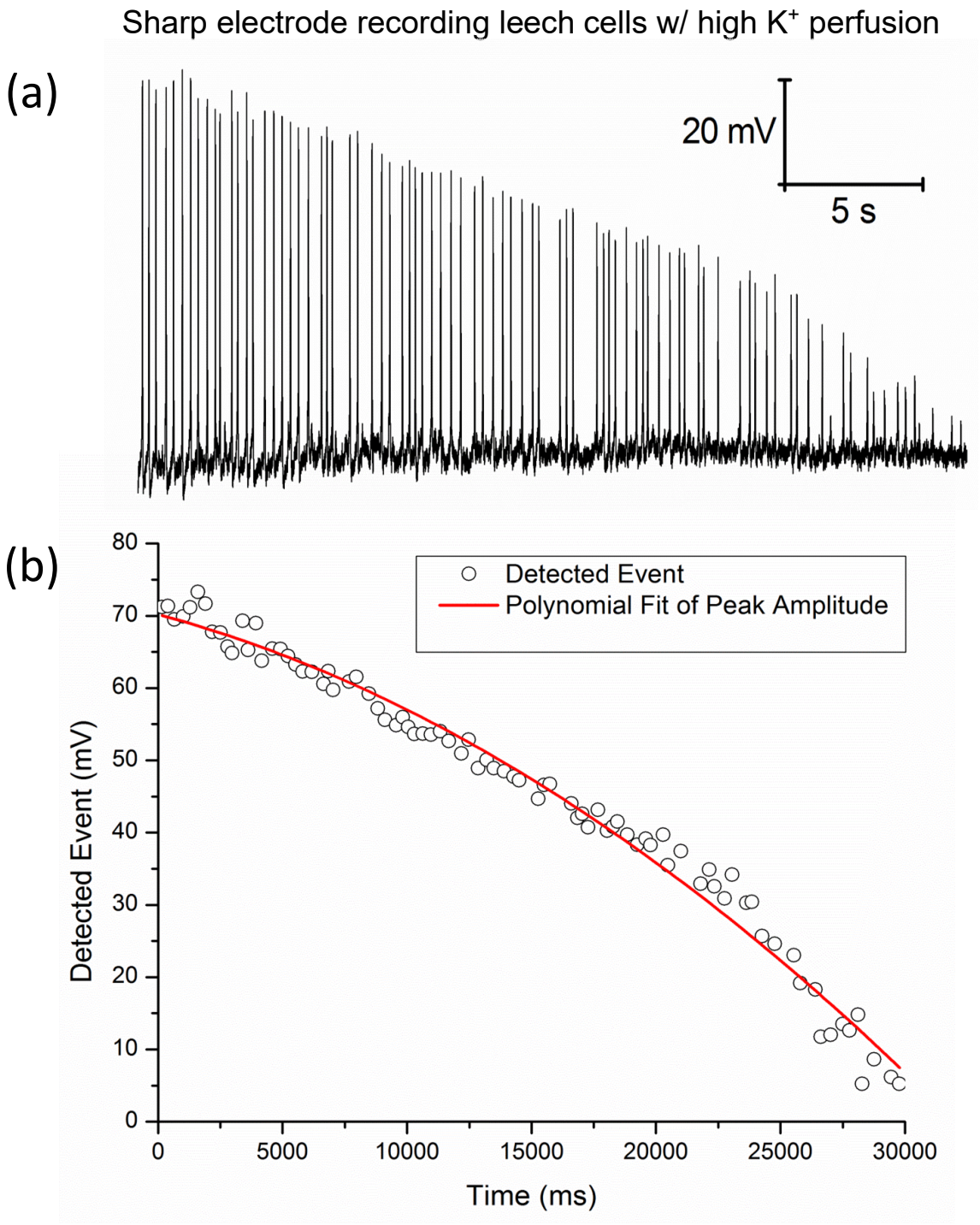

Figure 3.8 Intracellular measurement of high K^+ solution. High K^+ solution was perfused into extracellular solution during sharp electrode measurement. Magnitude of action potentials and frequency both start to decrease with increasing recording time, indicating cell death.

from intracellular recording with sharp electrodes to extracellular recording with the cNEA.

In order to measure from the cNEA a new platform had to be made to connect the device to a Digidata 1440 analog-to-digital (ATD) converter and amplifier system. A PC board was designed, using PCB express software, with pin out regions corresponding to the macro-pad locations on the cNEA (Figure 3.9a). An aluminum bud box was used as a base and BNC connectors were fixed along the perimeter, each corresponding to an individual sensing region (Figure 3.9b). This set-up facilitated recording from two individual sensing regions by connecting the device via coaxial cables to 2 SR560 pre-amplifiers which were then connected to the ATD converter. Prior to extracellular measurements, a plastic well had to be fixed to cNEA in order to contain the PBS solution and cells within the pillar region. A Makerbot 3D printer was used to print a rectangular well and it was attached to the device using PDMS (see Figure 3.5). In the initial experiments, the leech nerve cord was cut from the body with 2 or more de-sheathed ganglia and placed over one or more sensing regions. The nerve cord was then weighed down with a PDMS mold. To minimize the distance between the neuronal assembly and the cNEA, a different PDMS mold with 2 stages was made. Figure 3.10 shows a dissected ganglion sac attached to one of the stages prior to recording. This new stage yielded higher precision in locating and manipulating the ganglion sac, which led to successful extracellular recordings.

To test the efficacy of the device, various experiments were performed. First, we attempted to test the device in parallel with a sharp electrode by coupling both to a Retzius cell extracted from leech ganglion. The sharp electrode served as an intracellular

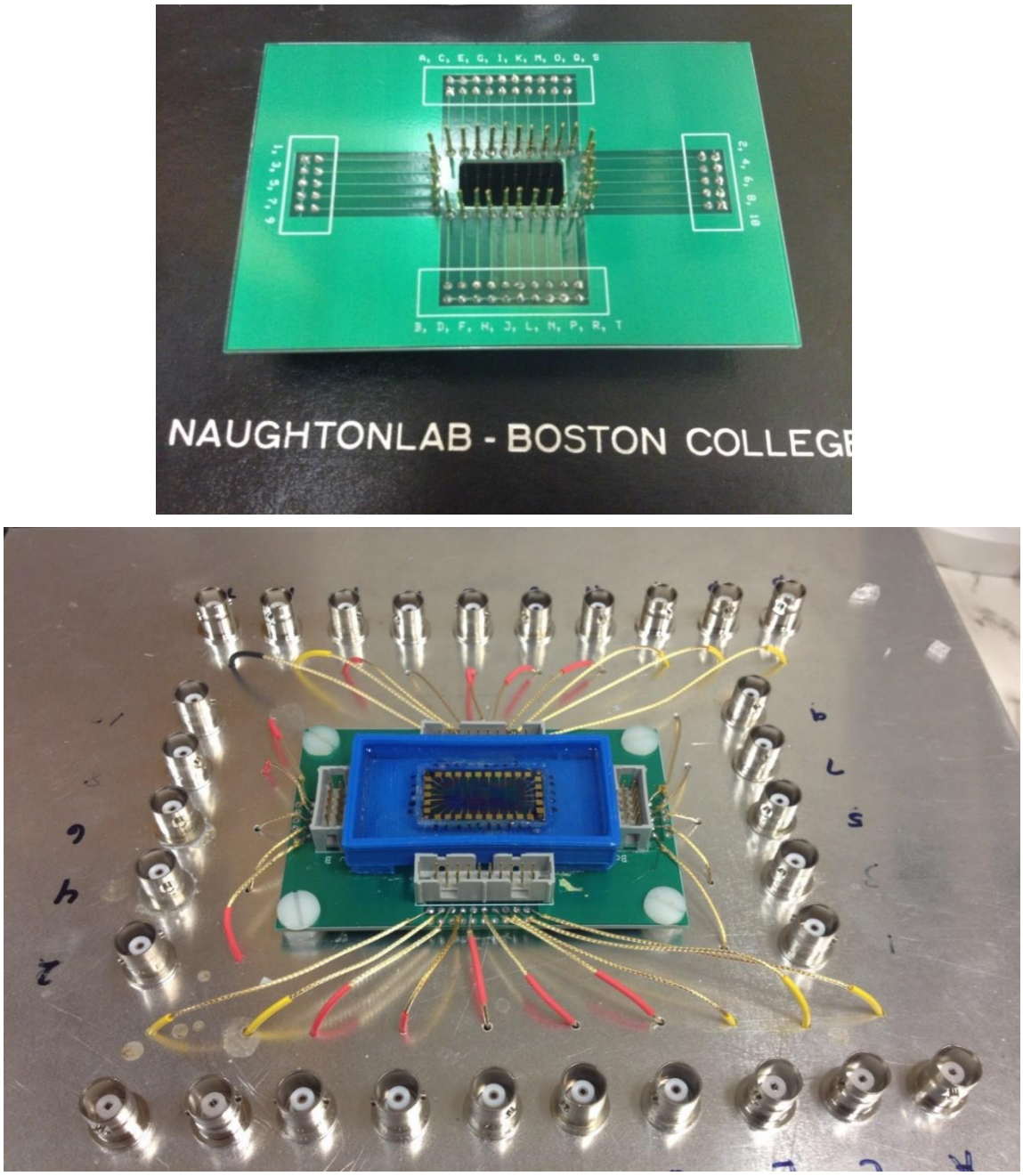

Figure 3.9 PC board pin-out and Bud box platform. A PC board was designed to connect device to a data acquisition system. The PC board connect to a series of BNC connecters, which were attached to a modified to the perimeter of the top surface of the Bud box.

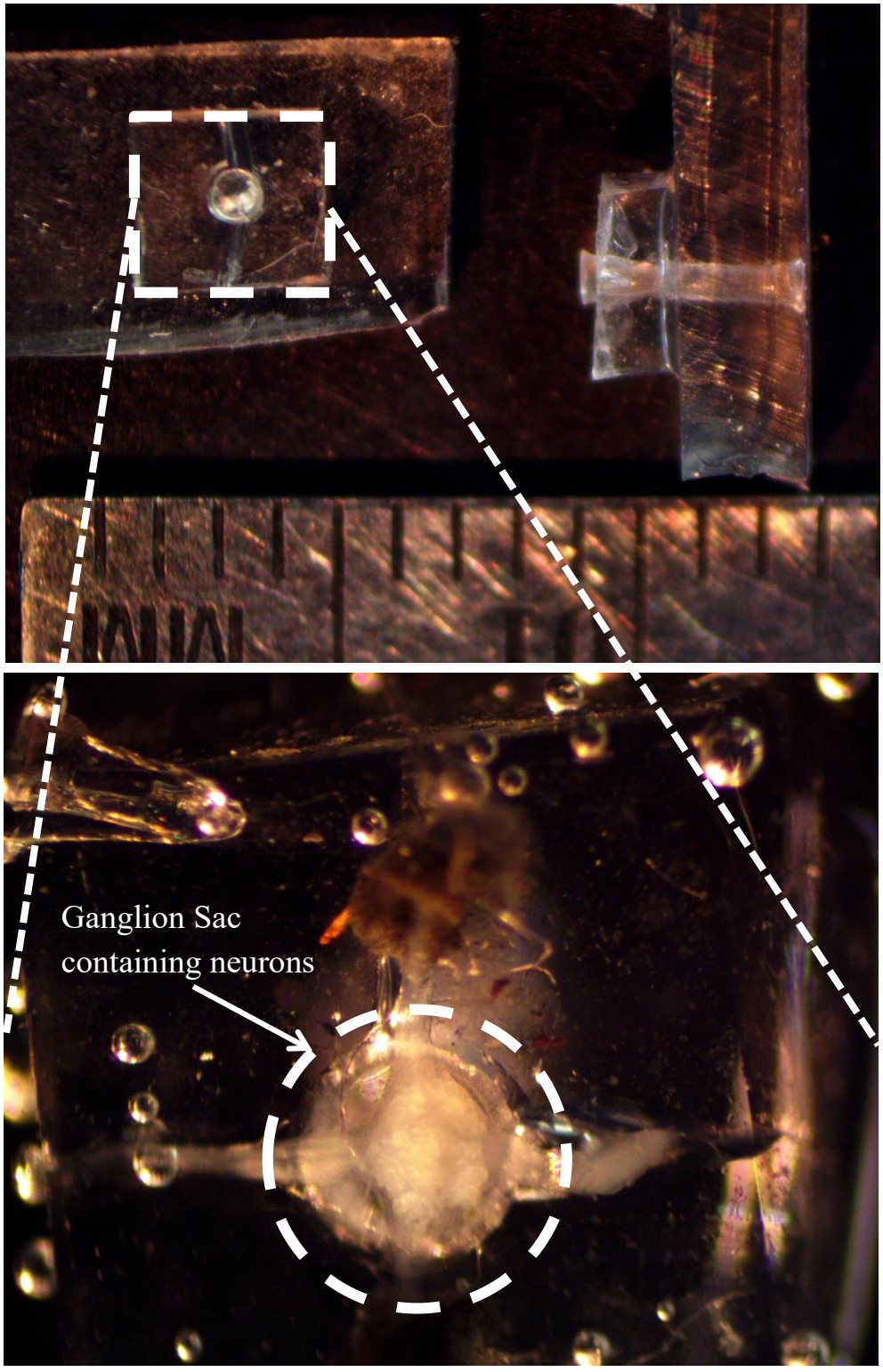

Figure 3.10 PDMS platform used to hold extracted ganglion sac. To facilitate accurate placement of neuronal assembly, a PDMS mold was made for holding ganglion sac. The sac is de-sheathed, then pinned to stage of PDMS, and gently placed over sensing area. Metal pin was attached to the backside for added weight to increase coupling by pressing the ganglion sac to the sensing area.

probe while our device sensed electrical perturbations extracellularly. Unfortunately, we were unable to successfully puncture the ganglion sac and have the assembly in close proximity to the sensing region. After many unsuccessful attempts this was abandoned.

We then pivoted to use the cNEA in a dual intra/ extracellular measurement using a novel experimental technique. A highly valuable neurophysiological tool would be one capable of making intracellular measurements while using an extracellular probe. Recently, novel tools have been developed that use a process called electroporation combined with nanoelectrode arrays to achieve this[5,6]. In our approach, we extracted two ganglia still attached by the central nerve cord and laid them over two individually addressed sensing regions (with a 1.5 cm separation between sensing regions). A PDMS slab was then laid over the nerve cord and ganglia to bring them into contact with the extended core coaxes. We then used one sensing region for electroporation (stimulating the neuronal assembly with a train of 50 mV/ 500 µs square wave pulses) and intracellular measurement, while recording extracellularly from the other region (Figure 3.11). The magnitude and biphasic waveform, associated with extracellular sensing, of the data is supported by previous studies of Leech neurons[7]. The monophasic waveform (associated with intracellular measurements) has an amplitude much lower (an order of magnitude) than typical action potentials. This could be due to poor coupling between the coaxial core and the neuronal assembly as a result of electroporation. If the seal impedance (as defined in the background chapter) is lower than the impedance between the ganglion sac and the electrode, there will be attenuation in the recorded waveform. From data in Figure 3.11 we can calculate the conduction velocity by marking 2 points on

the waveforms (blue lines), measuring the time difference, and using a simple kinematics equation:

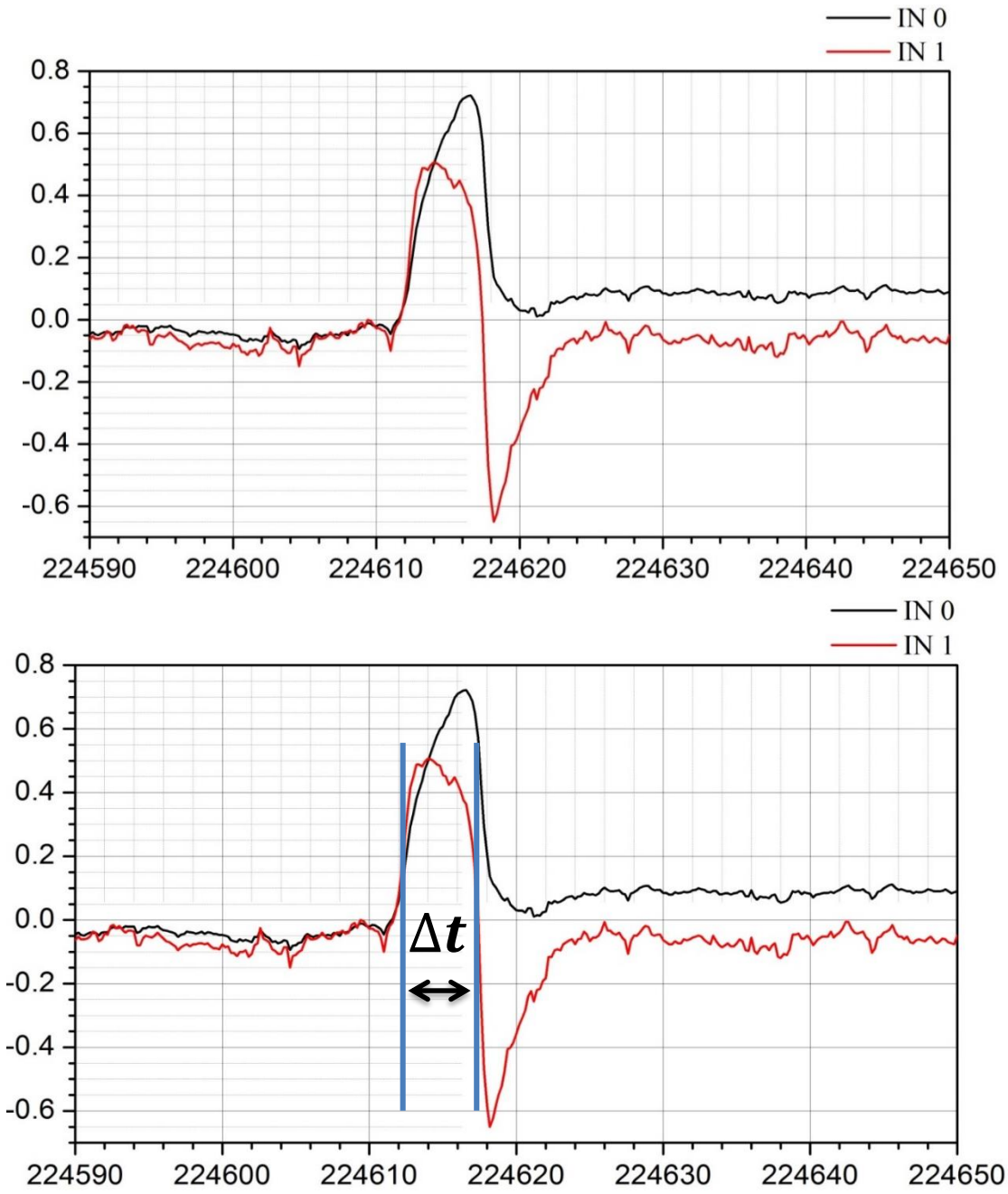

Figure 3.11 Intracellular measurement and electroporation. Neuronal assemblies were recorded in dual intra- and extracullar experiment entirely on the cNEA device (no sharp electrode). Electroporation technique was used to create nanopores in the cell membrane, thereby facilitating intracellular recording with an extracellular electrode. Blue lines indicate change in spatial position with respect to time (Intracellular measures action potential first, then extracellular device senses action potential). From this, the conduction velocity can be calculated.

$$\Delta t = 4.8\,ms \rightarrow v = \Delta d/\Delta t \approx 3\,m/s \qquad (4)$$

This is found to be on the same order of magnitude found in the literature[8,9]. This experiment was repeated and yielded some interesting results. Figure 3.12 shows preliminary data from another dual intra- (sharp electrode) and extracellular (cNEA) recording. The coaxial array data appears to be anomalous due to the large magnitude of the action potential (typically extracellular recordings of leech neurons are on scale of hundreds of microvolts). Also, while the cNEA data is clearly biphasic, there seems to be an intermittent period between the two peaks. This would indicate the current in the extracellular solution stayed constant for a brief moment before reversing direction, which is unlikely. The sharp electrode data, while monophasic (typical of intracellular measurements), has a low magnitude considering typical recordings have magnitudes on the order of tens of mV. This could be due to poor coupling between the pipette and the cell due to a low seal resistance. If this was the case, and a large portion of the transmembrane current leaked into the extracellular space, it could explain the anomalous signal (large current density = large voltage measured) seen by the cNEA. However, this is just speculation. In subsequent experiments, we moved to single site extracellular measurements as the electroporation technique and other multiple site simultaneous measurements were inconsistent.

In order to test the utility of our device as an extracellular neuroelectronic sensor, we passively recorded from leech neuronal assemblies contained within an individual ganglion sac using the cNEA device. In these experiments, a ganglion sac was chosen, desheathed and placed on top of the PDMS stage shown in Figure 9 to promote electronic

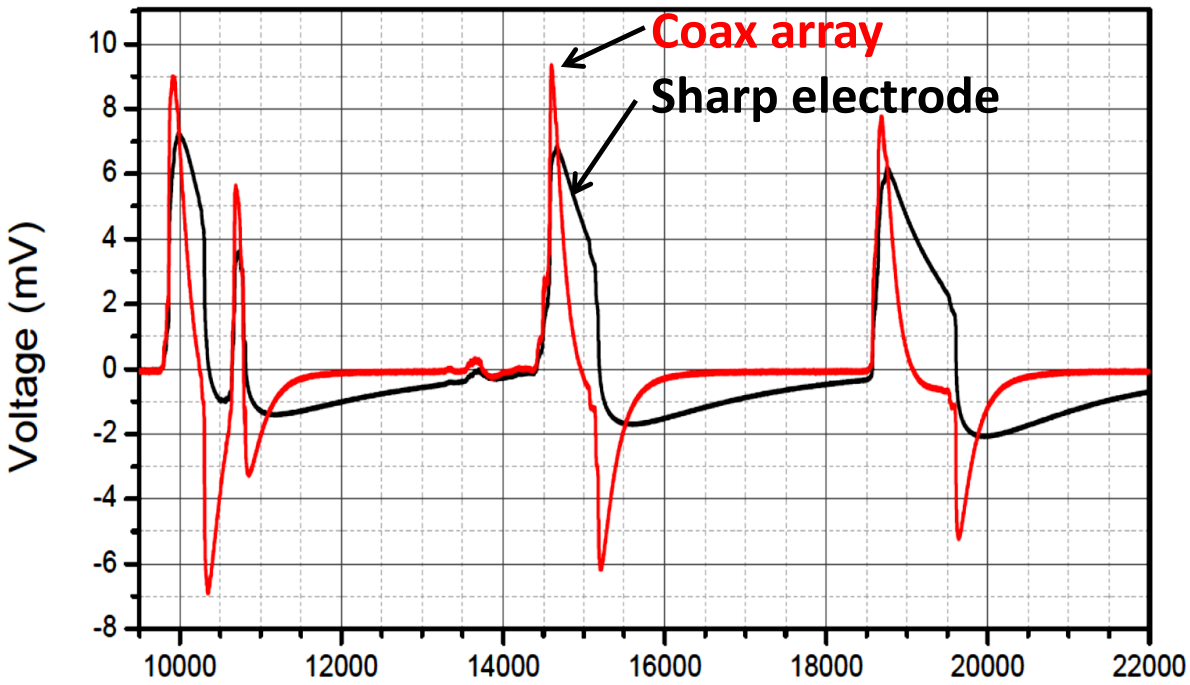

Figure 3.12 Preliminary Results from dual intra- and extracellular recording. Coax array (red data) extracellularly coupled to the neuronal array, while the sharp electrode (black data) was intracellularly coupled. Ganglion sac was placed onto sensing array and then a sharp electrode was brought into contact with top side of ganglion sac. Both devices recording passively.

coupling (contact) with the electrode array. The cNEA sensing region was 50 μm in diameter and contained approximately 1,300 nanocoaxes wired in parallel. Multiple spontaneous activity bursts were clearly seen over a recording time of 5 min (Figure 3.13) with a 10 kHz sampling rate. The experiment was repeated several times, each with a different neuronal assembly, with spontaneous bursts seen each time. Events were considered as anything reaching a threshold of 3 times the peak-to-peak noise level (noise ~ 10 μV). Post-waveform data analysis was performed and produced two unique waveforms (Figs. 3.13c,e and 3.13d,f), as seen in previous works, showing successful extracellular recording[10,11]. An aggregate of the two waveforms from a single experiment is shown in Figure 3.14 and match those found in the literature for Retzius and N-cell types. These data proved the utility of the device as an extracellular sensor. The next step in our effort of using coaxial arrays as a neuroelectronic device was to show the capability of culturing neurons on top of the device and measuring changes in the local field potential.

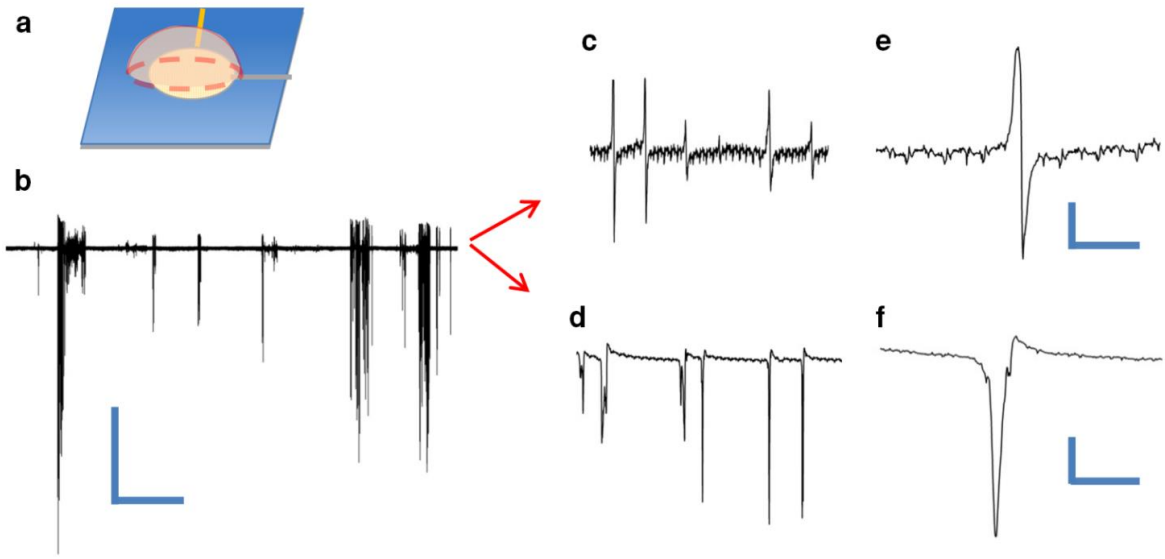

Figure 3.13 Extracellular recording of disassociated leech neurons mechanically placed on top of coaxial sensing region of a cNEA. (**a**) Schematic of ganglion sac placement onto an individual sensing region within the device. (**b**) Spontaneous bursts during 60 s recording. Scale bars, 400 µV / 10 s (**c**) One waveform type found within burst. (**d**) Second waveform resembling extracellular action potential found during post-recording spike sorting analysis. (**e**), (**f**) Closer look at two distinct waveforms extracted during post analysis spike sorting. Scale bars, upper right: 50 µV / 10 ms, lower right: 200 µV / 3 ms.

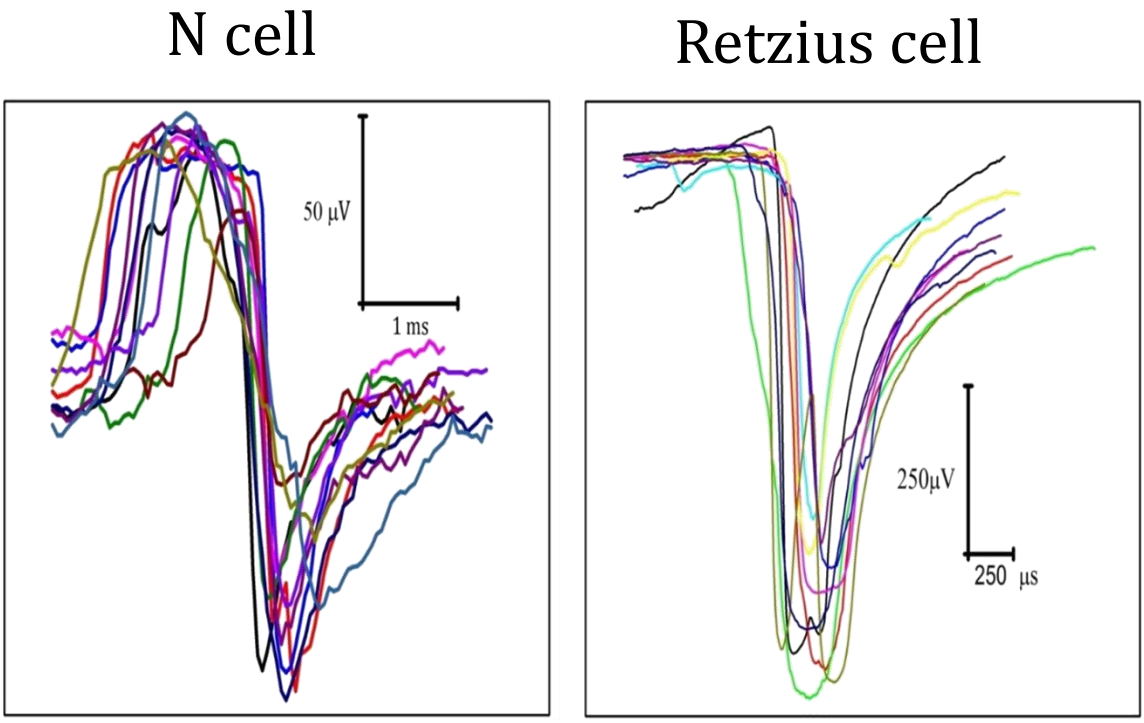

Figure 3.14 Waveforms extracted from extracellular data. Multiple firings superimposed extracted from extracellular recording of neuronal assembly (Figure 3.13).

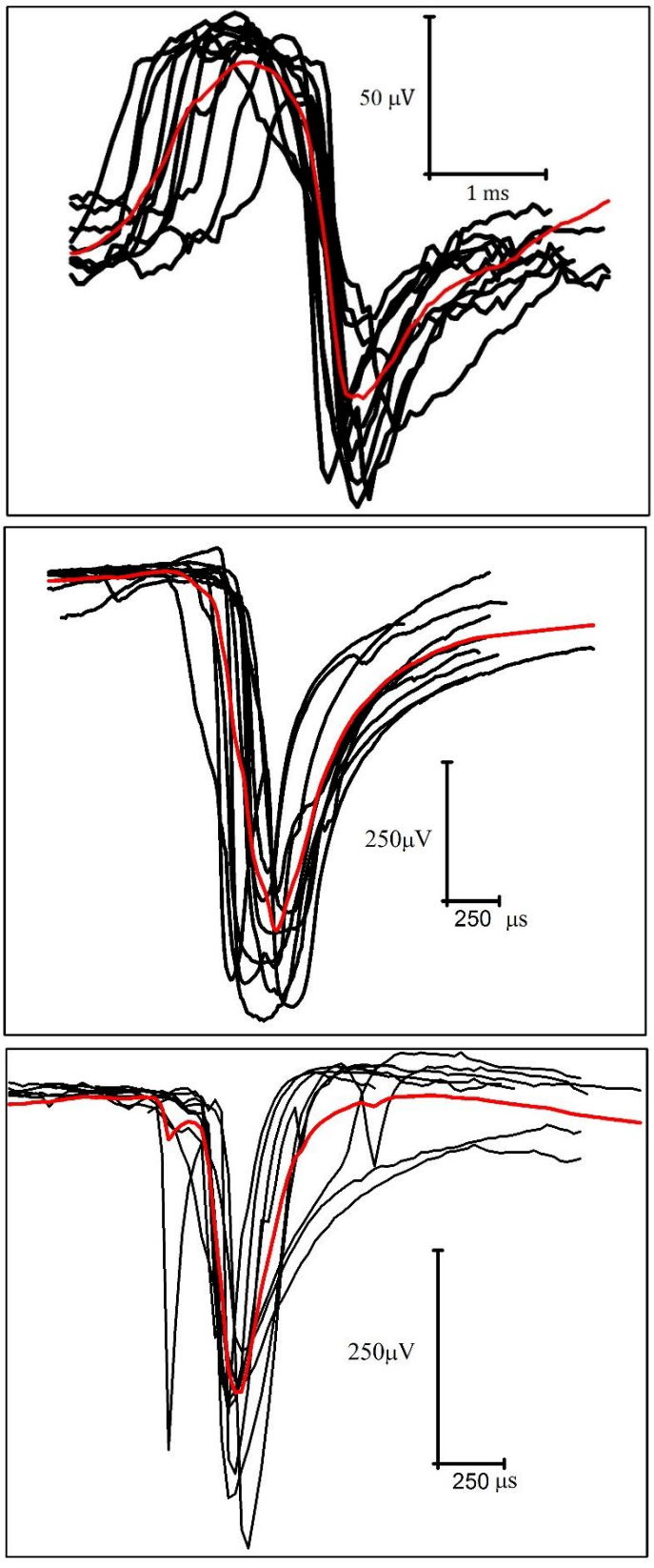

Figure 3.15 Similar waveform shape extracted from data. Various waveforms could be seen within the data. Waveforms of similar shape were extracted then superimposed. Red lines indicate averages of the superimposed waveforms. From References 11 and 12, these appear to be Retzius and N-cell types.

3.5 References

[1] Huber, J. *Nicander – Theriaca*. Apud guil. Morelium. Dtsch Arch. Klin Med. 67:522 (1891)

[2] Muller, K. J., Nicholls, J. G., Stent, G. S., & Cold Spring Harbor Laboratory. Neurobiology of the Leech (N.Y, Cold Spring Harbor) (1981).

[3] Nicholls, J. Gr, & Baylor, D. A. Specific modalities and receptive fields of sensory neurons in CNS of the leech. J. of Neurophys. **31**, 740-756 (1968).

[4] Buzsáki, G., Anastassiou, C.A., & Koch, C. The origin of extracellular fields and currents - EEG, ECoG, LFP and spikes. Nat. Rev. Neurosci. **13**, 407-420. (2012). doi:10.1038/nrn3241

[5] Spira, M & Hai, A. On-chip electroporation, membrane repair dynamics and transient in-cell recordings by arrays of gold mushroom-shaped electrodes. Lab Chip. **12**, 2865-2873 (2012).

[6] Xie, C., Lin, Z., Hanson, L., Cui, Y., & Cui, B. Intracellular recording of action potentials by nanopillar electroporation. Nature nanotechnology. **7**, 185-190 (2012).

[7] Jenkner, M. & Fromherz, P. Biostability of Membrane Conductance in Cell Adhesion Observed in a Neuron Transistor. Phys. Rev. Lett. **79**, 4705 (1997).

[8] Baccus, S. A., Sahley, C. L., & Muller, K. J. Multiple sites of action potential initiation increase neuronal firing rate. J. of Neurophys. **86**, 1226-1236 (2001).

[9] Cruz, G. E., Sahley, C. L., & Muller, K. J. Neuronal competition for action potential initiation sites in a circuit controlling simple learning. Neuroscience. 148, 65-81 (2007).

[10] Fromherz, P. Semiconductor chips with ion channels, nerve cells and brain. Physica E: Low-Dim. Syst. and Nanostruc. **16**, 24-34 (2003).

[11] Fromherz, P., Offenhausser, A., Vetter T., & Weis, J. A neuron-silicon junction: A Retzius cell of the leech on an insulated-gate field-effect transistor. Science **252**, 1290-1293 (1991).

Chapter 4: Extracellular recording of cultured Human Embryonic Kidney cells using coaxial microelectrode arrays

4.1 Introduction

One type of assay for studying the electrical properties of biological cells and tissues through the use of multielectrode arrays (MEA) involves culturing neurons or some other cell type onto the device (*in vitro* studies). Common cell types used in neurological research include PC-12, cardiomyocytes, and human embryonic kidney (HEK293) cells. While we had some familiarity with PC 12 cells, cardiomyocytes, and primary cell lines, we ultimately decided to use HEK293 cells transfected with a pcDNA3.1/hChR2(H134R)-EYFP plasmid. This plasmid transfers the Channelrhodopsin genes to the HEK293 cells, facilitating the expression of light-mediated ion channels. This enabled us to further develop our cNEA device by slightly altering the architecture, resulting in the fabrication of a coaxial optrode array for use in optogenetic studies.

Although HEK cells are not a neuronal cell model, they are a very popular cell-line to work with for studies investigating neuronal pathologies. Their fundamental utility comes from the fact that that they are easy to handle, grow rapidly, have a high robustness when it comes to expressing alien proteins through transfection, and are thus amenable to quantitative studies. Other cell types, specifically PC-12 cells, require a neuropeptide called nerve growth factor for differentiation to occur. Developmentally, HEK293 cells and neurons originate from the same precursor line[1]; this means that the fundamental biological processes and their regulatory mechanisms (*e.g.* transcription,

translation, protein folding, etc.) are similar, however, not identical[2,3]. Therefore, HEK293 cells provide a reasonable approximation for addressing numerous questions of basic biology also relevant to neurons. Furthermore, HEK293 cells are devoid of several key proteins which play a critical role in the biology of neurons *e.g.* ion channels, receptors, and enzymes[2]. As such, they provide a sufficient low 'noise' paradigm for studying the biology and physiology of these proteins since there will be a minor number of interfering currents. Finally, their accessibility for patch-clamping (smooth membrane, compactness and cell size/capacitance) makes them suitable for assessment of the biophysical and pharmacological characteristics of ion channels and receptors[4].

4.2 HEK 293 Cell preparation

HEK293 cells were cultured in Dulbecco's modification of Eagle's medium (DMEM) containing 10% fetal bovine serum (FBS) and 1% of PenStrip Antibiotic in a 6 well culture dish. The pcDNA3.1/hChR2(H134R)-EYFP plasmid[5] (# 20940, Addgene, Cambridge, MA) was transfected into HEK293 cells using Lipofectamine 2000 (Invitrogen) according to the user manual. In brief, approximately 4 μg of plasmid and 10 μl of lipofectamine was transfected into HEK293 cells. After 16 hours post transfection, the cells were transferred to a 6 well plate and grown in DMEM 10 % FBS media supplemented with 500 μg/ml Geneticin (G418). Cells were cultured under G418 selection for approximately 2 weeks to obtain cultures of ~ 100 % EYFP-expressing cells. A high percentage of EYFP-expressing HEK293 cells were observed upon culturing the cells in the presence or absence of G418 in the media suggesting the plasmid had stably integrated. After 2 weeks, the cells were then subsequently cultured in DMEM media containing 250 μg/ml G418 to maintain a stable channelrhodospsin-EYFP expressing cell population.

To contain the cells to the array sensing area, either a PDMS or teflon well (approximately 3 cm diameter) was attached to the device. For promoting adhesion to the coaxial structures the devices were then incubated in a sterile solution of 0.01% poly-l-lysine overnight at 37 ºC in 5% CO_2. HEK293 cells expressing CH2R-EYFP protein were trypsinized from cell culture dishes and recovered by centrifugation at 595 *g* for 6 mins at 4ºC. The cells were re-suspended in DMEM 10 % FBS media containing 250 μg/ml G418 at a density of 1 x 10^6 cells/ ml. A 0.1 ml aliquot of cells was added to one

well of a coaxial device and cultured overnight at 37 ºC 5 % CO_2. The seeding density of cells almost completely covered the coaxial structures within 24-48 hours of subsequent cell culture and adherence.

4.3 Coaxial microelectrode array (cMEA) design and fabrication

Typical commercially available MEA technologies consist of an array of 60 or more sensing regions, each comprised of a metal circular electrode (usually platinum) with an address line that terminates in a macro-pad along the perimeter of the device. The individual sensing regions range from tens to hundreds of microns in diameter with an edge–edge distance in the same range. With this design in mind, we chose to build our coaxial microelectrode array (cMEA) to shadow/ mimic the Multichannel Systems 8x8 MEAs (actually 60 input channels); whose sensing regions varied from 20 to 30 μm and edge–edge distance of 60 to 200 μm. A finished cMEA can be seen in Figures 4.1 with a PDMS well attached to contain the cultured HEK293-ChR2 cells and the SEM images in 4.2a–c. Since the cMEA had 60 inputs while the cNEA only had 10, a new PC board/ platform had to be fabricated. Figure 4.3 shows the new PC board and Bud box with 60 coaxial inputs along the perimeter, mimicking the one built for cNEA. This setup still required connecting to the two SR560 pre-amplifiers and therefore would only allow us to measure 2% of the 60 sensing regions simultaneously, hardly ideal for the intended experiments. Fortunately, we gained access to a Multichannel Systems USB-MEA1060 60 channel amplifier DAQ and MC_Rack software (Multi Channel Systems MCS GmbH) system, permitting us to monitor 60 channels simultaneously (Figure 4.4).

The coaxial array device was constructed using nanoimprint lithography (NIL) to prepare 100 μm^2 area SU8 polymer nanopillar arrays (2 μm diameter × 5 μm height at 10 μm hexagonal pitch) on glass substrates. The glass substrates (rather than Si substrate similar to one used with the cNEA) were necessary due to the nature of the experiments

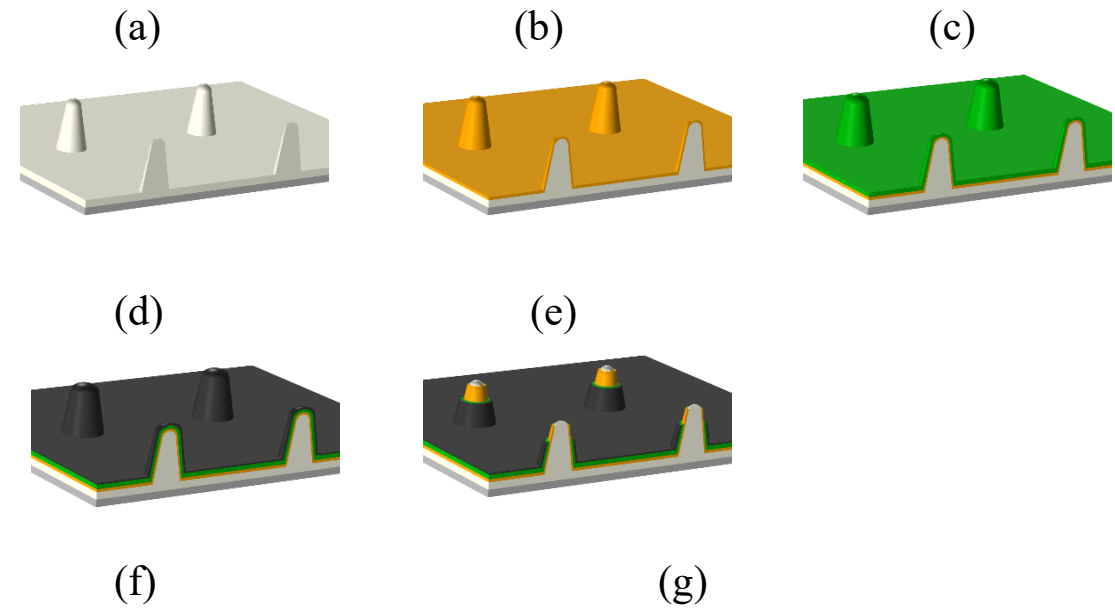

Figure 4.1 Fabrication of cMEA. (a) – (e) Fabrication process of NIL followed by metal – dielectric – metal deposition on glass substrate. (f) Finished cMEA with PDMS well attached. (g) cMEA in placed in hand to show scale.

that had been planned. Since we were using transfected HEK cells, which optically actuated, and intended to show the cMEA's ability to confine the light to local area, we needed an optically transparent substrate so as to have the ability for backside illumination (thought the coax). Standard contact photolithography was used to generate ~700 μm^2 and ~300 μm^2 subarrays each containing fewer than 10 pillars. Coaxial electrodes were then prepared by sequential metal, dielectric and metal coatings (Figures 4.1a-c) onto the nanopillars, yielding the structure shown in Fig. 4.1d. In order to prepare this structure for opto-neuroelectronic recording and stimulation, the inner coaxial electrode must be exposed to have physical proximity to neurons. We achieve this by mechanically polishing the array, thereby "decapitating" the structures and leaving behind the open-ended microscale coaxial electrodes shown in Fig. 4.1e. In order to facilitate this polishing, a polymer film (SU8) was spin-coated over the array and hardened, mechanically stabilizing the structure. Selective chemical wet etching (using a proprietary Cr-etchant from Transene) of the outer shield and annulus was performed to expose a greater core surface area. Figure 4.1f shows optical micrographs of a completed extracellular interface device. The combination of a glass substrate and the SU8 stabilizing layer made taking an SEM of the device difficult. This was due to the charging that would occur in a very short amount of time. In scanning electron microscopes, dielectric materials can be problematic as the number of incident electrons exceeds that escaping from the specimen. This causes a negative charge to build up at the point where the beam hits the sample. This causes a problem in image contrast. Therefore, for clarity sake an outline of the sensing region has been overlaid onto the micrograph

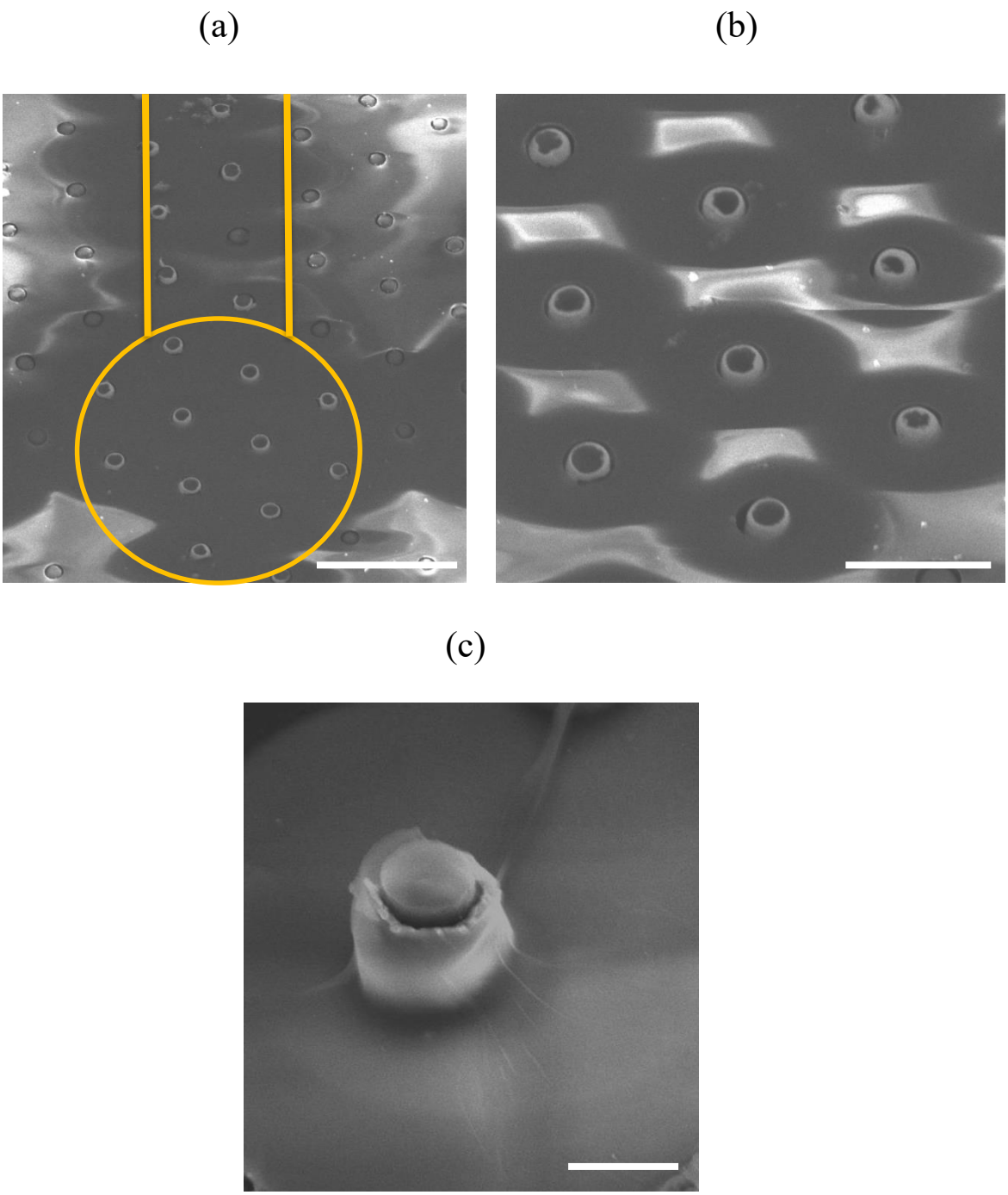

Figure 4.2 SEM images of cMEA and single coax. (a) Decapitated coaxial region of cMEA. Lines are drawn for illustration of coaxial region (not clear due to charging). (b) Magnified view of the coaxial region. (c) Single coax with core extended. Scale bars are 10, 10, and 5 μm.

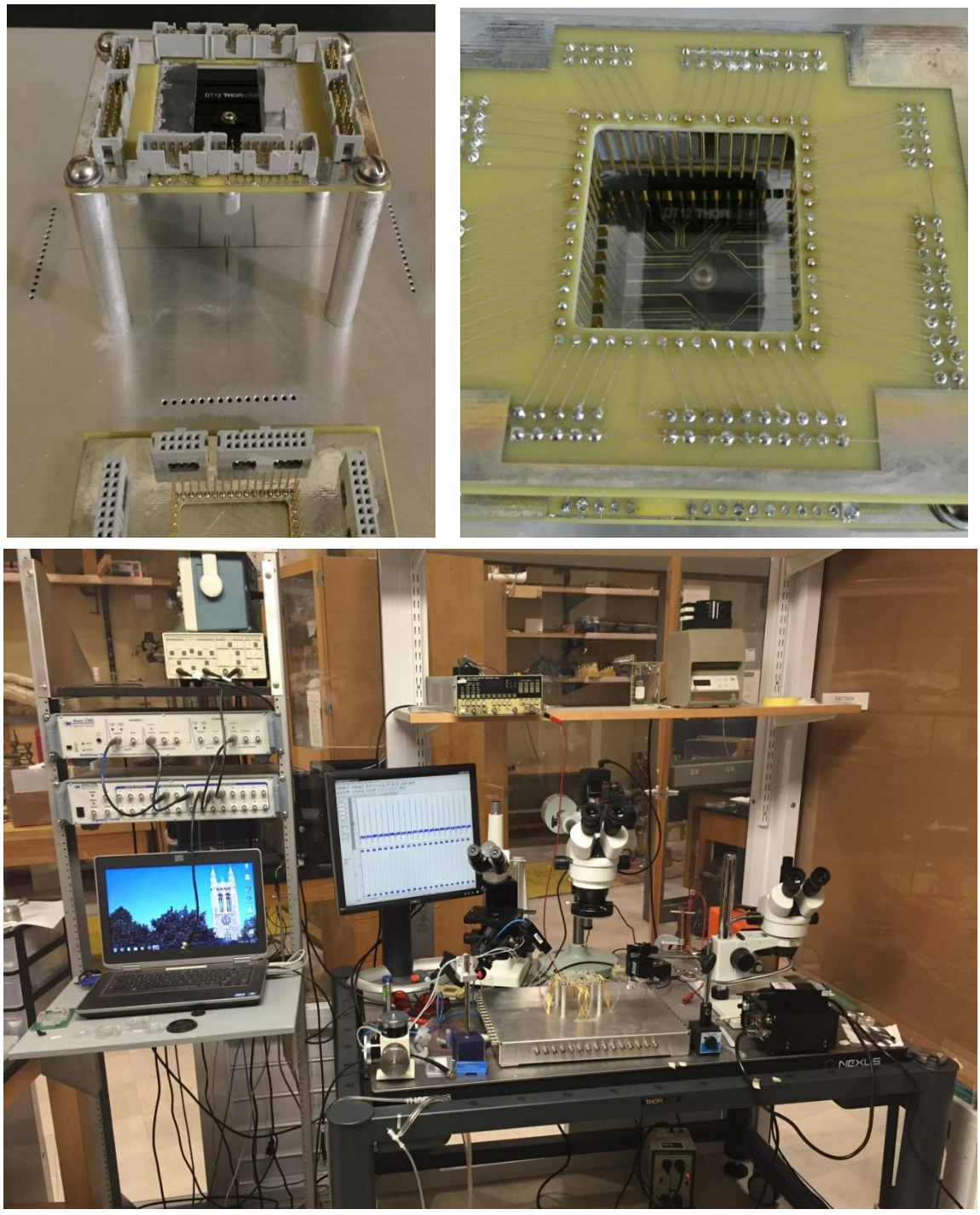

Figure 4.3 PC board layout and measurement area. Upper right image shows new Bud box and PC board that were designed and fabricated for cMEA device. PC board (upper right) has 60 Pin-outs leading to BNC connectors, which can be connected to SR560 pre-amp (shown in bottom image).

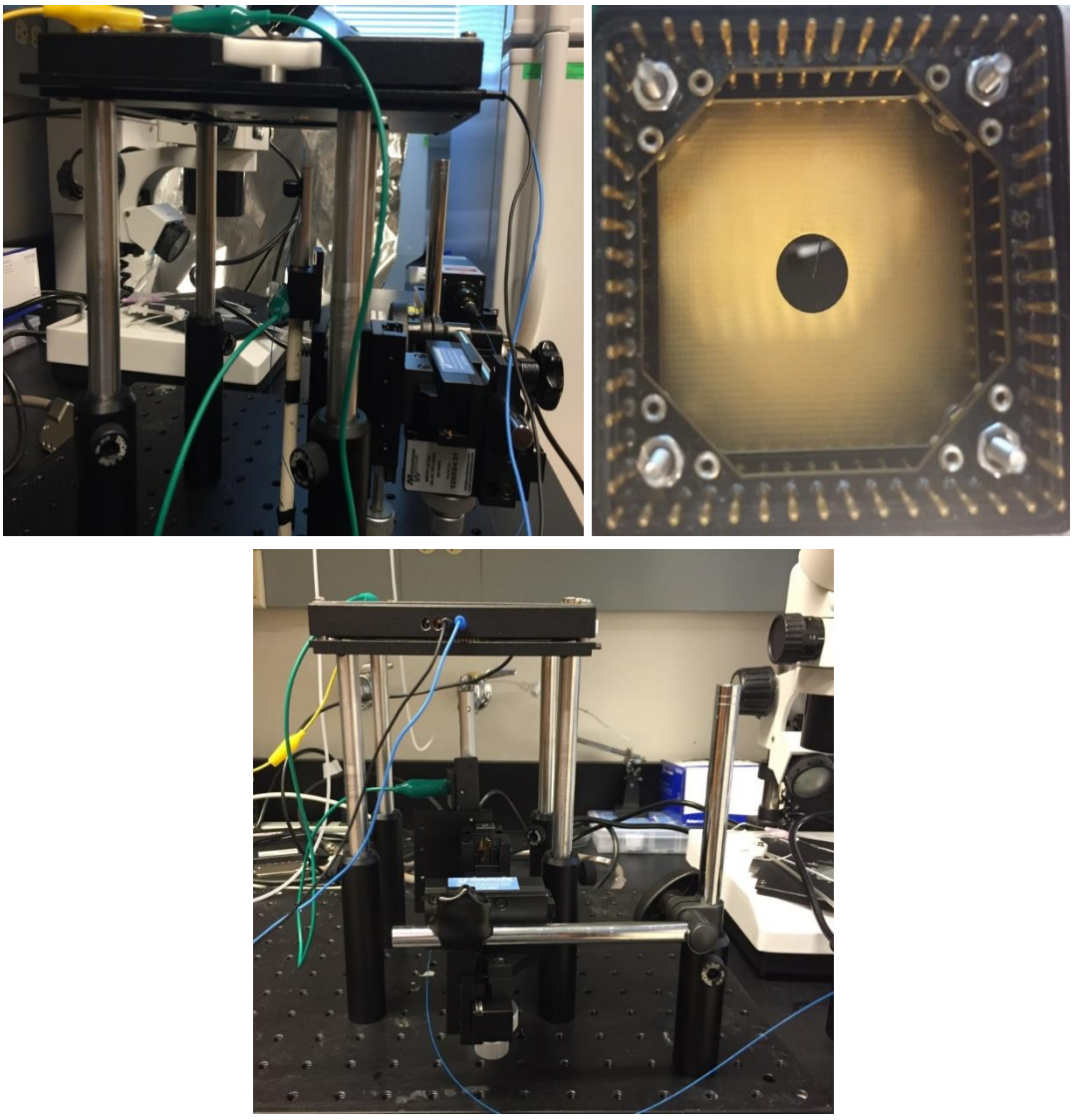

Figure 4.4 Stimulation set up. Upper left image shows side view of laser incident on the backside of the Multichannel Systems amp board. Upper right, void in the base of the amplifier allowed use to stimulate from the bottom (end of fiber optic cable can be seen in the middle of the void).

Figure 4.2a,b) . Figure 4.2c shows a single coax, whose shield has been lowered by using the extended core fabrication technique. The coax inner (core) and outer (shield) conductors are sputtered Ti:Au (10 nm: 120 nm thickness), and the dielectric is 225 nm thick atomic layer-deposited Al_2O_3. The final area of the coaxial region in Fig 4.2a,b is 315 μm^2 and contains 8 ± 1 individual coaxes.

To characterize the cMEA, the same procedure as in the cNEA characterization was used: DC resistance (between the inner and outer electrode) measurements were made first in air to verify device integrity (open circuit), with typical resistances in the GΩ range, as anticipated. The high resistance is expected given the material properties of the alumina, which separates the two metals. The resistivity of alumina is on order of 100 TΩ · cm. Again, a capacitance bridge was used to measure the capacitance of the devices, and the measured values were on the scale of the calculated value based on geometry and material parameters (Chapter 2). Electrochemical impedance measurements were then made across a 100 Hz – 200 kHz frequency range (desirable range for neurological measurements)[6]. As seen in Figure 4.5, both the cMEA and cNEA devices compared favorably to similar devices found in the literature, as well as commercial microelectrode arrays[7,8,9,10]. The cMEA device had a higher impedance ($|Z| = 52.9 \pm 26.4$ kΩ) than the cNEA ($|Z| = 1.5 \pm 0.7$ kΩ) at 1 kHz, due to the latter having more coaxial pillars per coaxial sensing region and therefore more total electrode surface area (roughly twenty times more). Increased surface area of the 3D coaxial architecture is also the reason the impedances of our devices are lower than the other technologies represented in Fig 5. The variation in impedance (roughly 50%) is most likely due to different shield heights as a result of the extended core process (the chemical etch rate tended to vary by 20%).

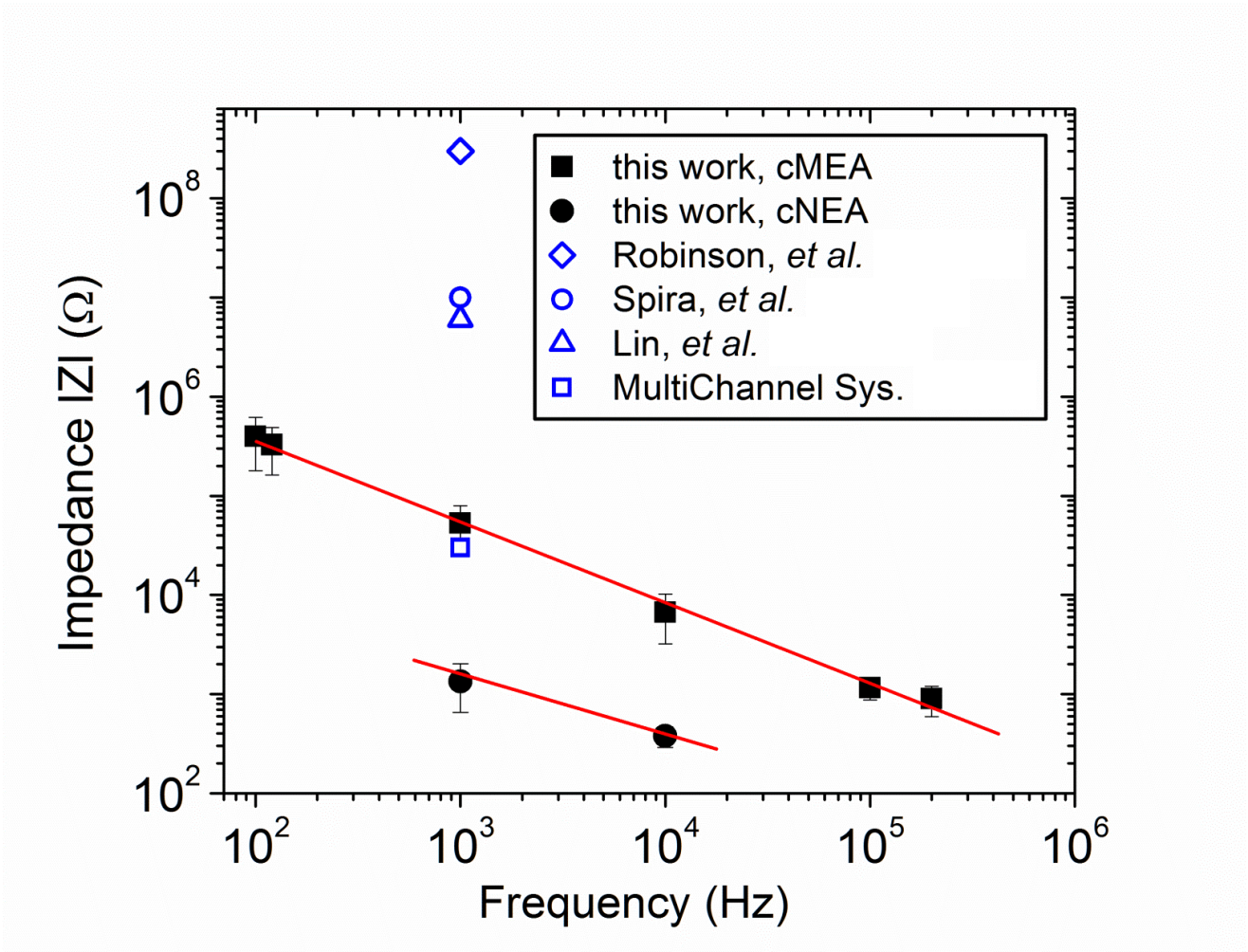

Figure 4.5 Characterization of cMEA. Impedance measured as a function of frequency for an individual coaxial sensing region for 2 different coaxial devices (solid squares: cMEA, solid circles: cNEA). Lines are guides to the eye. Related devices found in the literature are included for comparison.

4.4 Optically evoked current deflections: Top-side illumination

A 473 nm DPSS laser (Model BL473-100FC ADR-700A, Shanghai Laser & Optics Century Co., Ltd.) coupled to a multimode 200 μm diameter optical fiber (0.39 NA, Thor Labs) with a spot size of ~350 μm was used for photo stimulation. Figure 4.6 shows the calculation of the laser spot size. The optical fiber was brought into contact with a glass substrate containing a pattern of known size constraints on its surface (Fig 4.6b). The laser was turned on and an image was taken (Fig. 4.6c). Throughout the experiment the laser was triggered using a TTL signal (Stimulus Generator STG4002, Multichannel Systems) with a 1 s square wave pulse. In our first preparation, the tip of the optical fiber was positioned directly above the cMEA after plating with HEK-ChR2 cells. In the second preparation, the same scanning sequence was used but the optical fiber tip was placed underneath the cMEA substrate to achieve optical illumination through the transparent SU-8 coax cores.

Once the fabrication and characterization of a coaxial microelectrode array was completed we recorded current transients from genetically-altered HEK293 cells with light-actuated channelrhodopsin (ChR2) ion channels. In the first recording, the device consisted of a 5 × 6 array of individually-addressed coaxial regions spaced 100 μm apart. Each 20 μm diameter region contained 8 coaxes wired in parallel. The tip of the optical fiber was initially fixed in a specific position over the array, and the cultured cells were illuminated with the 473 nm laser (power 20 mW/cm^2) for 1 s to activate inward ChR2 currents, which appeared as deflections in the extracellular field potentials. Optical power was measured with a commercially available power meter according to the

(a) (b)

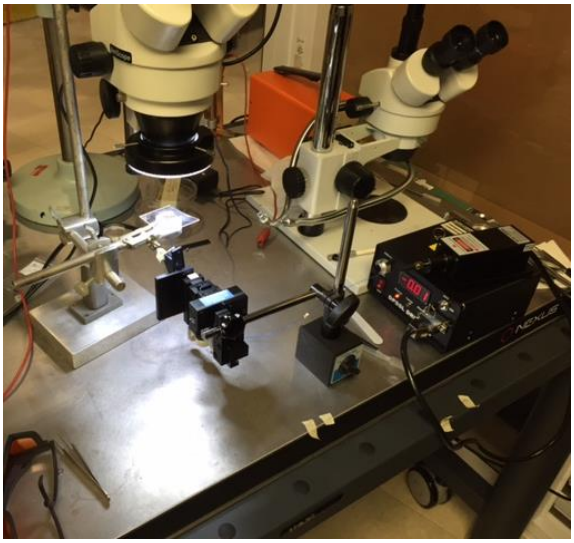

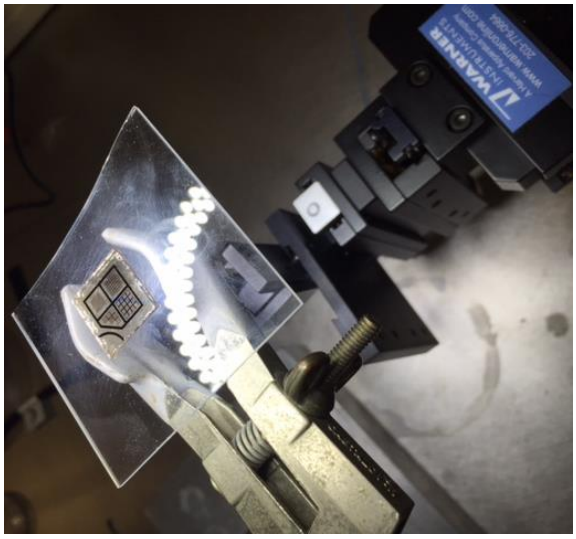

(c)

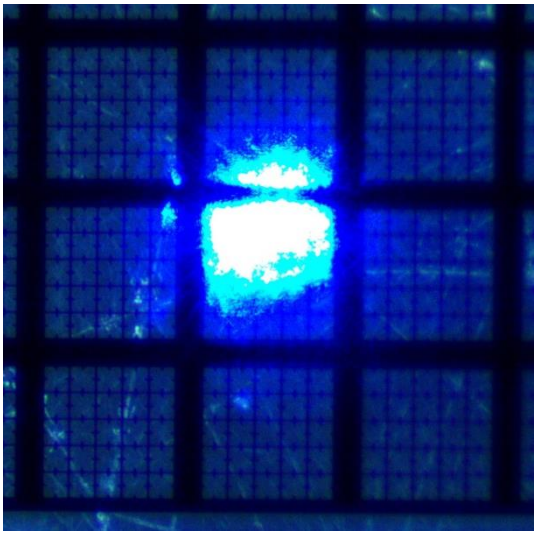

Figure 4.6 Laser spot size measurement. (a) Set up for spot size measurement. Fiber optic cable connected to laser brought to backside surface of 1 mm thick glass while camera was fixed overhead. (b) Substrate with known feature sizes placed above fiber optic cable. (c) Micrograph of laser spot size. Smaller squares are 50x50 µm while larger squares are 300x300 µm.

manufacturer's instructions (Model 1916-R, Newport Corp.). The optical fiber was then repositioned using a micromanipulator before being actuated again. Throughout this illuminate-position-illuminate scanning sequence, all 30 available channels were monitored for light-evoked potentials. Upon event detection, a dose-response test was performed in order to characterize the sensitivity of each individual coaxial sensing region using a range of power settings up to 30 mW/cm^2. This was performed by fixing the light directly above a particular coaxial region under study and varying its intensity from 0 to 30 mW/cm^2 in 2 mW/cm^2 steps. One such dose test is shown in Figure 4.7a. The response magnitude varied slightly (~20%) among regions tested. Each showed a characteristic spike upon initial stimulation (in response to cellular depolarization) before settling into a steady state and followed by an after-potential once the laser was turned off. The after-potential is most likely due to the delayed rectifying K_v channels native to HEK-293 cells[11]. Figure 9b shows the peak voltage recorded as a function of light intensity. The data appear to show the response starting to saturate at 30 mW/cm^2; however, we were unable to explore this further as this was the maximum output of our light source. In subsequent tests, light-evoked field potentials were evident at intensities as low as 0.5 mW/cm^2. Cell coverage was confirmed by epifluorescence microscopy in ~40% of the regions within the 5×6 array. Importantly, a response to light stimulation was found in these regions with, and not in those without, cell coverage. An image of cell coverage on a cMEA with 59 and 7 sensing regions is shown in Figures 8 and 9 respectively. From these figures we can see the cells do not readily avoid the coaxial sensing areas.

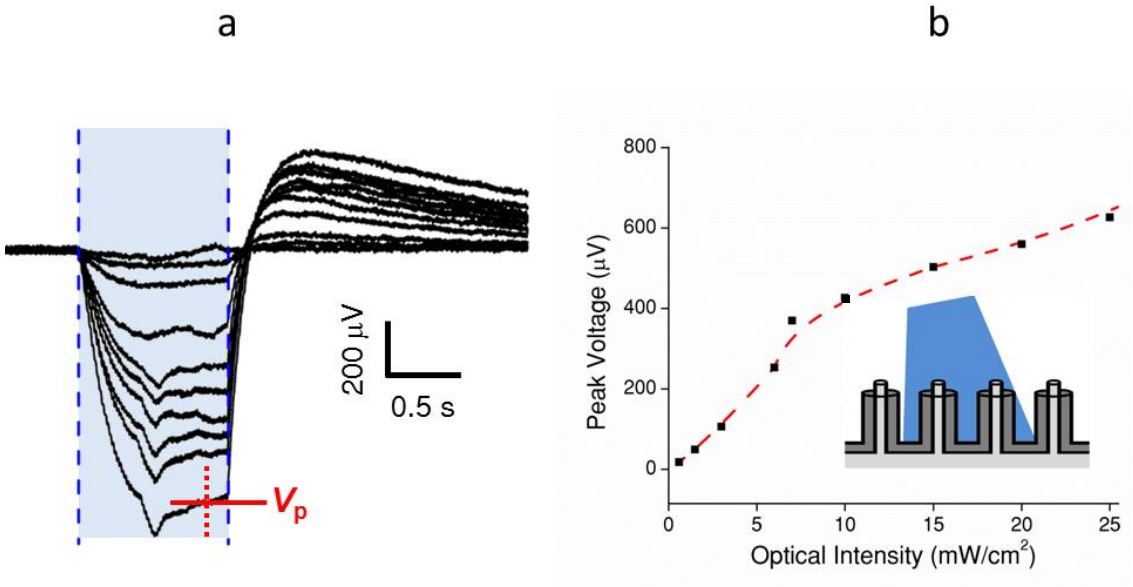

Figure 4.7 Dose test of optogenetic HEK-ChR2 cells cultured onto cMEA. (**a**) Dose test of top side illumination (using 473 nm wavelength) of HEK-ChR2 cells cultured onto the device. The vertical (blue) dotted lines and shaded blue region indicate light on/ light off, respectively and the red arrow indicates the time at which peak voltage was determined (signal having reached a local steady state). (**b**) Peak voltage as a function of power density with parametrically fitted line to guide the eye. Inset depicts blue light-from-above configuration.

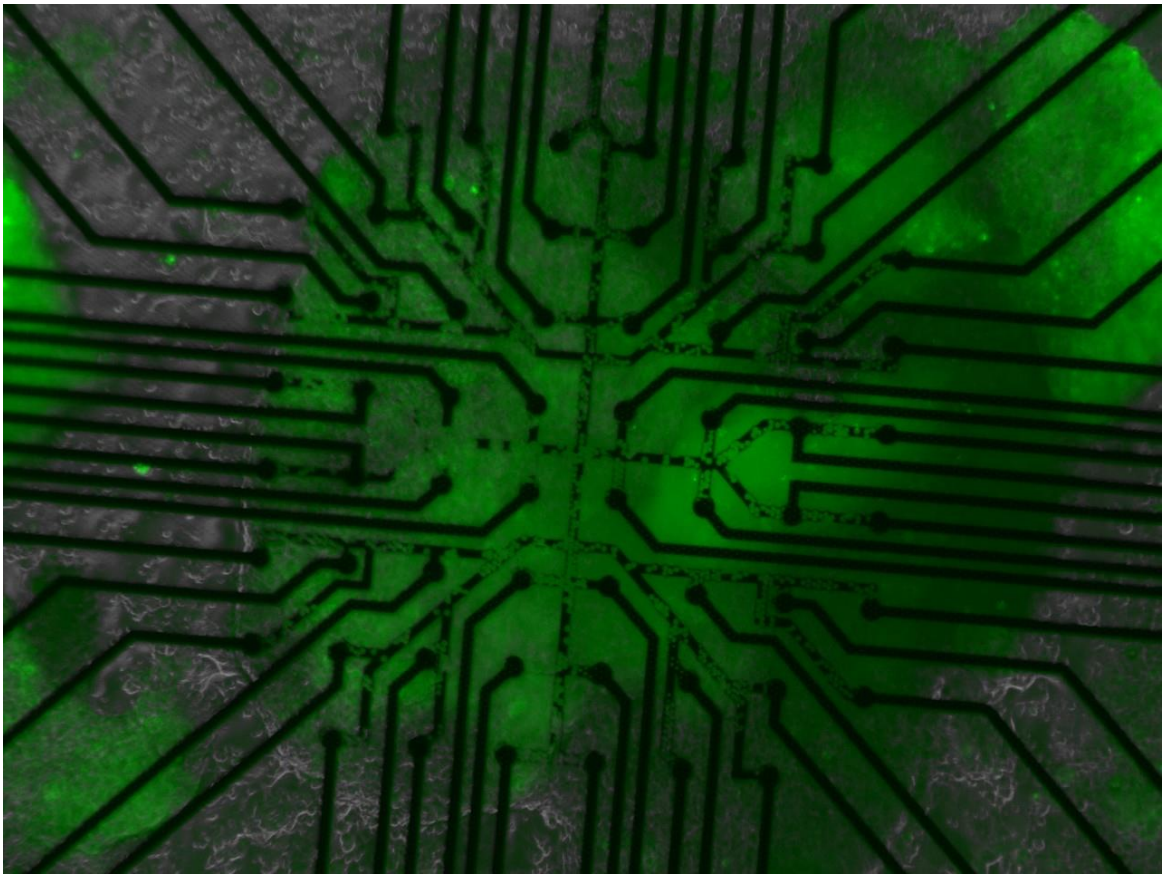

Figure 4.8 HEK cells on 60 input cMEA. Phase contrast fluorescent image of transfected HEK293 cells (green) on cMEA with 60 sensing regions. It is clear the HEK cells do not avoid coaxial area.

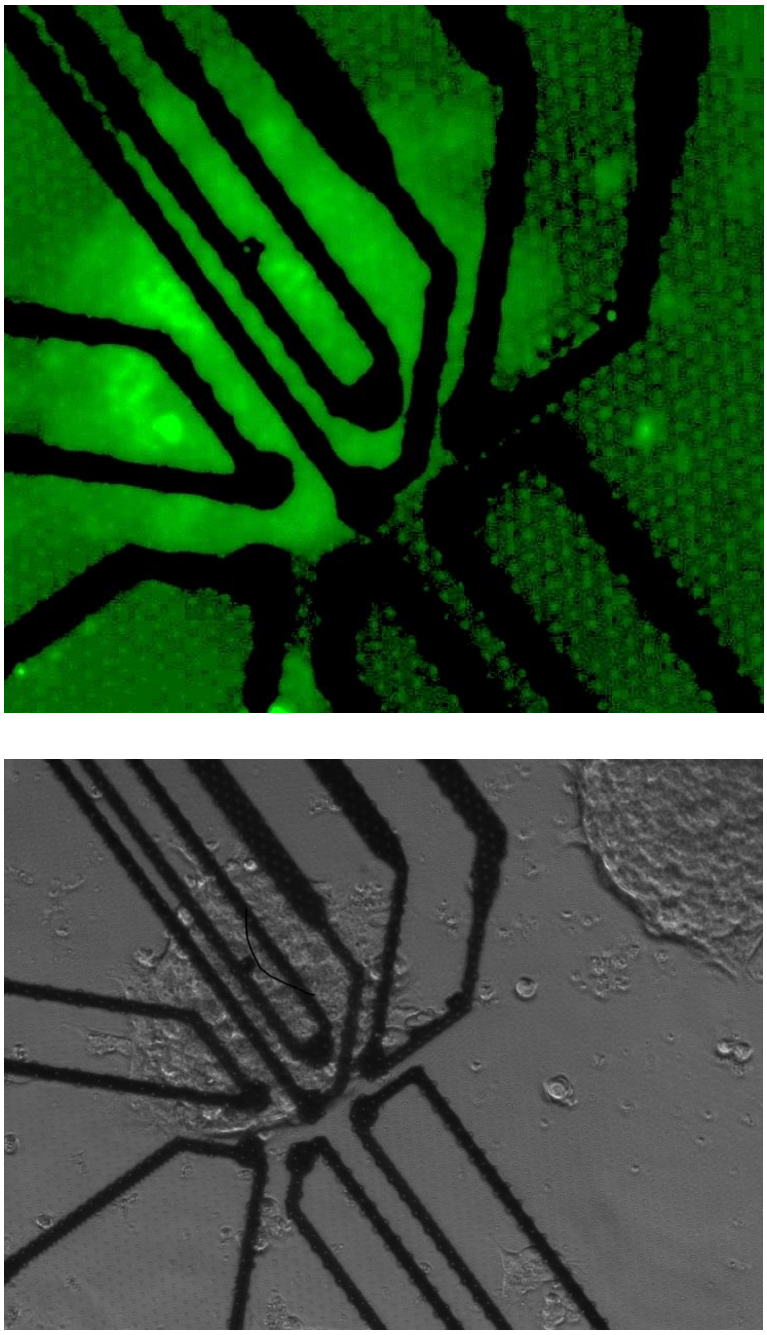

Figure 4.9 HEK293 cells on cMEA. Fluorescence image of transfected HEK cells on cMEA device.

Our next experiment was performed on a cMEA comprised of 4 discrete areas spaced 1.5 mm apart, each containing 7 individually-wired coaxial regions (again, with ~ 8 coaxes per region) of 20 μm diameter at 60 μm internal pitch. One such area was imaged by epifluorescence in order to determine the cell coverage, as shown in Figure 4.10a. This image revealed 4 of the 7 regions to have good cell coverage, while the other 3 regions showed little or no coverage. Figure 4.11 shows a blown up image of Figure 4.10a with lines to guide the eye toward the cell coverage. This area was then illuminated with 20 mW/cm^2 light and changes in the LFP were recorded 4.10b. Given the spot size of the laser and the pitch of the electrodes, all 7 electrodes were illuminated. Again, in areas of no cell coverage, no response or change in the LFP was seen. Conversely, an average response of $\Delta V \sim 100$ μV (steady state, at the given dose) was seen in areas with coax electrodes in sufficient contact with cells to record LFPs, showing a direct correspondence with the cell coverage observed from fluorescence microscopy, Figure 4.10a. Furthermore, there was no response seen in regions 6 and 7, despite being close to regions where the LFP had been perturbed. These initial data showed the possibility of crosstalk suppression. Similar results were found in the 3 other areas containing coaxial regions.

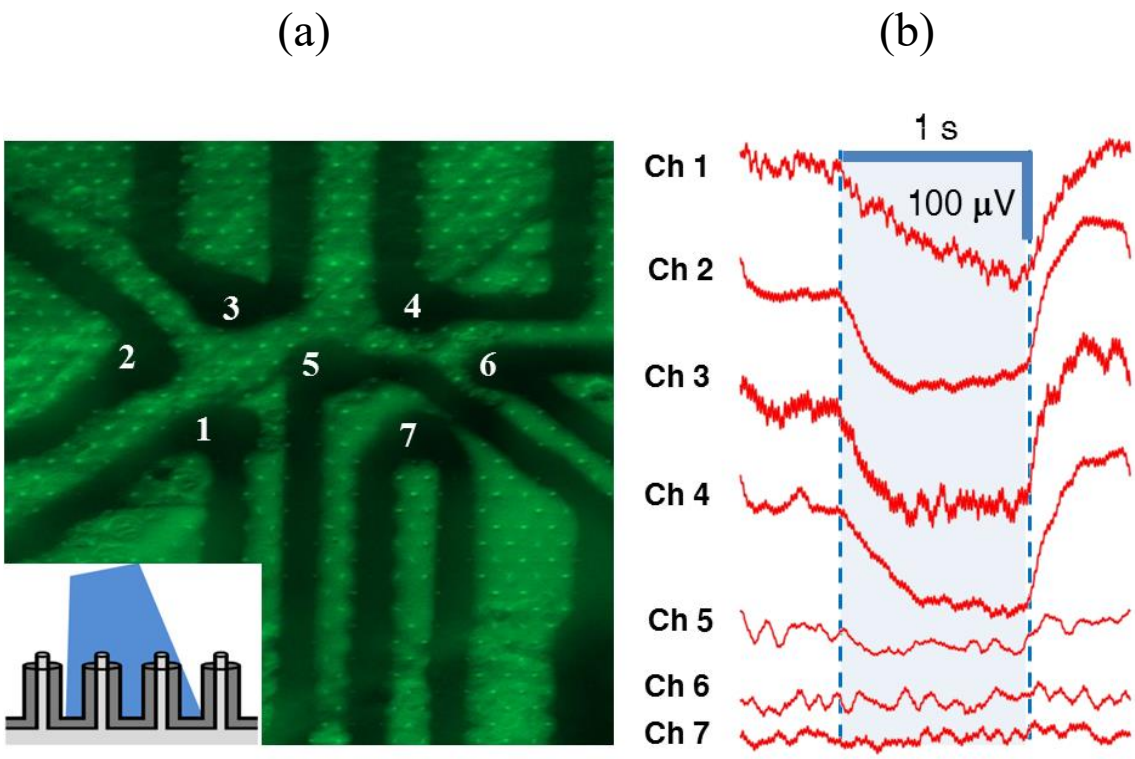

Figure 4.10 Individually-addressed coaxial regions in cMEA. (**a**) Fluorescent microscope image of HEK-ChR2 cells covering a portion of 7 individually-addressed coaxial regions each containing 8 coaxes (60 µm pitch). Inset depicts blue light-from-above configuration. (**b**) Coaxial regions measured changes in the local field due to optical stimulation (473 nm wavelength; 20 mW/cm^2) denoted by the vertical blue bars and shaded region.

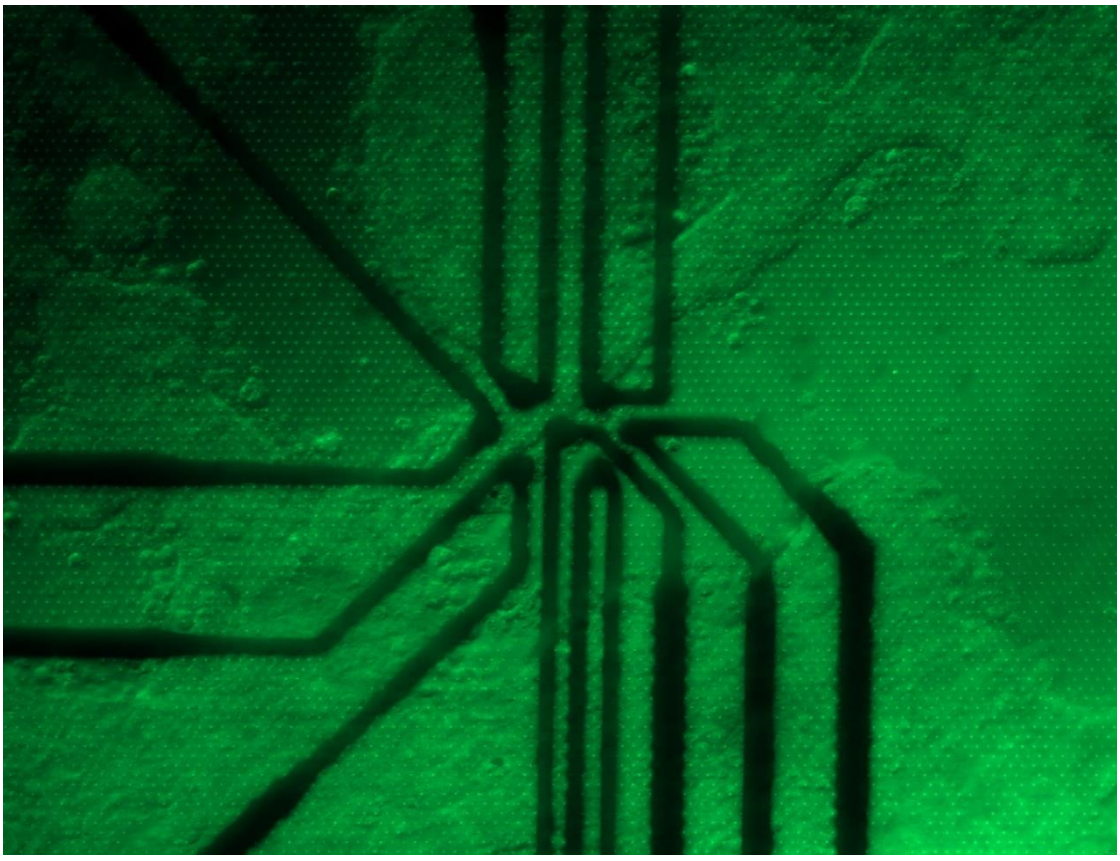

Figure 4.11 Hek293-ChR2 cells on cMEA. Magnified image of fluorescence image in figure 4.12. Rough looking areas are HEK cells whereas smooth areas represent the absence of cells.

4.5 Optically evoked current deflections: Through coax illumination

In subsequent experiments, we modified the orientation of our optical source to be incident on the backside of our cMEA (Figure 4.4), which was opaque everywhere except through the coax cores. Again, the optical fiber was attached to a micromanipulator for x and y scanning and the diameter of the port in the bottom of the amplifier platform was larger than the sensing array area, allowing for full array coverage. As shown previously, the optical stimulator was characterized prior to experiment to have a spot size of ~ 350 μm. Initial recordings of the device in medium (the same as used to grow the HEK293-ChR2 cells in) alone (*i.e.* without cells) were made to establish a baseline noise level, and to determine and record photoelectric artifacts induced by the laser, should any occur, for the purpose of post-data analysis filtering. However, no optical artifacts were seen throughout these initial measurements. As above, HEK293-ChR2 cells were grown on the device and coverage of multiple sensing areas was confirmed by microscopy. The laser was then moved to several sites below the area containing the individual sensing regions and a 5 sweep trial was performed at each spot. All 60 channels were monitored throughout each trial and the approximate laser location was noted prior to stimulation, as shown in Figure 4.12 for trial 1. In addition, when an event (LFP deflection) was detected, a subsequent dose test was performed. Once again, the location of detected events on the cMEA corresponded directly to the location of the laser and was roughly confined to the extent of the spot size, as shown in Figure 4.12. The magnitude of cell response appears to correspond directly with ChR2 expression (seen in variability of

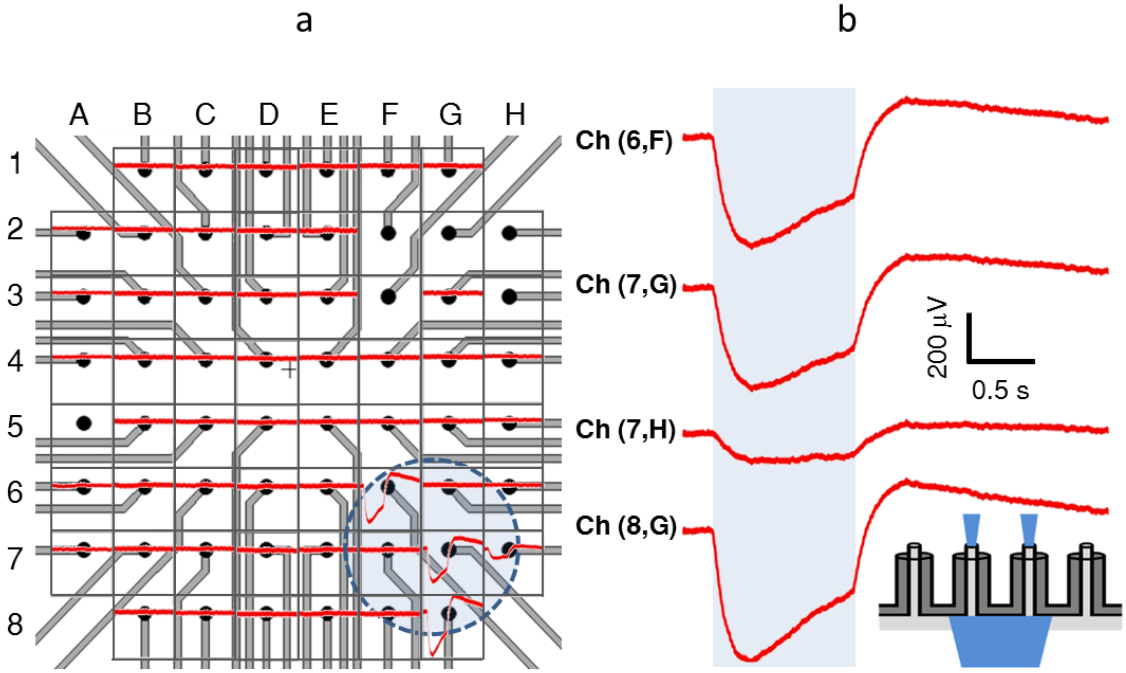

Figure 4.12 Backside stimulation of HEK-ChR2 cells cultured on cMEA. (**a**) 60 data channel windows (with data in red; window scale: 3 s width / 725 µV height) overlaid onto cMEA spatial layout; blank windows represent non-working amplifier inputs, prior to experiment. Numbers correspond to channel number using familiar matrix representation (row, column). Shaded region in lower right corner represents approximate location of laser. (**b**) Magnified view of regions of clear current deflection due to stimulus. Shaded region represents laser on. Inset depicts blue light-from-below configuration.

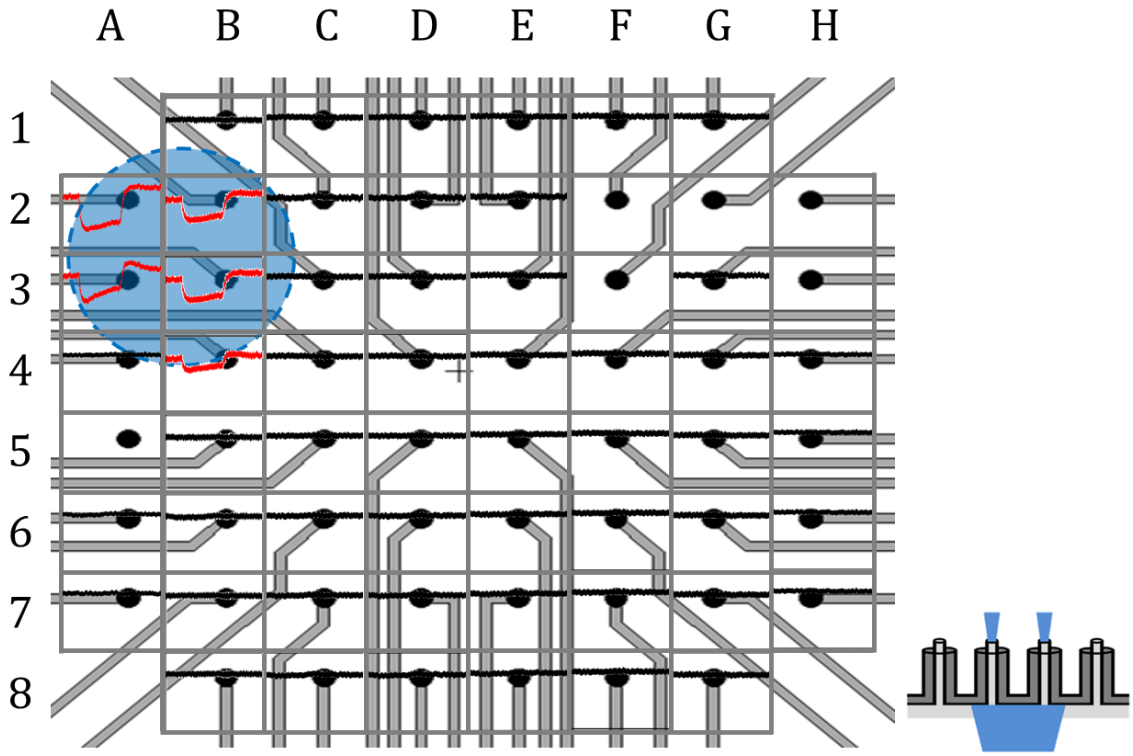

Figure 4.13 Backside stimulation of HEK-ChR2 cells cultured on cMEA. 60 data channel windows (with data in red; window scale: 3 s width / 725 µV height) blank windows represent non-working amplifier inputs, prior to experiment. Shaded region in upper left corner represents approximate location of laser.

fluorescence intensity in previous imaging) within the illuminated area and thus varied across the cMEA.

The laser was then moved from the lower right corner of the cMEA to the upper right corner and actuated. While it was not possible to verify exactly the location of the laser, with extended use of the micromanipulator, one could get a sense of how far the fiber was moved with the dial rotation amount. Figure 4.13 shows deflections in the local field potential for the region corresponding to the laser location. The red data lines represent a response whereas the black lines in each window show a lack of response. The laser spot image in the figure has a slight eccentricity due to the outline of the data windows being asymmetric. Again we see the response is confined to the laser area. After roughly 90 minutes of this process, there was a noticeable drop in response amplitude. This could be due to affects associated with temperature or possibly optical toxicity due to prolonged exposure. The chip was then removed and moved to a refrigerator to attempt to fix the cells for SEM imaging. However, we were unsuccessful in obtaining micrographs of the cells, as the cell structure was indiscernible on top of the cMEA.

The ultimate goal of any MEA technology is to record from networks of cells and analyze their circuit dynamics in an effort to provide insight into physiological behavior. To this end, high-density MEAs utilizing complementary metal oxide semiconductor (CMOS) technology have greatly increased the number of recording sites on a single device[3,9,12,13]. However, signals generated from electrogenic cells have been shown to spread beyond 100 μm, which presents a problem as unshielded electrodes will have overlapping sensing regions[14,15]. Traditional spike sorting methods (principal component analysis, wavelet transform, *en bloc*, etc.) require high computational demand and

become unreliable due to waveform variability, small spike amplitude and synchronous firing events[16]. Implementing the coaxial architecture to high density arrays represents a potential alternative way to obtain high density (network) recording while at the same time suppressing electrical crosstalk. While HEK293 cultures tend to grow in colonies, making cell isolation difficult, we successfully recorded 4 distinct waveforms (LFP perturbations upon stimulation) from a cluster of cells. Each detected event in Figure 10 reached a steady state potential of ~100 μV (± 20 μV) after 400 ms (±100 ms). While these signatures of induced currents may not necessarily emanate from individual regions, given the 60 μm pitch of the array, we note that during the backside illumination experiment shown in Figure 4.12, Channels (7,F) and (8,F) showed zero voltage change despite neighboring Channel (8,G) having ΔV ~ 450 μV. We consider it unlikely that all 4 coaxial regions are detecting the same signal. From Figure 4.13 we see a similar response in that the signal is confined to the laser region and the neighboring electrodes do not show any deflections. Therefore, the coaxial architecture minimizes crosstalk through local shielding and thus enables closely-spaced electrodes with non- or minimally-overlapping sensing regions

In addition to minimizing crosstalk, the fact that propagation of light through specific coax regions caused large LFPs from HEK293-ChR2 cells demonstrates the ability of the coaxial architecture to facilitate custom localization of the stimulating light source. The localization of applied light is important when using minimum light intensities to mediate the behavior of a particular cell type, as the light incident from above the neural assembly will scatter and attenuate upon entering the medium prior to being absorbed by the opsin. Ozden, *et al.*[35] have previously shown peak intensity to be

inversely proportional to aperture diameter and, since the individual coaxes are capable of being fabricated at sub-cellular dimensions[30] (~1 μm), the cNEA provides a solution for lower power consumption as well as facilitating direct stimulation of an individual cell. In contrast, when using large diameter optical fibers for such stimulation, the technical problems of tissue damage and unintentional illumination of distal neurons are unavoidable[1]. Furthermore, the increased distance from the cell in the fiber case necessitates a higher input power, which can cause undesired artifacts. Our device detected a change in the LFP using as little as 0.5 mW/cm^2 light intensity, something that could be achievable with micro-light-emitting diodes (μLED).

The results presented in this chapter thus encouraged the study of the device architecture and materials and the logical next step was to first study the optical throughput of coaxial multielectrode arrays at various core diameters and then to characterize the crosstalk suppression capability of the device. For the subsequent work on investigating crosstalk, we chose to study how related devices (bare electrodes) deployed *in vitro* compare to our arrays with regard to spike sorting and thus able to assess the true gain in spatial resolution.

4.6 References

[1] Shaw, G., Morse, S., Ararat, M., & Graham, F. L. Preferential transformation of human neuronal cells by human adenoviruses and the origin of HEK 293 cells. The FASEB Journal, **16**, 869-871 (2002).

[2] Varghese, A., TenBroek, E. M., Coles, J., & Sigg, D. C. Endogenous channels in HEK cells and potential roles in HCN ionic current measurements. Prog. in Biophys. and Mol. Bio., **90**, 26-37 (2006).

[3] Lin, Y. C., et al. Genome dynamics of the human embryonic kidney 293 lineage in response to cell biology manipulations. Nature communications **5**, 4767 (2014).

[4] Fredj, S., Sampson, K. J., Liu, H., & Kass, R. S. Molecular basis of ranolazine block of LQT-3 mutant sodium channels: evidence for site of action. Brit. J. of Pharm. **148**, 16-24 (2006).

[5] Zhang, F., *et al*. Multimodal fast optical interrogation of neural circuitry. Nature **446**, 633-639 (2007).

[6] Buzsáki, G., Anastassiou, C.A., & Koch, C. (2012). The origin of extracellular fields and currents - EEG, ECoG, LFP and spikes. *Nat. Rev. Neurosci.* **13**, 407-420.

[7] Spira, M.E. & Hai, A. Multi-electrode array technologies for neuroscience and cardiology. Nat. Nanotechnol. **8**, 83-94 (2013).

[8] Robinson, J. T., Jorgolli, M., Shalek, A. K., Yoon, M. H., Gertner, R. S., & Park, H. Vertical nanowire electrode arrays as a scalable platform for intracellular interfacing to neuronal circuits. Nat. Nanotechnol. **7**, 180-184 (2012).

[9] Lin, Z. C., Xie, C., Osakada, Y., Cui, Y., & Cui, B. Iridium oxide nanotube electrodes for sensitive and prolonged intracellular measurement of action potentials. Nat. Commun. **5**, 3206 (2014).

[10] Multichannel Systems MCS GmbH, Reutlingen Germany.

[11] Jiang, B., Sun, X., Cao, K., & Wang, R. Endogenous Kv channels in human embryonic kidney (HEK-293) cells. Molec. & Cell. Biochem. **238**, 69-79 (2002).

[12] Huys, R., *et al.* Single-cell recording and stimulation with a 16k micro-nail electrode array integrated on a 0.18 μm CMOS chip. Lab Chip **12**, 1274-1280 (2012).

[13] Ballini, M., *et al.* A 1024-Channel CMOS microelectrode array with 26,400 electrodes for recording and stimulation of electrogenic cells in vitro. IEEE J. Solid-State Circuits **49**, 2705-2719 (2014).

[14] Kajikawa, Y., & Schroeder, C. E. How local is the local field potential? Neuron **72**, 847-858 (2011).

[15] Buzsáki, G. Large-scale recording of neuronal ensembles. Nat. Neurosci. **7**, 446-451 (2004).

[16] Einevoll, G. T., *et al.* Towards reliable spike-train recordings from thousands of neurons with multielectrodes. Curr. Op. Neurobiol. **22**, 11-17 (2012).

Chapter 5: Characterizing optical throughput of cylindrical structures– extraordinary optical transmission (EOT) in 3D geometry

5.1 Introduction

In this Chapter, we discuss the far-field transmittance of visible-NIR light through cylindrical structures. In the context of the rest of this thesis, these structures were fabricated with the intention of utilizing them in optogenetic neurological studies. Initially, we had some concerns that sufficient throughput of light could be achieved in small-diameter (on the order of the wavelength or below) 3D cylinders. We were unable to find any experimental results on such structures within the scientific literature. Therefore, we set out to fabricate devices and determine the throughput for ourselves.

Here, we performed a longitudinal study (sub - to supra-wavelength apertures, spanning the ray and wave optics realms) of optical transmission through 3D dielectric-filled cylindrical metal micro/nanostructures. The cylinders are comprised of a polymer core (SU8) coated with a metal whose thickness is sufficient to be optically opaque. Several novel phenomena are observed when the metal is plasmonically active in the frequency range employed (Au) that are absent in a metal with strongly attenuated plasmon interactions (Cr). We begin with a brief background discussion on the physics of light transmission though subwavelength apertures, followed by an introduction to surface plasmon polaritons (SPPs; we will also refer to these phenomena as surface plasmons or SPs) and extraordinary optical transmission (EOT). Next, the fabrication process and experimental techniques are discussed. Following this, data from subsequent experiments involving Au and Cr cylinders are presented and various features in the data

are discussed. Finally, we explore the plasmonic behavior found in the Au samples with a series of experiments in which the geometry is changed slightly and the plane of incidence is inverted by 180 degrees.

The physics of electromagnetic radiation passing through an aperture can be described by geometrical or ray optics when the radiation wavelength is small compared to the aperture, and by physical or wave optics in the converse situation. In ray optics, if the aperture is in a nontransmitting, vanishingly thin medium of unit area, the fraction of longitudinally transmitted radiation is equal to the scaled aperture area (and so vanishes at zero size). In wave optics, Huygens-Fresnel-Kirchoff (HFK) aperture theory describes how the phenomenon of diffraction dominates and modifies the throughput, generating transverse wave vector components and a spatially-varying throughput (far field Fraunhofer or Fresnel pattern depending on the geometry involved[1]). When the medium and thus the aperture is of finite thickness, along the direction of propagation, additional considerations enter, such as photonic modes along the length of the aperture. Further, when the medium is a real metal (as opposed to idealized) and the radiation is in the visible regime, interactions other than diffraction can arise, such as the excitation of bulk and surface plasmons (SP).

Kirchoff scalar diffraction offered an early solution to the far field transmission of a plane wave incident on an opaque screen containing a small aperture of diameter *d* (Figure 5.1)[2]. The theory assumes the solution to the Kirchoff wave equation given by:

$$\nabla^2\psi + k_0^2\psi = 0 \qquad (1)$$

will be of the form $\Psi(r,t) = \psi(r,t)e^{-i\omega t}$, where $\psi(r,t)$ is the wavefunction, k_0 is the propagation parameter, $r^2 = \sqrt{x^2 + y^2 + z^2}$, ω is the wave frequency, and *t* is the time. In this approach, the first step is to invoke Green's theorem:

$$\psi(r) = \frac{1}{4\pi}\int\left[\frac{\partial\psi}{\partial n}\frac{e^{ik_0 r}}{r} - \psi\frac{\partial}{\partial n}\left(\frac{e^{ik_0 r}}{r}\right)\right]ds \qquad (2)$$

with *S* being the entire surface of the screen, which extends to infinity in the *x* and *y* directions and whose ends are joined (enclosing the space on the right side of the screen in Fig. 5.1), and *n* is the direction normal to the surface. If the values of ψ or $\partial\psi/\partial n$ are known on *S*, they are known for all points interior to the bounding surface, and thus, the right side of the screen. The Kirchoff approach sets $\psi = 0$ and $\partial\psi/\partial n = 0$ on the right side of the screen and $\psi = \psi_0$ at the hole. Here, ψ_0 represents the unperturbed incident wave. When *d* is large compared to the incident wavelength λ_0, the Kirchoff scalar approach gives good results because most of the diffracted wave is distributed in the forward propagating direction +*z*. Therefore, the assumptions made for ψ_0 and $\partial\psi/\partial n$ largely hold true. However, as *d* becomes small compared to λ_0, the lobes of the diffracted wave begin to bend toward the surface of the screen, thus rendering the assumptions no longer valid[3]. Another issue with this theory is that it does not generally satisfy Maxwell's equations, since it is solving a scalar equation and not a set of coupled field equations[4]. These shortcomings were addressed by Bethe in 1944, with a new theory of wave diffraction[5].

Bethe theory attempts to find the *E* and *H* fields in the hole using continuity and boundary conditions, while assuming the field amplitudes are essentially constant over

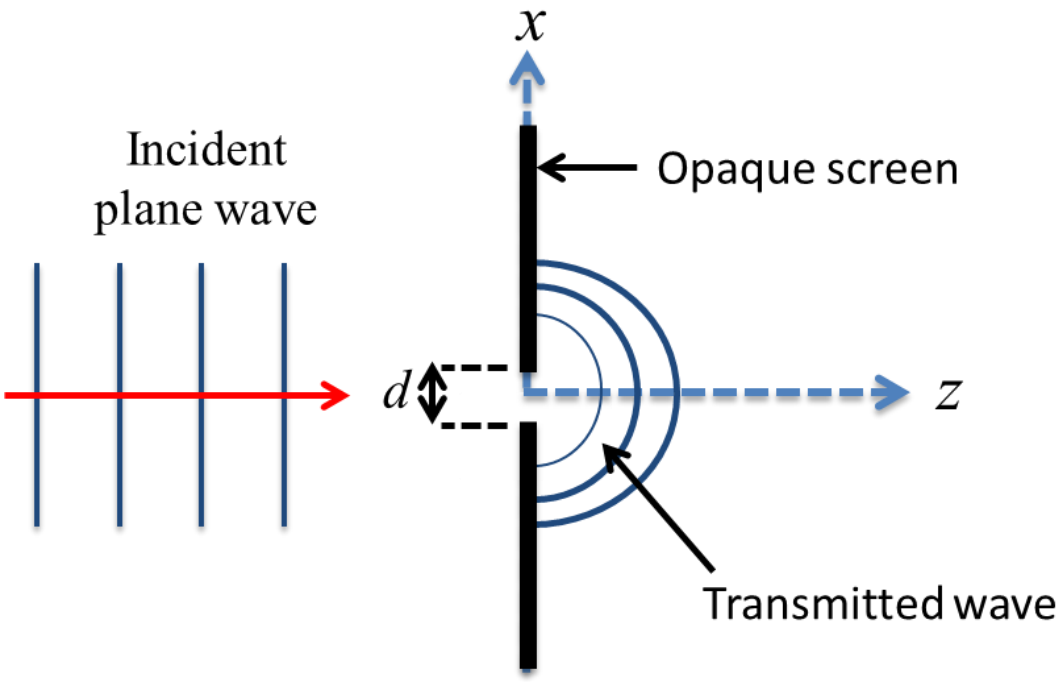

Figure 5.1 Transmission of light through small aperture in opaque screen. An opaque screen, containing an aperture of diameter d, lies in the x-y plane at $z = 0$. A plane wave propagates toward the screen at normal incidence and transmits through the opening.

the area of the hole. Another slight difference from Kirchoff theory is that the screen is now considered to be an opaque, "perfectly conducting" metal screen. In a perfectly conducting metal (also known as a perfect electrical conductor or PEC) the conductivity is infinite and therefore an incident *E–M* field does not penetrate the surface (zero skin depth). We will not go deeper into the details of Bethe theory here, but instead focus on an important result of the calculation: the light power of wavelength λ transmitted through a small aperture of radius *a* and normalized to the cross section of the hole ($A = \pi a^2$) is given as

$$\frac{P}{A} = \frac{64}{\pi^2 27}\left(\frac{a}{\lambda}\right)^4 \qquad (3)$$

Here, we see that the transmittance falls off as λ^{-4}, whereas in Kirchoff scalar diffraction theory, the transmittance falls off as λ^{-2}. Also, while Kirchoff theory was valid when $d \gg \lambda$, Bethe theory is valid when $d \ll \lambda$. Furthermore, while Bethe theory is correct in the far-field, it is extremely limited in the near-field[6]. Both Kirchoff and Bethe theory posit solutions to the far-field transmittance where only propagating waves carry diffracted power. However, both theories exclude surface modes evanescent in the *z* direction. As we will see, for real metals, these waves can play an important role in an enhancement in the far-field transmittance due to the phenomena of the resonant excitation of surface plasmons.

A surface plasmon is a conduction electron density wave that forms at the surface of a metal (*i.e.* at a metal-dielectric interface). Among other origins, this can occur due to coupling of free electrons in the metal to the electromagnetic field of transverse magnetic

(TM or *P*-polarised) light. TM light is required due to the condition that some component of the incident electric field must be normal to the metal-dielectric interface to generate the necessary polarization charge[7] (Figure 5.2a). The occurrence of surface waves in the metal, whose conduction electrons are modeled as an electron gas, derives from the dispersion relation[8] for charge density waves in an electron plasma given by:

$$k_{spp} = \left(\frac{\omega}{c}\right)\sqrt{\frac{\epsilon_d \epsilon_m}{\epsilon_d + \epsilon_m}} = \left(\frac{\omega}{c}\right)\sqrt{\frac{\omega^2 - \omega_p^2}{2\omega^2 - \omega_p^2}} \qquad (4)$$

Here, ϵ_d and ϵ_m are the dielectric constants of the dielectric and metal, respectively, and ω_p is the bulk plasmon frequency:

$$\omega_p^2 = \frac{n_e e^2}{\epsilon_0 m_e} \qquad (5)$$

where n_e is the electron density, m_e is the mass of an electron, and e is the charge of an electron. From (4) we can see that as $\omega \to 0$, k_{spp} approaches ω/c which is the dispersion relation for light in free space. In this regime, the momentum of the SPP ($p = \hbar k_{spp}$) remains higher than a free space photon, ($p = \hbar k_0$) and therefore is non-radiative. However, when $\omega < \omega_p$, k_{spp} becomes purely imaginary and the wave $\psi = \psi_0 e^{ik_0 x}$ becomes evanescent, decaying exponentially into the material according to $E_z \sim e^{-|k_z|z}$ (Figure 5.2b,c). If we assume the dielectric constant of the metal has an imaginary component (i.e. a real metal), we will obtain a complex wave number $k_{spp} = k'_{spp} + ik''_{spp}$ with the real part (k'_{spp}) given by (4) and the imaginary part given by:

$$ik''_{spp} = \left(\frac{\omega}{c}\right)\left(\frac{\epsilon'_m \epsilon_d}{\epsilon'_m + \epsilon_d}\right)^{3/2} \frac{\epsilon''_m}{2(\epsilon'_m)^2} \qquad (6)$$

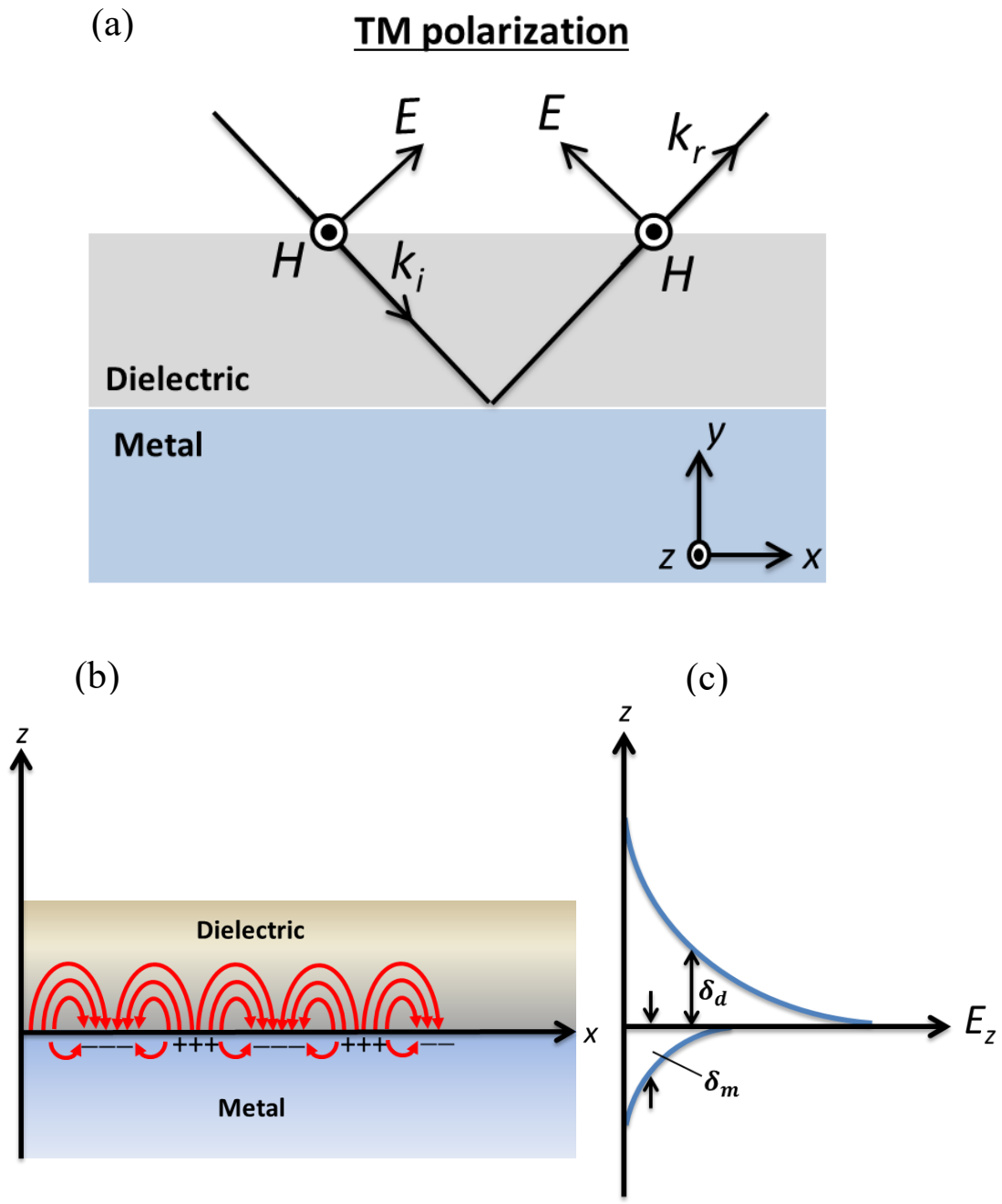

Figure 5.2 TM polarization of $E-M$ wave and SPs generation. (a) Light wave with wave vector k_i incident on metal – dielectric interface. (b) SPs at the surface of metal – dielectric interface. Electric field lines can be seen in red, while H field is into the page. (c) Exponential dependence of the *E*-field in the dielectric and metal regions. The decay length of the E-field in the dielectric $\boldsymbol{\delta_d}$ is roughly half the wavelength, while the in the metal $\boldsymbol{\delta_m}$ is determined by the skin depth.

where the single and double primes indicate real and imaginary parts, respectively. From (6), we can calculate the intensity of SPs propagating along the surface of the metal, also yielding a plasmon propagation length L, using known[9,10] optical constants and the following equation:

$$L = \left(2k''_{spp}\right)^{-1} \tag{7}$$

Two metals, Au and Cr, were used in our experiments and their SPP propagation lengths are shown in Figure 5.3. From the Figure, we can see that in the visible-NIR spectrum, Cr has a very small propagation length (nanometers). Au however, has a propagation length on the micron scale for wavelengths above 600 nm, but drops below one micron for wavelengths less than 600 nm. This cutoff is likely due to Au being highly absorbing for wavelengths below 600 nm as well as the plasmon propagation length. As we will see later, the difference in plasmon propagation length of both metals will have a large effect on the far-field transmittance through our cylindrical structures.

By structuring a metal surface, the properties of localized and propagating (polariton) SPs can be manipulated for use in a number of applications, including SERS[11,12], photonic circuits[13], and sensors[14,15]. A fundamental constraint in aperture theory (seen in Kirchoff and Bethe theory), that being the decrease in transmission of incident light (of wavelength λ) as the aperture diameter approaches and becomes less than λ, can be overcome through the phenomenon of SPs. Exceeding this limit is possible due to photonic modes coupling to SPs, which then couple back to photonic modes, thus facilitating the transfer of near-field information into the far-field. Recently, it was found that sub-wavelength size apertures in metallic films facilitate transmission orders of

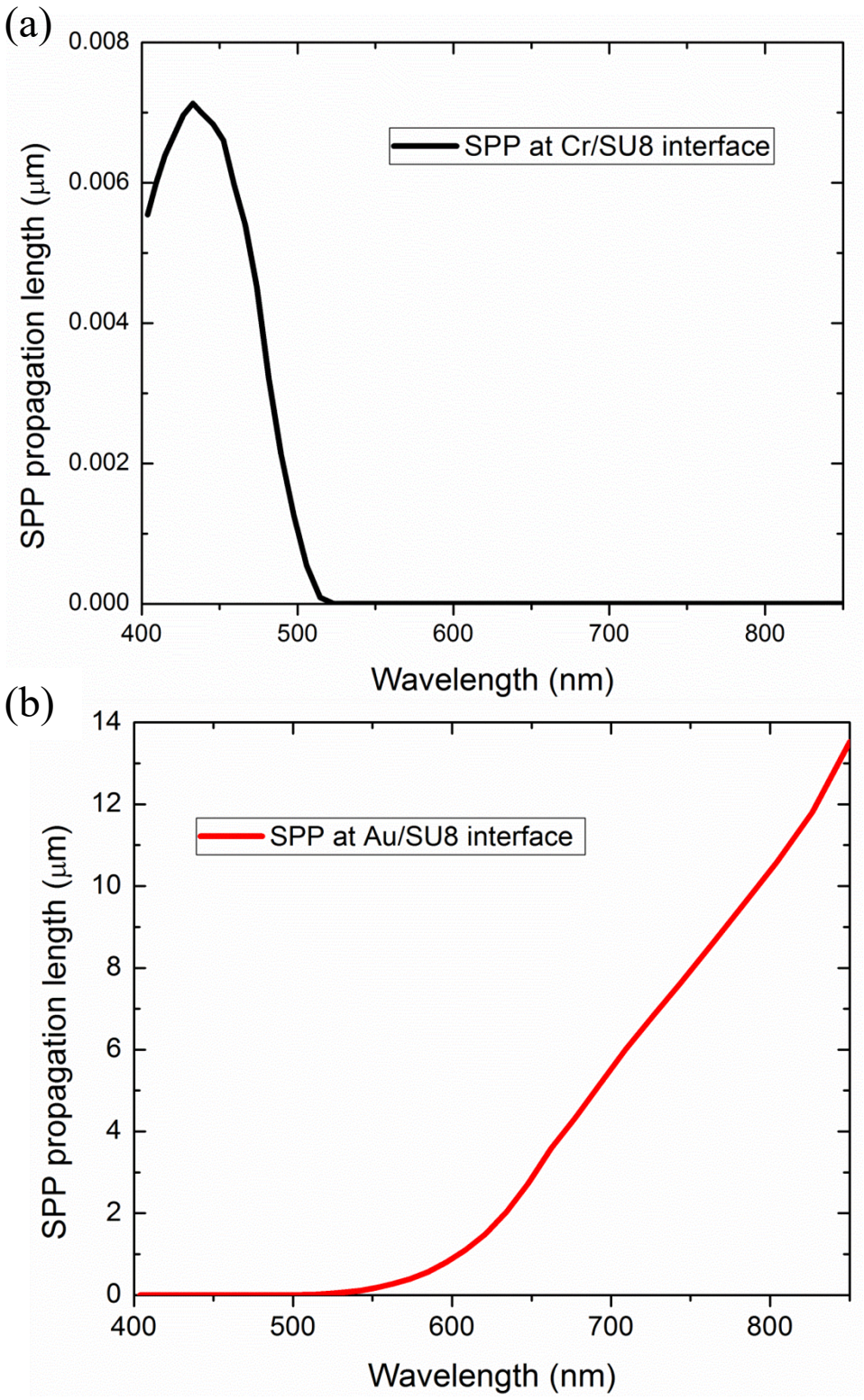

Figure 5.3 SPP propagation length for Cr and Au. Using known optical constants, the calculated plasmon propagation length is plotted for (a) Cr and (b) Au

magnitude larger than predicted by Kirchoff and Bethe theory[16]. In those "extraordinary optical transmission" studies involving essentially 2D hole array systems, the array pitch is on the order of visible wavelengths and the film thickness is not necessarily optically opaque. This Chapter features a 3D system with an array pitch being an order of magnitude larger than the visible-NIR wavelengths incident on the sample. As such, there are similarities, but also important differences in comparison to previous EOT structures.

5.2 3D cylindrical array design and fabrication

Our 3D micro/nanocylinder structures were fabricated on 0.5 mm thick borosilicate glass substrates. A “master” silicon substrate containing 18 regions of 4 μm tall cylinders, each region with a specific cylinder diamter ranging from d = 170 nm to 3 μm, was fabricated, and from that a polydimethylsiloxane (PDMS) mold was made. The master (from which dielectric cylinder arrays were later replicated) was fabricated as follows: a 16 × 30 mm Si substrate was cleaned using a piranha etch and subsequent isopropyl alcohol (IPA)/ acetone sonication bath. The substrate was then placed on a hot plate at 200 C for 10 minutes. To prepare the substrate for electron beam lithography (EBL), a bilayer poly(methyl methacrylate) or PMMA e-beam resist (EBR) was spun onto the substrate; each layer (PMMA 495 followed by PMMA 950) was baked at 180 C for 90 seconds. The coated substrate was then placed into a scanning electron microscope (SEM) and a pattern was transferred onto the resist layer through EBL. The pattern consisted of 2 columns of 9 regions (R), giving 18 total regions. The 2 columns were separated by 10 mm and each of the 9 regions were separated by 5 mm in the y-direction. Each region was comprised of a 500 x 500 μm^2 array of dots of a selected diameter, ranging from 0.3 μm for R1 and 3.5 μm for R18. After exposure, the sample underwent a typical development process using MBK / IPA as a developer.

After microscopic inspection of the pattern for defects, the samples were put through a plasma etch process to remove any excess EBR. Afterwards, e-beam deposition was used to deposit a 100 nm thick layer of aluminum, to be used as a mask layer for a subsequent deep reactive ion etch (DRIE) process. The samples were then left in acetone

overnight to complete a lift off process, leaving arrays of dots corresponding to the aforementioned EBL pattern. After lift-off, DRIE (SF_6/C_4F_8 gases) was used to etch the samples, creating cylinders of a desired height. While the aforementioned 0.3 μm diameter cylinders are certainly sub-wavelength for the visible spectrum, we wished to move further into this sub-wavelength regime and therefore needed to decrease the diameter of the Si cylinders. This was done with a combination process of oxygenation, by placing the sample in a tube furnace set to 1000 C, followed by a wet etch using buffered oxide etch (7:1 $HF:NH_4F$). With this, we were able to prepare cylinder diameters ranging from ~0.17 μm to 3 μm. The aluminum mask was removed and the sample was then coated with a release layer. Finally, a PDMS mold of the Si substrate was prepared and a release layer (1H,1H,2H,2H-Perfluorodecyltrichlorosilane + N-Heptane) was added to the mold. Nanoimprint lithography (NIL) was then used to transfer the cylinder array pattern onto a glass substrate coated with a polymer (SU8), using the mold taken from the master silicon substrate.

These solid polymer cylinders now form templates for subsequent metal coatings to form dielectric-filled Au and Cr cylinders. For Au, physical vapor deposition (PVD) by sputtering was used to deposit a 220 nm thick layer onto the substrate (preceded by 5 nm Ti for adhesion). The Au thickness was chosen due to the desire for the "floor" between and sidewalls on the 3D cylinders to be optically opaque when illuminated from below. Prior to this experiment, transmission measurements of planar Au samples on glass were performed at various Au film thicknesses. It was found that at 160 nm thickness, the transmittance of Au is less than 0.1% and therefore a suitable minimum thickness to be considered opaque. However, given the 3D structure of the nanocylinders

and the directionality of sputtering, it was necessary to deposit a thickness greater than 160 nm to ensure the sidewalls of the cylinders are opaque (*i.e.* at least 160 nm of Au). Figure 5.4 shows an opacity test for 4 Au thicknesses on planar SU8 + glass. Thicknesses were measured with a profilometer and a "witness" sample included in the deposition. The uncertainty of the deposition thickness was ± 10 nm. From the figure it is difficult to quantify the transmittance of thicknesses above 80 nm (other than it being very low) and therefore Figure 5.5 provides a log plot of the data. From the Figure it is clear a 10 nm Ti (sticker layer) + 160 nm Au yields a transmittance of 0.1% or lower. Thus, we have chosen this as our maximum transmittance value for a metal to be considered opaque. Similar structures were also made using Cr as the metal and again, while it's plasma frequency is near Au, the plasmon propagation length in Cr is very small (nanometers, Fig 5.3a) in the visible- N-IR region and therefore does not support extended surface plasmon propagation like Au[8]. As a proof, we remind the reader that we calculated the SP propagation length for both Cr and Au was using *n* and *k* coefficients found in References 9–10 and provided the results in Figure 5.3. From experiments on planar Cr films (Figure 5.6), it was found that 150 nm was a suitable minimum thickness to be considered opaque (Figure (5.7). Again, to ensure opacity of the medium between and sidewalls of the cylinders, we sputtered 225 nm of Cr. To verify metal thickness, cross-sections of individual cylinders were prepared using focused ion beam (FIB) milling, and images were taken using SEM (Figure 5.8a).

In order to facilitate transmission of light out the tops of these cylinders, a final "decapitation" step was peformed using a chemical mechanical polishing process[17]. First, a mechanical stabilization layer of SU8 was spun onto the sample (filling the inter-

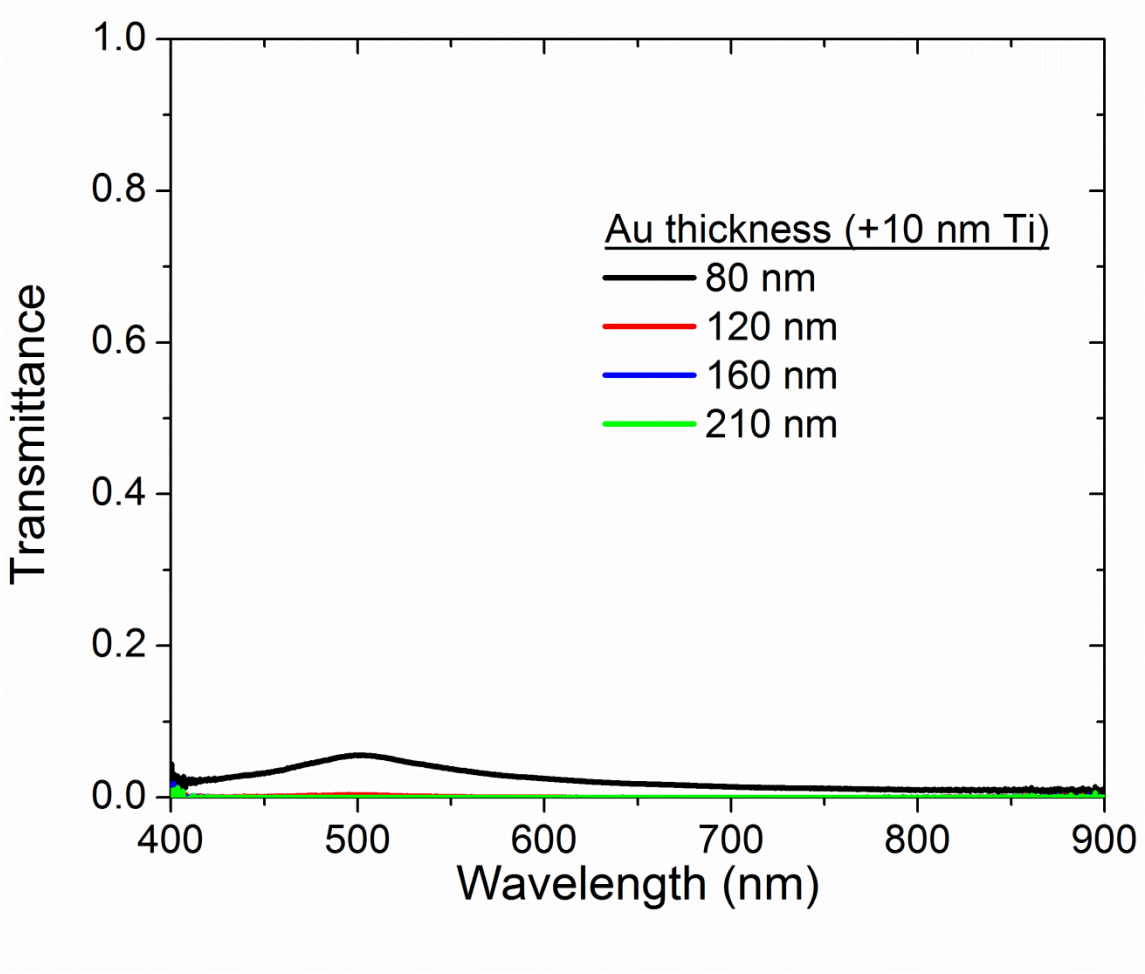

Figure 5.4 Opacity test for Au sample. Various thicknesses of planar Au (+10 nm Ti sticker layer) were deposited on a SU8+glass substrate. Thicknesses were measured with a profilometer.

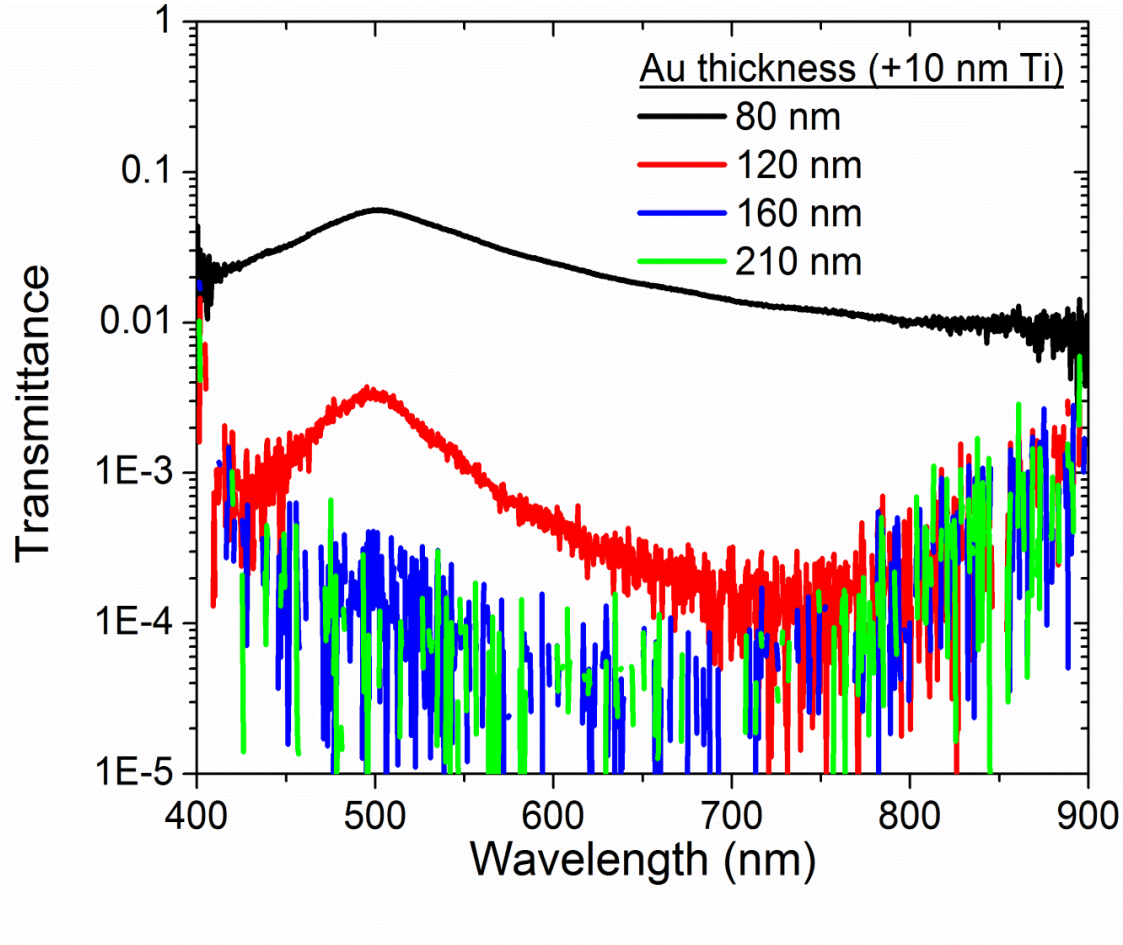

Figure 5.5 Log plot of opacity test for Au sample. To magnify transmittance of Au sample, data from previous plot has been plotted on a log scale.

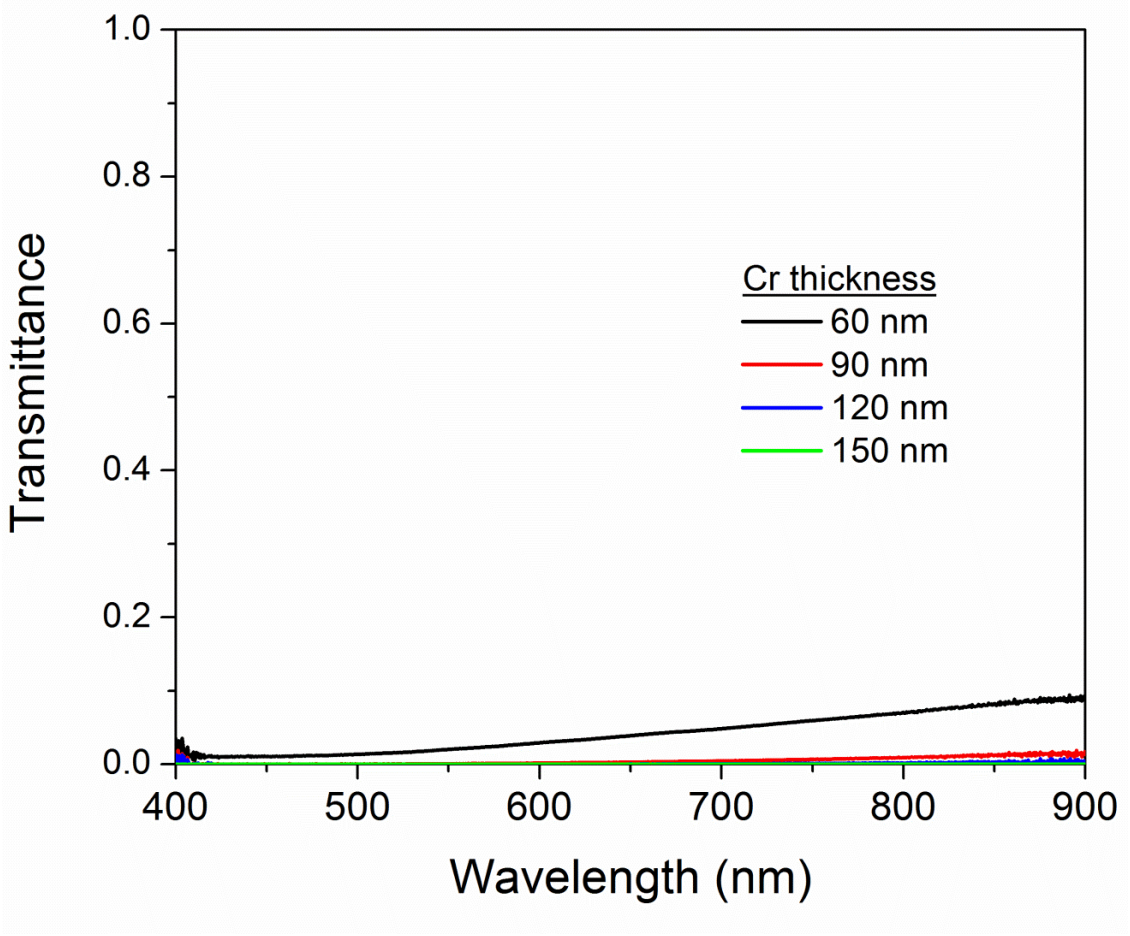

Figure 5.6 Opacity test for Cr sample. Various thicknesses of planar Cr were deposited on a SU8+glass substrate. Thicknesses were measured with a profilometer.

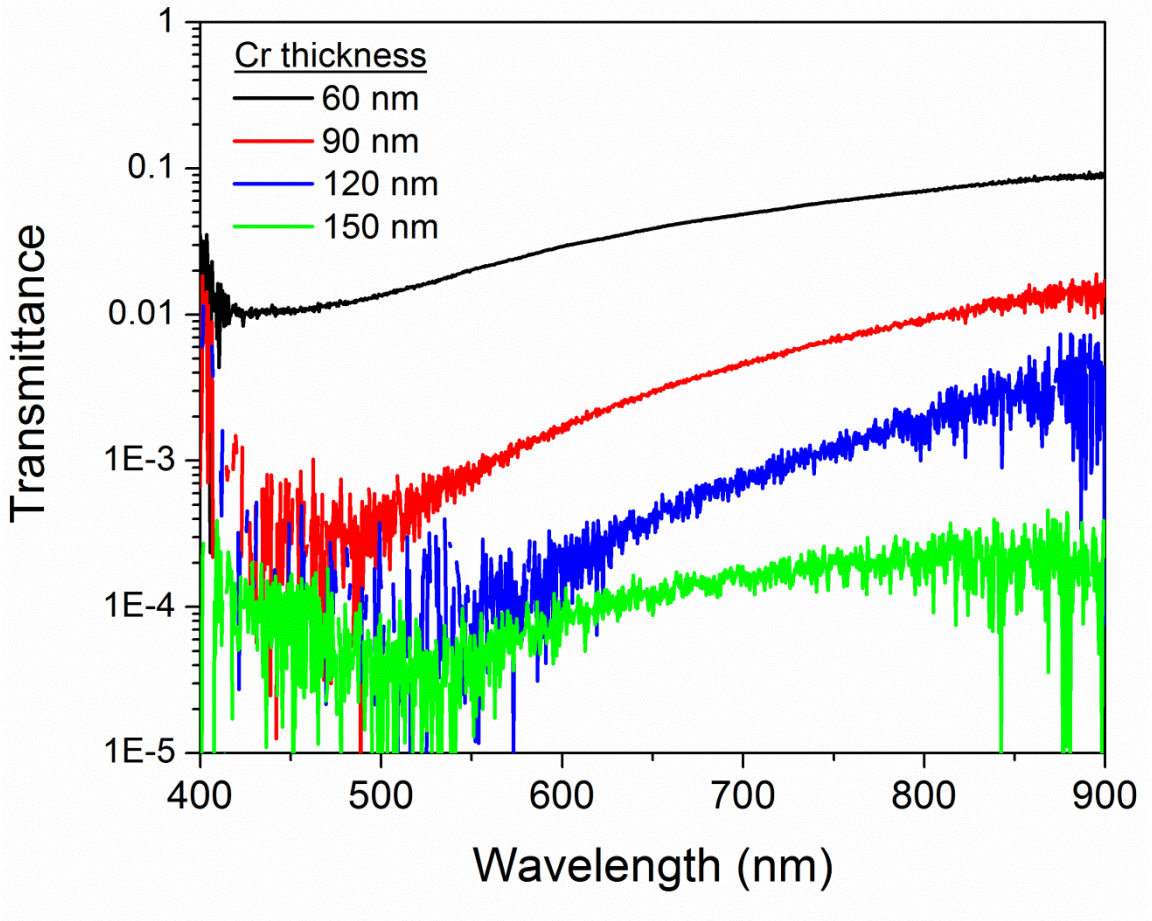

Figure 5.7 Log plot of opacity test for Cr sample. To magnify transmittance of Cr sample, data from previous plot has been plotted on a log scale.

cylinder volume) and cured with a series of baking and exposure steps: 3 min bake at 65 C, 5 min at 95 C, flood expose (24 mW/ cm^2 optical power) for 90 s, 2 min bake at 95 C, 2 min at 120 C, 2 min at 150 C, 2 min at 180 C, 30 min at 210 C, followed by turning off the hot plate and letting the sample cool to room temperature. The intended thickness of the SU8 was to match the cylinder height. Next, the sample was polished in a colloidal solution (MasterPrep suspension, 0.05 μm), diluted with 50 ml of deionized water. The sample was polished for 60 minutes, and then checked every 20 minutes until the cylinders within every region were decapitated. The final structures are thus metal (Au or Cr) cylinders with optically-thick walls, filled with an optically-transmitting dielectric (SU8), and with height controlled by the initial template and final polishing steps. Finished samples and a schematic of the sample are shown in Figure 5.8b, c.

(a)

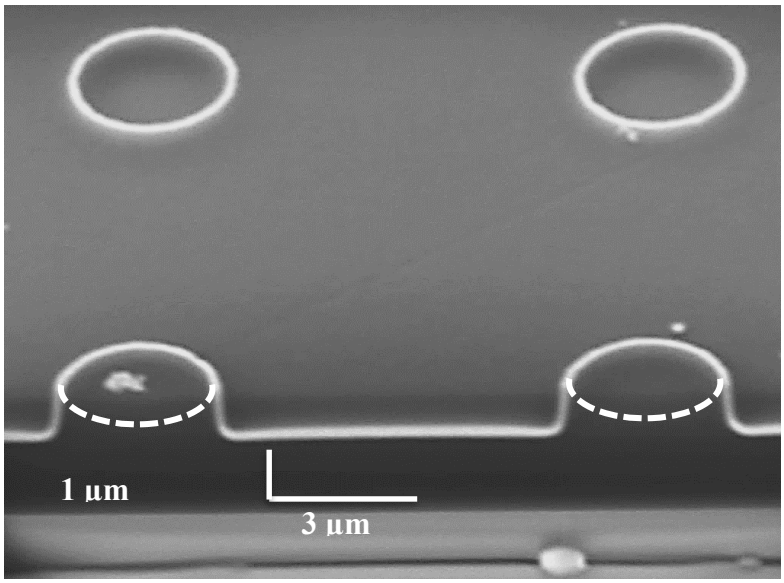

(b) (c)

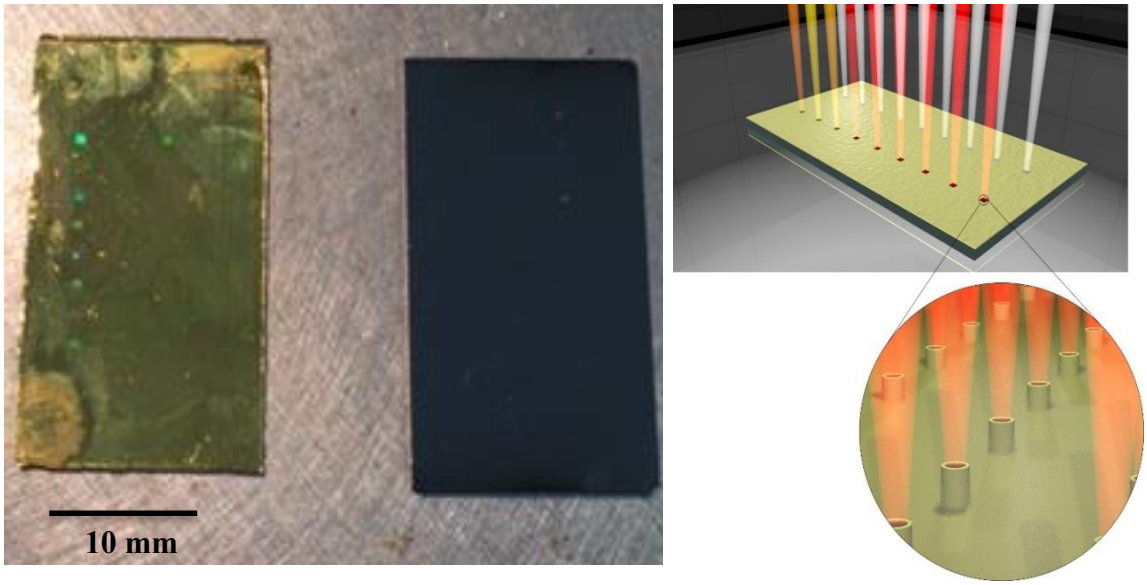

Figure 5.8 Images of Au and Cr samples. (a) FIB cross section images of Au sample, post-measurement. (b) Finished Au (left) and Cr (right) samples. Cylinder arrays can be seen on the left side of the Au sample (greenish-blue squares) and on the right side of the Cr sample (dim reddish square). (c) Schematic of light propagating through regions of cylinder arrays.

5.3 Experimental methods

5.3.a Optical area determination

Prior to any sample being measured, knowledge of the collection area of the spectrometer was required in order to calculate the effective transmittance of a particular region within a sample. This is due to the face that the effective transmittance is determined in part by the number of pillars located within the spectrometer collection region. To this end, we fabricated a sample by depositing (e-beam deposition) 300 nm Al on to a glass substrate (same 0.5 mm thickness used for other samples) and etched an array of 75x75 and 100x100 μm^2 holes spaced 5 mm apart (Figure 5.9a). We assumed that the intensity of the collection area acted like a point source function with a Gaussian shape. Thus, the location of the maximum in intensity (for all wavelengths) should reside in the center of the collection area (Figure 5.9c). If this is the case, then the maximum transmittance for all wavelengths should occur when the opening is scanned though the center of the collection area. If the transmittance vs location plot showed wavelength dependence, then that would mean that the collection area had wavelength dependence and that we scanned off center. The general procedure for determining the spectrometer collection area started by centering an opaque sample with a 100 μm sided square aperture onto the computer screen in the Leica program. The stage location of the sample was recorded using the Leica software. Once this was done, the stage (and thus the aperture) was incrementally moved only in the + x direction and spectral data were taken every 10 μm. Upon the spectral data falling to zero and showing little to no change in counts (as compared to the dark spectrum), the sample was brought back to its original location and scanned in the

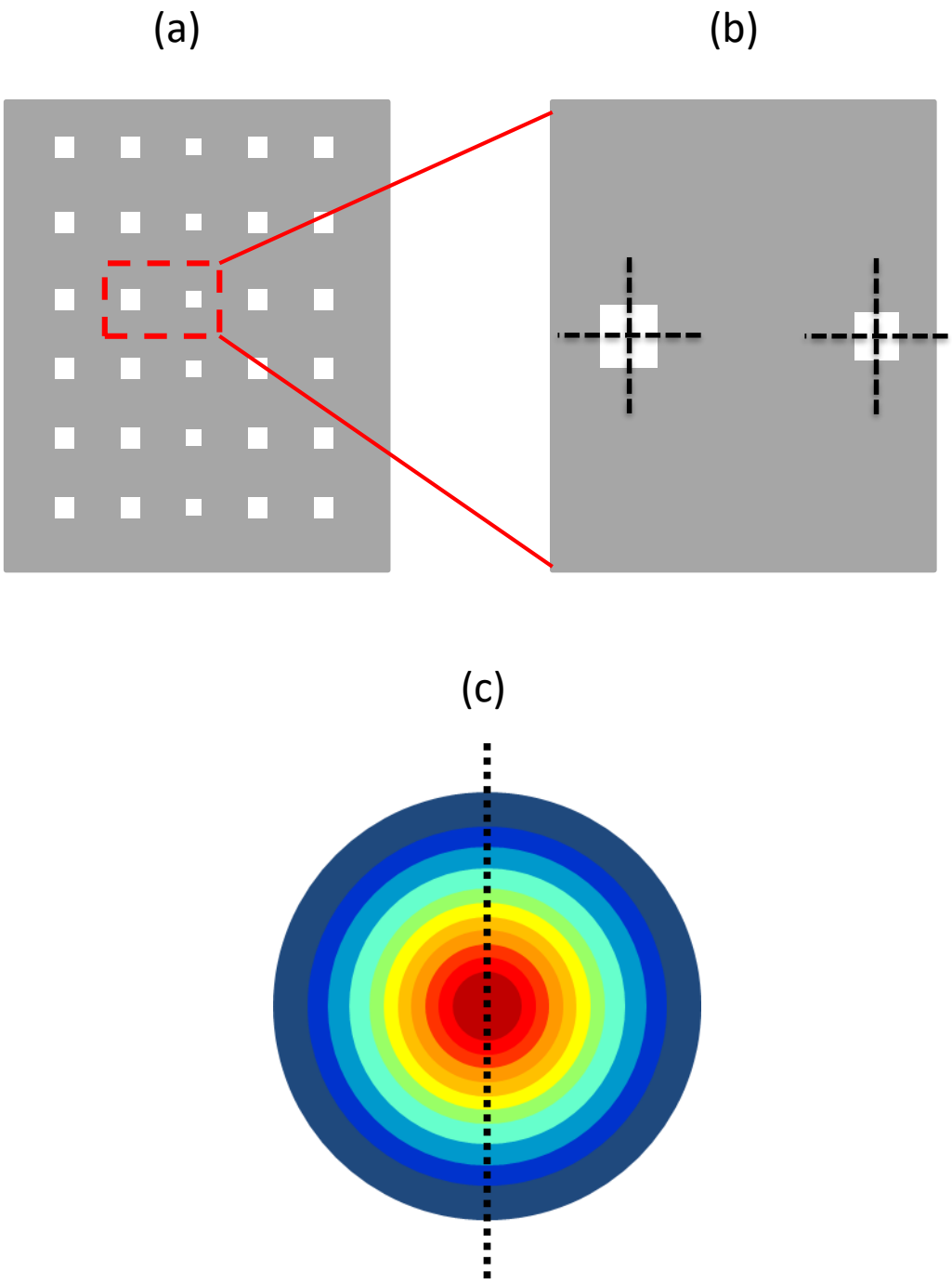

Figure 5.9 Schematic of measurement sample. (a) The sample used to measure the spectrometer collection area consisted of an array of 100x100 and 75x75 μm^2 openings spaced 5 mm apart. (b) Magnified view of openings. Black dashed lines represent the scanning path lines made during measurement. (c) Assumed contour profile of intensity of collection area (dark red center indicating high intensity and dark blue indicating low intensity). Black dashed line indicates intended scan path.

– x direction. The sample was then brought back to x = 0 and scanned in both the ± y directions. Transmittance (T) plots were made using the following equation:

$$T_{region} = \frac{I_S}{I_r} = \left(\frac{N_S - N_d}{N_r - N_d}\right)\left(\frac{A_r}{d^2}\right) \quad (8)$$

Here, N_s and N_r are the number of counts of the sample and reference, N_d is the dark spectrum, A_r is the assumed area of the collection area (taken from the Leica screen), and d is the size of the side of the opening (i.e. 75 μm or 100 μm). Transmittance versus x and y position plots were made to verify that the maximum transmittance was found approximately at the origin for all wavelengths, as this would indicate the aperture had been scanned through the center of the collection region. It is important to note that the collection region of the spectrometer was assumed to be a circle even though we used the Leica screen as a reference area. This does not affect the overall purpose of the experiment (only the magnitude of the transmittance). From the plots in Figure 5.10 and 5.11, we calculated the diameter of the collection region to be 180 ± 10 μm and was therefore smaller than each cylinder array region. The transmittance data was averaged and fitted with a Gaussian curve (Figure 5.12) and a 3D contour plot was also made to visualize the point spread function of the collection area (Figure 5.13). This process was later repeated with the 75 μm square aperture and yielded similar results (Figures 5.14 and 5.15). It is interesting to note that the FWHM value for both experiments match the corresponding aperture size (the FWHM is roughly 100 μm for the 100 μm^2 square aperture and 75 μm for the 75 μm^2 square aperture). Furthermore, by averaging the transmittance for all wavelengths and then applying a Gaussian fit we see that the peak has been flattened. This is most likely do to the aperture size, as our parsing window was

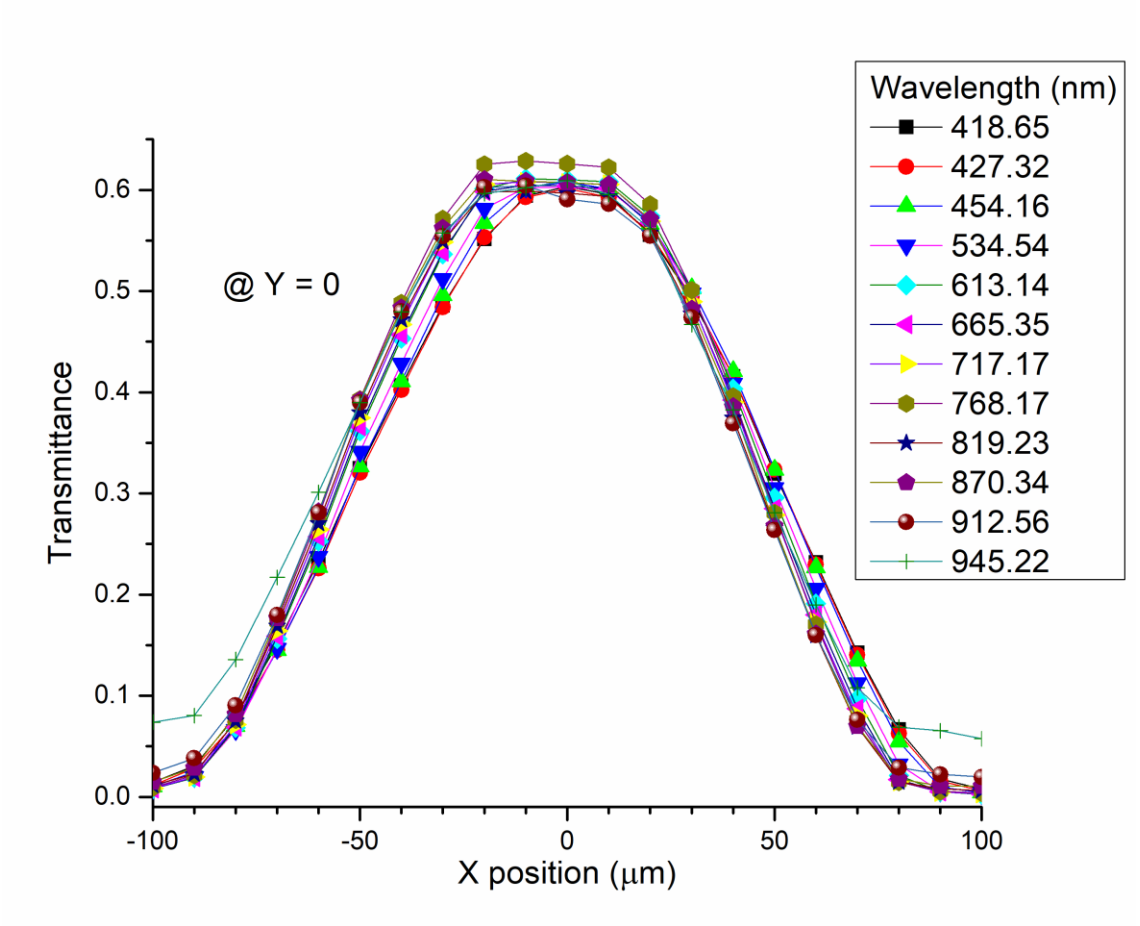

Figure 5.10 Scanning 100 µm square opening in *x*–direction. To measure the spectrometer collection area, a 100 µm square opening was scanned in the *x*–direction and the transmittance was calculated for various wavelengths.

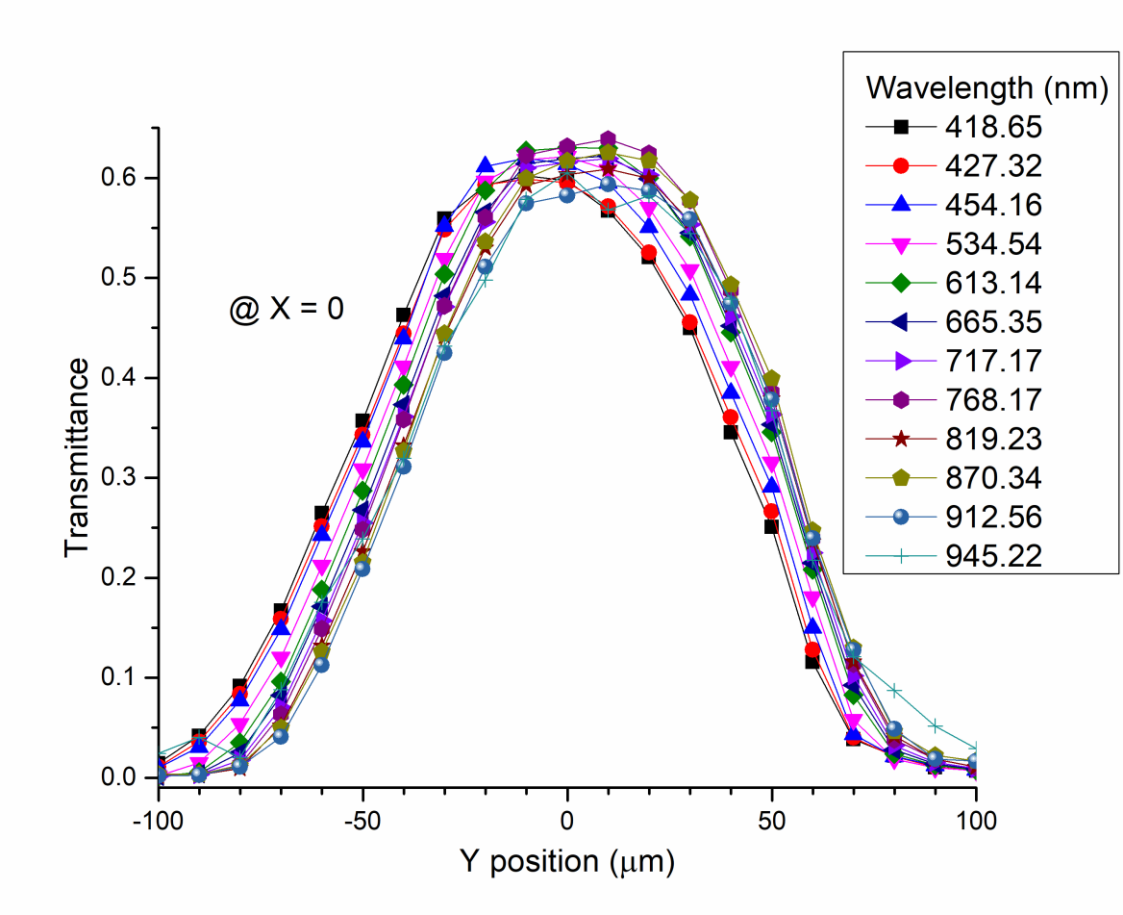

Figure 5.11 Scanning 100 µm square opening in *y*–direction. To measure the spectrometer collection area, a 100 µm square opening was scanned in the *y*–direction and the transmittance was calculated for various wavelengths.

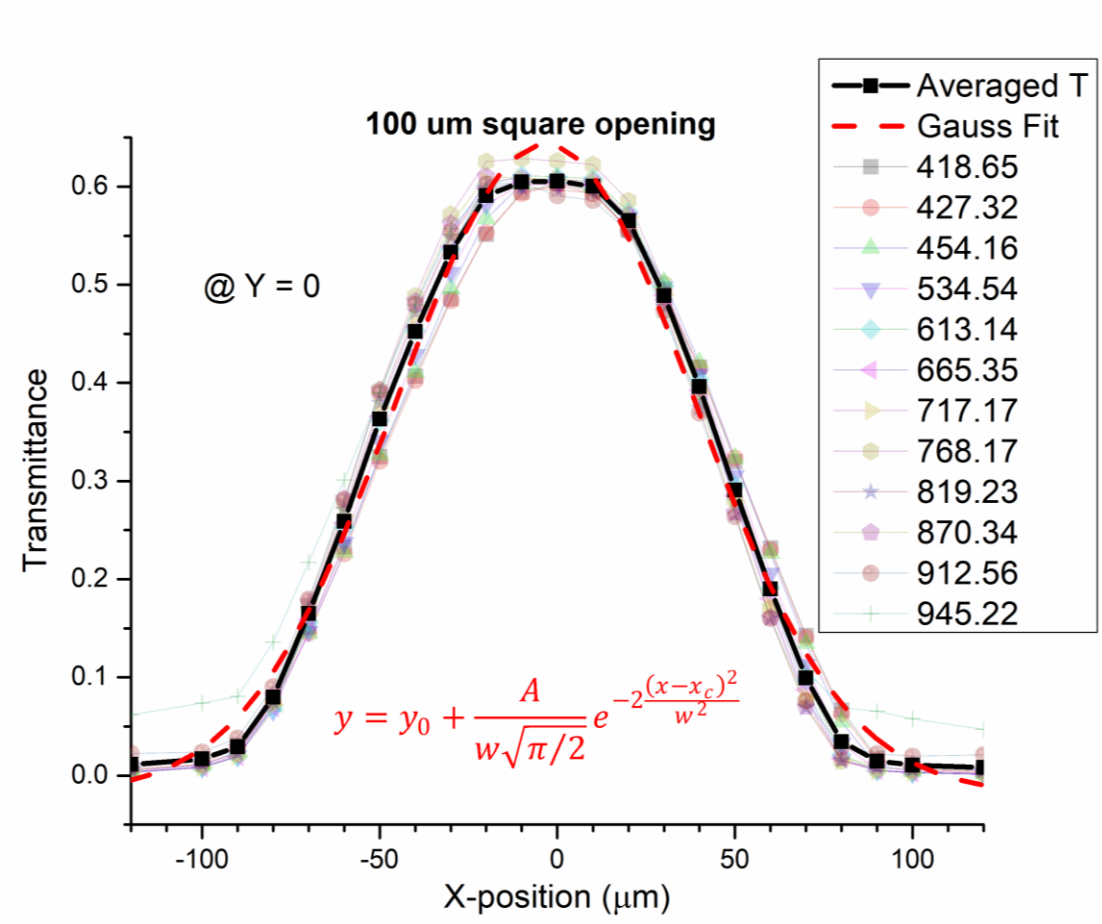

Figure 5.12 Gaussian fit of Averaged *T* for 100 μm opening.

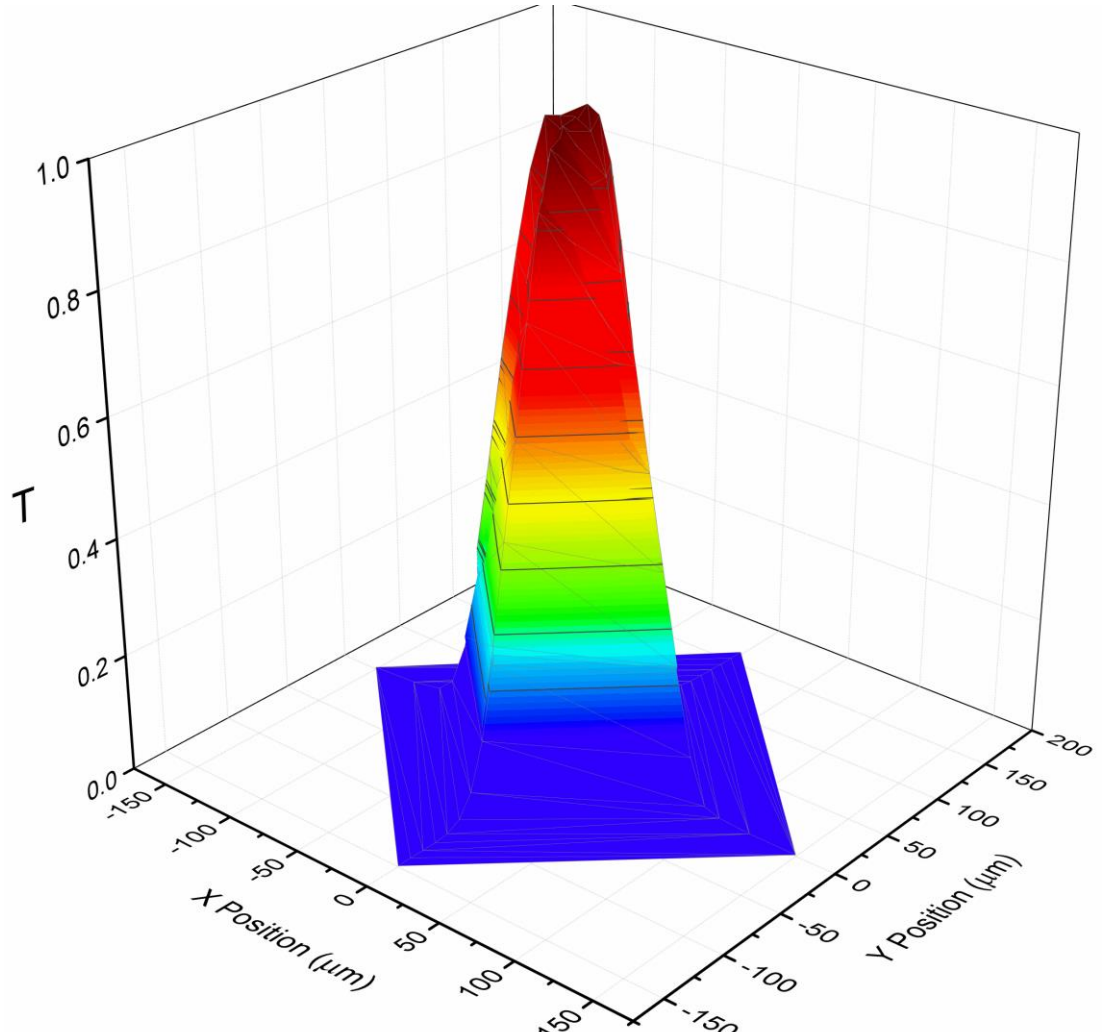

Figure 5.13 3D plot of *x* and *y* scans. To measure the spectrometer collection area, a 100 μm square opening was scanned in both the *x* and *y* directions and the transmittance was calculated for various wavelengths.

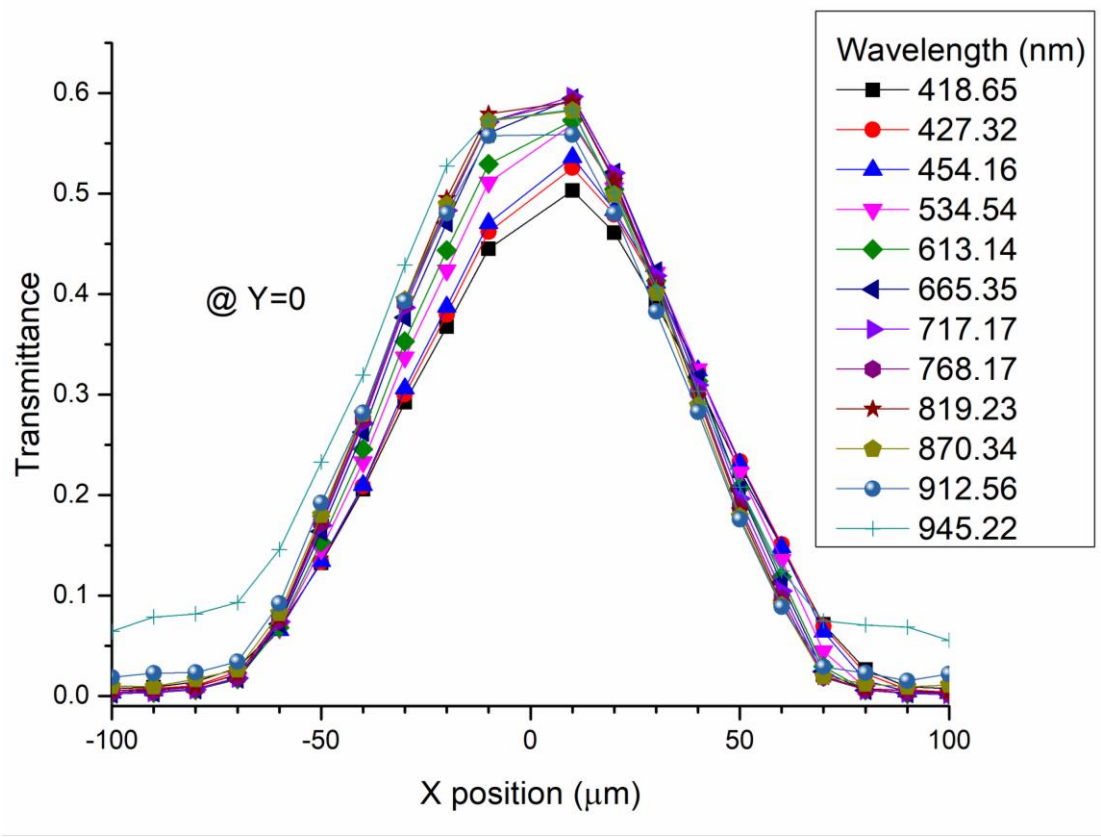

Figure 5.14 Scanning 75 μm square opening in *x*–direction. To measure the spectrometer collection area, a 75 μm square opening was scanned in the *x*–direction and the transmittance was calculated for various wavelengths.

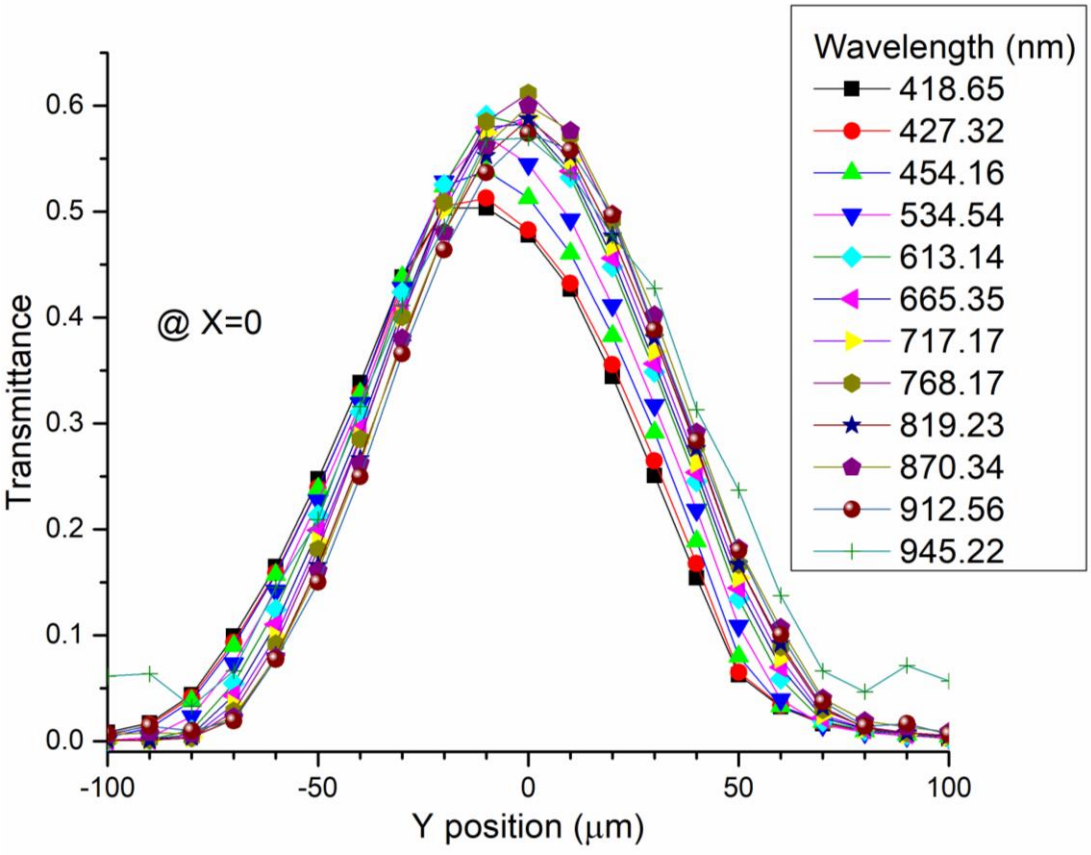

Figure 5.15 Scanning 75 μm opening in *y*–direction. To measure the spectrometer collection area, a 75 μm square opening was scanned in the *y*–direction and the transmittance was calculated for various wavelengths.

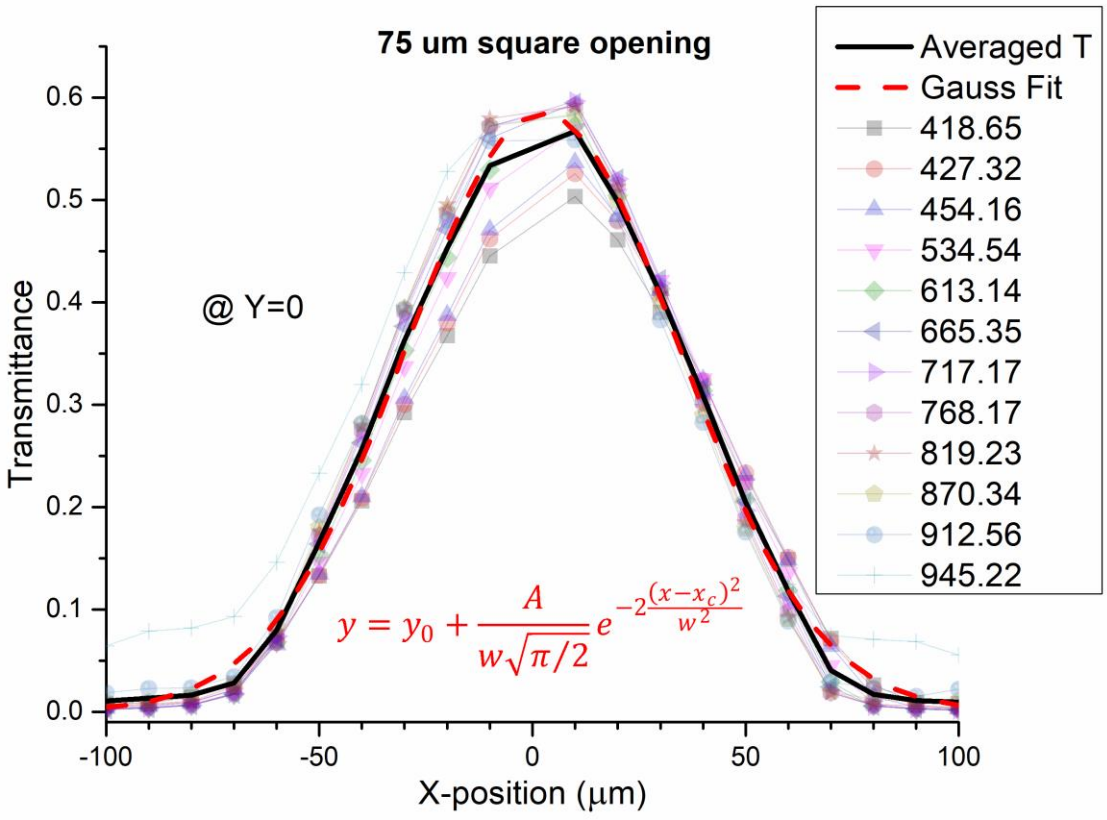

Figure 5.16 Gaussian fit of Averaged *T* for 75 μm opening.

too large compared with the spectrometer collection area (the ratio of aperture to collection area is roughly 0.5). Another noteworthy occurrence in the data shown in Figures 5.14 and 5.15, is the wavelength-dependent transmittance. As mentioned before, this indicates the sample was not scanned through the center of the collection region. From the Figures, it appears the sample was off-center by roughly 5 μm in the *y*-direction and 10 μm in the *x*-direction. Had the samples been moved and re-scanned the transmittance data from all wavelengths would tightly overlap as seen in Figure 5.10.

Since the spectral data showing the intensity profile of the collection region is not binary-like and instead shows a Gaussian-like shape, this distribution needs to be taken into account when considering the contribution of each aperture within the collection region. For instance, an aperture at the center of the collection region will have a higher transmittance than one near the edge of the collection area. Assuming the center of the collection region to be fully contributing and the fact that the sample contains a 500 x 500 μm^2 square lattice of pillars, the total number of pillars within the collection region was calculated as follows: given a pillar's distance from the center of the collection region, the average transmittance value (from the *T* data above normalized to 1) corresponded to the fraction of the pillar contribution. For example, a pillar located at the center of the collection region was counted as an entire pillar since, according to the transmittance data in Figures 5.10-5.16, it's transmittance sensitivity value is at a maximum. A pillar located at a distance where the transmittance value was 50% would only be counted as half a pillar. Figure 5.17 shows part of the calculation process. Once the total effective number of pillars in the collection area was known, the effective transmittance of the sample region could be calculated.

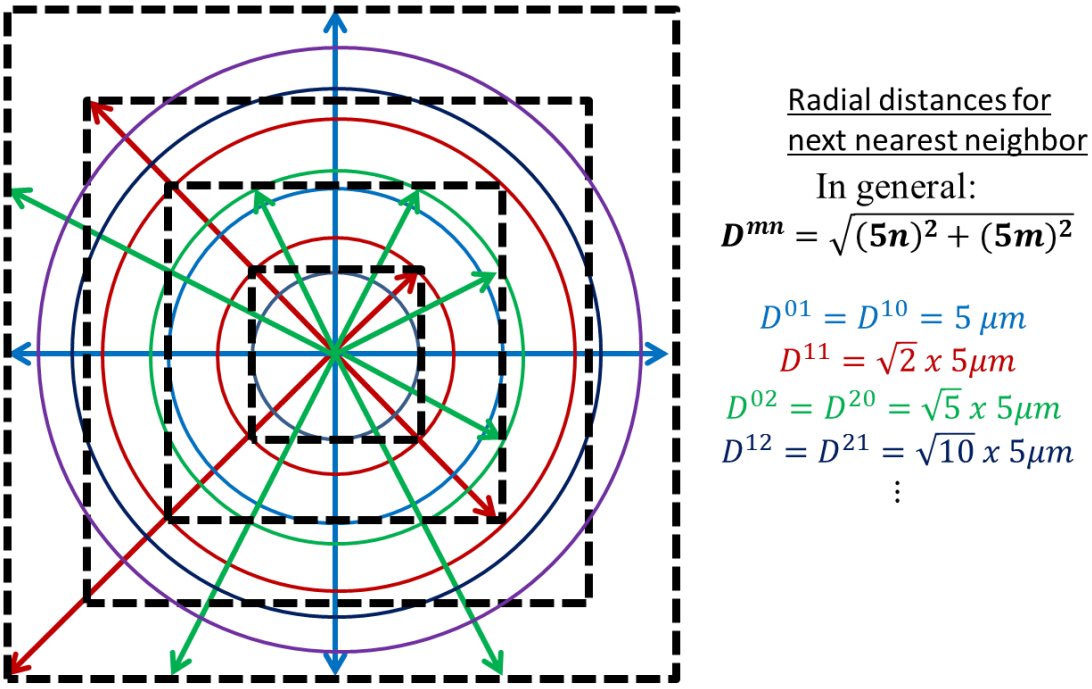

Figure 5.17 Effective *n* calculation. The distances of cylinders in a square lattice from the center of illumination were calculated. This distance was then correlated with previous spectrometer area transmission measurements to calculate the fractional contribution to the transmittance in the Au and Cr samples.

Another consideration in calculating the effective number of pillars, is the wavelength dependence of collection region. In an ideal scenario the collection region would not exhibit any wavelength dependence as the focal point for all wavelengths would be the same. However, during one of the scans meant to determine the collection area, we realized we were off the central axis by 65 μm. In analyzing these data, we found a discrepancy in the calculated transmittance of various wavelengths (Figures 5.18 and 5.19). This confirmed a wavelength dependence in the collection region, most likely due to chromatic aberration (Figure 5.20). While most of the lenses used in the Leica microscope have chromatic aberration correction coatings, we did not account for the lens in the c-mount adapter. We were unable to independently confirm (through literature from the manufacturer) whether this lens had a correction coating, but according to the data in Figs 5.18 and 5.19, it did not.

Unfortunately, we did not take the wavelength dependence of the collection region into account when we first analyzed the Au and Cr transmittance data shown throughout this Chapter. From the data in Figs 5.18 and 5.19, we see a monotonic decrease in transmittance with respect to wavelength. Therefore, the transmittance values at shorter wavelengths represents an underestimate due to having a smaller effective n than what was used in the calculation. For example, the pillars located 65 μm from the center of the collection region were given an effective value of 15% rather than 8%. While we don't unequivocally know the shape of the wavelength dependence profile of the collection region (unlike the intensity profile) we can use the center and off–center data to estimate its dependence versus distance. With this in mind, we estimate that the effective number of pillars drops from 237 to 212, which represents an error of 11%.

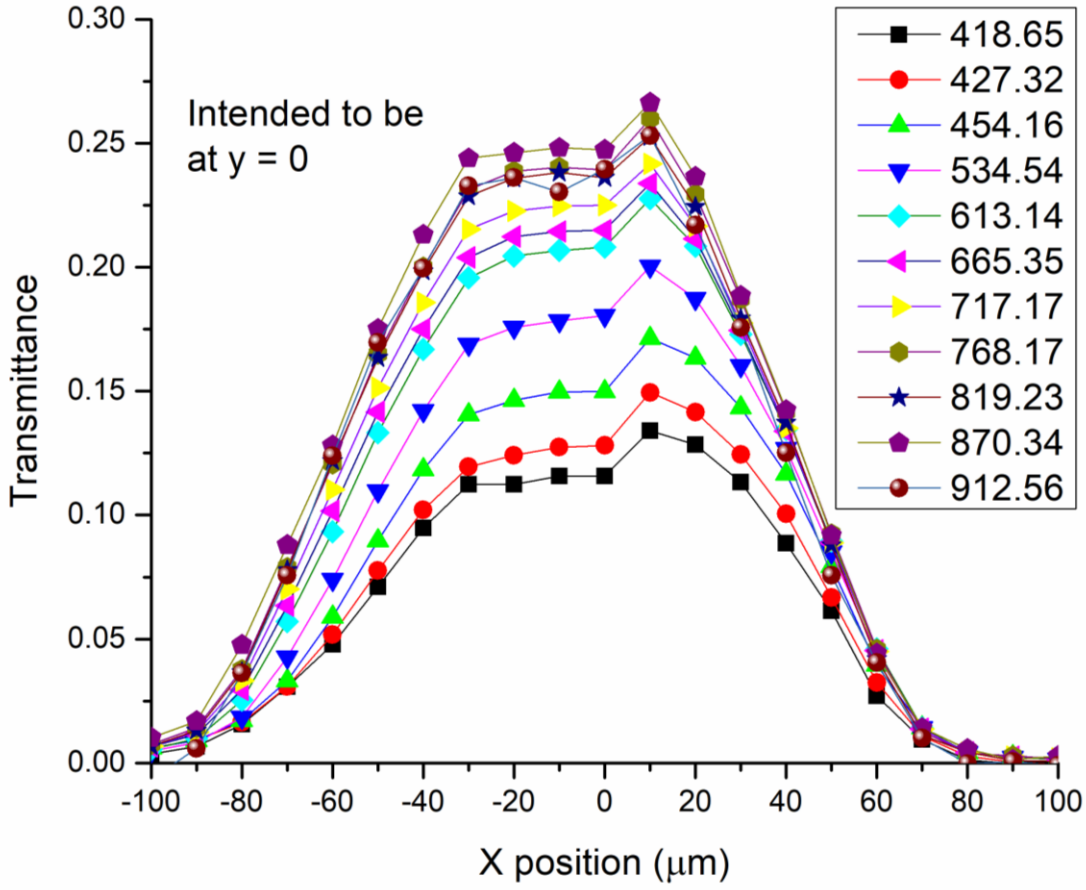

Figure 5.18 Transmittance vs. position for off–center scan in 100 μm opening.

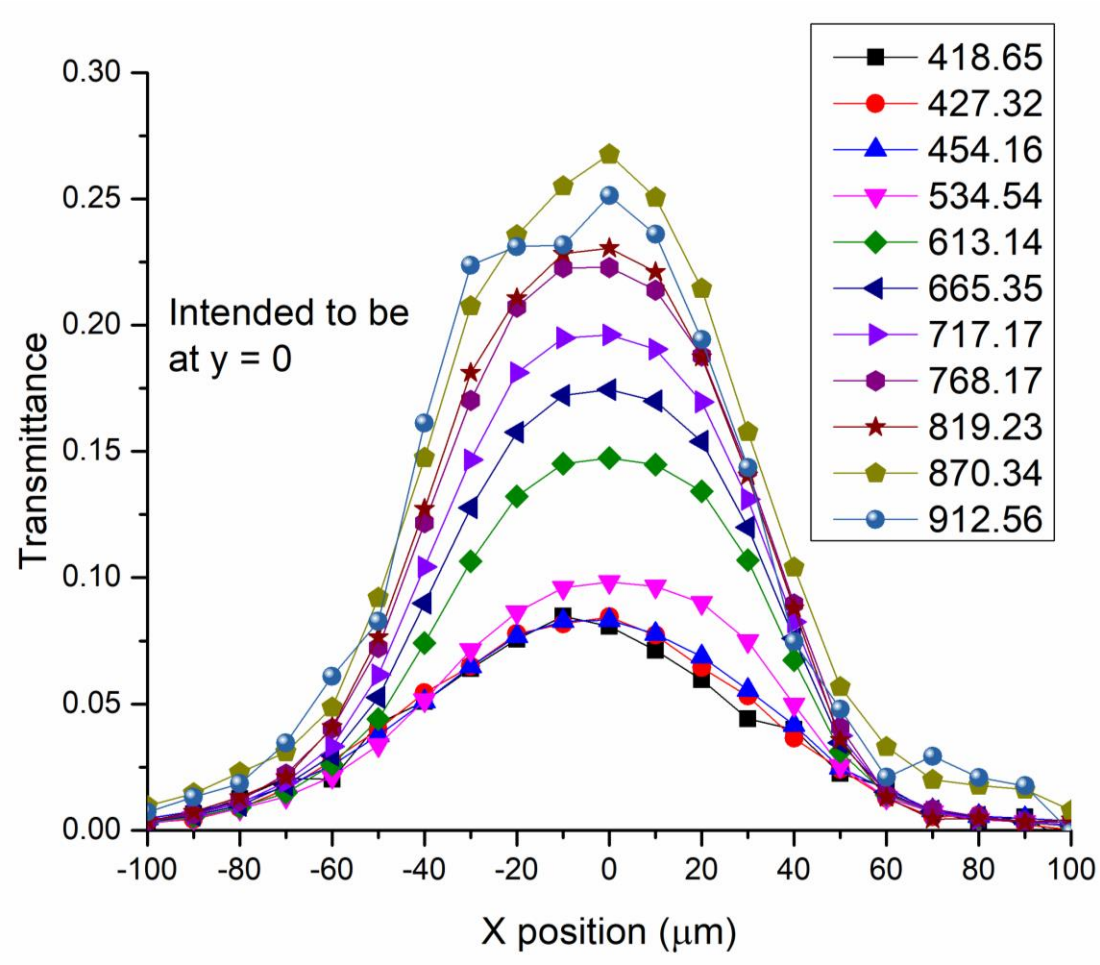

Figure 5.19 Transmittance vs. position for off–center scan in 75 μm opening.

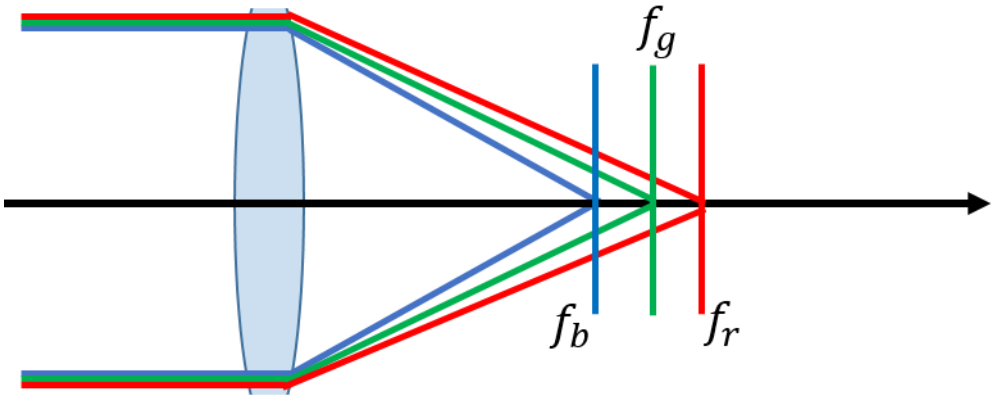

Figure 5.20 Schematic of chromatic aberration. When light rays enter a dispersive media the resulting location of the focal points (focal length) on the optical axis (black arrow) will be wavelength dependent. Shorter wavelengths (blue) will have a shorter focal length, while longer wavelengths (red) will have a longer focal length.

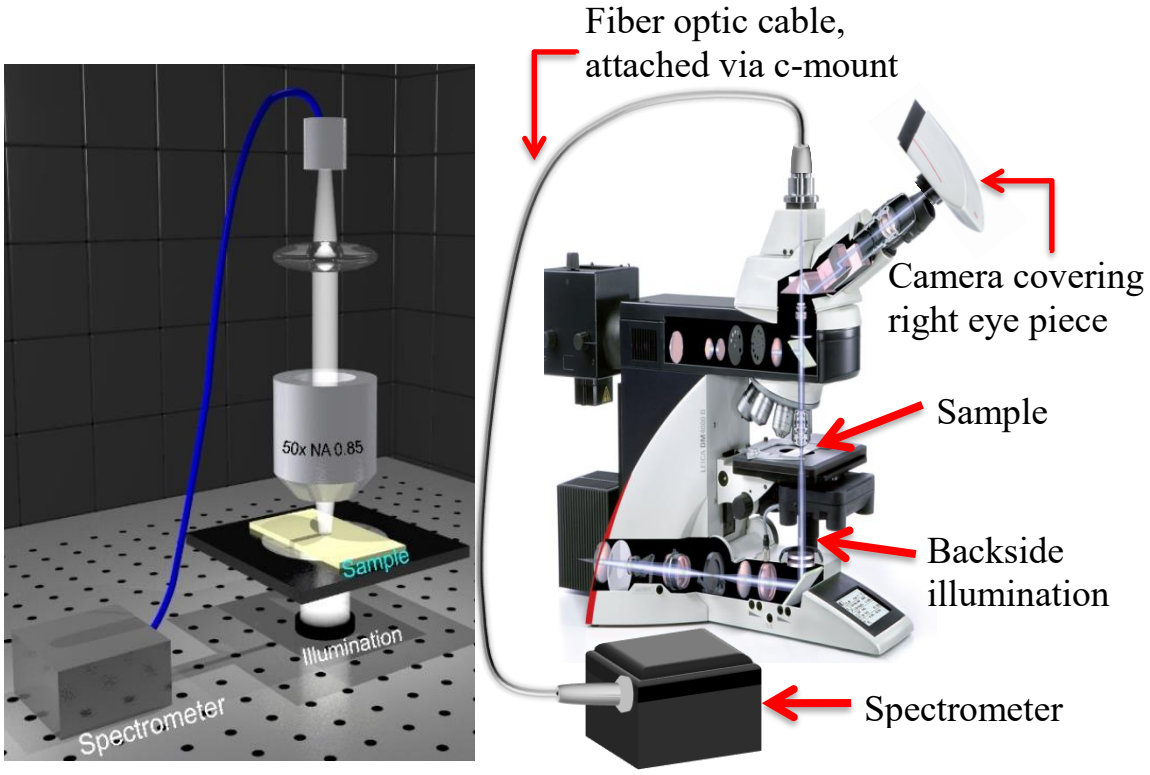

Figure 5.21 Schematic of experimental procedure. Left side shows cartoon of the basic set up of the experiment. Right side shows schematic with image of the actual microscope used during the experiment.

5.3.b General layout and procedure

Once the spectrometer collection area was calculated, we proceeded with measuring the transmittance of the Au and Cr samples. A schematic for the experimental procedure is shown in of Figure 5.21. A Leica DM6000 optical microscope was used to focus unpolarized light onto the backside of the sample while the top side of the sample was viewed with a 50× objective (NA = 0.8). This orientation will be referred to as the normal orientation throughout (Figure 5.16). The light source was a 100 W halogen lamp and the sample was illuminated at full intensity. An optical fiber (Ocean Optics QP600-20UV-VIS) was mounted onto the microscope and attached to a photospectrometer (Ocean Optics Maya2000 Pro) with a specified spectral response range of 200–1100 nm. To avoid or suppress Fabry-Perot related artifacts in the data, strips of electrical black tape were attached to the microscope stage and samples were placed on the strips rather than directly on the glass stage as shown in the schematic in Figure 5.22. Initially a glass + SU8 planar sample was used as a reference and recorded with an integration time of 8 ms. Spectral data were taken at 3 different locations in each of the 18 regions so that an average transmittance (per region) could be calculated. Each of the 3 locations within each region where data were taken was structurally consistent. When data were taken on the sample, the integration time was changed to 100 ms to allow a significant number of photons to be collected. In the Au sample, dark references for both integration times were taken by blocking the light source as well as by moving to a cylinder-free area of the sample. Upon inspection, both dark spectra (blocked and opaque) were consistent with one another and the data from the opaque dark spectrum were used for the transmittance calculation. The Cr sample, however, showed signs of cracking, possibly due to stress in

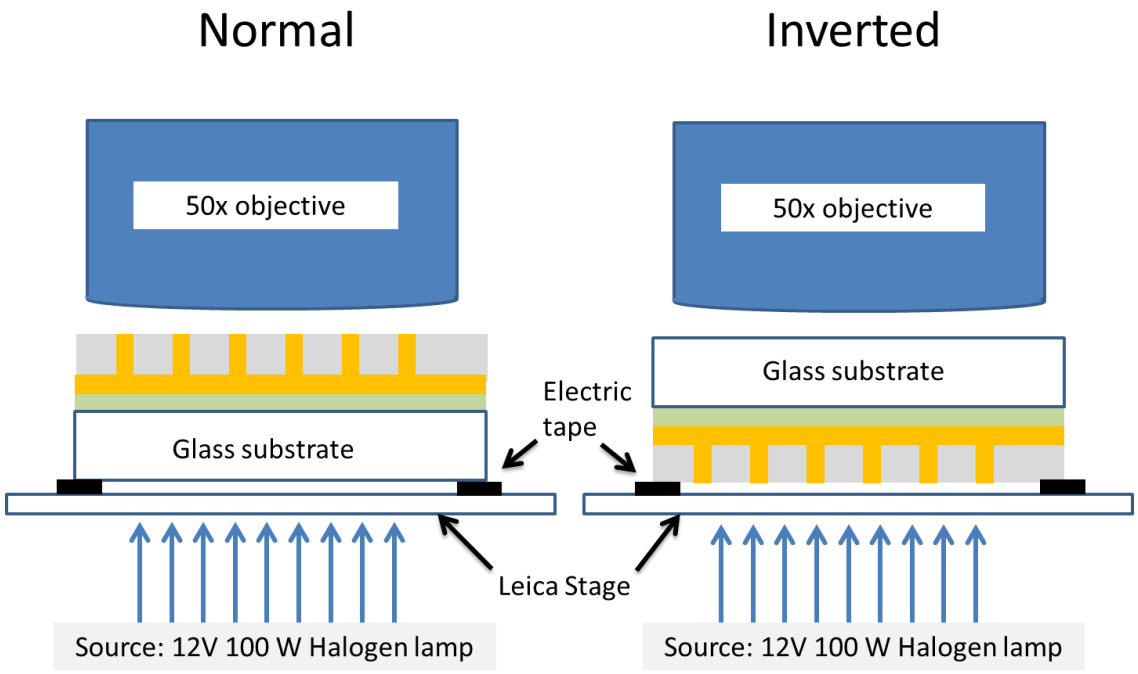

Figure 5.22 Orientation schematic. Left side shows "normal" orientation of sample on Leica stage. Right side shows "inverted" orientation of sample on Leica stage. Black electrical tape used to suppress Fabry–Perot effects.

the film or by SU8 swelling during the mechanical stabilization layer step. To mitigate this problem, dark spectrum measurements were taken at various cylinder-free locations throughout the sample. These data were then averaged and used as the dark spectrum for the Cr sample. Later, the samples were inverted (light now incident on the tops of the cylinders) and remeasured. For these measurements, all microscope parameters were the same as for the normal orientation. During both measurement types, adjusting the fine focus did not noticeably change the spectrum until the sample was obviously out of focus.

5.4 Far-field measurement of transmittance: Backside incidence (normal orientation)

Once raw spectral data were collected and averaged, the effective transmittance of each region was calculated in the following way:

$$T_{region} = \frac{I_s}{I_r} = \left(\frac{N_s - N_d}{N_r - N_d}\right)\left(\frac{A_r}{n\pi r_p^2}\right) \quad (9)$$

where n = the effective number of cylinders in the spectrometer collection area, r_p is the average inner radius of the cylinders in that particular region, and A_r is the spectrometer collection area. Transmittance vs. wavelength for both the Au and Cr are shown in Figures 5.23–5.27. The raw data is for Au and Cr is shown in Figures 5.23 and 5.25, respectively. Figures 5.24 and 5.26 show data that has been filtered by adjacent averaging (we chose to use a filtering value of 25 pts, since it had a noticeable effect, but didn't distort the original waveform) for the Au and Cr samples respectively. For a comparison purposes the filtered data from the Cr and Au samples have been stacked and shown in Figure 5.27. The general behavior anticipated by aperture theory / ray optics is observed for both materials: high transmittance for cylinder diameters (apertures) much larger than the wavelength. However, in the Au sample, there are clear deviations from this trend. First, one will note that the absolute transmittance is greater than 1 (100%) for large diameter cylinders. Second, the greater than unity transmittance is only for wavelengths above ~500 nm. Third, after systematically decreasing at all wavelengths as r is reduced (ray optics), T anomalously increases in small diameter cylinders at wavelengths above ~600 nm.

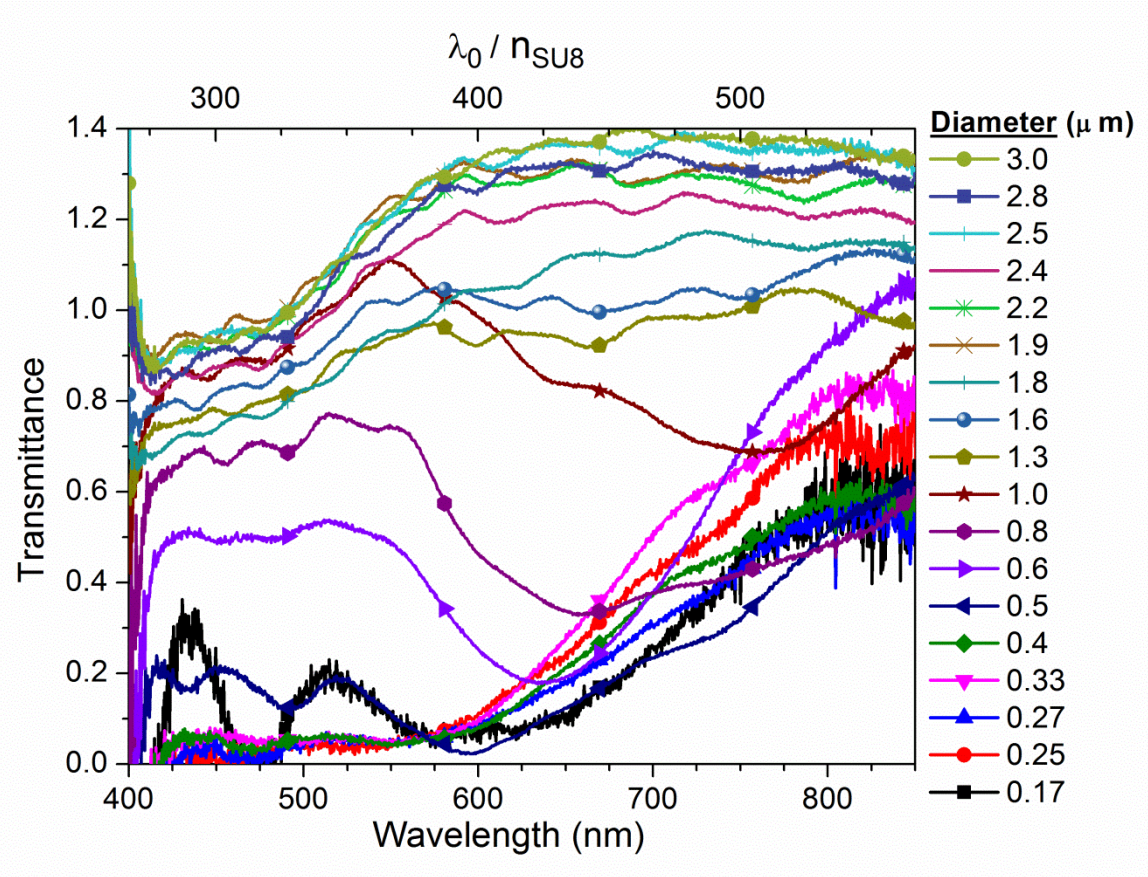

Figure 5.23 Raw transmittance data for 1 μm tall pillar array in Au sample.

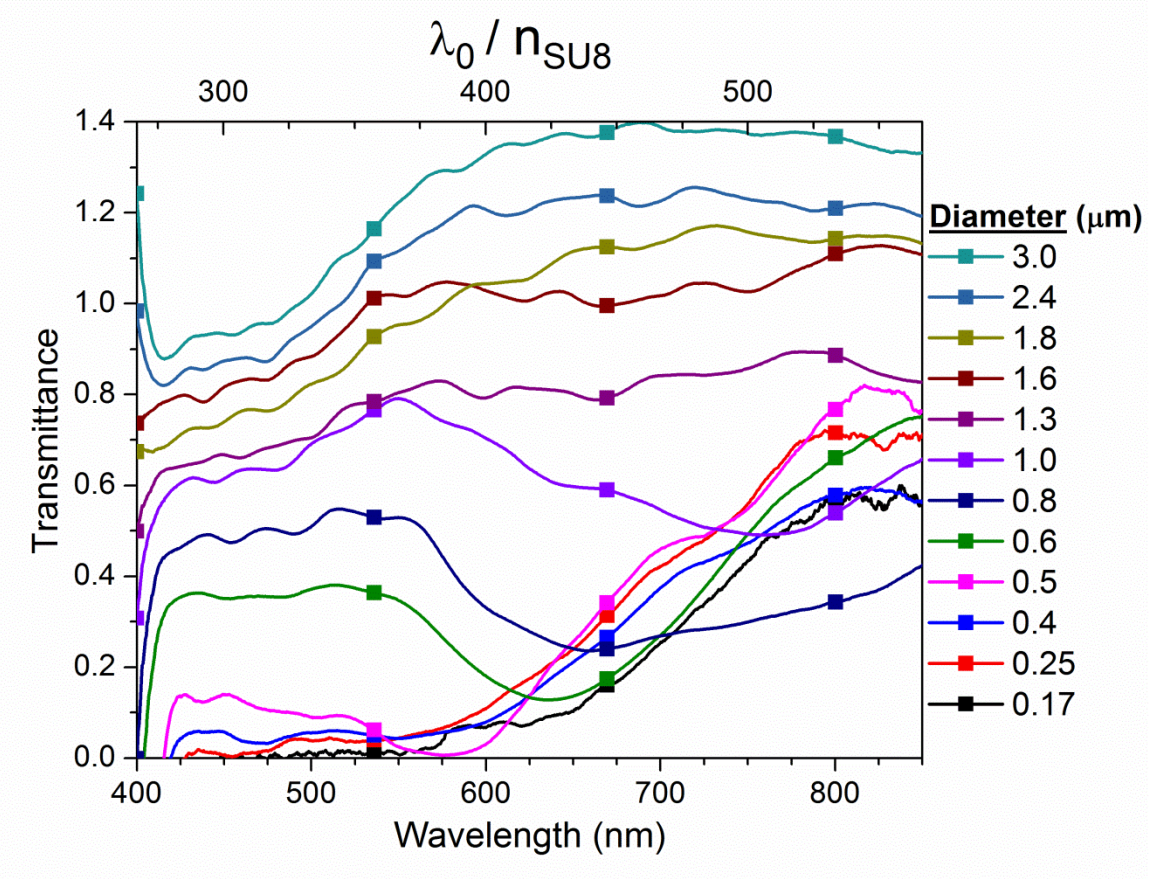

Figure 5.24 Smoothed transmittance data for 1 μm tall pillar array in Au sample.
Data has been smoothed with 25 pts adjacent averaging

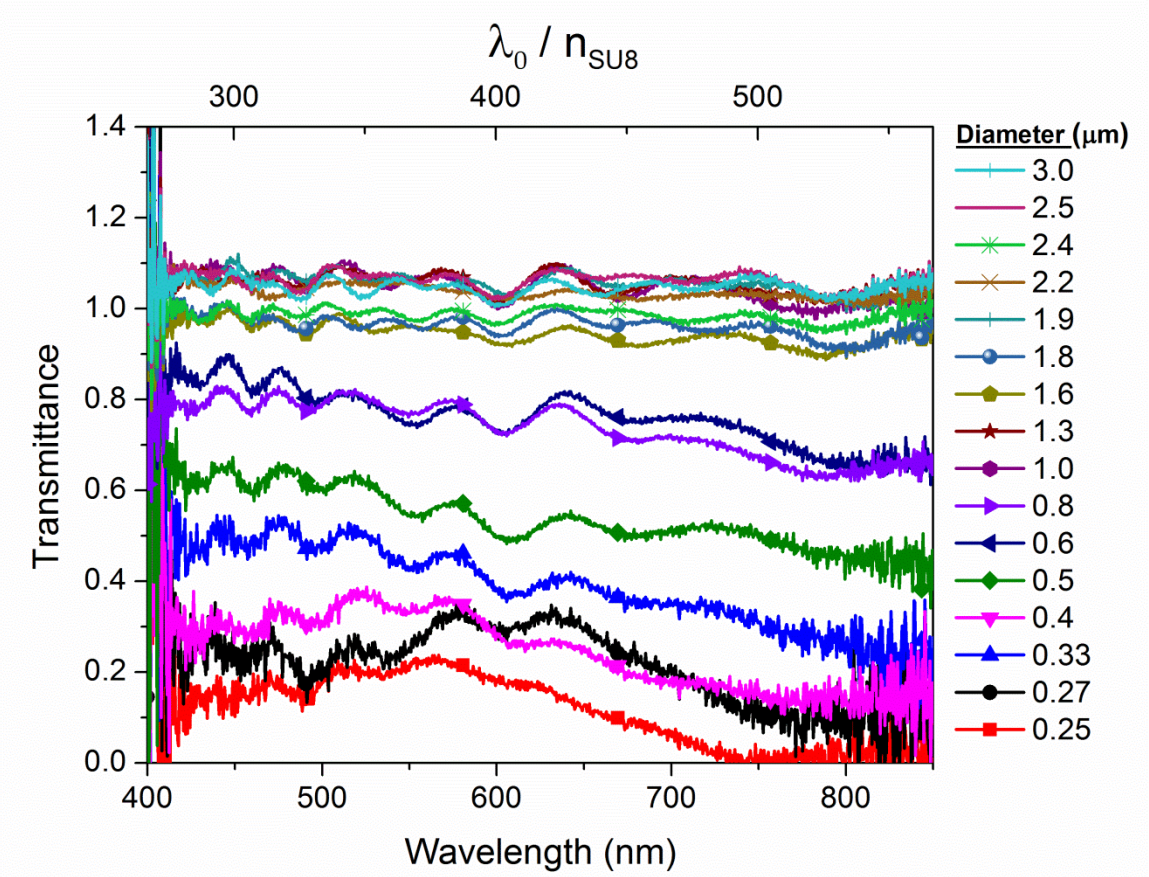

Figure 5.25 Raw transmittance data for 1 μm tall pillar array in Cr sample.

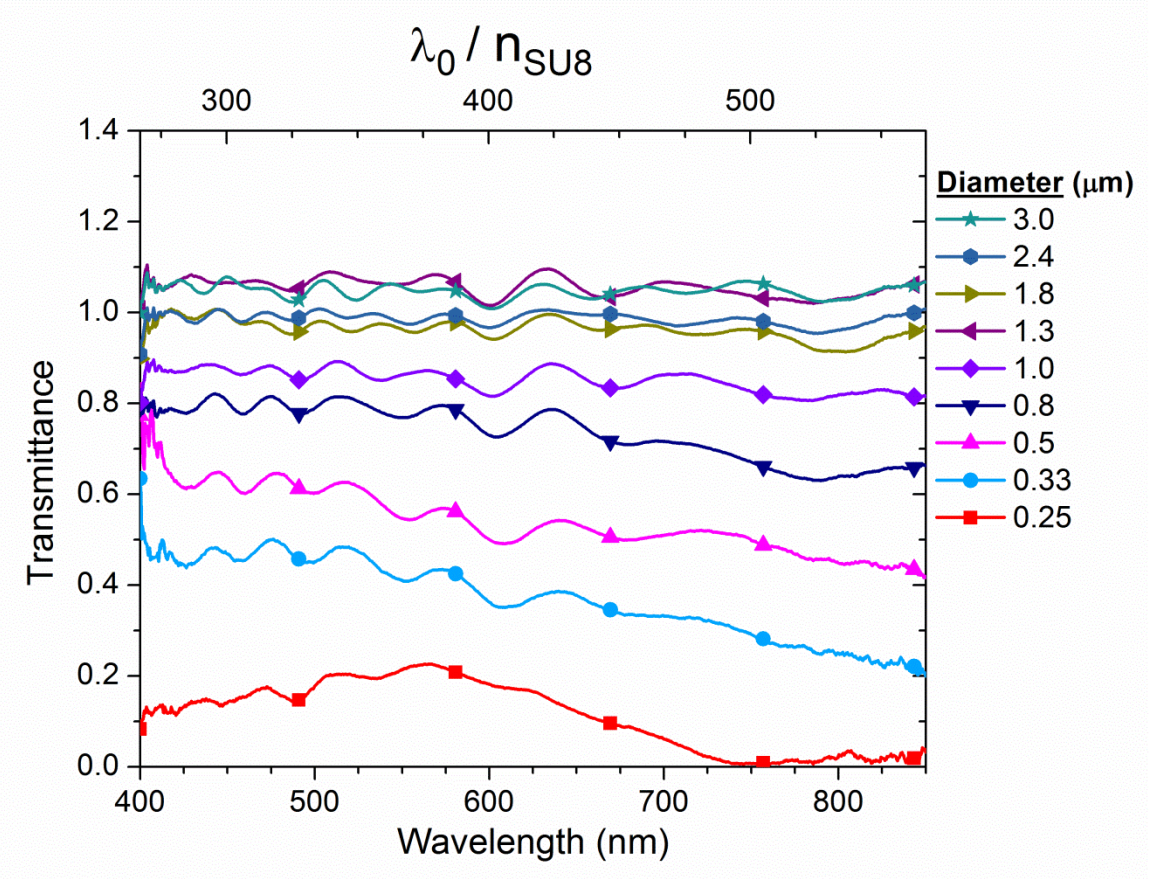

Figure 5.26 Smoothed transmittance data for 1 μm tall pillar array in Cr sample. Data has been smoothed with 25 pts adjacent averaging

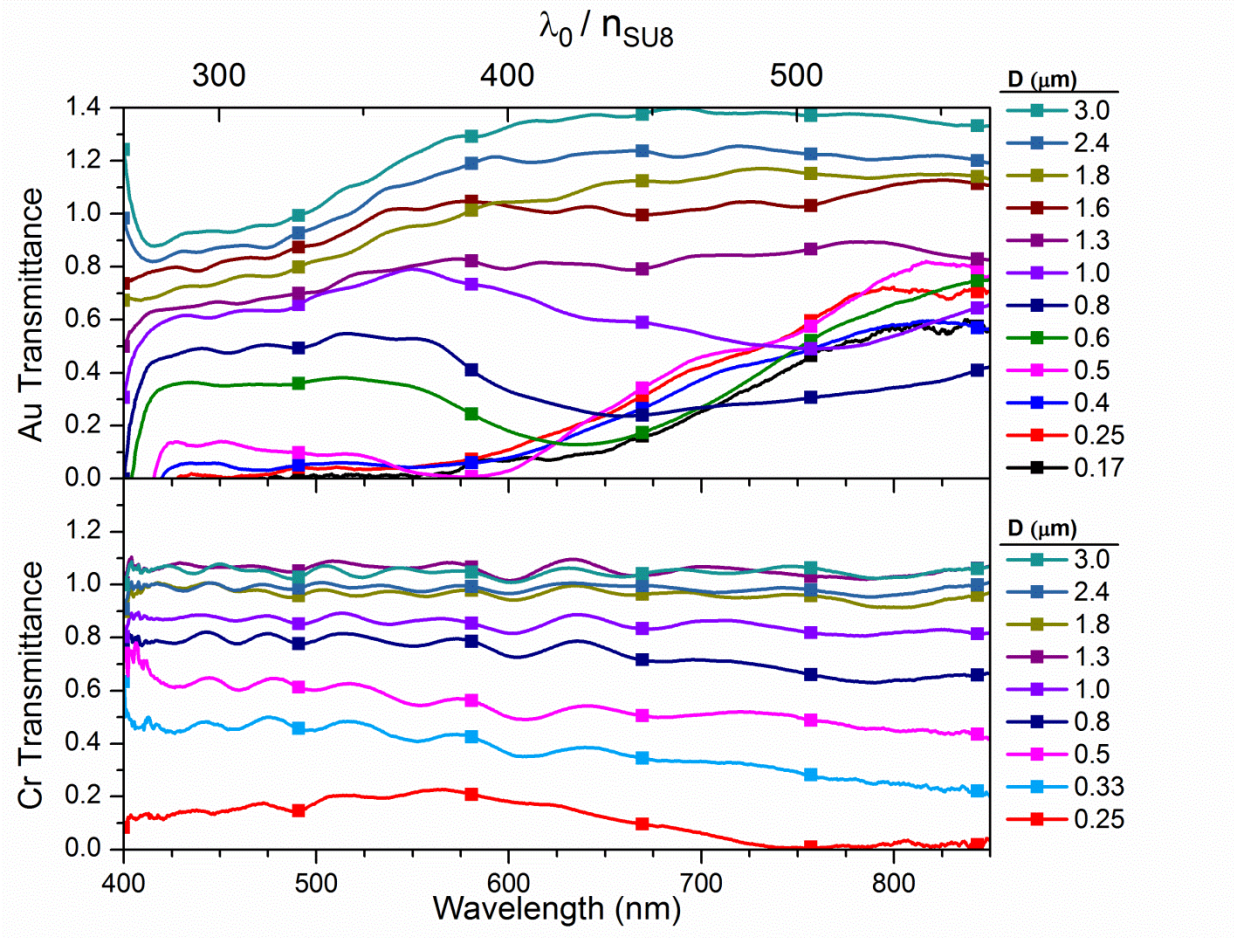

Figure 5.27 Stacked transmittance data for 1 μm tall pillar array in Au and Cr samples. Transmittance plots are shown for various diameters of the pillar array in the Au (top) and Cr (bottom) samples. Data has been stacked for better comparison.

Each of these anomalous features can be described by surface plasmon physics. For the first effect, in addition to photonic modes, surface plasmons forming on the backside surface of the sample (at the planar Au / SU8 interface) can get "funneled" into and propagate through the cylinder, along the walls of the inner metal surface, and eventually scatter as photons into the far field. One can think of this mechanism as creating an effective cylinder diameter larger than the physical diameter, and thus facilitating a type of EOT. If we assume the large (supra-wavelength) diameters are nearly 100 percent transmitting, we can calculate the effective diameter as the transmittance multiplied by the measured diameter. For the 3 μm diameter cylinder, the long wavelength transmittance is $T \sim 1.4$, giving an effective diameter of 4.2 μm. This number is less than the pitch of the array (~10 μm), such that we can reasonably conclude that the increase in T is not due to collective modes or interactions between the cylinders in the array. Although Figure 5.3b shows the surface plasmon propagation length, L_{spp}, is larger than 10 μm for wavelengths above 800 nm, that calculation does not take surface defects into account. Furthermore, it does not factor in the 3D nature of the cylinder. Both of these factors would cause a descrease in $L_{spp,}$ since both would cause a decrease in momentum[8]. As discussed earlier, the surface plasmon propagation length in Au falls off starting at ~550 nm wavelength, due to enhanced absorption in the metal[18]. This would cause only photonic modes to contribute to the far-field transmittance and would explain the dip in T below 550 nm for large diameters. A schematic of this process is shown in Figure 5.28. From 5.28a we see that at small diameters and small wavelengths (blue arrows), there is little contribution to the far-field transmittance due to the L_{spp} not being long enough to reach the end of the cylinder (indicated by the blue line on the side wall of

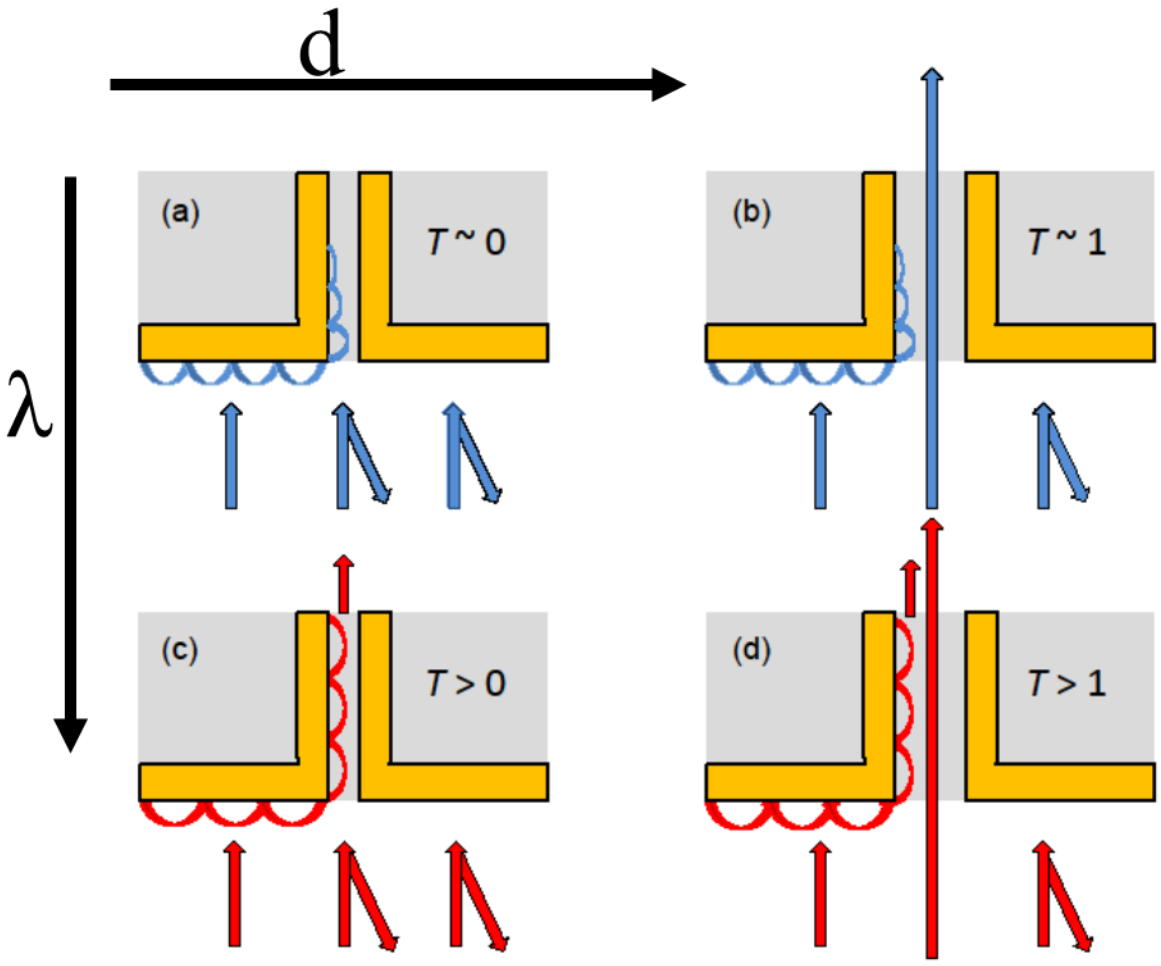

Figure 5.28 Schematic of transmission in Au sample. (a) At large wavelengths and small diameter the plasmon propogation length and the sub-wavelength diameter cut off both photonic and plasmonic modes. (b) At large diameter and large wavelengths, photonic modes are able to propagate through the cylinder. (c) For small diameter and large wavelengths, photonic modes are cut off and plasmonic modes (from SPs originating on the backside of the sample) are able to propagate to the far field creating an effective diameter larger than the actual diameter. (d) At large diameter and larger wavelength, both plasmonic and photonic modes are able to contribute to the far field transmittance.

the cylinder becoming shorter). For large diameters and small wavelengths (5.28b) there is only a photonic contribution to the far-field transmittance. Figure 5.28c shows that at small diameters and large wavelengths (red arrows) there is a plasmonic contribution to the far-field transmittance due to L_{spp} being long enough to reach the end of the cylinder and couple to a photonic mode (smaller red arrow above cylinder). At large diameters and large wavelengths (5.28d), there is both a photonic and plasmonic contribution to the far-field transmittance, indicated by both the large and small red arrows.

In the Cr sample, the transmittance decreases monotonically as the cylinder diameter decreases which, as discussed, is expected absent of any plasmonic contribution. While at some large diameter (650 nm and higher), there is a calculated transmittance slightly above $T = 1$, we posit this to be caused by microcracks forming in the side walls of the cylinders, rendering them slightly transmissive. Eventually, as the diameter becomes sub-wavelength, the transmittance goes to zero, as the photonic modes are cut off. The oscillatory behavior seen in the Fig. 5.27 is most likely Fabry-Perot resonances in the SU8 layer between the metal and the glass, as the separation between adjacent local peaks increases with wavelength as predicted by the free spectral range of etalons: $\Delta\lambda \approx \lambda_0^2/2nlcos\theta$ [19]. Further support is given by Figure 5.29, which shows the oscillations in transmittance are periodic with respect to energy where the spacing between peaks is the free spectral range. It is unclear why the Fabry-Perot resonances are more pronounced in the Cr sample versus the Au sample. The lack of etalons seen in Au could be due to some interaction between the reflected light (Fabry-Perot) and the SPs, that are not present in the Cr sample.

During each measurement, the cylinder region of interest was viewed on screen, to ensure the transmission collection was taken from the same area(s) in each region. While measuring the Au sample, it was clear that some of the photonic modes were being cut off (as seen in the data in Figures 5.27) as the colors of the cylinder openings were changing. Micrograph images of the Au and Cr samples were taken for each region (Figure 5.30). As the cylinder diameter of the Au sample decreased the color changed from initially being yellow, to blue/green around 700 nm diameter, and finally red in the smallest regions (170 nm diameter). From looking through the eye piece and one screen, the Cr sample didn't seem to change color and instead just appeared to lose its intensity. The final panel for both samples is a magnified view of a single cylinder to clearly show the difference. The green appearance of the Cr sample could be due to an artifact in the post-imaging process as through the eye piece; no-color change was discernable.

Transmittance versus cylinder diameter for both Au and Cr samples at 4 chosen wavelengths (500, 600, 700 and 800 nm, representing a range of small to large wavelength) is plotted in Figure 5.31. The Cr sample data represent what is expected in standard aperture theory: the transmittance decreases with decreasing diameter and is overall lower at larger wavelengths. However, we see in the Au sample data that as the diameter decreases, the transmittance does two unique things: 1) it is initially lower for smaller wavelengths and 2) it initially decreases then rebounds slightly with a shillelagh-like feature for larger wavelengths. The start of the rebound occurs roughly when d / λ equals 1, which could be the transition point for when plasmonic modes begin to dominate over photonic modes. By increasing the cylinder height, the path length necessary for the SPs to couple back to a photonic mode and contribute to the far-field

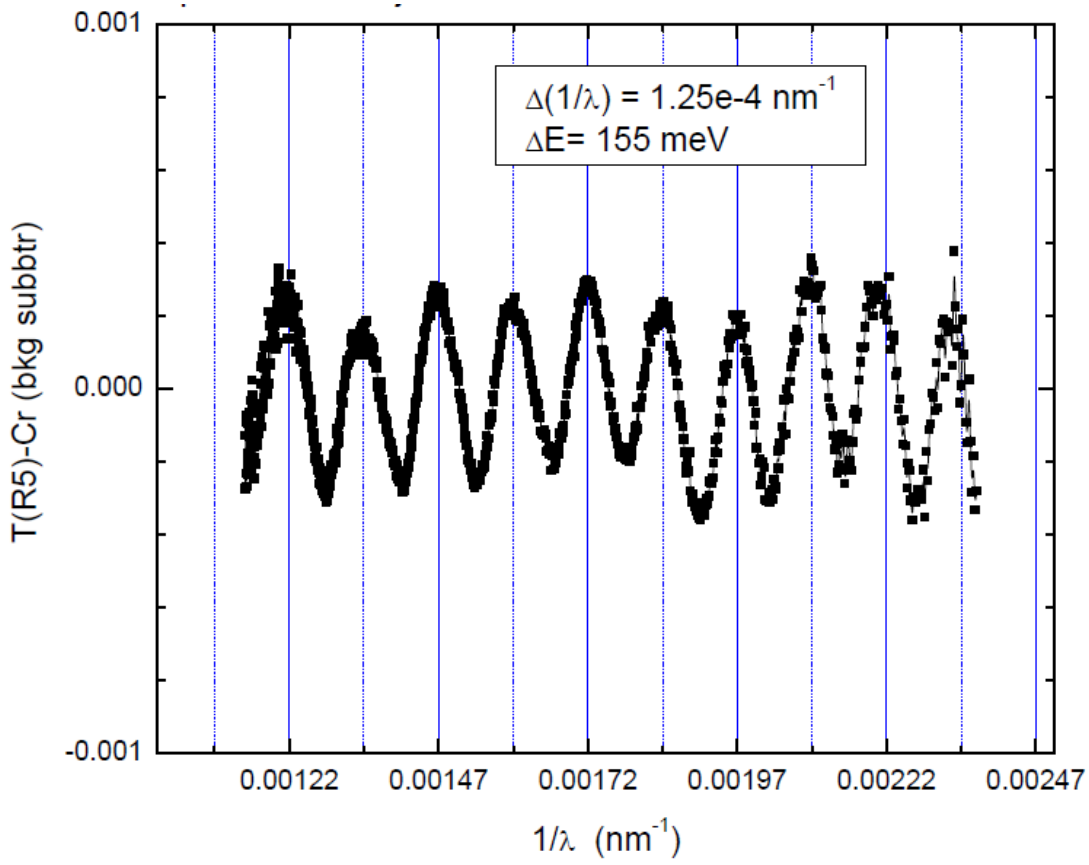

Figure 5.29 Proof of Fabry-Perot effects in Cr film. Transmittance data taken from a region in the Cr sample (shown in bottom of Figure 5.27) is plotted vs. energy. A periodicity in energy can be seen which is supported by etalon theory where the spacing between peaks is known as the free spectral range.

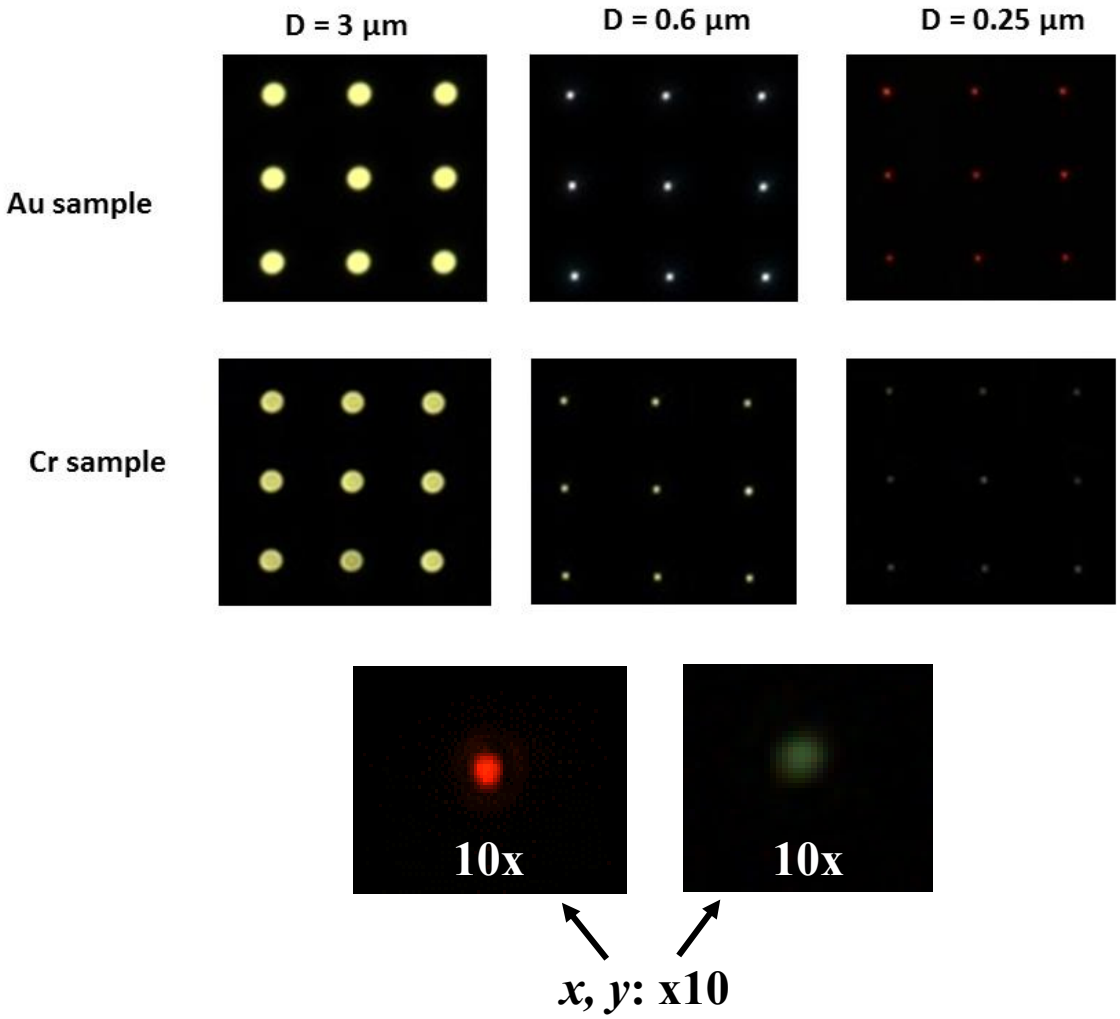

Figure 5.30 Optical micrographs for Au and Cr sample. Upper row shows optical micrographs of Au sample for 3 diameters. Bottom row, left side shows a 10x magnification in of 250 nm region in Au sample. Middle row shows optical micrographs for Cr sample of same diameter. Image on the right side of the bottom row shows 10x magnification of 250 nm region in Cr sample. Au sample shows red wavelengths propagating to far field due to plasmonic behavior.

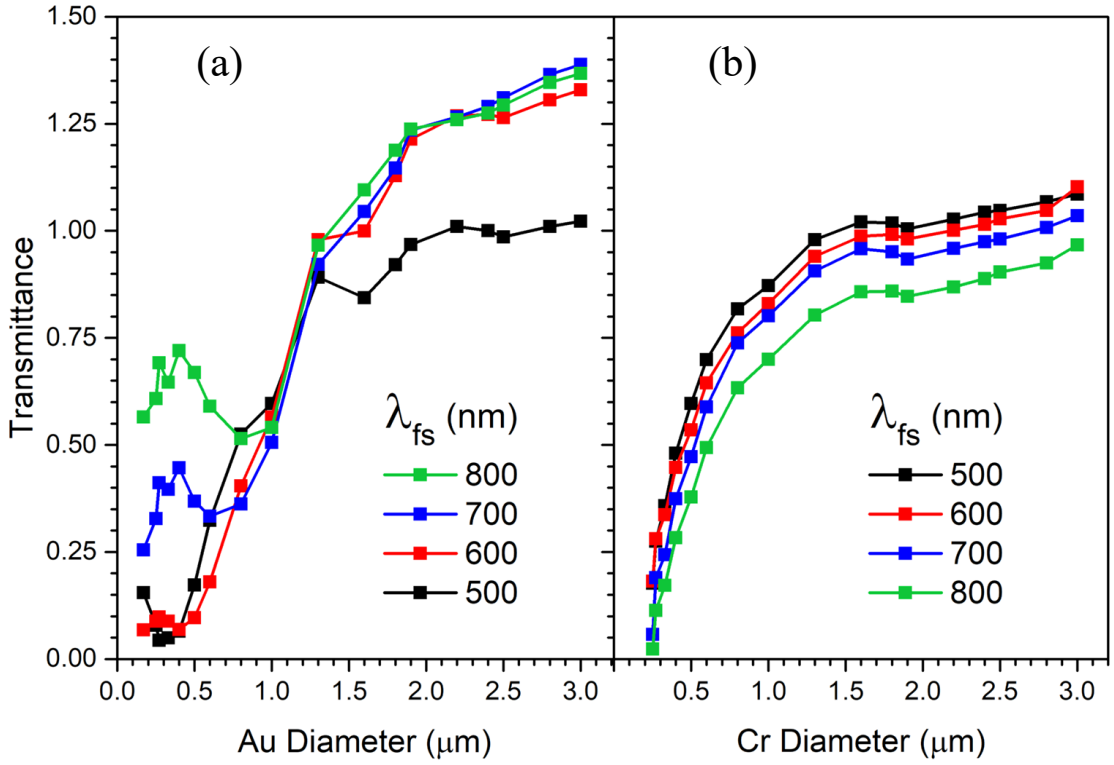

Figure 5.31 Transmittance vs. diameter of 1 μm tall pillar in Au and Cr samples. (a) Transmittance of 1 μm tall pillars in Au sample for various wavelengths. Data show plasmonic behavior with shillelagh–like feature around 0.5 μm diameter at 700 and 800 wavelengths. (b) Cr transmittance following standard aperture theory. Data has been smoothed with adjacent averaging (2 pts).

transmission would also increase. As the SP propagation length is material dependent (and not cavity length dependent) the higher *T* value should go away as the cylinder height is increased. Figure 5.32 shows transmittance as a function of cylinder diameter for 3 pillar heights (1, 2, and 4 μm) at 3 different wavelengths. For the λ_{fs}= 700 and 800 nm data, the uptick in *T* occurring at roughly 0.8 μm diameter cylinders can be seen for all 3 pillar heights. However, the 2 and 4 μm pillars have an overall lower *T* magnitude for all diameters, indicating an inverse dependence on height. Again, this is expected, given that increasing the height of the cylinder simultaneously increases the path length required for the SPs to funnel out of the cylinder and scatter to the far field.

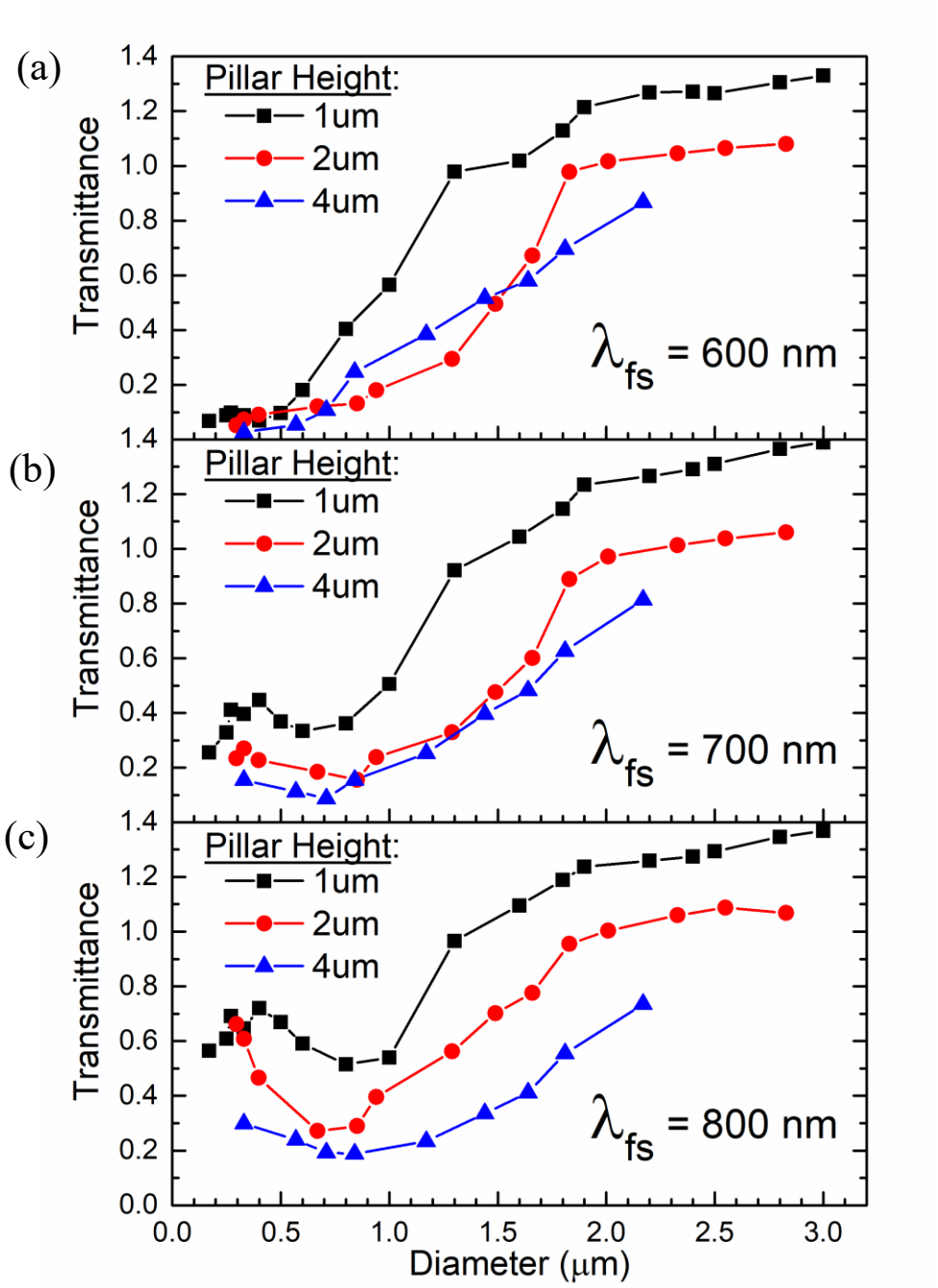

Figure 5.32 Comparison of transmittance for different pillar height. (a) transmittance of 600 nm wavelength for 1, 2, and 4 μm tall pillars. (b) Transmittance of 700 nm wavelength. At this wavelength, plasmonic behavior, shown by the uptick in tranmittance, starts around 0.8 μm diameter and can be seen for all 3 pillar heights. (c) Transmittance of 800 nm wavelength featuring plasmonic behavior for all 3 heights (starting around 0.8 μm diameter). Data has been smoothed with adjacent averaging (2pts).

5.5 Far-field measurement of transmittance: Topside incidence (inverted orientation)

Given the asymmetry of the sample in a direction normal to the wafer, it was possible to effectively double the output path length by requiring the SPs (formed on the planar part of the sample) to travel both up the outside and down the inside of the cylinder before scattering to the far-field. This was achieved by simply inverting the sample and having the light incident on the top-side of the cylinders. Figures 5.33a and 5.33b show a comparison of the normal (closed symbols) vs inverted (open symbols) orientation for the 1 and 4 μm pillar height samples at λ_{fs}= 700 and 800 nm. The data from wavelengths below 700 nm, included in previous Figures, were omitted due to a negligible amount of features attributable to SPs. For both the 1 and 4 μm heights, an overall drop in transmission can be seen. This could be due to a difference in the impedance (mismatch) that occurs for the two orientations: in the inverted orientation, the light coming out of the cylinder core (SU8) travels through the glass substrate before reaching free space, while in the normal orientation, the light propagating through the cylinder core immediately reaches free-space. The expected decrease in plasmonic behavior caused by doubling the path length can be seen in both samples; and in the 4 μm height sample, the uptick in *T* attributed to SPs is no longer seen, as the data follow a trend similar to the data seen for the (non-plasmonic) Cr sample in Figure 5.31b. These data further support the argument that increasing the cylinder height beyond the SP propagation length effectively suppresses plasmonic behavior from contributing to the far-field transmittance.

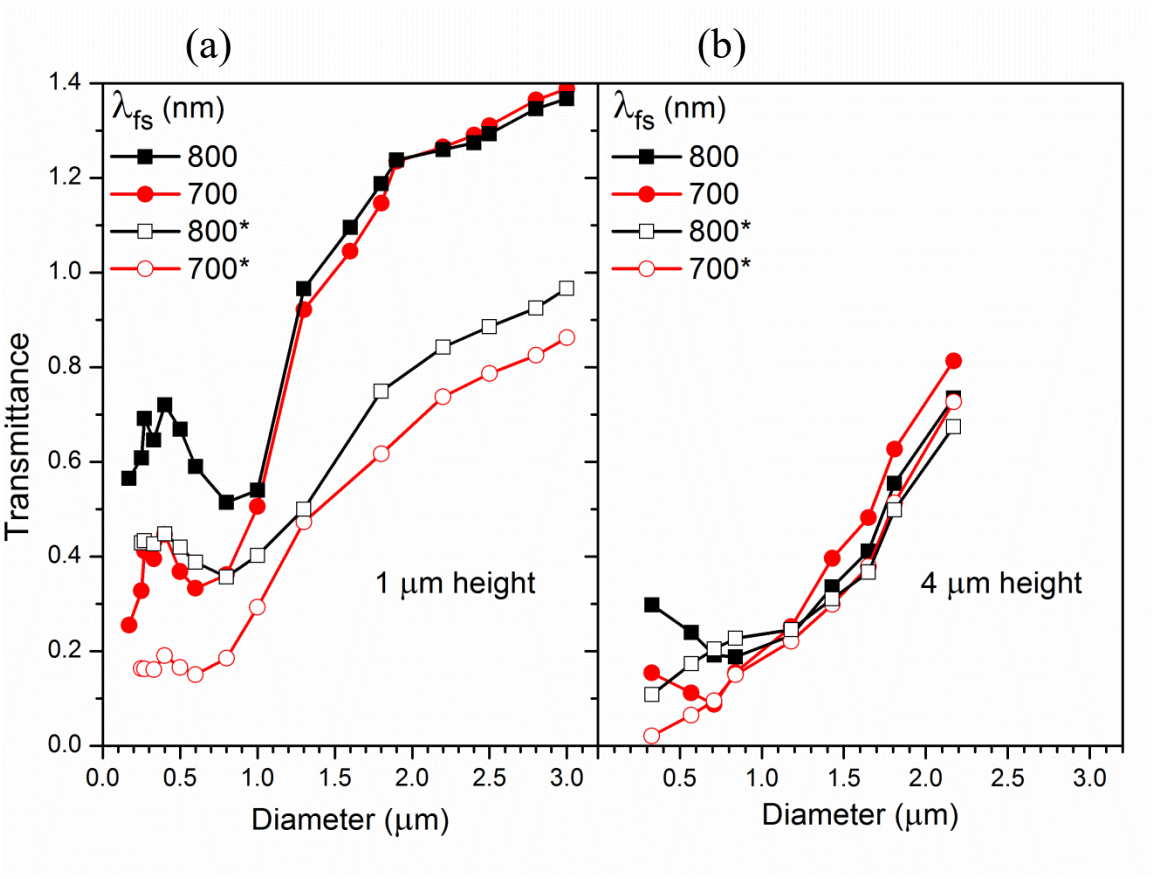

Figure 5.33 Transmittance vs. diameter comparison of normal and *inverted orientation for 1 and 4 μm tall pillars (Au sample). Transmittance data were taken for the normal and inverted orientations and are compared for 1 and 4 μm tall pillars. (a) The 1 μm tall pillars still show plasmonic behavior in the inverted position. (b) For the 4 μm tall pillars the plasmonic behavior is no longer evident, probably due to the doubling of the path length required to reach the end of the cylinder.

5.6 Simulations and discussion

Simulations were made using FEM analysis of a 2D model containing a single 1 μm tall cylinder in a 10 μm cell without periodic boundary conditions. We thank Aaron Rose for performing the COMSOL simulations and providing us the data. Since the effective diameter calculation showed the individual cylinders to be non-interacting (non-overlapping effective diameters) modeling the system as a collection of individual cylinders is an acceptable approximation. TM polarized light (E-field polarized in-plane) was used and the diffraction orders (those that are within an angle of 53 degrees from the normal, which is the acceptance angle of our objective) were calculated and summed to get the total transmission for a particular angle of incidence. Four angles were simulated (0-30 in 10 degree increments) and the transmission of each of these angles was averaged to get the final transmission. In Figure 5.34, the photonic mode cut off with decreasing diameter is seen for wavelengths below 500 nm, as seen in the experimental data in Figure 5.27. Furthermore, the simulation data follow the trend seen in the experimental data of an uptick in transmission for small diameters at large wavelengths. Surface plots from the simulation also reveal SPs propagating up the sidewalls of the cylinder.

In order to characterize the optical transmission seen at long wavelengths (700 and 800 nm) for the sample containing 1 μm tall Au cylinder arrays (transmittance data in Figure 5.23), we calculated the expected transmission values using the Bethe equation discussed earlier and shown in (3). Although this equation is purported to be valid when $d \ll \lambda$, we calculated the transmission for diameters up to $d = \lambda$ (Figure 5.35), where λ spanned the

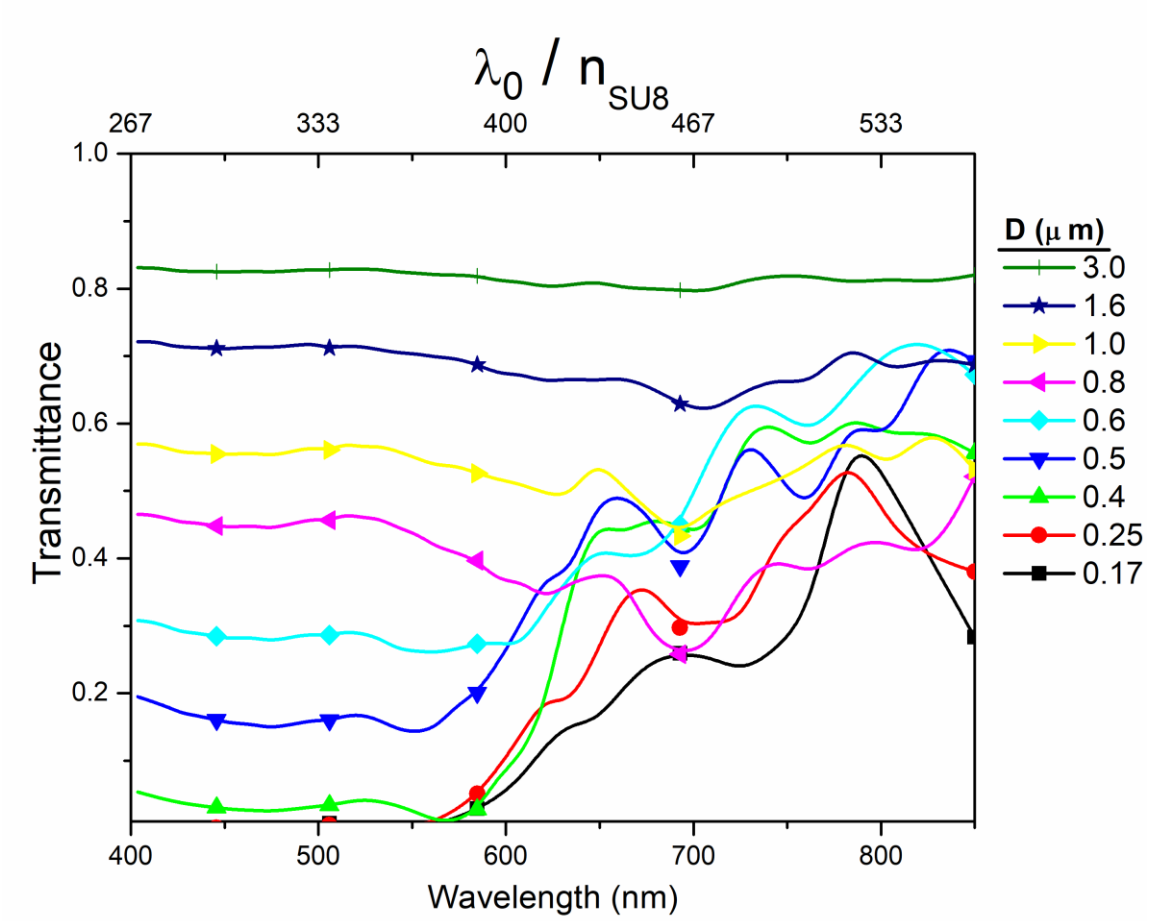

Figure 5.34 Simulation of transmittance vs. wavelength of 1 μm tall pillars in Au sample. Simulations using the FEM analysis of a 2D model of the system was done using the COMSOL software. Results are similar to experimental data in Figure 5.13.

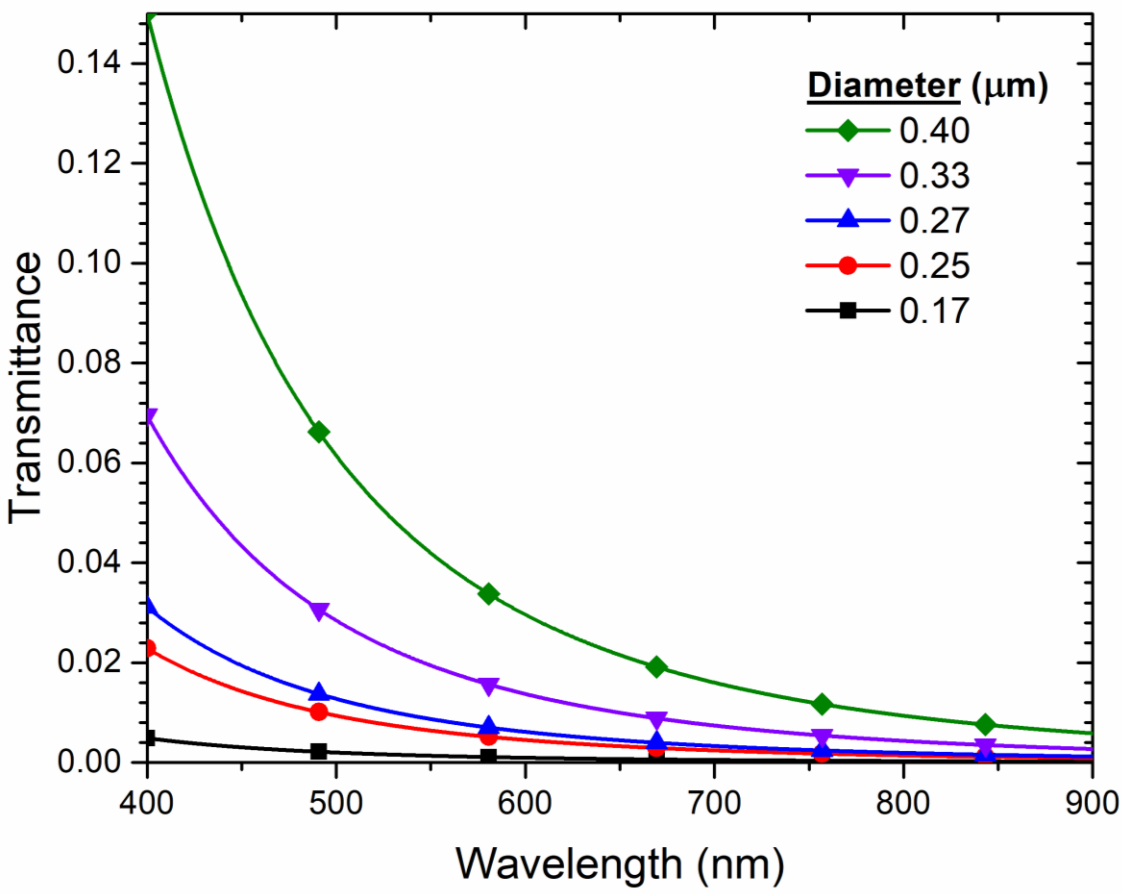

Figure 5.35 Expected transmittance according the Bethe theory. Using normalized transmittance equation proposed in Bethe theory, the transmittance versus wavelength of 4 diameters is shown.

visible-NIR spectrum (400–900 nm). The Bethe equation doesn't take into account pillar height, as it only considers a thin, perfectly opaque metal (E-field goes to zero at the surface). From Figure 5.35 we see the $(d/\lambda)^4$ dependence of the transmittance and the larger diameter (0.40 μm) having the highest transmittance. Using these data, we were able to calculate the enhancement factor T_{meas}/T_{calc} seen in the transmittance. Figure 5.36 and 5.37 shows the transmission enhancement factors for Au pillar diameters less than or equal to the smallest wavelength of the chosen spectrum (400 nm). From the figure, we see that the transmittance is approximately equal to the expected value, $T_{meas}/T_{calc} \sim 1$ for wavelengths below 575 nm. Above this value, we start to see extraordinary optical transmission, with the smallest diameter (0.17 μm) having the largest enhancement factor (up to 25-fold increase in transmittance). Except for the 0.27 μm diameter data being lower than the 0.33 μm diameter data, the transmittance enhancement factor monotonically decreases with pillar diameter. Considering that, according to the equation taken from Bethe, the transmitted power varies as the 4th power of the hole diameter, and given our own transmittance equation's dependence on hole diameter, an under– (for the 0.27 μm diameter) or overestimate (for the 0.33 μm diameter) of the true hole size could have a significant effect on the results. The hole size was determined using the manual scaling lines in the SEM software and the uncertainty of the hole size is ±30 nm.

More recently, the far-field diffraction[20,21,22] and scattering modes[23] from single subwavelength holes have been studied by other groups and found to have a far-field transmittance slightly different than what Bethe theory predicts[24]. Figure 5.38, far-field transmittance versus the ratio of hole diameter and wavelength for our Cr and Au data,

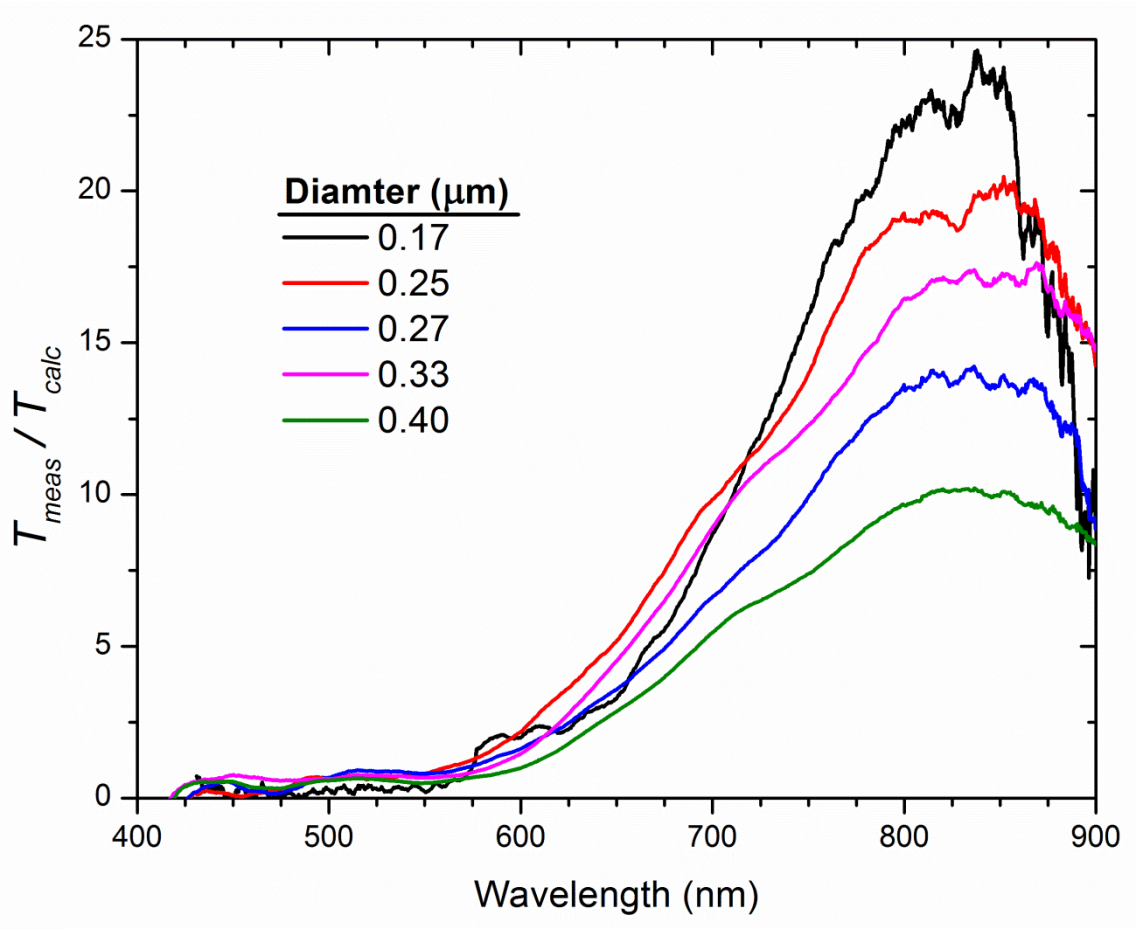

Figure 5.36 Transmission enhancement for subwavelength diameters. Transmittace values are compared to the Bethe equation for transmitted power. Enhancement seen for all diameters, with the smallest diameter (0.17 μm) exhibiting the greatest enhancement factor.

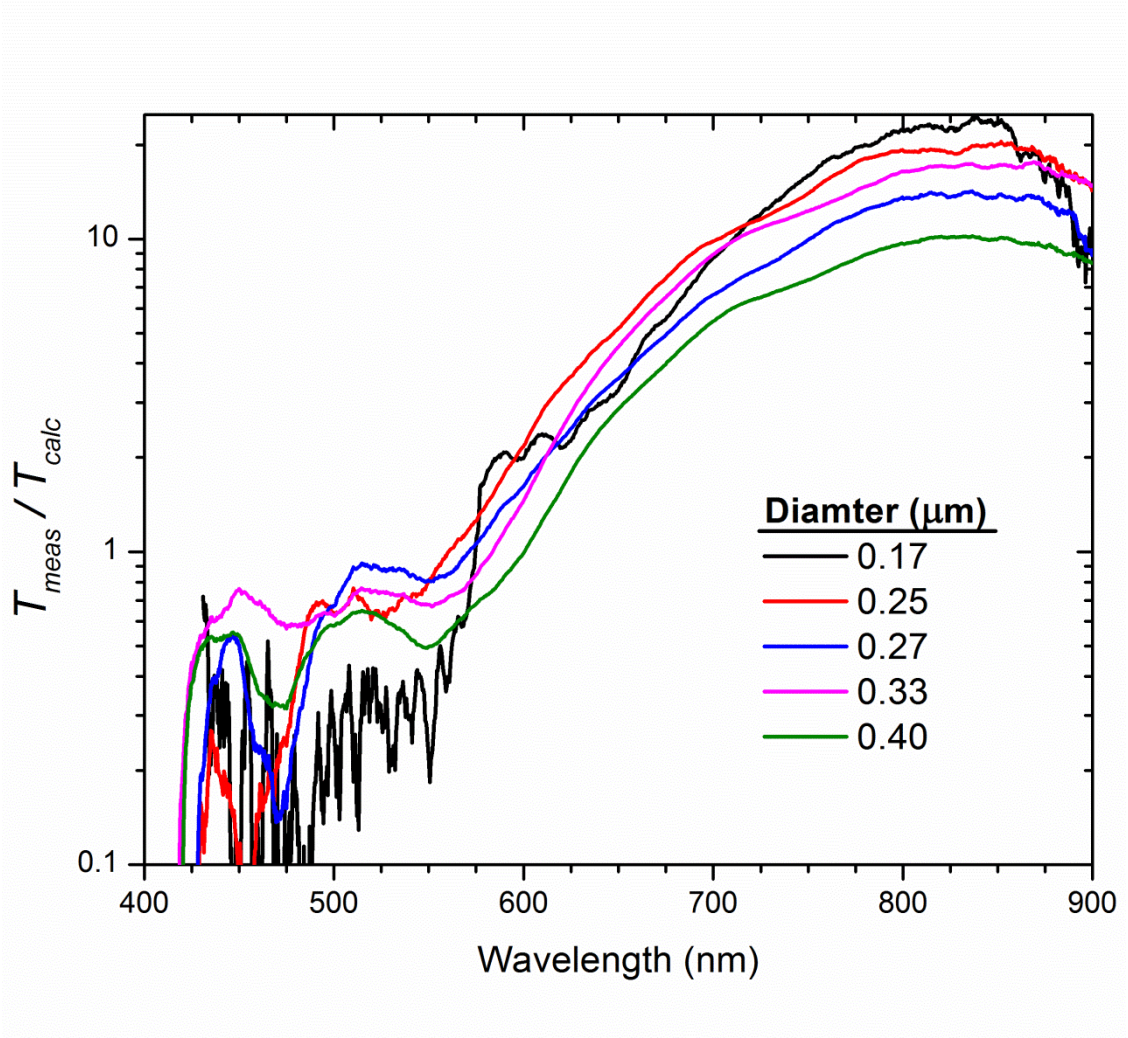

Figure 5.37 Semilog plot of data in 5.36, transmission enhancement for subwavelength diameters.

are plotted along with Bethe-theory (quartic dependence) and Yi-theory (from Reference 20). Despite a somewhat sparse amount of data, from the figure we can see the data for the 700 and 800 nm Cr sample follow Yi-theory rather well. Interestingly, the transmittance of the Au sample falls off much sooner than both the Cr sample and what Bethe or Yi-theory predict, but it then rebounds at small d/λ, presumably due to plasmonic behavior. It's possible there is some interaction between photonic and plasmonic modes, not predicted by either theory, and that is not immediately obvious from empirical study.

At this time, it is unclear why there is a larger enhancement in transmittance for smaller diameters. The origin of the enhancement is presumed to be plasmonic (given the hole diameter, we are below the cutoff for photonic modes), however the larger diameters should exhibit the same plasmonic behavior; perhaps more so, since a larger diameter correlates to larger surface area. One possible reason for the greater enhancement seen for smaller diameters than for larger diameters is due to the penetration of the *E*-field in the SU8. According to Figure 5.2c, the decay length of the *E*-field in the SU8 is roughly half the wavelength. This means that inside the cylinder, the *E*-fields on the sidewalls overlap, potentially causing constructive interference and therefore a higher intensity. A schematic of this phenomenon is shown in Figure 5.39 where the blue lines indicate the E-field penetration depth (*x*-direction) and intensity (*y*-direction) and the red-dashed-line indicates the superposition of the SP wave from the sides of the cylinder. At large diameters, (Fig. 5.39a), there is no overlap, as the wave penetration depth into the SU8 is not large enough. However, as the hole diameter begins to decrease, an overlap starts to develop (Fig. 5.39b), thus the *E*-field intensity inside the SU8 increases (red-dashed-line

is slightly higher than the blue line). As the hole diameter decreases further, there is a large overlap, and therefore a higher intensity (indicated by the red-dashed-line being overall higher than the blue line). The hybridization of the SP wave on the Au/SU8 surface could account for the anomalous transmittance enhancement.

An alternative explanation for the enhancement in transmittance of large wavelengths for small diameters is given by plasmonic refraction[25]. Here, the energy of a transmuted plasma wave is trapped at a resonance determined by the geometry of a perforated metal (here the critical parameter is the hole diameter). When on-resonance, the wave cannot propagate (small wavelengths), while at higher frequencies the wave is off resonance and can propagate freely.

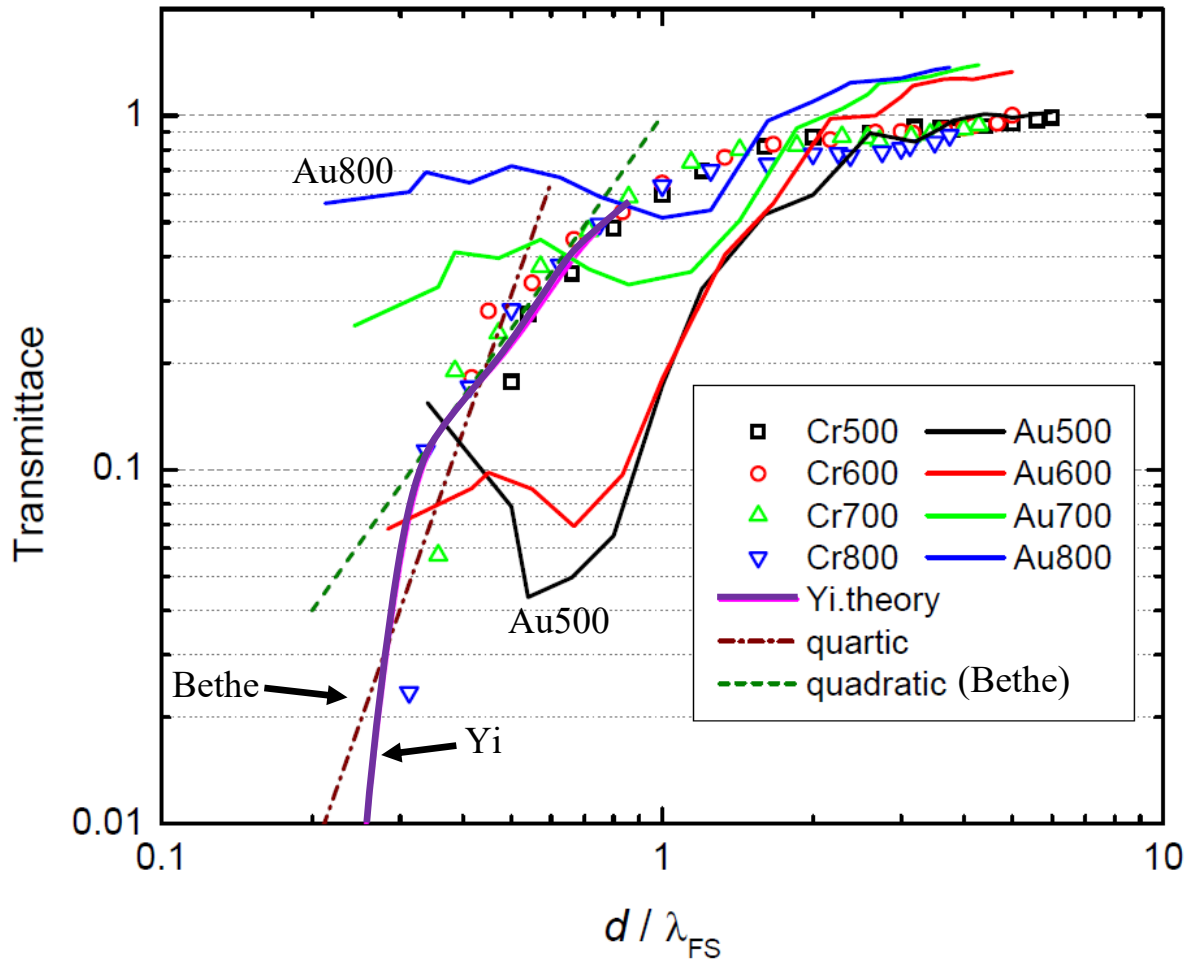

Figure 5.38 Far-field transmittance theory vs data. The far-field transmittance vs the ratio of hole diameter to free-space wavelength is plotted for the Cr and Au data as well as Bethe and Yi-theory. Cr data appear to follow Yi-theory while Au appear to follow neither Bethe nor Yi-theory. Legend format "XXyyy" refers to XX metal (Cr or Au) pillars measured at yyy nm free space wavelength.

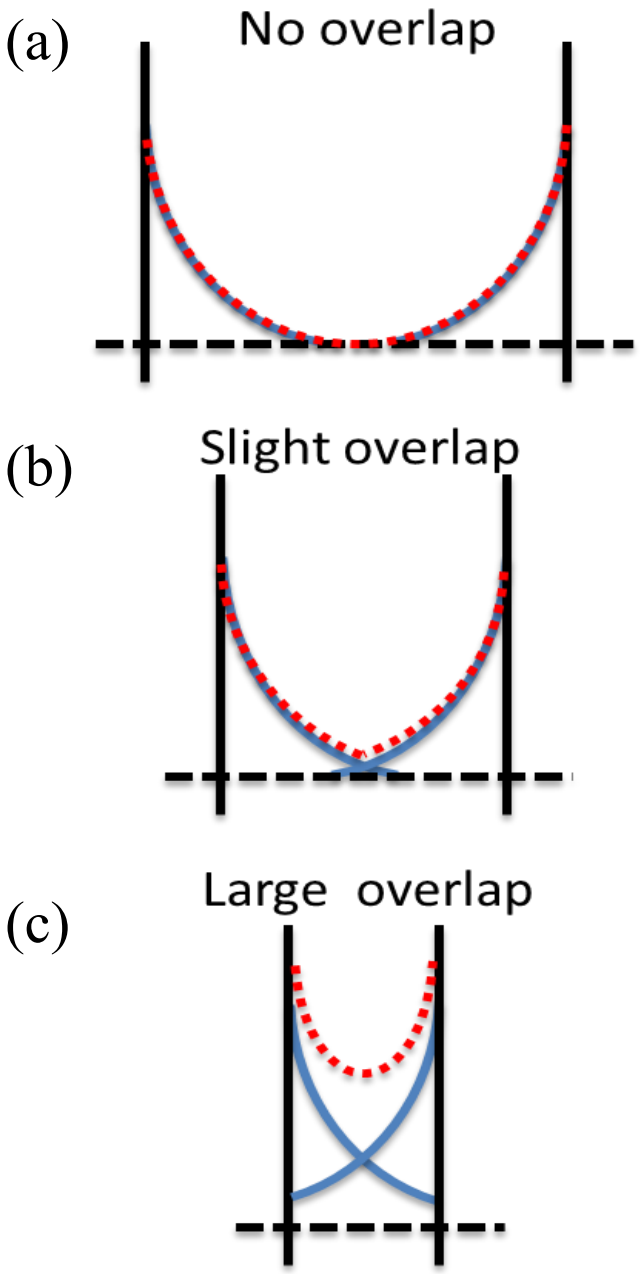

Figure 5.39 Schematic of SP hybridization. SP wave on the side walls of a cylinder (black vertical lines) has a penetration depth of approximately half the wavelength of incident light. The penetration depth of the *E*-field is shown at a certain point in a cylinder (indicated by the black dashed line). Red-dashed-line indicates superposition of wave. As the cylinder diameter decreases, the penetration depth of waves on opposing sidewalls begins to overlap. This could potentially result in constructive interference and thus a higher intensity (red-dashed-line being higher than blue lines).

Regardless of the reason, it is clear from the experimental data and simulations that the coaxial geometry (with a hollow core) is a viable candidate for use as an optrode in optogenetic studies. Furthermore, the enhancement in the far-field transmittance shows that a lower input power can be used to reach the threshold intensity needed to actuate cell-behavior.

[1] Jackson, J. D. Classical electrodynamics. New York, NY: Wiley. ISBN: 9780471309321 (1999)

[2] Weiner, J. The physics of light transmission through subwavelength apertures and aperture arrays. Reps. on Prog. in Phys. **72**, 064401 (2009).

[3] Novotny, L., & Hecht, B. Principles of nano-optics. Cambridge university press (2012).

[4] Courjon, D. Near-field microscopy and near-field optics. Near-field Microscopy and Near-field optics. (Ed. Courjon, D). World scientific press, (2003).

[5] Bethe, H. A. Theory of diffraction by small holes. Phys. Rev. **66**, 163 (1944).

[6] Bouwkamp, C. J. Diffraction theory. Rep. on Prog. in Phys. **17**, 35 (1954).

[7] Zakharian, A. R., Moloney, J. V., & Mansuripur, M. Surface plasmon polaritons on metallic surfaces. Opt. Express **15**, 183-197 (2007).

[8] Raether, Heinz. Surface plasmons on smooth and rough surfaces and on gratings. Vol. 111. Springer, (2006).

[9] P. B. Johnson and R. W. Christy. Optical Constants of the Noble Metals, Phys. Rev. B **6**, 4370-4379 (1972).

[10] P. B. Johnson and R. W. Christy. Optical constants of transition metals: Ti, V, Cr, Mn, Fe, Co, Ni, and Pd, Phys. Rev. B **9**, 5056-5070 (1974)

[11] Kneipp, K., Wang, Y., Kneipp, H., Perelman, L. T., Itzkan, I., Dasari, R. R., & Feld, M. S. Single molecule detection using surface-enhanced Raman scattering (SERS). Phys. Rev. Lett. **78**, 1667 (1997).

[12] Zheng, P., Li, M., Jurevic, R., Cushing, S. K., Liu, Y., & Wu, N. A gold nanohole array based surface-enhanced Raman scattering biosensor for detection of silver (I) and mercury (II) in human saliva. Nanoscale, **7**, 11005-11012 (2015).

[13] Ozbay, E. Plasmonics: merging photonics and electronics at nanoscale dimensions. Science **311**, 189-193 (2006).

[14] Homola, J., Yee, S. S., & Gauglitz, G. Surface plasmon resonance sensors: review. Sens. Actuators, B: Chem. **54**, 3-15 (1999).

[15] Liedberg, B., Nylander, C., & Lunström, I. Surface plasmon resonance for gas detection and biosensing. Sens. Actuators **4**, 299-304 (1983).

[16] Ebbesen, T. W., Lezec, H. J., Ghaemi, H. F., Thio, T., & Wolff, P. A. Extraordinary optical transmission through sub-wavelength hole arrays. Nature **391**, 667-669 (1998).

[17] Buehler Vibromet 2

[18] Creighton, J. A., & Eadon, D. G. Ultraviolet–visible absorption spectra of the colloidal metallic elements. J. Chem. Soc. Farad. Trans. **87**, 3881-3891 (1991).

[19] Hecht E. Optics. 5 ed. Boston: Pearson; 2017

[20] Yi, J-M., A. Cuche, F. de León-Pérez, A. Degiron, E. Laux, E. Devaux, C. Genet, J. Alegret, L. Martín-Moreno, and T. W. Ebbesen. Diffraction regimes of single holes." Phys. Rev. Lett. **109**, 023901-5 (2012).

[21] Nikitin, A. Yu, F. J. García-Vidal, and L. Martín-Moreno. "Surface electromagnetic field radiated by a subwavelength hole in a metal film." Phys. Rev. Lett. **105**, 073902-6 (2010).

[22] Reismann, M., Dahmen, C., & Von Plessen, G. Diffraction of obliquely incident light by single nanoholes in thin noble-metal films. Appl. Phys. B **84**, 229-232 (2006).

[23] Rotenberg, N., Spasenović, M., Krijger, T. L., Le Feber, B., de Abajo, F. G., & Kuipers, L. Plasmon scattering from single subwavelength holes. Phys. Rev. Lett. **108**, 127402-7 (2012).

[24] Degiron, A., Lezec, H. J., Yamamoto, N., & Ebbesen, T. W. Optical transmission properties of a single subwavelength aperture in a real metal. Opt. Commun. **239**, 61-66 (2004).

[25] K. Kempa, in a private correspondence

Chapter 6: Crosstalk suppression: comparing locally shielded electrodes with bare electrodes

6.1 Introduction

This Chapter discusses the concept of electrical crosstalk where, in the context of neuroelectrophysiology, electric fields originating from neurons spatially and temporally overlap and obfuscate the signal recorded at a particular electrode site. We contend that having locally shielded electrodes, versus the bare, unshielded electrodes of all extant techniques and devices, will reduce electrical crosstalk, both simplifying and rendering more accurate electrophysiological measurements. To test this hypothesis, we compared the crosstalk level between bare electrodes and locally shielded electrodes using quantitative modeling (COMSOL simulation) and experiment through extracellular recording (using both optical and electrical stimulation).

In the brain, there is both large-scale and small-scale spatiotemporal organization, as different functions take place on multiple spatial and temporal scales. To understand or gain insight into the rules that underlie brain function, it is generally accepted that networks of neurons need to be studied,[1] as opposed to individual neurons in isolation. The extracellular multielectrode array (MEA) is an appropriate device for recording from large numbers of neurons, as it is capable of simultaneously recording both the slow activity associated with changes in the local field potential (an aggregate of the surrounding synaptic inputs) and the fast activity associated with multi-unit neuronal discharges nearby. In order to gain a mechanistic description of a neuron's role in specific neuronal network processes, for use as a predictive descriptor rather than a gross correlator of brain activity, it is necessary to isolate single-unit activity. Given the size

and spacing of neurons within networks (both on the few μm-scale), this requires a device capable of high spatial resolution. While it has been clearly demonstrated that MEAs can be fabricated at high densities (down to ~10 μm pitch), this does not necessarily translate into high spatial resolution.

Given the spread of the extracellular current into surrounding ionic medium originating from action potentials, the number of distinct recording channels in a device will be effectively reduced if they are of a critical spacing or smaller. The extent to which an electrical field originating from a neuron is recorded by multiple electrodes, rather than by/at a single recording site, may be defined as electrical crosstalk. The reciprocal of this situation, coinciding fields from multiple neurons at a single recording site (which then aggregate as a single input instead of two or more distinct inputs) is equally problematic. Overlapping electrical fields are undesirable for both recording and stimulation, the latter being an issue in *e.g.* MEA technology used for visual prostheses[2]. The degree to which a single pixel of an electrode array dominates all neighboring pixels was defined by Hilke, *et al.* (Ref. 2) as the crosstalk coefficient (*CT*):

$$CT_{(x,y,z)} = \frac{|E|_{N-1(x,y,z)}}{|E|_{N(x,y,z)}} \quad (1)$$

where $|E|_{N(x,y,z)}$ is the electric field magnitude at a point (*x, y, z*) with all electrodes in the array active, and $|E|_{N-1(x,y,z)}$ is the electric field at the point (*x, y, z*) with a chosen electrode inactive. Although this equation involves electric fields and during the measurement we're measuring either voltage or current, we can plug in voltage and the equation will be the same. This due to the magnitude of *V* and *E* being related by $E = -\nabla V$ which says that the electric field is the gradient of the scalar potential. Since we'd

be measuring the gradient along the same path for $|V|_{N(x,y,z)}$ and $|V|_{N-1(x,y,z)}$ the path lengths would cancel out and we'd simply be dividing the magnitudes of the voltage at a point in space (which is what we're doing with the electric field in equation 1). From equation 1, it is clear that *CT* ranges from 0 to 1, with the low end being minimal crosstalk (measured electric field dominated by the measuring electrode of interest) and the upper end being high crosstalk (multiple electrodes contributing to the measured electric field). This figure of merit is similar to what was plotted in the COMSOL simulations shown in Chapter 2.

If the overlap between neuronal events (spikes) is small enough, one of the most powerful and common tools used by neuroscientists to isolate individual neurons in multi-unit recordings is a post-data acquisition process called "spike sorting". It involves grouping recorded spikes into clusters based on the similarity of their shapes, as it is an accepted principle that neurons tend to have a characteristic action potential shapes[3] (*i.e.* voltage or current versus time responses).

Figure 6.1 shows the basic steps for spike sorting. The first step in processing recorded data is to apply a band pass filter, typically between 300 and 3,000 Hz, in order to remove any low frequency activity. It is important not to make the band too narrow as the filter could distort the shape of the spikes[4]. The next step is called spike detection and it involves using an amplitude threshold to distinguish the spikes from the background noise. The threshold can be set manually, although it is occasionally set automatically as a multiple of the standard deviation of the signal[5,6]. However, in cases where there are burst patterns or spikes with large amplitude, spikes could be missed due to a biased (high) threshold value. A number of studies have been done to try to refine this limitation

and determine an optimum threshold function[7,8,9]. Once the spikes are detected, they are separated from the band-pass data and stored, superimposed in a single window (Figure 6.1b). This window can have hundreds of spikes superimposed (aligned to their maximum), with two or more different waveforms buried in the data.

Therefore, the third step for spike sorting extracts the individual spikes or spike waveforms out of this window of collected spikes and is highly dependent on the sampling rate. Each datum point of a spike is a possible "feature" to be used for extraction (differentiation from other spikes) and therefore the problem starts off being an *N*-dimensional one, where *N* is the number of data points per spike. The duration of an action potential is on the order of a few milliseconds and so a 40 kHz sampling rate will give one 50 – 100 points per spike. If the sampling rate is too low, it risks becoming insufficient, as cutting out data points can cause an unintentional shift in the maximum point used for alignment. A higher sampling rate corresponds to more data points and a higher accuracy in representing the signal, but requires more computational power. To lower this burden, methods have been developed in order to lower the dimensionality of the problem.

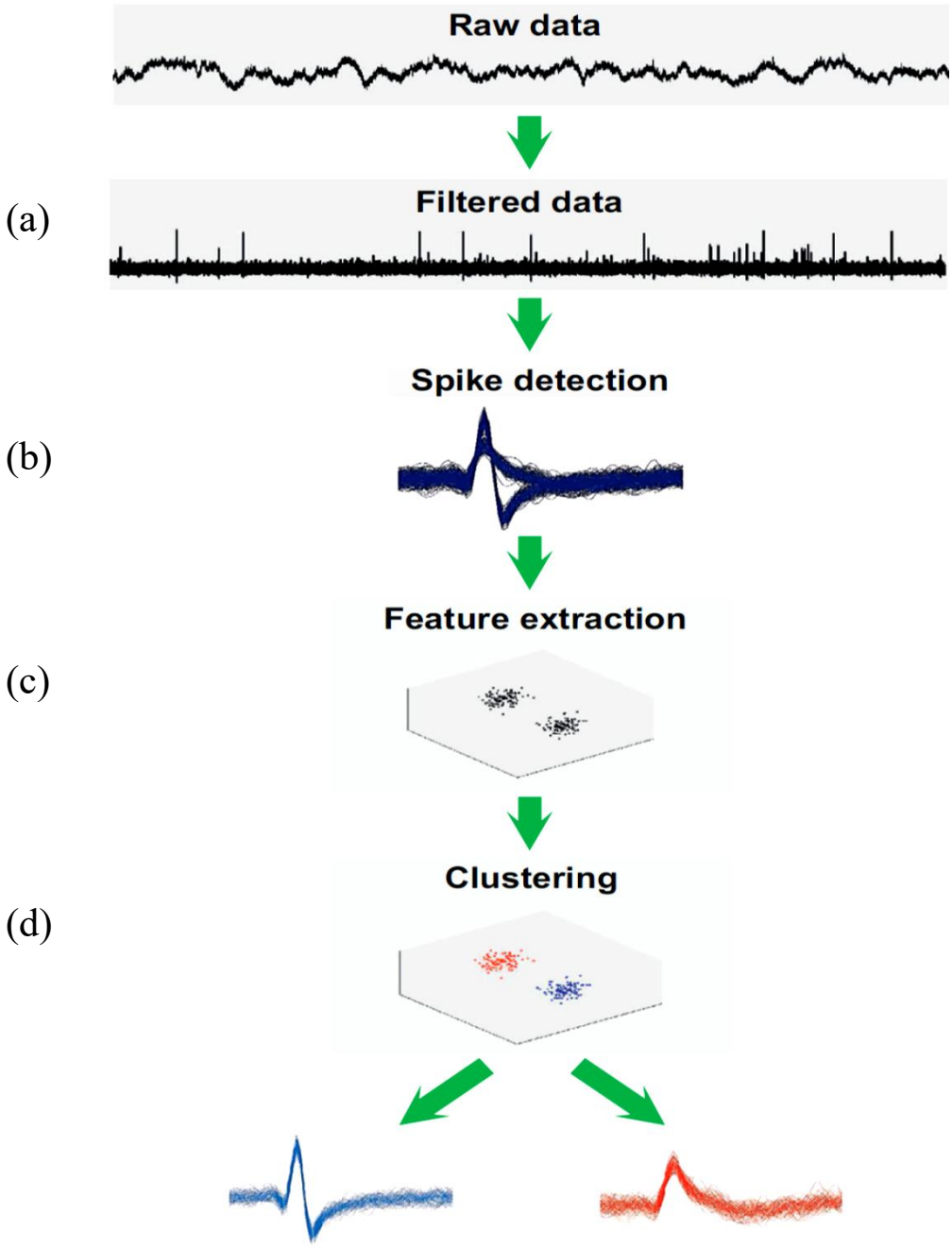

Figure 6.1 Spike sorting process. (a) Raw data is put through a band pass filter to remove drift from LFP. (b) Spikes are detected and overlaid in a single window with alignment according to spike maximum. (c) feature extraction is used to isolate individual spikes. (d) Spikes with similar features are clustered together resulting in unique classification.

One simple method for feature extraction is to take the basic characteristics of a waveform (amplitude, duration/width, rise time, square of the signal, etc.) and use them to differentiate signals. However, it has been shown this is not always reliable[10]. Another simple approach called template matching relies on choosing template spike shapes for each unit[11]. The shape is then used as a metric in assigning and matching waveforms. However, in addition to manual intervention being problematic, sparsely firing neurons could be missed with this approach[12]. The most common feature extraction and dimensionality reduction method is principal component analysis (PCA)[13,14]. While the details of this method are beyond the scope of this thesis, the idea is to find an ordered set of orthogonal basis vectors that capture the directions of largest variance in the data and represent any waveform as a linear combination of those principal components[15,16]. In other words, any particular data point (spike) can be represented by scaling and adding the principal components together. This method usually reduces the dimensionality down to 2 or 3 because most of the principal components beyond the second or third are variations in the noise and simply add progressively smaller corrections to the spike. An alternative to PCA and the other methods discussed is the use of wavelets, the details of which will not be discussed here. The important point, at least for use in this thesis, is that there is a number of methods that are used to extract waveforms with similar features.

The final step of spike sorting is to group or "cluster" spikes with similar features in order to assign them to a particular neuron. This step is quite subjective and time consuming as the user or an algorithm defines the boundary for each cluster[17]. The problems compound going from 2D to 3D projections of clusters. Despite these

challenges, spike sorting algorithms currently remain a standard process in analysis of neurological data and new methods or refinements are continually being made[18,19,20].

The most challenging issue to the spike sorting method is the subject of focus for this Chapter: overlapping spikes or, as defined above, crosstalk. Two or more neurons in close proximity firing synchronously or with a small enough delay will have overlapping extracellular action potentials. This might be interpreted as the signal from a single neuron, rather than from a group of neurons. Furthermore, as was shown in the Chapter 2 section on current-source-density analysis, the extracellular waveform originating from an action potential changes shape as it travels through space. Given that field potentials can travel hundreds of microns, the waveform picked up at one location could be drastically different at another and therefore incorrectly interpreted as 2 unique signals[21]. Outside of spike sorting, various techniques have been utilized to try to minimize the effect of crosstalk by designing devices that constrain the generated electric fields[22,23,24]. From the experiments shown in this Chapter, local shielding through a coaxial structure greatly reduces crosstalk when compared to bare electrodes.

6.2 Device fabrication

Two types of devices were fabricated for the optical stimulation experiment using HEK293-ChR2 cells: bare microelectrode arrays (bMEA) and coaxial microelectrode arrays (cMEA). Devices used in the optical stimulation experiment are shown in Figure 6.2. Initially, a 10/300 nm Ti/Au layer (optically opaque for 400 - 700 nm wavelengths) was deposited on borosilicate glass via sputtering, followed by standard photolithography and chemical wet etching to open eight 20 μm-diameter holes spaced 300 μm apart. These openings were necessary to confine the light (472 nm laser), later used to evoke ion currents in the HEK cells, to a specified region rather than macro-illuminating the sample (to the full diameter of the light cone and thus covering multiple sensing regions). The light cone of the laser was previously measured to be approximately 300 μm in diameter in the geometry employed, such that only one region should be illuminated at a time. Nanoimprint lithography (NIL) was used on 3 μm-thick SU8 to create a 10 mm^2 pillar array (5 μm tall pillars at 10 μm pitch) [25]. After depositing a 10/120 nm Ti/Au layer by sputtering, an 8 x 8 array (20 μm diameter and 100 μm edge–to–edge) was patterned using standard photolithography, and a subsequent wet chemical etch left 59 individually addressed sensing areas. Eight of these sensing areas were aligned with the holes in the light-confining metal layer mentioned above. ALD was used to deposit a 225 nm thick aluminum oxide layer covering the entire sample, and photolithography + wet etching was used to open up holes over the macroscale pad (pin out) regions.

For the coaxial sample, an outer metal layer of 120 nm thickness Cr was further deposited and photolithography + wet etching was used to pattern the metal. To expose

the inner metal as well as to decapitate the pillars to facilitate the transmission of light through the 2 μm core of each pillar in the sensing area, and thus allow for optical stimulation, two processes were used. An SU8 layer was spun on and baked to form a mechanical stabilization layer. Next, a chemical mechanical polisher was used to decapitate the pillars and standard wet chemical etching was used to lower the Cr and alumina layers similar to methods discussed in Chapters 3 and 5. A plasma etch process was then used to lower the height (thickness) of the SU8. In order for the HEK cells to be grown and contained within the electrode region, a PDMS liquid-confining well (5 mm inner diameter, 6 mm outer diameter, 10 mm height) was attached to the substrate using PDMS.

For the electrical stimulation experiment, the sample / devices were fabricated on borosilicate glass substrate. Figure 6.3 shows completed devices. Again, a similar standard NIL process described above was used to create 2 SU8 pillar array regions (10 mm^2, 5 μm tall pillars, 10 μm pitch). The two regions were separated by 50 mm. Within each region, two sets of sensing areas were fabricated, one with 10 μm diameter areas and another with 20 μm diameters. The 10 and 20 μm diameter areas contained approximately 3 and 7 pillars, respectively. The sensing areas were aligned in 14 rows (2 sensing areas per row, 7 rows per diameter) and each row had a different separation distance (sensing area edge–to–edge) starting at 1,000 μm and ending at 10 μm for the 20 μm diameter set and 5 μm for the 10 μm set.

One region was designated as the coaxial multi-electrode region (cMEA), while the other was designated as the bare multi-electrode region (bMEA). A metal layer (10/110 nm Ti/Au) was deposited via physical vapor deposition and standard

photolithography plus wet chemical etching was used to designate the 28 individually addressed sensing areas in each of the two pillar regions (56 total sensing areas). Next, a 200 nm thick aluminum oxide layer was deposited on the entire sample using atomic layer deposition. Holes were etched in the alumina layer in order to access the Au layer macro pads (where the address lines originating from the sensing areas terminated) corresponding the pin locations on the pre-amplifier board. Finally, a Cr (120 nm) layer was deposited using physical vapor deposition. Standard photolithography was used to pattern one of the array regions, so as to leave Cr covering 28 sensing areas and to have subsequent address lines coming from each area. To expose the inner metal, an anisotropic lithographic process was combined with subsequent wet etching in order to lower the Cr and alumina layers. The resulting outer metal to inner metal height ratio was roughly 60%. 2 plastic wells fabricated using a 3D printer (inner diameter: 5mm, outer diameter: 6 mm, 10 mm height) were attached with PDMS to contain an electrolyte buffer solution (aCSF) within the bare and coaxial electrode regions.

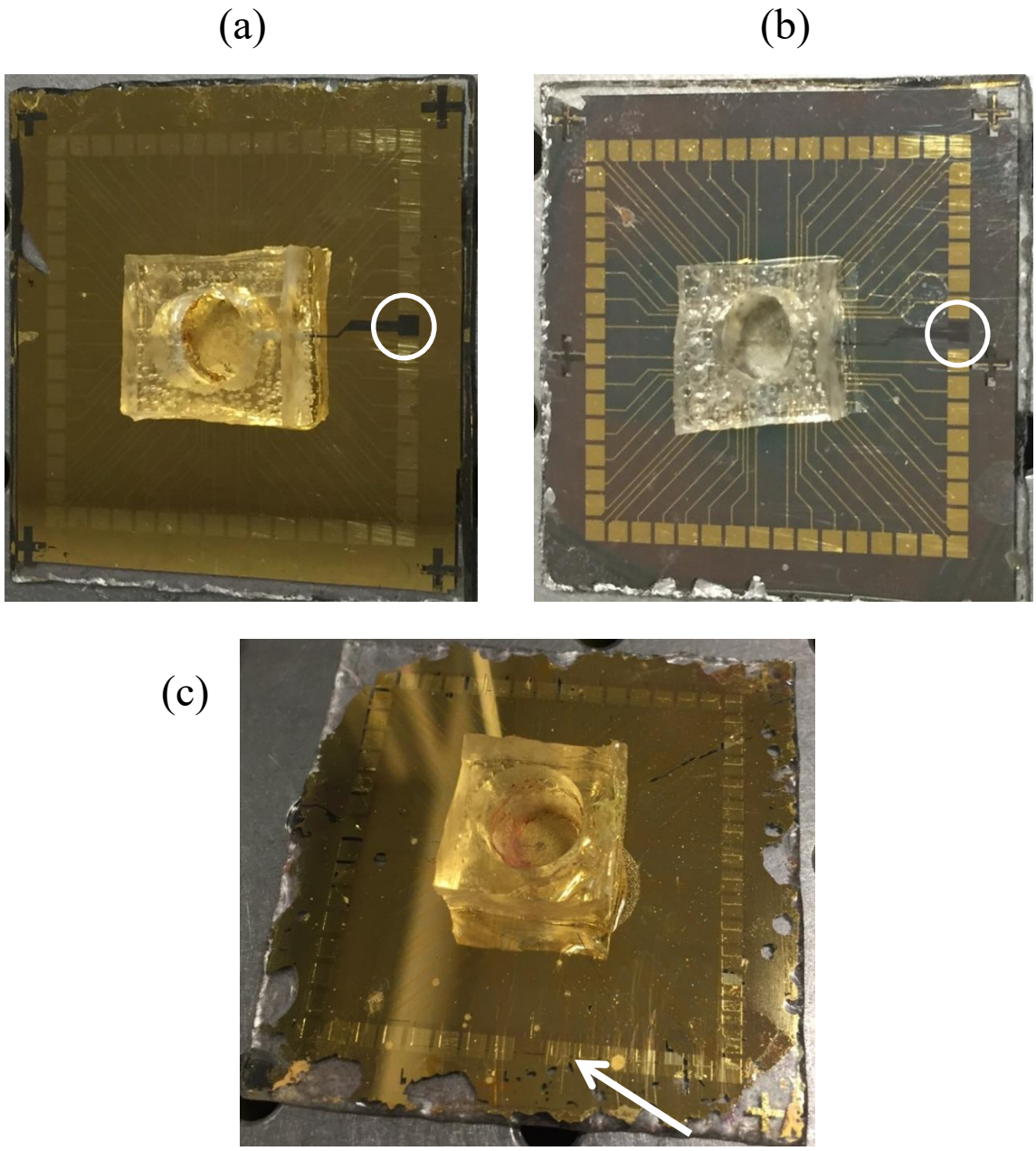

Figure 6.2 Devices for optical stimulation experiments. Substrates for devices in optical stimulation experiments were made opaque by depositing 300 nm of either Ti+Au or Cr. Then holes were etched in the metal to confine light stimulation to desired region. (a) and (b) are coaxial arrays (ground electrode is circled for clarification). (c) Bare electrode array (white arrow points to empty pad normally assigned to ground, included for clarification).

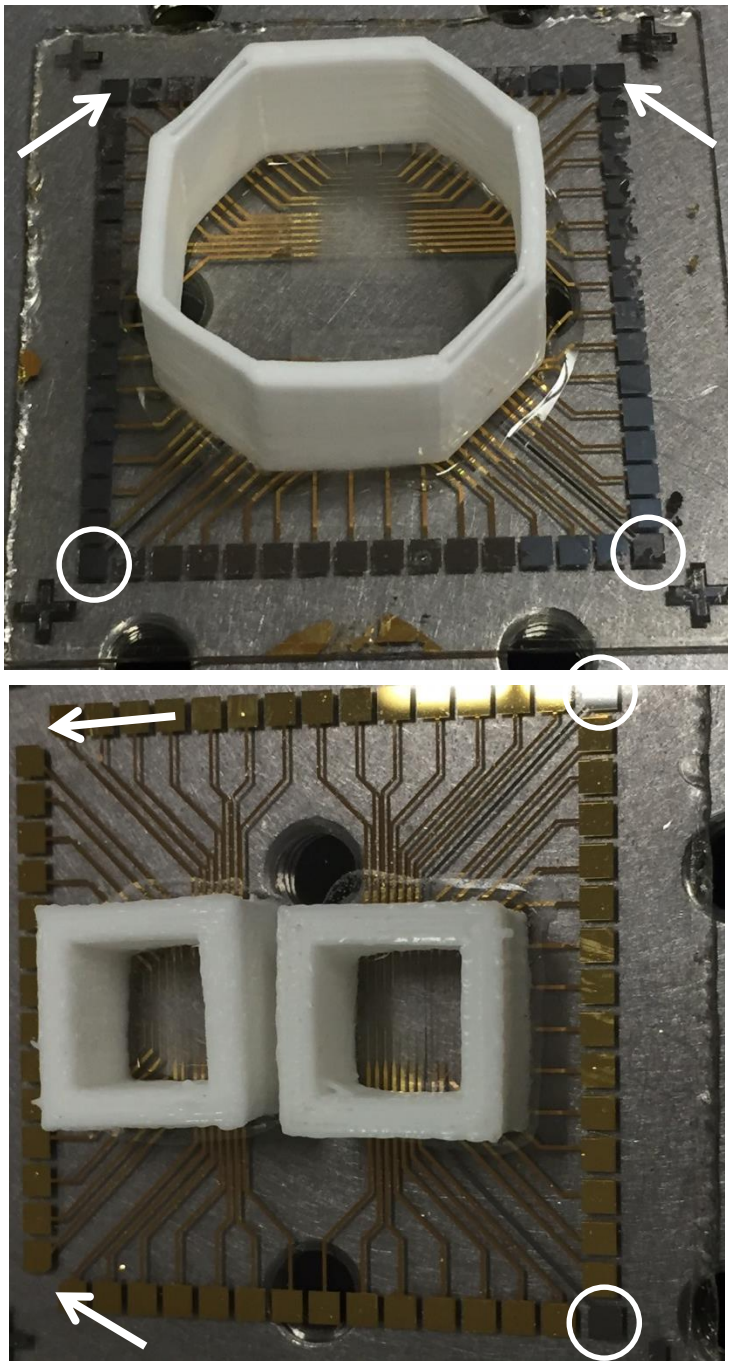

Figure 6.3 Devices for electrical stimulation experiments. Devices used in electrical stimulation experiment. Each device includes a bare electrode region and a coax region. Top image shows device with single plastic well (fabricated with 3D printer), while bottom shows device with 2 individual plastic wells separating the bare electrode and coaxial regions. White circles show ground pads for coax region, while white arrows show empty macro pad (due to lack of ground electrode) for bare electrode region.

6.3 Simulations

Using the finite element method (FEM) simulation software COMSOL Multiphysics, a computational model of the device was made employing realistic materials parameters, intending to show the overlap of a pair of electrode sensing areas as a function of separation (edge–to–edge) distance. A pattern of 7 rows of electrode pairs, arranged with each row having a specific edge–to–edge distance (1,000 μm down to 5 μm), were placed in an electrolyte solution (having nominally the same electrical properties as the medium used in the electrical experiment, *i.e.* static dielectric constant $\varepsilon \sim 80$, dc electrical conductivity $\sigma \sim 1.5$ S/m). Although crosstalk and the detection of field potentials *in situ* is influenced by a myriad of factors including cell type, distance from electrode and the nature of the contact with electrodes, the purpose of this simulation was to find the amplitude of the potential at the recording electrode surface generated by a source (*e.g.* neuron spike) as a function of separation distance. Green-Lorentz reciprocity reduces this problem to solving Poisson's equation for the scalar potential generated from the recording electrode as a voltage source[26].

The simulations, shown in Fig. 6.4, were performed for non-shielded electrodes (Fig. 6.4a) and coaxial electrodes with an outer shield electrode comprising 60% of the inner (recording) electrode height (Fig. 6.4b). Experiments were later performed with bare electrodes and coaxial electrodes having such 60% shielding. For clarification, the simulations were performed with a single edge–to–edge separation and the results are shown in Figures 6.5a–g. In each figure, the top image is a simulation of shielded electrodes, while the bottom image is a simulation of unshielded electrodes. Dark red

represents the region where the electrode would see 95% of the source signal, yellow represents between 60-70% of the signal, while the light blue represents 35–40% of the signal. It is clear, both from the images in Figure 6.4 and the images in Figure 6.5, that bare electrodes experience an overlap in the sensing regions of adjacent electrodes at a distance far greater than shielded electrodes. For separation distances of 50-100 μm and less, the sensing regions of the unshielded electrodes appreciably overlap. This effectively replaces the two individual 20 μm diameter electrodes with one electrode of a larger diameter, representing a loss in pixelation density (and thus a crosstalk-dominated regime). The shielded electrodes continue to show separation of areas sensing 80% of original signal at separation distance down to 10 μm (Fig. 6.5g).

It is important to note that these simulations are scale invariant. That is, if the bare electrodes were made smaller (say 5 μm diameter), the sensing regions would overlap and be dominated by crosstalk at an edge–to–edge distance less than or equal to 2.5 times the diameter of the electrode (corresponding to 12 μm in the example). Therefore, the results of this simulation can give one a sense of the maximum pixelation allowed, given an electrode size, in order to avoid a large amount of crosstalk.

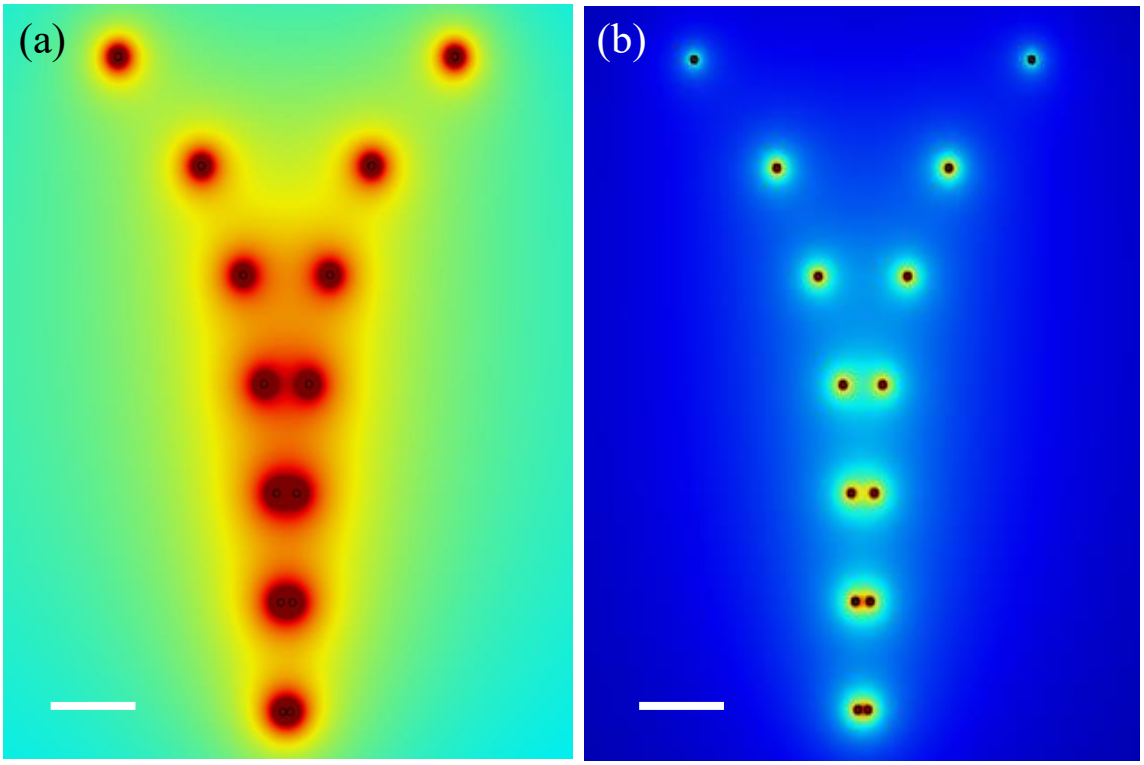

Figure 6.4 FEM modeling of experiment. Top view of equipotential contours for (a) bare electrodes and (b) shielded electrodes with descending pitch. Electrodes biased at 100 µV. First row (at the top of image) is 1 mm edge-to-edge separation while last row is 5 µm separation. Dark red represents areas where >95% of the signal from a source (e.g., action potential/neuron spike) would be seen by the electrode while light blue represents areas where 40% of the signal would be seen. Scale bars in lower left corner are 100 µm.

Figure 6.5a FEM modeling of 1,000 µm separation difference. Shielded (top) electrodes with a shield comprising 60% of the inner electrode height and unshielded (bottom) electrodes were simulated. Dark red represents region where > 95% of the signal will be seen while dark blue represents region where < 35% of the signal will be seen.

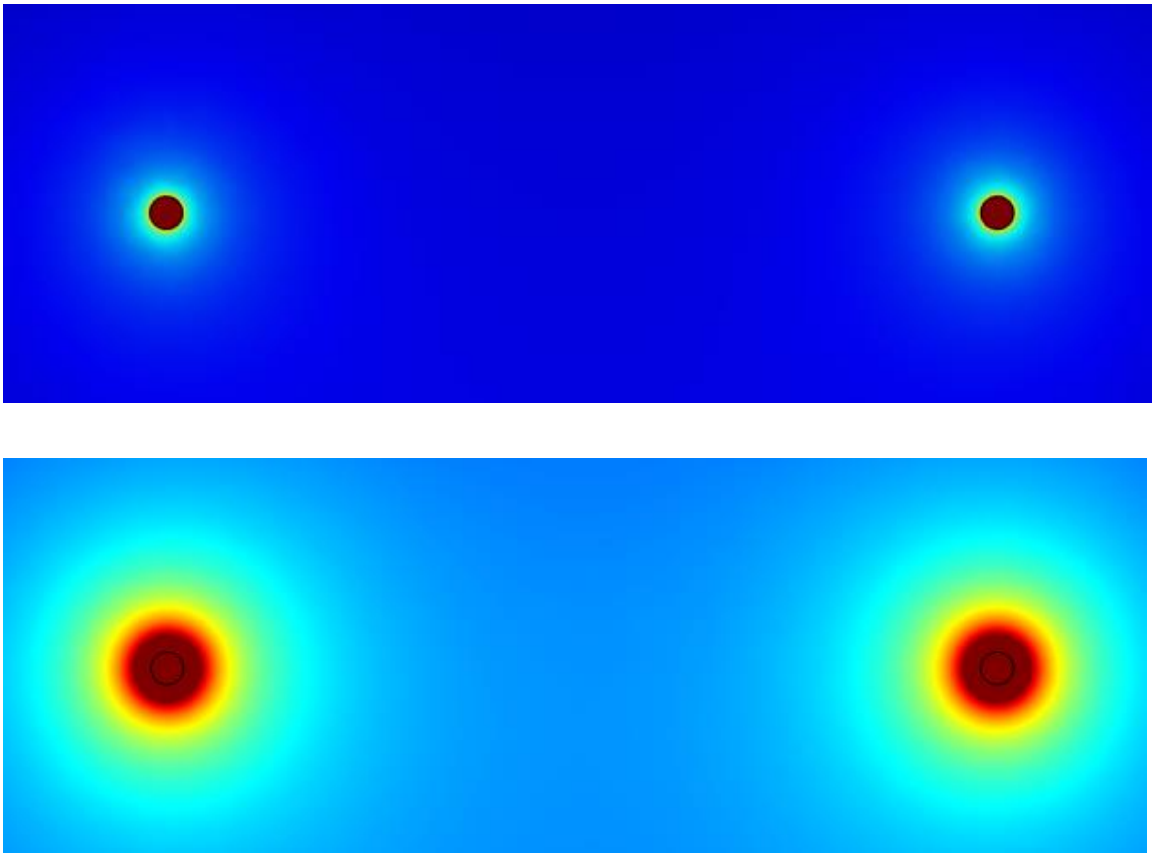

Figure 6.5b FEM modeling of 500 μm separation difference.

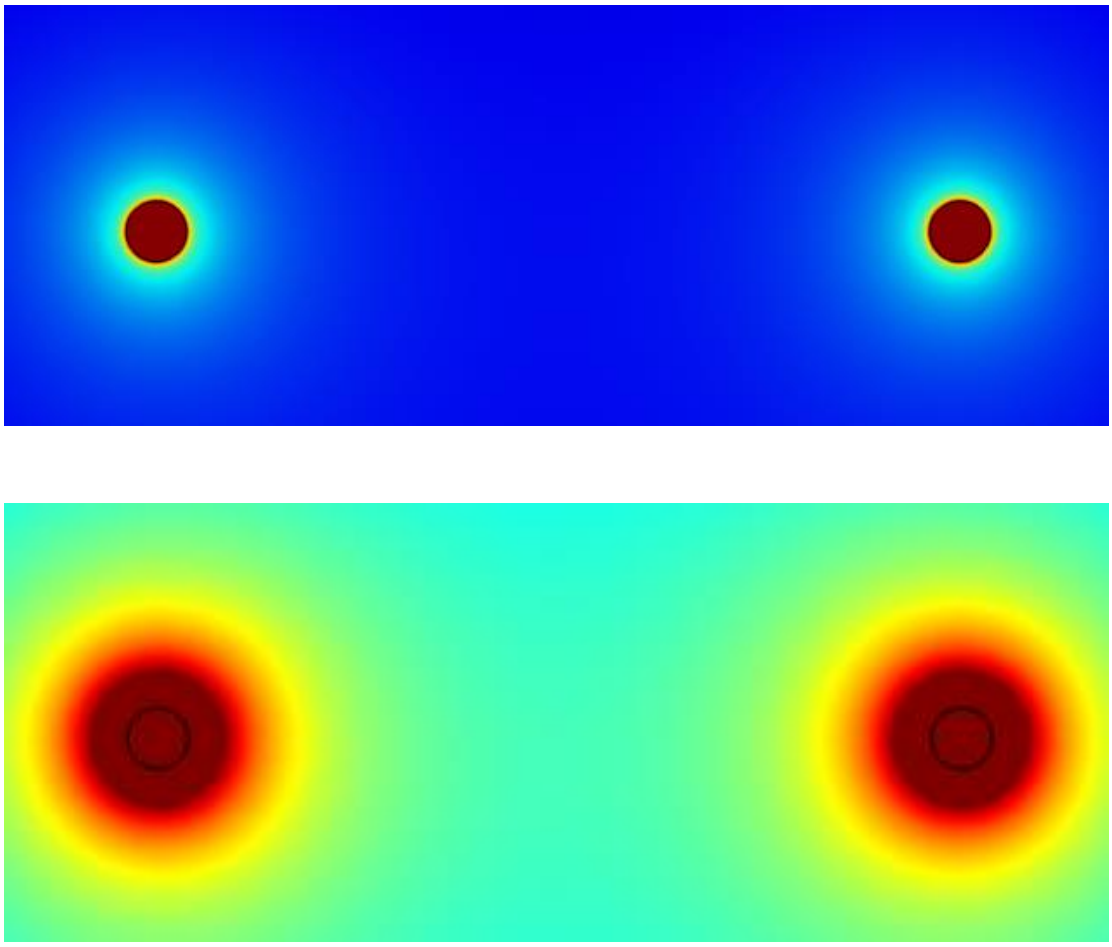

Figure 6.5c FEM modeling of 250 µm separation difference.

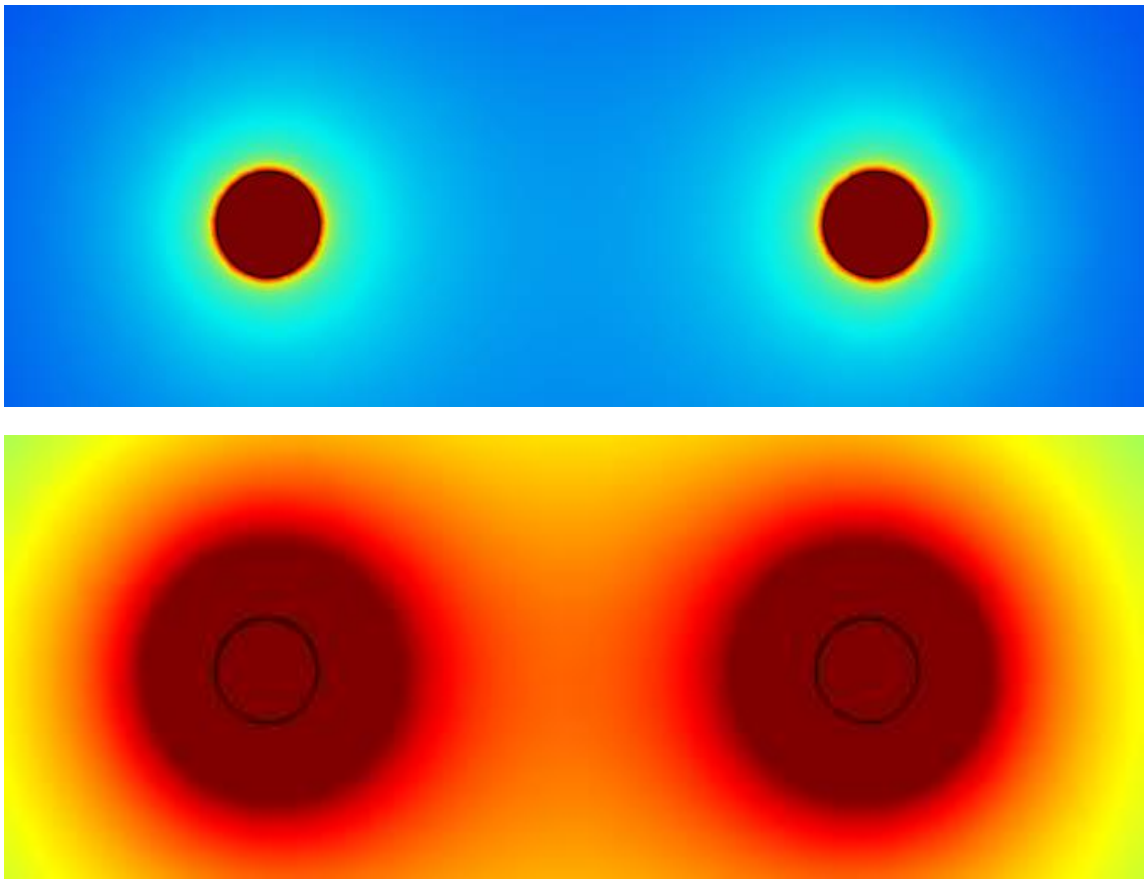

Figure 6.5d FEM modeling of 100 μm separation difference.

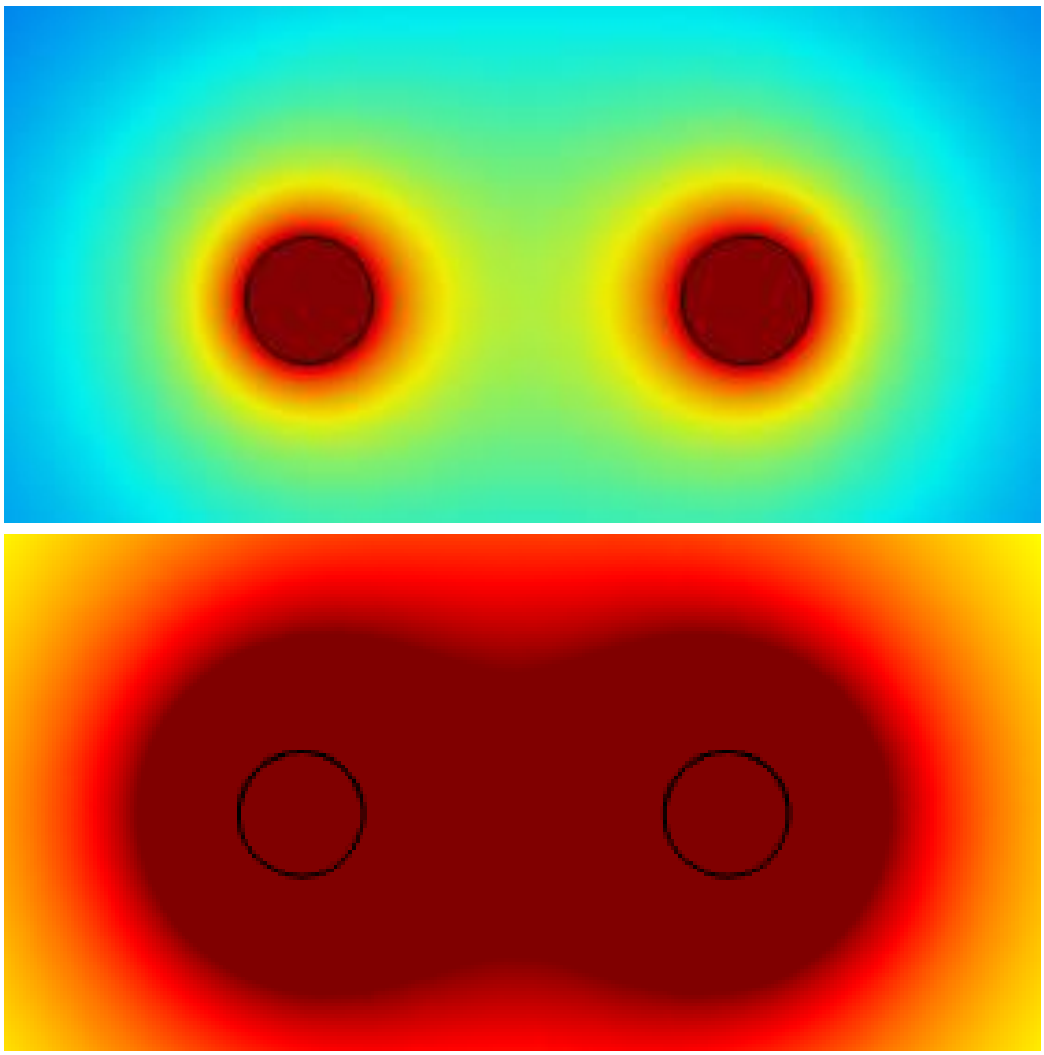

Figure 6.5e FEM modeling of 50 µm separation difference. Overlap in sensing purview of unshielded electrodes can be seen, while there is still separation between the shielded electrodes.

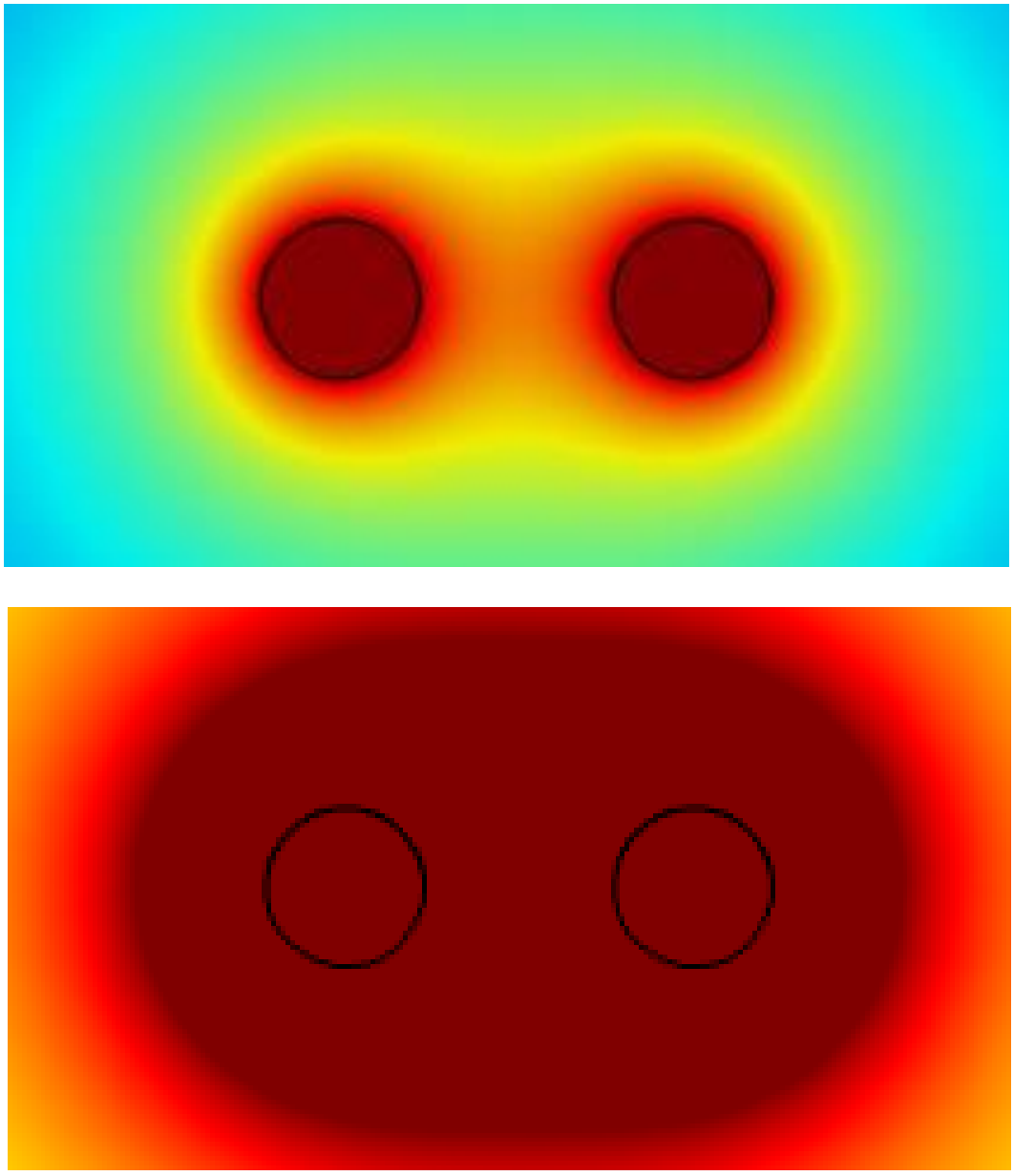

Figure 6.5f FEM modeling of 25 µm separation difference. Due to sensing regions completely overlapping, the unshielded electrodes effectively become 1 larger electrode. Shielded electrodes continue to show separation for greater than 70% of the source signal (yellow region).

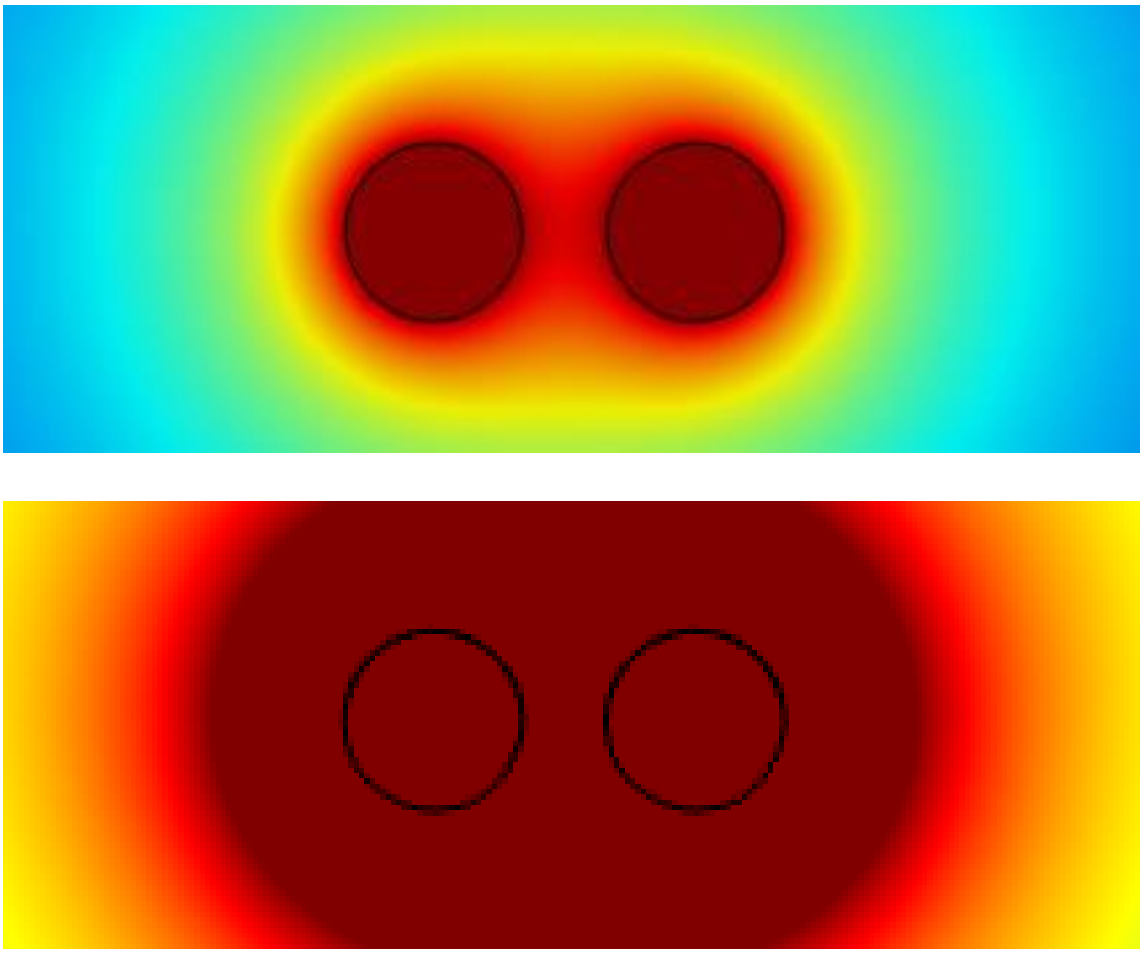

Figure 6.5g FEM modeling of 10 µm separation difference. Shielded electrodes still show discretization for sensing areas capturing 80% or greater of the source.

6.4 Extracellular recording with bare and shielded electrodes: Optical stimulation

Prior to experiment, the cMEA and bMEA regions were characterized by measuring DC resistance (in air) between the individual electrodes for the bare electrode region and between all terminals (inner and outer electrode as well as inter-electrode) for the coaxial region. Typical resistances were in the GΩ range, indicating no shorts in the circuit were present. The capacitance of the coaxial samples was also measured by connecting the sample to a capacitance bridge and the measured value was checked against the calculated value according to the aforementioned equation for a coaxial capacitor: $c = 2\pi l\epsilon/\ln(r_{outer}/r_{inner})$.

The devices needed to be sterilized prior to cell culture. This was done by placing them in a sterilization packet: this expands to let steam pass to its inner contents during the sterilizing process and then contracts during a cooling phase to insulate the inside from any foreign contaminates. The packet was placed inside a steam autoclave and a standard dry process was run (215 F for 30 minutes with a 30-minute cool down phase). After the devices were autoclaved, they were placed inside a sterile hood until the HEK cells were ready to be plated (placed on the devices).

As was discussed in previous chapters, optically-evoked field potentials were detected using HEK-293 transfected with the blue-light sensitive channelrhodopsin protein ChR2(H134R)[27]. The transfection and culture process described in Chapter 4 was unnecessary for this experiment, as we were able to use frozen cell lines from our previous work. After the experiments described in Chapter 4, we continued to grow and

split the HEK cell lines in order to create a stockpile of transfected cells. This is a common practice when there is a long period of time between experiments, as it is more convenient than continually splitting and maintaining a healthy cell line or re-transfecting a new line of HEK cells. Aliquots of frozen HEK293- ChR2 cells were thawed in a warm bath for roughly 10 minutes, spun in a centrifuge at 595 g for 6 min, and then plated in a cell culture dish with DMEM 10% FBS media containing 250 µg/ml G418. The cell growth was slower than previous cultures, but after two weeks of growth, the cells were ready to be plated on the devices.

To ensure cell adherence to the bare electrode and coaxial structures contained in 2 separate PDMS wells, the two devices were incubated in a sterile solution of 0.01% poly-l-lysine overnight at 37 ºC 5% CO2. HEK-ChR2 cells were trypsinized from cell culture dishes and recovered by centrifugation at 595 g for 6 min at 4 ºC. The cells were resuspended in DMEM 10% FBS media containing 250 µg/ml G418 at a density of ~ 10^6 cells/ ml. A 0.1 ml aliquot of cells was added to one well of a coaxial device and cultured overnight at 37 ºC 5% CO2. The seeding density of cells almost completely covered both the bare electrode and coaxial structures within 24-48 hours of subsequent cell culture and adherence. The color of the medium was carefully monitored to ensure cell health. From previous experiments, we noticed that dark yellow meant the medium needed to be changed and that there was cell overgrowth. Since we selected for cells of successful transfection, we wanted the entire pillar region to be covered in HEK293-ChR2 cells to ensure every sensing region was covered and therefore was a potential stimulation zone. Once it was evident there was cell overgrowth (yellow colored media), the old medium was aspirated and replaced with fresh media. Immediately after this, the devices were

completely covered in aluminum foil (as a precautionary measure to avoid prematurely exposing the cells to stimulating light) and the devices were brought to the Multichannel Systems amplifier for measurement. A 473 nm DPSS laser (Model BL473-100FC ADR-700A, Shanghai Laser & Optics Century Co., Ltd.) coupled to a multimode 200 μm diameter optical fiber (0.39 NA, Thor Labs) with a spot size of ~350 μm was used for photo stimulation. Prior to placing the devices in the amplifier system, the laser light was characterized using the same process described in Chapter 4. The maximum intensity was found to be 20 mW/cm^2 and this level was used throughout the experiment.

The bMEA was uncovered, placed in the amplifier system, and the macropads were aligned with the pins. A Ag/Cl pellet was placed into the electrolyte buffer solution to act as a ground, since no other ground was present in the area. The pellet was attached to a wire and the wire was connected to the amplifier ground system. All 60 channels were monitored simultaneously to ensure the baseline voltage reached a steady state for each sensing region. Unfortunately, a number of pins were broken on the amplifier board such that there were 46 working channels out of a possible 60. Initially, the data acquisition program was run continuously and the laser was aligned for topside illumination. The laser was manually actuated and the illumination area was moved throughout the entire sensing region. This was done to ensure a positive response from the cells. Unfortunately, however, these data were not recorded. Once cell response due to optical stimulation was visually confirmed, the laser was adjusted and attached to a micromanipulator for backside illumination. The data acquisition program was changed to a trigger capture program using a TTL signal (Stimulus Generator STG4002, Multichannel Systems) with a 1 s square wave pulse. The laser was then moved to several

sites below the area containing the individual sensing regions and a 5 sweep trial was performed at each spot. All 46 channels were monitored throughout each trial and the approximate laser location was noted prior to stimulation. Throughout the experiment, deflections could be seen in all illuminated working channels. Raw data plots of all 60 channels are shown in Figure 6.6 and overlaid on 60 window schematic representing what is seen during the experiment. The bMEA was measured for about 30 minutes before being replaced with the cMEA.

The cMEA was aligned in the amplifier and channel 15 was set to ground. Again, to ensure we had working cells throughout the array (working: meaning capable of optical actuation) we aligned the laser above the pillar region and illuminated the sample. Once cell viability was confirmed the laser was moved to backside alignment. Just as in the bMEA experiment, the laser was moved to several sites below the array and a 5 sweep trial was performed. For each site, the deflections in the local field appeared to be confined to 4 or less sensing regions. However, the magnitude of the deflections seen by the cMEA was roughly 75% smaller than that of the deflections seen by the bMEA. Raw data traces are shown in Figure 6.7. From the Figure, it appears the waveform of the defection captured by the cMEA is difference from the bMEA. While both the bare electrodes and inner electrodes of the shielded array are capacitively coupled to the signal from the HEK cells, the shielded electrodes have an additional capacitance due to the coaxial structure. This could be the cause of the observed different waveforms between the bMEA and the cMEA.

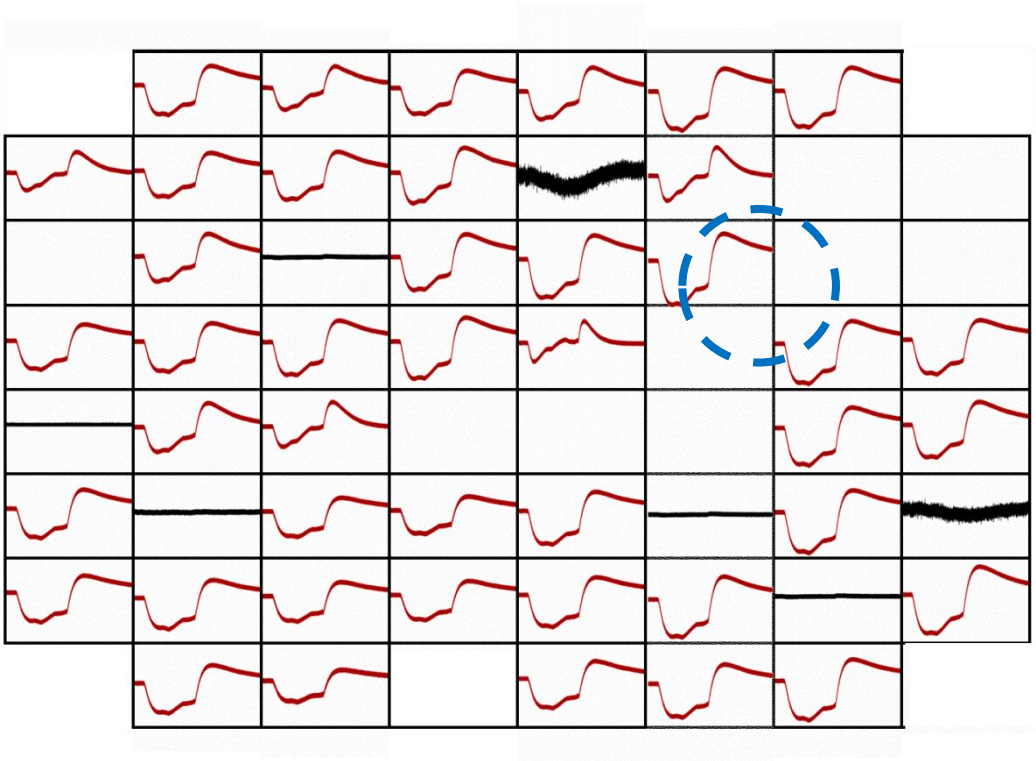

Figure 6.6 Raw data traces of recording with bMEA under backside illumination. The 350 μm-diameter nominal illuminated area is indicated. Blank windows represent non-working electrodes (due to pin on amplifier malfunctioning). Black lines represent background noise (lack of deflection). The red deflections show captured signal.

In order to quantitatively compare the two devices, the data were collected and the trials for each experiment were averaged. The electrode that recorded the largest deflection was designated as the point of origin for the signal and its voltage was called V_{max}. The distance of the surrounded electrodes was calculated and a variation of the crosstalk coefficient discussed above was extracted for each electrode: $CT^* = |V|/|V_{max}|$, where CT^* is the new effective crosstalk coefficient and $|V|$ is the signal of a particular sensing region. Like the CT discussed in the introduction, a large CT^* corresponds to high crosstalk, since the sensing region is capturing a large portion of the source. The effective crosstalk was calculated for both the bMEA (red data) and the cMEA (black data) devices and plotted in Figure 6.8. The red and black dashed lines are guides to the eye. From the figure, one can see the effective crosstalk coefficient for the shielded electrodes is lower than that of the bare electrode for all distances from the source. This corresponds to better suppression or filtering of the stray electric fields from sources far from the recording device. In the bare electrodes device, sensing regions within 100 μm of the signal still show a CT^* of roughly 0.9, which corresponds to a large amount of crosstalk. This experiment shows the virtue of crosstalk suppression by local shielding through using a coaxial architecture.

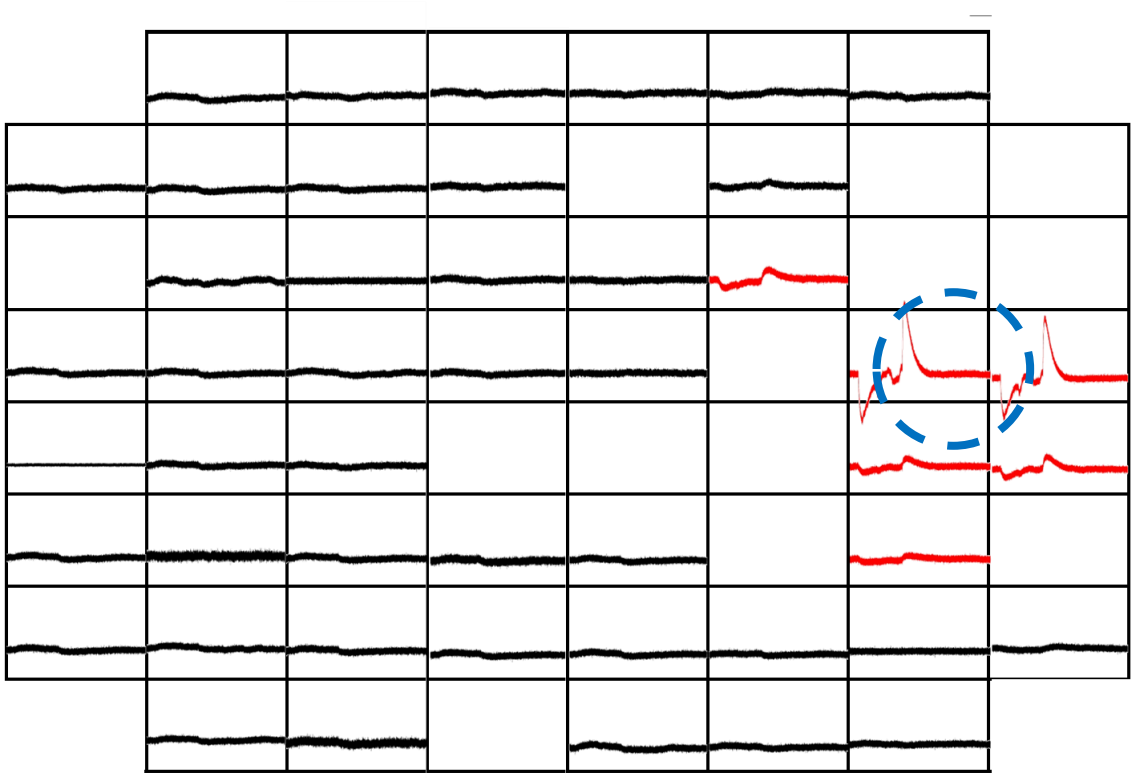

Figure 6.7 Raw data traces of recording with cMEA under backside illumination. The 350 μm-diameter nominal illuminated area is indicated. Blank windows represent non-working electrodes (due to pin on amplifier malfunctioning). Black lines represent background noise (lack of deflection). The red deflections show captured signal.

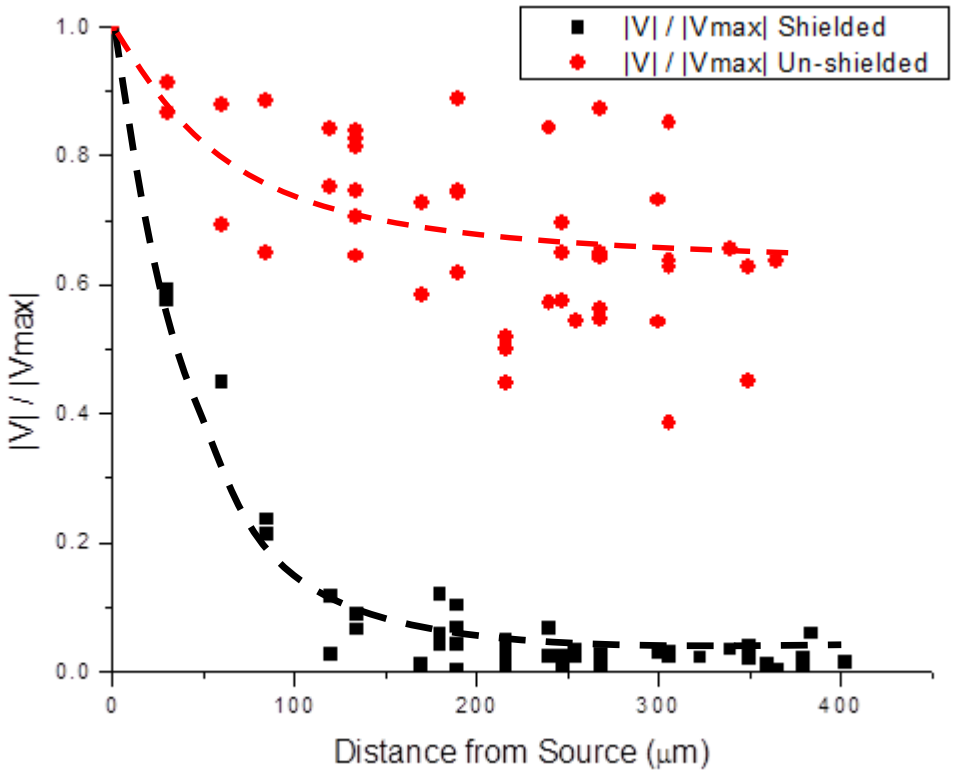

Figure 6.8 Comparison of bMEA and cMEA in optical stimulation experiments. Crosstalk coefficient (V/V_{max}) vs. distance from the source shows the shielded electrodes have a faster fall off (and thus crosstalk suppression) than the bare electrodes.

6.5 Extracellular recording with bare and shielded electrodes: Electrical stimulation

Prior to experiment, the cMEA and bMEA regions were again characterized as mentioned above. Since no biological media were to be grown on these samples, it was not necessary to sterilize the devices. However, they were sterilized anyway as this gave us the opportunity to see if there was any degradation in the devices after being in the autoclave. This test wasn't possible with the previous samples (those used in biological studies), as remeasuring the electrical properties of the device could introduce contamination. No significant differences were noticed upon remeasuring the devices. The samples were properly aligned in the pre-amplifier system and the wells were filled with an electrolyte buffer solution using a pipette.

For the bMEA region, a Ag/Cl pellet was once again placed into the electrolyte buffer solution to act as a ground, since no other ground was present in the area. A pulse generator program was used to send in a train of 500 μV square-wave pulses spaced 1s apart. Starting with the 1 mm edge–to–edge separation row and moving incrementally to the 5 μm separation row, the signal was sent to the left electrode, while the rest of electrodes were left as recording regions. All sensing regions (both cMEA and bMEA) were viewed on screen and the pulses appeared in the bMEA region only (as expected). The experiment was repeated using the right electrode of a particular row as the stimulating electrode, to ensure mirror symmetry.

The cMEA region was filled with the same electrolyte buffer solution and the appropriate (meaning the one intended by design) electrode was set to ground. The same

procedure was performed (first sending the signal to electrodes on the left followed by the right, to confirm symmetry). It was obvious from the window traces that the magnitude of the signal recorded was lower than that of the bMEA. Once all the rows were stimulated the data were collected and averaged. Figure 6.9 shows the CT^* value versus edge−to−edge separation (distance from the source) for the electrical stimulation experiment. The red circles are the data from the unshielded sample, the black squares are the data from the shielded sample, and the dashed lines are guides to the eye. Again, we see a much sharper fall off in the signal for the cMEA. Conversely, the unshielded sample stays at the upper end of the crosstalk coefficient range until we are 250 μm from the source. It is important to note that in calculating the CT^* value we are normalizing to a maximum value of 1. However, it is incorrect to assume that the real magnitude (non-normalized) of the recorded signals for the bMEA and cMEA are the same as in fact they were not (the cMEA recorded signals 50-90% lower than the bMEA). The difference in the real magnitude of the signal measured by cMEA devices could be attributed defects in the inner electrode or an error in the dielectric etching step (which would lead to less inner electrode surface area).

By combining the data from both the optical stimulation and electrical stimulation experiments (Figure 6.10) we see a common trend. For both the optical and electrical excitation experiments the cMEA outperforms bare electrodes in reducing crosstalk. The signal fall-off for shielded electrodes is almost immediate while for unshielded electrodes it is gradual. From this we can conclude that in order to avoid signal overlap in high density multielectrode arrays, a shielded (coaxial) architecture should be utilized.

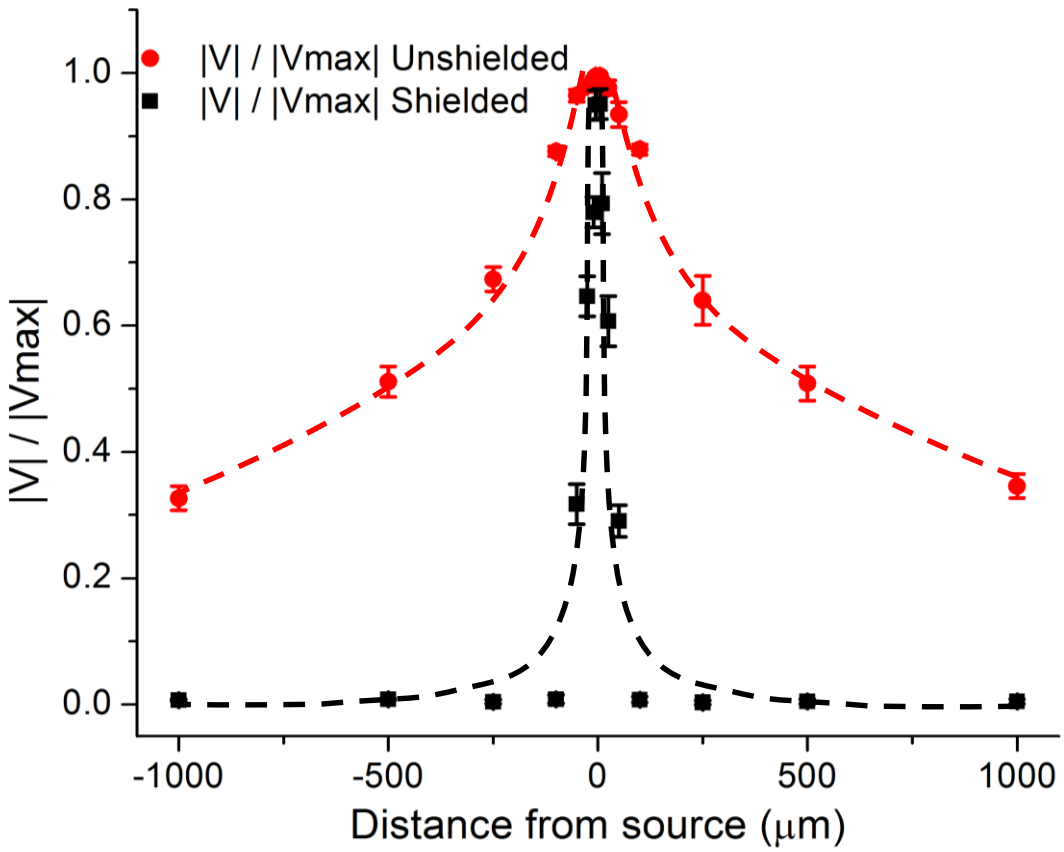

Figure 6.9 Effective crosstalk coefficient vs. distance from source. Data from 5 experiments were averaged and plotted above. Red circle data points are from the unshielded (bMEA) sample. Black square data points are from the coaxial (cMEA) sample. Bars extending from data points are the calculated standard deviation. Dashed lines represent guides to the eye.

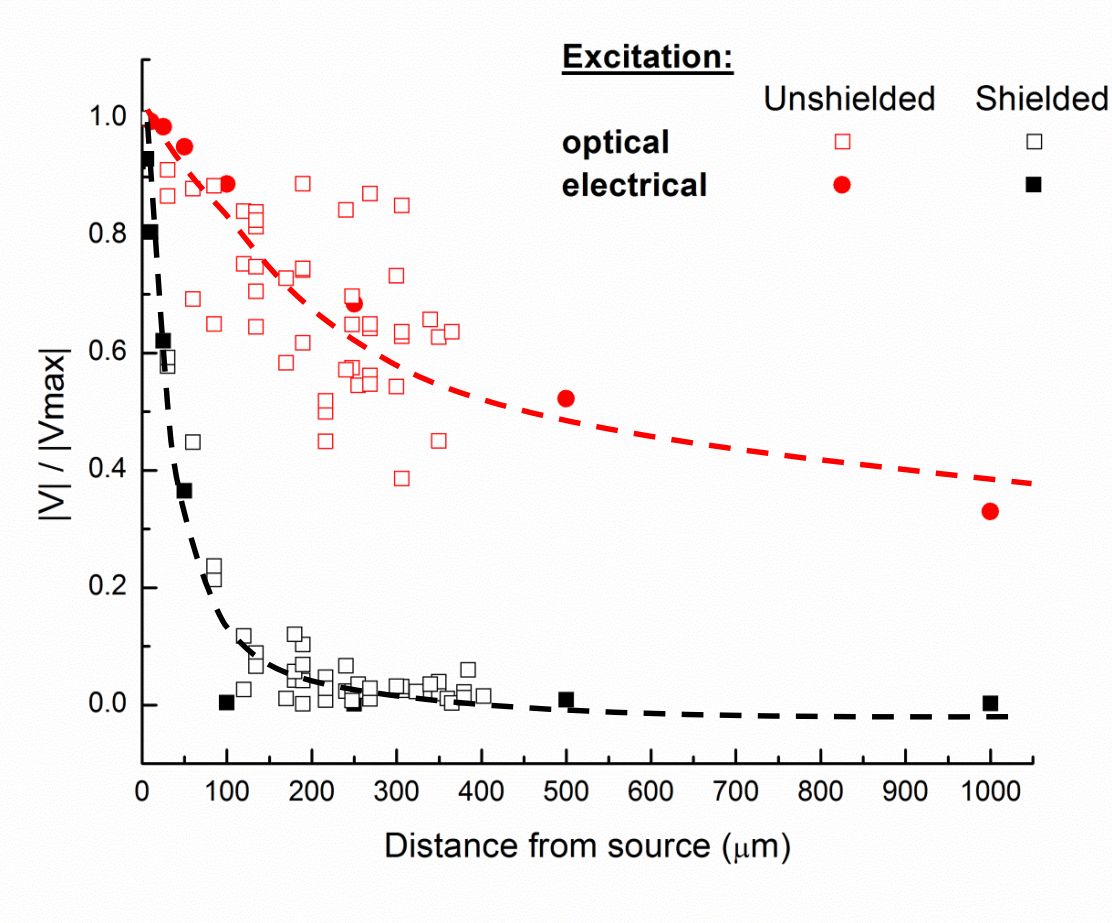

Figure 6.10 Comparison of both excitation types. Crosstalk coefficient vs distance from the source for the optical and electrical excitation experiments are compared for both the bMEA (unshielded) and cMEA (shielded) devices. The bMEA data are in black while the cMEA data are in red.

6.6 Summary

In this Chapter we compared the ability of shielded and non-shielded electrodes to reduce crosstalk in a neurophysiological environment. Both simulations and data from experiments show the sensing region of a locally shielded electrode falls off (as a function of space) faster than a bare electrode, thereby resulting in a lower *CT** value. There was a slight difference between the simulation and the experimental data, as the simulations showed a lower *CT** value than the data from experiments. This could be due to the possibility of the simulation and the experiments measuring the potential at different distances above the electrodes. We were unable to measure the distance between the transfected HEK cell line and the core electrode for the optical stimulation. Also, it is possible the shield height of the devices was lower than that shield height of the model used in the simulations. Despite this difference, qualitatively the results unambiguously show that locally shielded electrodes reduce electrical crosstalk.

6.7 References

[1] Nadasdy, Z., Csicsvari, J., Penttonen, M., Hetke, J., Wise, K., & Buzsaki, G. Extracellular recording and analysis of neuronal activity: from single cells to ensembles. In: Neuronal Ensembles: Strategies for Recording and Decoding, edited by Eichenbaum H.B. & Davis J.L. New York: Wiley-Liss, pp. 17–55 (1998).

[2] Hilke, R. G. H., Moghadam, G. K., Lovell, Suaning, G. J., Electric crosstalk impairs spatial resolution of multi-electrode arrays in retinal implants. J. Neural Eng. **8**, 046016-27 (2011)

[3] Rey, H. G., Pedreira, C., & Quiroga, R. Q. Past, present and future of spike sorting techniques. Brain Research Bulletin **119**, 106-117 (2015).

[4] Quiroga, R. Q. What is the real shape of extracellular spikes?,. J. Neurosci. Meth. **177**, 194-198 (2009).

[5] Pouzat, C., Mazor, O., & Laurent, G. Using noise signature to optimize spike-sorting and to assess neuronal classification quality. J. Neurosci. Meth. **122**, 43-57 (2002).

[6] Gibson, S., Judy, J. W., & Markovic, D. Comparison of spike-sorting algorithms for future hardware implementation. In Engineering in Medicine and Biology Society, EMBS 2008. 30th Annual International Conference of the IEEE (pp. 5015-5020) (2008).

[7] Quiroga, R. Q., Nadasdy, Z., & Ben-Shaul, Y. Unsupervised spike detection and sorting with wavelets and superparamagnetic clustering. Neural Comp. **16**, 1661-1687 (2004).

[8] Vargas-Irwin, C., & Donoghue, J. P. Automated spike sorting using density grid contour clustering and subtractive waveform decomposition. J. Neurosci. Meth. **164**, 1-18 (2007).

[9] Rebrik, S. P., Wright, B. D., Emondi, A. A., & Miller, K. D. Cross-channel correlations in tetrode recordings: implications for spike-sorting. Neurocomputing **26**, 1033-1038 (1999).

[10] Lewicki, M. S. A review of methods for spike sorting: the detection and classification of neural action potentials. Network: Computation in Neural Systems **9**, R53-R78 (1998).

[11] Gerstein, G. L., & Clark, W. A. Simultaneous studies of firing patterns in several neurons. Science **143**, 1325-1327 (1964).

[12] Quiroga, R. Q., Reddy, L., Koch, C., & Fried, I. Decoding visual inputs from multiple neurons in the human temporal lobe. J. Neurophysiology **98**, 1997-2007 (2007).

[13] Harris, K. D., Henze, D. A., Csicsvari, J., Hirase, H., & Buzsáki, G. Accuracy of tetrode spike separation as determined by simultaneous intracellular and extracellular measurements. J. Neurophysiology **84**, 401-414 (2000)..

[14] Shoham, S., Fellows, M. R., & Normann, R. A. Robust, automatic spike sorting using mixtures of multivariate t-distributions. J. Neurosci. Meth. **127**, 111-122 (2003).

[15] Person, K. On Lines and Planes of Closest Fit to System of Points in Space. Phil. Mag. **2**, 559-572. (1901).

[16] Quiroga, R. Q. Spike sorting. Scholarpedia **2**, 3583 (2007).

[17] Pedreira, C., Martinez, J., Ison, M. J., & Quiroga, R. Q. How many neurons can we see with current spike sorting algorithms?. J. of Neurosci. Meth. **211**, 58-65 (2012).

[18] Ekanadham, C., Tranchina, D., & Simoncelli, E. P. A unified framework and method for automatic neural spike identification. J. Neurosci. Meth. **222**, 47-55 (2014).

[19] Kadir, S. N., Goodman, D. F., & Harris, K. D. High-dimensional cluster analysis with the masked EM algorithm. Neural Comp. **26**, 2379-2394 (2014).

[20] Swindale, N. V., & Spacek, M. A. Spike sorting for polytrodes: a divide and conquer approach. Front. Syst. Neurosci. **8**, 6 (2014).

[21] Einevoll, G. T., Franke, F., Hagen, E., Pouzat, C., & Harris, K. D. Towards reliable spike-train recordings from thousands of neurons with multielectrodes. Curr. Op. Neurobio. **22**, 11-17 (2012).

[22] Wong, Y. T., Chen, S. C., Seo, J. M., Morley, J. W., Lovell, N. H., & Suaning, G. J. Focal activation of the feline retina via a suprachoroidal electrode array. Vision Res. **49**, 825-833 (2009).

[23] Chai, X., Li, L., Wu, K., Zhou, C., Cao, P., & Ren, Q. C-sight visual prostheses for the blind. IEEE Engineering in Medicine and Biology Magazine **27**, 20-28 (2008).

[24] Moghaddam, G. K., Wilke, R. G., Dokos, S., Suaning, G. J., & Lovell, N. H. Electrode design to optimize ganglion cell activation in a retinal neuroprosthesis: A modeling study. In Neural Engineering (NER), 2011 5th International IEEE/EMBS Conference, 542-545. (2011, April).

[25] Rizal, B., Archibald, M.M., Connolly, T., Shepard, S., Burns, M.J., Chiles, T.C. & Naughton, M.J. Nanocoax-based electrochemical sensor. Anal. Chem. **85**, 10040-10044 (2013).

[26] Lorentz H.A., het theorema van Poynting over energie in het electromagnetisch veld eneen paar algemeene stellingen over de voorplanting van het licht, *Vers. Konig. Akad. Wetensch*. **4**, 176, (1896).

[27] Zhang, F., Wang, L.P., Brauner, M., Liewald, J.F., Kay, K., Watzke, N., *et al.* Multimodal fast optical interrogation of neural circuitry. Nature **446**, 633-639 (2007).

Chapter 7: Conclusions and Future Work

7.1 Summary

From the outset, the goal of the research described in this dissertation has been the development and characterization of a shielded electrode architecture that can both reduce crosstalk and integrate an optical element. Along the way, we were able to provide proof-of-concept for use of the device in conventional extracellular recording and optogenetic studies, as well as provide the first, to our knowledge, the first study of plasmonic behavior in 3D systems for the visible-NIR spectrum. In this chapter, we will review the work discussed in the previous chapters, while adding context by comparing our device to current state-of-the-art multielectrode array technology. Additionally, we will propose some directions for continuing the research contained within this thesis.

From the data shown in Chapter 3, we can reasonably conclude the cNEA's success in being implemented as an extracellular sensing device containing nanoscale elements. However, while the device contains nanoscale elements, the sensing area or pixel size was still on the microscale level (25 μm diameter) and therefore calling the device a "nano"-electrode array maybe a slight exaggeration. This subtle distinction also applies to the "nanoscale" devices[1,2,3] discussed in Chapter 2, as those devices are comprised of nanoscale elements within a microscale sensing area. More importantly, the goal of moving multielectrode array technology to the nanoscale is to improve spatial resolution by increasing the electrode density. Therefore, the figure of merit for ultra-high resolution is not necessarily electrode dimensions, but more specifically, the inter-electrode spacing. Future work should include bringing the sensing area down to the nanoscale level (i.e. recording from a single nanocoax) as well as fabricating ultra-high

density arrays by minimizing electrode pitch. Current state-of-the-art packing for a fixed wire array is exhibited by the Multichannel Systems MCS GmbH 256MEA-30 which contains 256 electrodes at 30 μm spacing. Packing large numbers of electrodes (i.e. greater than 256) into a spacing smaller than this becomes problematic for fixed wire arrays without multiplexing capabilities, as they are limited by the interconnection distance as well as the number of pads able to fit along the perimeter of the chip. Presently[4,5,6], there are CMOS-based arrays with multiplexing capabilities, as well as active circuitry, that contain much higher electrode numbers and densities (4096-26,400 electrodes in a 5-10 mm^2 area). In its current state, the multielectrode array technology described in this thesis is a fixed wire array. Therefore, in order to compete with the packing densities of CMOS arrays, a multiplexing component should be integrated with the cNEA. However, the goal of future research work involving the cNEA should not be to match all aspects of every MEA technology (an impossible task), but rather to categorically (electrode density, SNR, etc.) improve the cNEA to what is physically possible. Given the cross-sectional size of an individual neuron and computing power required for recording, there will be a diminishing return for pushing the inter-electrode density beyond a given point that, in this author's opinion, the cNEA is capable of reaching.

Another interesting experiment that was briefly touched on, but should be explored more thoroughly, is the use of the extended core nanocoaxial structure along with the electroporation technique for simultaneous intra- and extracellular recording. One suggestion to aid in the success of this experiment would be to use taller pillars and lower the outer metal so as to facilitate engulfment of and/or protrusion into the cell. 3D

structured electrodes such as Au mushrooms[7], vertical nanowires[1], and hollow nanopillars[3], have shown the ability to record subthreshold signals and, coupled with electroporation, intracellular activity by penetrating the cell membrane. However, the coaxial structure's unique shielding capability could potentially lead to recording an intracellular signal with one electrode and subsequent distinct field potentials with neighboring electrodes. This would distinguish the coaxial multielectrode array from results published in the aforementioned studies.

In Chapter 4, we provided data showing the use of the cMEA as an extracellular sensor in optogenetic studies. One improvement that should be explored is removing the external aspect of the light source. Figure 7.1 shows the fabrication of a microscale coaxial array onto an OLED board. This was accomplished using the same NIL + deposition processes described in Chapter 4 with one exception: the maximum temperature used in the NIL process was 150 C and the dielectric was sputtered onto the device rather than ALD (due to the required substrate temperature of the ALD having a minimum of 180 C). These changes were to ensure the OLED would survive the fabrication process. From the Figure, one can see light propagating through the cores of the individual coaxes in the array. The size of the individual elements in the OLED were too large (tens of microns) to match a high density multielectrode array, so a different board will have to be used. Also, the architecture of the Multichannel Systems amplifier and data acquisition system should be considered when selecting the LED board. The ultimate version of the cMEA or cNEA would be built on top of a matching illumination element array, where a single pixel is capable of optical and electrical stimulation and recording. While integrating an optical element with MEA technology is not unique

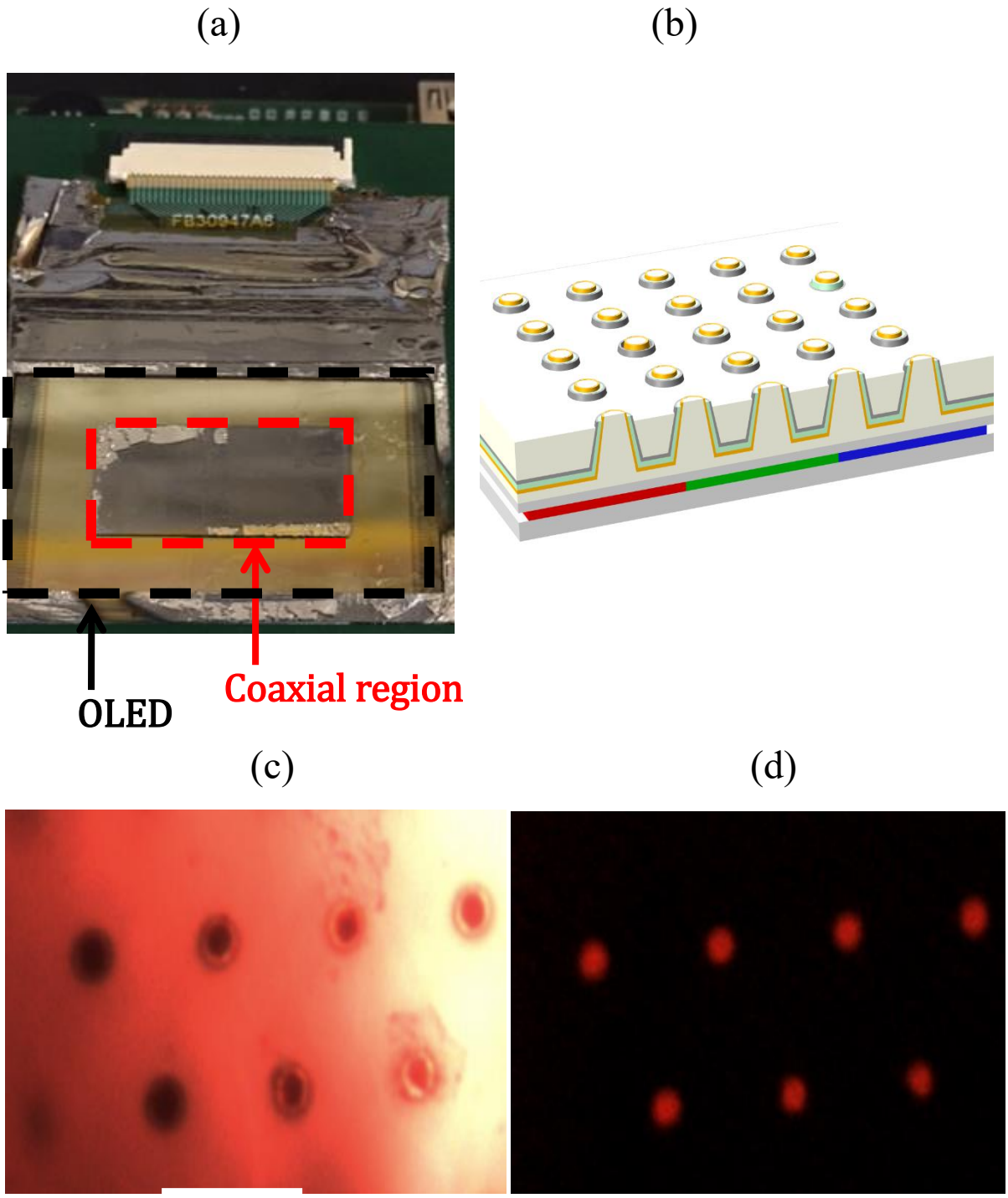

Figure 7.1 Coaxial array fabricated on OLED. (a) An array of microscale decapitated coaxes were fabricated on an OLED board (b) Schematic showing a unit cell of coax array on OLED (not to scale, coax pitch was 1.1 μm while each LED component was 15 μm). (c) Magnified image of coaxial region with topside illumination. White scale bar: 10 μm. (d) Topside illumination was turned off and the OLED was turned on. Light can be seen propagating through the cores of coaxes seen in (c).

(examples have been discussed in Chapter 2), presently, there do not exist arrays where each individual electrode contains an optical component. Other than using an external focusing mechanism coupled with an external light source (lenses or holographic focusing, for example[8]), only the cMEA and MEAs with an architecture similar to the hollow nanopillar array (see ref. 3) are capable of implementing an internal optical element, where the light source is confined locally to individual recording electrodes and thus, individual cells/neurons. Accomplishing this would make the cMEA the first of its kind: a large-scale recording device with built-in, individually addressable (e.g. optrode specific) optical and electrical modulation. A microscale optrode array would be a significant advancement in MEA technology.

Other future work should include fabricating high density arrays ($\leq$10 μm pitch) as well as larger arrays ($>$ 60 sensing elements). The latter of the two will require a different amplifier system as our current system can measure a maximum of 60 elements. Finally, different cell types should be explored and cultured onto the device to study the coax–cell interface. It would be interesting to culture cells onto sharp core electrodes to see if cell-engulfment of the core electrode would occur. This could facilitate access to the intracellular medium of the cell, thus allowing perturbation of the membrane potential, as alluded to earlier.

Chapter 5 provided the optical characterization of the cylindrical core electrode with respect to the visible–NIR spectrum. Plasmonic behavior could be seen at long wavelengths for the subwavelength diameter cylinders, leading the higher transmittance values than that predicted by Bethe diffraction theory. While the cylinder height and diameter were varied and studied in this Chapter, we did not include any studies with a

different pitch (all samples had a 10 μm pitch). Future work should include arrays with both larger and smaller pitch. To start, samples with an array pitch convincingly larger than the plasmon propagation length should be made. This should maximize the contribution of plasmonic modes to the far-field transmittance because the effective diameters of the holes in the array, a measure of the boundary within which plasmons can propagate through the core and into the far-field, would be non-overlapping. Therefore, making the array pitch larger than the plasmon propagation length ensures the holes are non-interacting. Conversely, it would also be interesting to see what happens when the pitch is smaller than the effective diameter calculated in Chapter 5 (4.2 μm). In this regime there should be a collective effect from the array (due to the overlapping diameters). Also, with extreme patience and effort, one could push deeper into the subwavelength regime (thinner diameters). An important experiment that should be redone with a smaller, circular aperture is the measurement taken to find the size of the collection region. The most profitable experiment would be one that maximizes the number of data points taken within the collection region and therefore attempts to fully map the 2D plane of the collection region (rather than only obtaining data points from the central axis and a line 60 μm off the central axis, as was shown and discussed in Chapter 5). In addition to calculating the true size of the collection region, data from such an experiment would allow one to visualize the spatial dependence of the intensity, as well as account for wavelength dependence or degree of chromatic aberration throughout the collection region. These data could then be used to calculate the normalized transmittance of the sample.

Future work should also include exploring the transmittance of the cylinders in the context of optogenetic applications. A logical conclusion from the plasmonic studies discussed in Chapter 5 is that optical power can still be delivered to the far-field despite having a sub-wavelength aperture. Therefore, it is possible to utilize nanoscale elements as "plasmon enhanced" optrodes in optogenetic studies. It is important to note that a 3D structure is not a requirement for plasmonic optrode technology, as one can imagine altering a conventional 2D MEA to include an aperture. While future studies may yield additional constraints to consider, currently the critical parameters include: metal-type (plasma frequency in particular), aperture diameter, pitch (according to 2D studies) and height (for 3D structures). Using data obtained from studies like those in Chapter 5, these parameters could be appropriately tailored to fabricate a nanoscale optrode array that is highly transmitting for a wavelength specific to a particular opsin. Furthermore, in addition to the enhancement in modes radiating to the far-field, there are evanescent modes (surface plasmons) which cause an enhancement of the local electric field intensity. As discussed in Chapter 2, cultured cells typically have a cell-electrode distance on the order of 100 nm and therefore will be located well within the region where there is an enhanced *E*-field intensity due to the surface plasmon. An enhanced *E*-field intensity implies that, with a plasmonic material, one could use a lower input power than that which would have to be used with a non-plasmonic material, as the plasmonic behavior would facilitate an enhanced output power being delivered to the cells. Therefore, some key questions still to be answered are: Does the plasmonic behavior facilitate a lower input power requirement to illicit a response in the cells (as predicted) than what is used in typical studies? If so, to what degree (if any) does this mitigate toxic thermal effects

caused by the light source? Finally, if it is possible to change the settings on the Leica microscope to match the optical power of an LED array, the experiments in Chapter 5 should be repeated with both the cMEA and cNEA.

In Chapter 6, we compared shielded and unshielded electrodes in order to measure the effect local shielding had on electrical crosstalk. From the data, one can see that local shielding indeed significantly suppresses crosstalk. Future work should include relating the crosstalk coefficient (*CT**) to spike-sorting algorithms and correlating *CT** to the accuracy of spike-sorting. In this way one could find the maximum allowable crosstalk for identifying unique signals. Currently, a large portion of electrophysiology research addresses the problem of neuron identification by creating automated spike sorting methods[9,10,11]. However, crosstalk (overlapping spikes) remains problematic and a highly reliable solution has been elusive[12]. The non-coaxial nanoscale arrays mentioned earlier, while able to increase electrode density, do not address the problem of crosstalk, regardless of electrode density. The problem of crosstalk is uniquely addressed by having a local shield, which is best facilitated by the coaxial architecture. While the local shield won't necessarily eliminate the need for spike sorting algorithms, it could substantially alleviate the heavy burden they now carry.

As mentioned earlier, other future work should include growing cells on high density arrays. One experiment to measure crosstalk in an optogenetic study would be fabricating a high density circular array with a single aperture underneath the central sensing element (similar to the devices with an opaque substrate mentioned in this Chapter), and using backside illumination to invoke a cellular response. Also, further comparisons to conventional MEA technology should be explored. One study could

involve using a bMEA and a cMEA in parallel to measure field potentials originating from hippocampal slices. Or another comparison study could include culturing a different cell type than HEK293 (*i.e.* cardiomyocytes) onto both the bMEA and cMEA. Given the typical magnitude of the action potential (mV scale) from a cardiomyocyte, this would really test the ability of local shielding to suppress crosstalk. Furthermore, improvements in fabrication could be made. Better control over the shield height would be highly valuable.

The work presented in this thesis was done with the intention of developing a multielectrode array technology that utilizes local shielding through the coaxial architecture. The data presented here show the effect of this architecture on mitigating crosstalk as well as the facilitation of an optical component to MEAs. This work thus represents a step toward improving conventional MEA technology.

7.2 References

[1] Robinson, J. T., Jorgolli, M., Shalek, A. K., Yoon, M. H., Gertner, R. S., & Park, H. Vertical nanowire electrode arrays as a scalable platform for intracellular interfacing to neuronal circuits. Nat. Nanotechnol. **7**, 180-184 (2012).

[2] Duan, X., Gao, R., Xie, P., Cohen-Karni, T., Qing, Q., Choe, H.S., et al. Intracellular recordings of action potentials by an extracellular nanoscale field-effect transistor. Nat. Nanotechnol. **7**, 174-179 (2012).

[3] Xie, C., Lin, Z., Hanson, L., Cui, Y., & Cui, B. Intracellular recording of action potentials by nanopillar electroporation. Nat. Nanotechnol. **7**, 185-190 (2012).

[4] Bakkum, D. J., Frey, U., Radivojevic, M., Russell, T.L., Müller, J., Fiscella, et al. Tracking axonal action potential propagation on a high-density microelectrode array across hundreds of sites. Nat. Commun. **4**, 2181 (2013).

[5] Ballini, M., Muller, J., Livi, P., Chen, Y., Frey, U., Stettler, A., et al. A 1024-Channel CMOS microelectrode array with 26,400 electrodes for recording and stimulation of electrogenic cells in vitro. IEEE J. Solid-State Circuits. **49**, 2705-2719 (2014).

[6] Frey, U., Heer, F., Pedron, R., Ballini, M., Müeller, J., Bakkum, D., et al. Switch-matrix-based high-density microelectrode array in CMOS technology. IEEE J. Solid-State Circuits **45**, 467-482 (2010).

[7] Hai, A., Dormann, A., Shappir, J., Yitzchaik, S., Bartic, C., Borghs, et al. Spine-shaped gold protrusions improve the adherence and electrical coupling of neurons with the surface of micro-electronic devices. J. R. Soc. Interface **6**, 1153-1165 (2009).

[8] Shemesh, O. A., Tanese, D., Zampini, V., Changyang, L., Piatkevich, K., Ronzitti, E., Boyden, E.S. Temporally precise single-cell-resolution optogenetics. Nat. Neur. **20**, 1796-1806 (2017)

[9] Knieling, S., Sridharan, K. S., Belardinelli, P., Naros, G., Weiss, D., Mormann, F., & Gharabaghi, A. An Unsupervised Online Spike-Sorting Framework. Int. J. of Neur. Syst. **26**, 1550042 (2016).

[10] Chung, Jason E., et al. A fully automated approach to spike sorting. Neuron **95**, 1381-1394 (2017).

[11] Hilgen, Gerrit, et al. Unsupervised spike sorting for large-scale, high-density multielectrode arrays. Cell Rep. **18**, 2521-2532 (2017).

[12] Pedreira, Carlos, et al. How many neurons can we see with current spike sorting algorithms?. J. of Neurosci Meth. **211**, 58-65 (2012).

Appendix A: Extended Core Coax Process

A.1 Summary

Over the past several decades, photolithography has become a ubiquitous step in the fabrication process for electronic devices due its key role in scaling up production and augmenting the packing density of individual electronic components[1]. Generally, photolithography (Figure A.1) is a process used to pattern a wide variety of features onto a substrate through the use of 3 components: An optical source (typically a UV source), a mask containing a pattern, and a photosensitive polymer (called a photoresist), in conjunction with etching and deposition processes. Given its repeatability, this process can be used to generate complex layered structures such as those contained in MEMS devices and the devices described throughout this thesis. Due to non-uniformity and inconsistency of the chemical mechanical polishing process, we became sufficiently motivated to develop an alternative method for exposing the core electrode within the vertical coaxial structures (a key step in our fabrication process). This resulted in our inventing a method for lowering the dielectric and outer metal layers of the coaxial structure, thereby "extending" the core electrode, using photolithography and selective wet chemical etching. After numerous iterations and refinements, the fabrication process, referred to as the extended core coax (ECC), was standardized, leading to high fidelity for both the cMEA and cNEA architectures. This Appendix contains a description of the process and a high level overview of the theory behind it.

Upon absorbing UV radiation transmitted through the aperture or pattern of a photomask, photoresist will undergo a chemical change which causes either the exposed (positive photoresist) or masked (negative photoresist) areas to be soluble in a developing

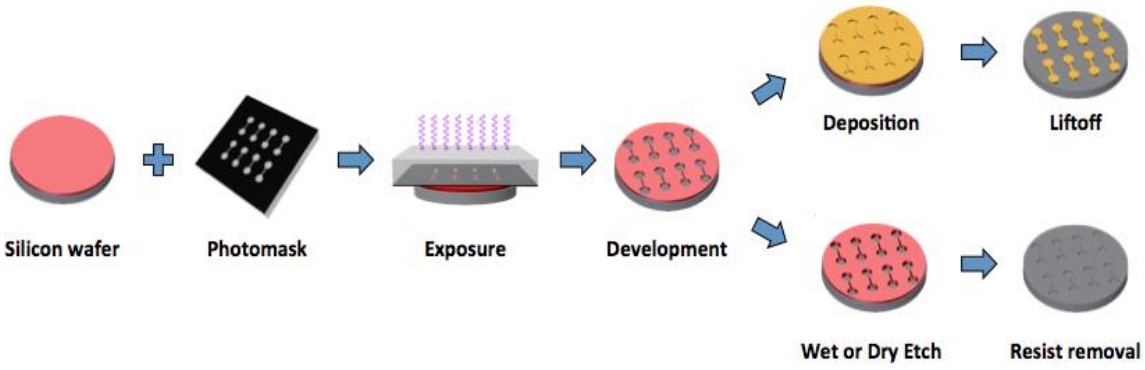

Figure A.1 Photolithography process. Initially a wafer is coated with photoresist and, using a mask aligner, UV light is passed through a photomask and onto the wafer + photoresist (rendering the photoresist either soluble or insoluble depending on the type). Next, the wafer is placed in a developing solution, leaving behind openings in the photoresist. Afterwards, the pattern is transferred onto the substrate through metal deposition or etching. Finally, the photoresist is removed, resulting in a patterned wafer.

Source: https://cleanroom.soe.ucsc.edu/lithography

solution. An intrinsic property of every photoresist, and a key parameter in determining its response to a localized electric field, is the photoresist contrast[2]. The sensitivity of a particular photoresist is given by its contrast curve, which shows the photoresist thickness as a function of exposure dose. This curve is typically included in a data sheet provided by the manufacturer (see Figure A.2a for an example contrast curve given by Rohm and Haas for its Microposit S1800 series photoresists). The value of the photoresist contrast is defined as the linear slope of this curve. Figure A.2b shows an example contrast curve highlighting two critical values, the threshold exposure dose and the critical exposure dose, respectively given by E_{th} and E_c. The threshold exposure dose represents the minimum dose for which the photoresist will respond to light and the critical exposure dose represents the dose for which the photoresist will be completely removed in a developing solution. The region between E_{th} and E_c represents a distribution of dose values where the photoresist will be partially removed.

When photoresist is initially spin-coated onto a substrate, the spin-speed determines the thickness (given by a spin-curve contained within the photoresist data sheet). Once the thickness is known, and given the height of a multilayered (i.e. coaxial) pillar array, one can use the contrast curve to calculate the appropriate dose that will remove enough photoresist so as to expose the tops of the pillars, but still leave a protective layer covering the rest of the pillar and floor. With the outer material now partially accessible, a selective-wet-chemical etchant with a known etch rate can be used to lower the outer material to a desired height. Wet chemical etching is the preferred removal method because dry etching (i.e. plasma etching) can cause photoresist to become heavily cross-linked which renders the film insoluble[3].

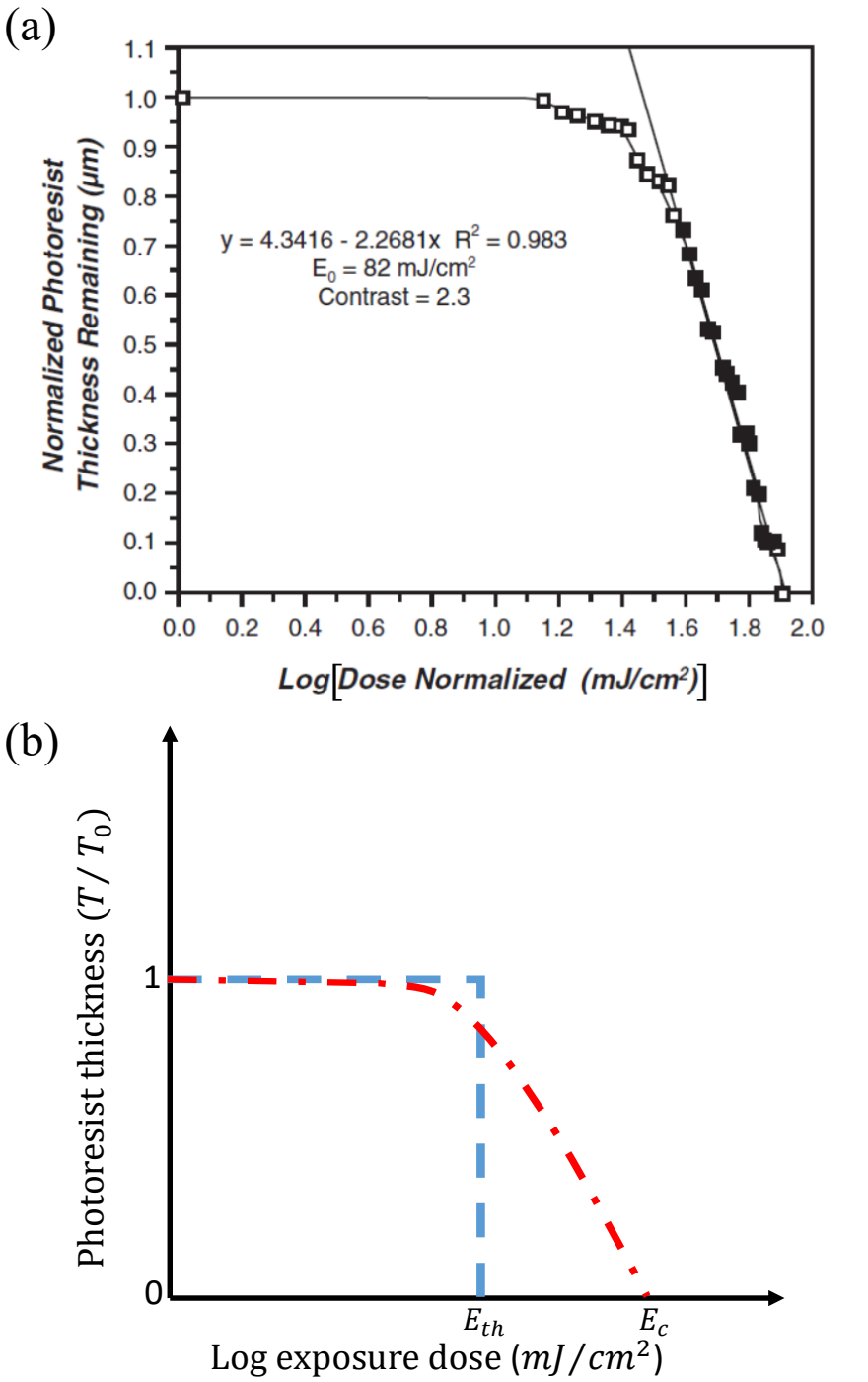

Figure A.2 Contrast Curve of Photoresist. (a) The contrast curve of Shipley 1800 series photoresist. (b) Contrast curve schematic showing critical parameter E_{th}, the threshold dose (minimum dose for photoresist to respond to radiation) and E_c, the critical dose rendering entire photoresist layer soluble. Dashed blue line represents theoretical photoresist where threshold dose equals the critical dose. Red dash-dot line represents realistic photoresist with a distribution dose values between the threshold dose and critical dose

Once the outer metal has been sufficiently removed, exposing the dielectric layer, the process can be repeated to lower one or more inner layers in the coaxial architecture, resulting in the core electrode being "extended" above the other layers. An emphasis is placed around the word extended because its use is somewhat misleading, as the core electrode is not actually

extended beyond its original height and instead results in being elevated above the outer layers, only post-etching. Given this reality, the initial pillar height (prior to material deposition) is a critical parameter when a particular height difference, between the core electrode and outer layers, is desired.

An SOP (intended to be used with the cNEA and S1813 PR) for the ECC process along with images to be used as guidance is contained below. One important note is to move quickly when using the SEM for verification. It is often difficult to image samples covered in photoresist and the electron gun can cause "burns" to appear in the form of irremovable photoresist when imaging the same area for too long. Therefore, when viewing the sample, use a low accelerating voltage and if a particular area cannot be quickly resolved, move to a different one.

1. *Spin on PR using the following recipe:*
    a. *500 rpm 5s (ramp step) + 2000 rpm 45s*
        1. *Acl=1 for both (lowest setting possible)*
    b. *Soft bake sample at 110 C for 3 minutes*
    c. *Expose sample (no mask) for 1.2-1.5s*
    d. *Hard bake sample at 120 for 1 minute then develop sample for 30s*
        i. *DO NOT LEAVE SAMPLE IN FOR LONGER THAN 30s*
    e. *Check with the SEM to make sure PR layer sits below outer metal as shown below:*

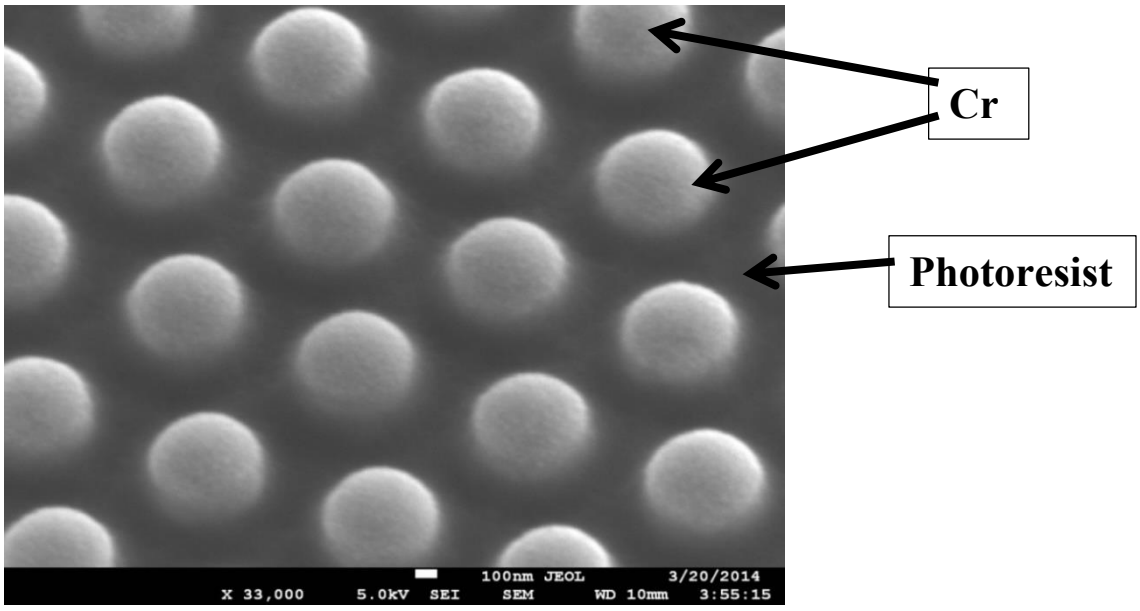

2. *Etching outer metal and dielectric layer*
    a. *To etch the Cr layer, use the Cr specific etchant (Cr 1020 etchant)*
        i. *The etch rate is listed as 4 nm/ s at 40 C however, I usually do not heat the solution*
        ii. *The pillars start out around 2 μm tall, therefore etch the Cr layer for 60-70s initially, rinse with DI-H_2O and blow dry with N_2 then check in the SEM (at 30-degree tilt) to make sure Cr layer has*

Post 70 s Cr etch

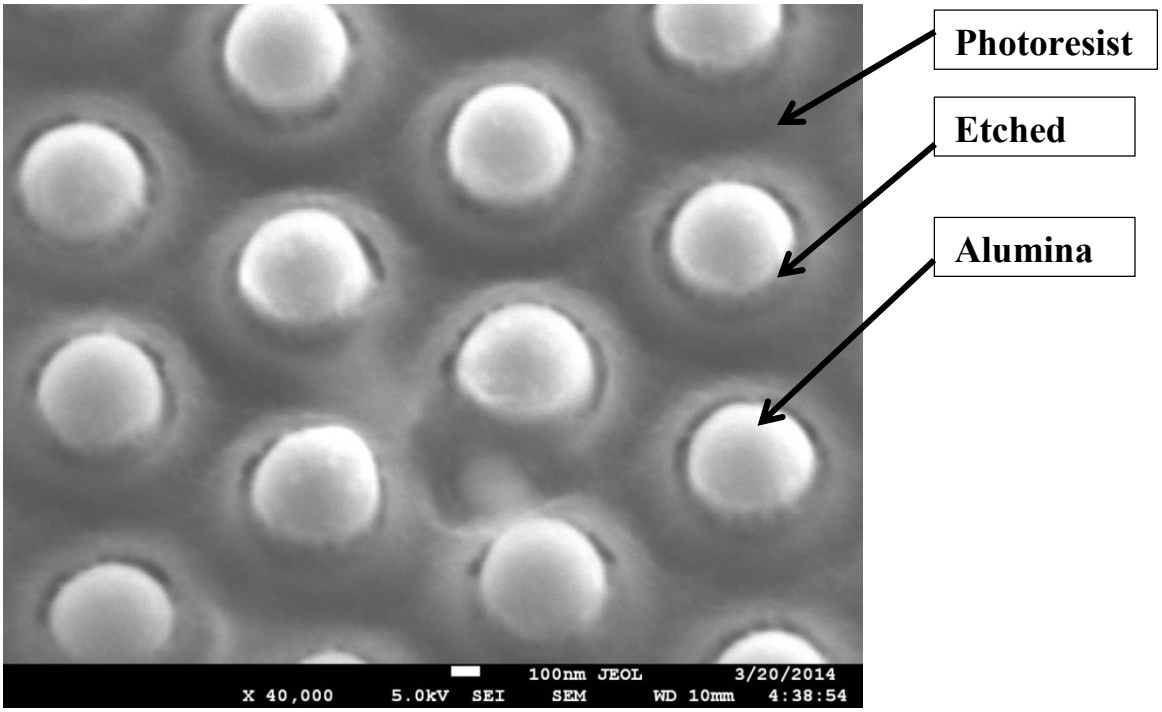

iii. *If Cr layer needs to be etched more, repeat previous steps adjusting for the appropriate etch time (anecdotal)*

b. *Once Cr layer is confirmed to have been etched, etch the Alumina layer using the Transetch-N solution*
   i. *The etch rate of this solution is 20 nm/ hr (very stable, error is < 10 nm)*
   ii. *Leave sample in solution for 15- 20 hr, rinse with DI-H_2O and blow dry with N_2*
   iii. *Check sample in SEM (at 30-degree tilt), it should look similar to this:*

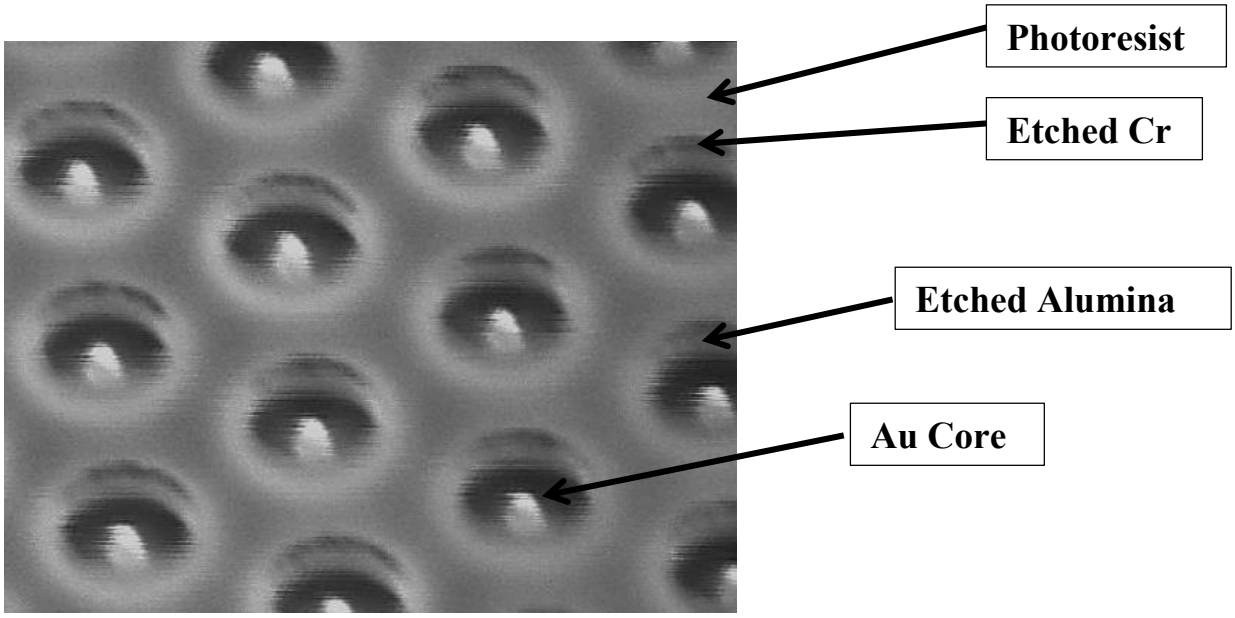

iv. *Adjust etch time as needed.*

3. *Outer metal height should be below the dielectric. Therefore after alumina layer has been etched, the sample should be placed in the Cr etchant to lower outer metal height.*
   a. *Confirm heights are correct in SEM*
4. *Remove the photoresist with either 1165 or Acetone (place sample in small cylindrical dish with either solution for 2-3 minutes, rinse with DI-H_2O and blow dry with N_2.*
5. *Take SEM images and be sure to measure height of core above Alumina and Cr layers (at 30-degree tilt, double to measured height to get the actual height).*

For the cMEA, the following changes should be made:

a. SPR-220 Photoresist
b. Spin speed: 3000 rpm for 30 s
c. Exposure time: 3 s
d. Soft bake/ hard bake at 115°C

The ECC process can be extended to different architectures and used with different photoresists, once the contrast curve is known. Therefore, the process represents a viable alternative to traditional fabrication methods used to create multi-tiered 3D structures.

A.2 References

[1] Mack, C. A. The new, new limits of optical lithography. Proc. SPIE **5374**, 1-8 (2004).

[2] Lee, E., Hahn, J. W., The effect of photoresist contrast on the exposure profiles obtained with evanescent fields of nanoapertures. J. Appl. Phys. **103**, 0835501-4 (2008).

[3] Kishimura, S., Kimura, Y., Sakai, J., Tsujita, K., & Matsui, Y., Dry etching resistance of resist base polymer and its improvement. Proc. SPIE **3049**, 944-955 (2002)

Appendix B: Fabrication Recipes

This appendix includes general recipes for most, if not all, of the cMEA and cNEA fabrication processes. While the true test of the robustness of a process is its repeatability, given the large number of known (and more importantly unknown) parameters involved in the fabrication process, its possible slight adjustments will need to made. Where it was pertinent, anecdotal advice is periodically given as a guide to how the recipe should be adjusted.

B.1 Preparation of 16x30mm^2 Si sharp pillar and glass wafer for metal deposition

1. Clean 16x30mm^2 Si wafer / glass wafer using the following *piranha* (3:1 H_2SO_4:H_2O_2) cleaning process:
    a. Set hot plate in chemical hood to 150 C
    b. Carefully pour 150ml of H_2SO_4 into small beaker and place on hot plate for 15 min
    c. Pour 50 ml of into H_2O_2 a graduated cylinder then SLOWLY pour H_2O_2 into small beaker on hot plate (reaction of acids should be visible)
    d. Wait 20 min then take wafer out of beaker and rinse THOROUGHLY with DI-H_2O. Dry with N_2 air
2. For Glass substrates, additional IPA or Acetone + sonication clean
3. Ensure hot plate is clean when placing substrates on for drying
    a. Cover hot plate with aluminum foil to ensure cleanliness.

B.2 Photolithography (PL) for bottom metal deposition (using LOR3B + S1813)

1. Prior to beginning PL the substrate needs to undergo a microwave plasma clean:
    a. Set O_2 flow to 400
    b. Set Power to 400
    c. Pump down to 60 mTorr
    d. Once Pressure reads 60, turn on O_2 flow, wait for pressure to stabilize (should be around 750 mTorr) then press power
    e. Run for 20 seconds
    f. Turn off power, Turn off Gas
    g. Vent slowly until 1000 mTorr is reached then open fast vent valve

h. Sample is now ready for photolithography

2. Using the Laurrel spinner, the program for spinning LOR3B is program A (2 steps):
    a. 500 rpm ramp for 8s (Acl = 4) followed by 1000 rpm for 30s (Acl = 11)
    b. Open compressed air valve (to the right of spinner). The valve is sufficiently opened once blinking "CDA" on screen becomes blinking "LID"
    c. Place substrate onto appropriate chuck (for 16x30mm^2 substrates, the proper chuck is shown above). Press vacuum and verify that vacuum reading is above 20 (shown on upper right of screen). Blow with N_2 air to ensure no unwanted particulates on the substrate
    d. Using plastic cup or pipette, dispense LOR3B onto substrate surface making sure to completely cover the substrate.
        i. It helps to pour LOR3B onto substrate then to manually (by hand) slowly rotate the chuck to allow LOR3B to spread over the sample.
    e. Press Run once substrate is covered.
    f. Set hot plate to 150 C.
    g. Bake sample at 150 C for 5 minutes.
    h. Switch Laurell spinner to program B (3 step spin process):
        i. 500 rpm for 5-8s (Acl = 4) followed by 2000 rpm for 35-45s (Acl = 11) followed by 3000 rpm for 5s (Acl = 16)
    i. After initial baking, briefly let sample cool by placing on metal surface of spinner hood. Place sample onto chuck and blow with N_2.
    j. Pour S1813 photoresist onto substrate, as before, making sure to fully cover the sample.
    k. Press run once substrate is covered.
    l. Set hot plate to 110 C and bake sample for 2 min.
3. Exposing sample using the Suss mask aligner.
    a. Open N_2 valve located above mask aligner
    b. Turn on power supply (located underneath the mask aligner) by pressing buttons in the following sequence: Power on (lower left of power supply), CP (lower middle of Power supply), the screen will read "Wait…" then once it says "Start" press Start (upper right of power supply).
    c. Turn mask aligner on by rotating power button (green knob) clockwise
    d. Press "load" button (blinking light) to start the machine
    e. Depending on which type of mask is being used (Cr vs. transparency)/ minimum feature size (Cr mask should be used for feature sizes less than 25.6 μm) the mode used will be hard contact mode or flood exposure:
        i. Hard contact: This procedure should be well known prior to use
            1. Verify that current mask holder is appropriate size (5" vs 4") and has the corresponding sample plate (also 5" vs 4").
            2. Turn on mask vacuum pump (switch on the wall to the right of the mask aliner)
            3. To change mask, press change mask button on mask aligner control board, turn off mask vacuum, remove current mask (if no mask, move to step d)

4. Place mask in mask holder (Cr side facing up so that it will face the sample once the holder is put in place) and turn on the mask vacuum (on control board; NOT the pump as it should already be on [see step b above]). Also, make sure clamp is snug on mask and that rubber strip on clamp is on top of mask not folded under.
5. Once mask is in place, slide mask holder into appropriate slot on mask aligner.

ii. Hard/Soft contact with transparency:
1. Tape transparency to 4" square glass piece located in front of computer screen. Make sure ink side is facing up so that it will be in contact with sample.
2. Repeat steps above using 4" glass piece as a Cr mask

iii. Hard/Soft contact exposure:
1. Press edit parameter button, use left and right buttons to scroll to exposure type, select hard contact or soft contact by pressing up or down buttons (depending on desired exposure type). Next press left or right button to scroll to critical parameter (exposure time adjustment) and use up and/or down arrays to adjust exposure.
    a. Current recipe (4/22/15): For S1813 PR expose for 7.5s
        i. Adjust for under/over development by adding/subtracting 10-15% of total time.
2. Place sample (after completing the soft bake step) in the middle of sample plate, press load, then press enter (following blinking lights for button locations). This will initially bring sample into contact with mask then leave a small (50-100μm gap).
3. To bring down microscope press F1 button then enter.
4. Move microscope with XY buttons on control board; move sample with knobs on the side of the sample stage.
5. When ready to expose press the expose button and look away from mask aligner.

iv. Flood exposure:
1. Select flood exposure under exposure type in the edit parameter screen.
2. Enter same exposure time as previously mentioned.
3. Press load then enter.

v. Turning off mask aligner:
1. Turn knob on control panel to off, turn off power supply, Wait 5 min, close N_2 valve

4. Developing sample.
    a. After exposure do not hard bake sample
    b. S1813 is developed by MF-319

c. Pour a small amount (1/4 of height) of appropriate developer into small cylindrical dish shown.
d. Fully submerge sample for 45-50 seconds.
    i. Agitate solution by "swishing" solution in a circular motion
e. Remove sample, immediately rinse with DI-H_2O and blow dry with N_2 air
f. Check that pattern has been developed under microscope.
    i. When turning on microscope do not put sample under illuminating light of microscope as that expose the PR and render that area soluble.
    ii. Pattern results:

Bad Develop

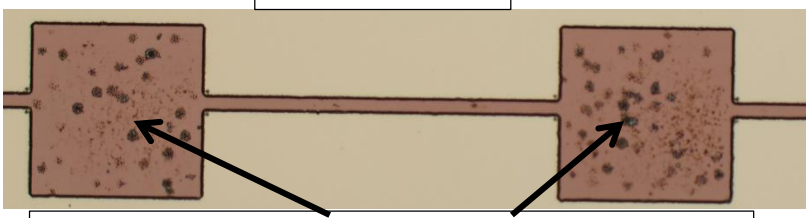

Underdeveloped: residual photoresist (increase exposure dose)

Gap too large between mask and substrate

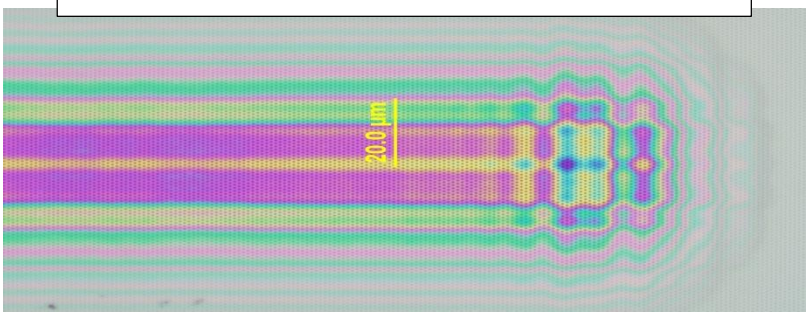

Overdevelopment: Pattern is larger than expected and edges are not sharp (squares become circles)

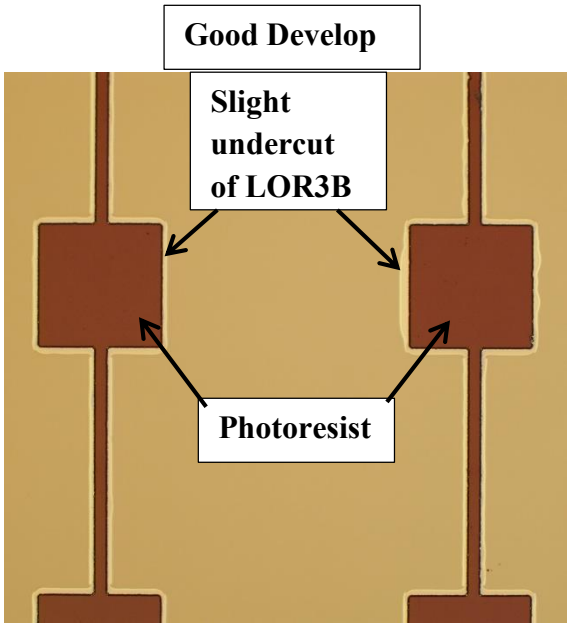

B.3 Deposition of metal (Ti/Au) using AJA sputter system

1. Pin wafer to substrate holder with 2 clips (try to cover as little of the wafer as possible) tape a piece of Si to holder to verify deposition thickness.
2. Load holder into AJA System main chamber (make sure holder is properly aligned).
3. Turn Rotation on, Turn on Ar gas, open pressure valve (press pressure button on screen)
    a. Pressure valve should initially be set to 20 mTorr
    b. Ar gas flow should be set to 18 sccm (default setting)
4. Run substrate clean process:
    a. Set Gun 1 (Gun with no target) to 15 V, Turn the gun on
        i. You should get a plasma
    b. Run for 1 min, then set Gun 1 to 0 V
    c. "Sticker layer" (Ti) deposition (10nm)
    d. If Ti target is on the RF gun:
        i. Turn on Ti gun and set voltage to 50 V with shutter closed
        ii. There should be a plasma
        iii. If there's no plasma set Gun 1 to 25 V to reignite plasma, once plasma is ignited and stable turn off gun 1. If plasma is unstable keep gun 1 on until Ti shutter is opened
        iv. Set pressure valve to 3 mTorr
        v. Set ramp time to 90
        vi. Set voltage to 250
        vii. Once voltage has reached 100 open and close the shutter quickly to minimize the reflected power (shown next to REF in the upper right corner)

viii. Once power reaches 250 open the shutter and set the deposition monitor timer to zero (press zero button). If the REF is non-zero you have to minimize it. This is done by adjusting the Tune and Load values.
ix. Press min and max buttons to lower the REF power. Usually the load lowers the REF. Don't worry if REF doesn't zero out, single digit REF is common, just try to get to the minimum value possible.
x. Run deposition for 6 minutes
xi. At 6 minutes, close shutter, set ramp time to 75 and set voltage to 50.
xii. Turn off Ti gun once voltage reaches 50

e. If Ti target is on the DC gun:
i. Turn on Ti gun and set voltage to 50 V with shutter closed
ii. There should be a plasma
iii. If there's no plasma set Gun 1 to 25 V to reignite plasma, once plasma is ignited and stable turn off gun 1. If plasma is unstable keep gun 1 on until Ti shutter is opened
iv. Set pressure valve to 3 mTorr
v. Set ramp time to 90
vi. Set voltage to 250
vii. Once power reaches 250 open the shutter and set the deposition monitor timer to zero (press zero button).
viii. Run deposition for 6 minutes
ix. At 6 minutes, close shutter, set ramp time to 75 and set voltage to 50.
x. Turn off Ti gun once voltage reaches 50

5. Au layer deposition (110nm)
a. Au will always be on the DC gun:
i. Turn on Au gun and set voltage to 50 with shutter closed
ii. Set ramp time to 90
iii. Set voltage to 200
iv. Once voltage reaches 200 open shutter and zero deposition timer
v. Deposit for 4 minutes
vi. After 4 minutes, close shutter, set ramp time to 60 and set voltage to 50.
vii. Turn off gun once voltage reaches 50.

b. Set pressure valve to 20 mTorr
c. Wait for pressure valve to stabilize and reach 20 mTorr
i. Press open on the pressure valve section
ii. Turn off Ar gas
iii. Turn off rotation
iv. Take sample out of AJA system

d. Lift off of Metal
i. Fill small cylindrical dish with 1165 solution (similar amount as performed with developer solution)

ii. Turn on small hot plate (metal surface) to between 70-75 C
iii. Place substrate in dish and place dish on hot plate.
iv. Lift off should take approximately 2 hours (time varies)
v. It helps to swish (agitate) the solution.
vi. When metal has lifted off and pattern remains take sample out and rinse with DI-H_2O and blow dry with N_2
    1. This may take a few iterations to completely remove metal
    2. Check under microscope to make sure metal has completely lifted off.
vii. DO NOT PLACE SAMPLE IN SONICATOR TO AID IN LIFTOFF. SONICATION WILL BREAK THE SHARP PILLARS

B.4 Measure/ record the thickness using either the profilometer or the ellipsometer

1. Best results are with Si substrate samples that have been taped with Kapton tape the substrate holder in the AJA.
2. Open the DekTak program
3. Place sample in chamber and make sure sample is underneath the tip
4. Lower tip onto the sample
5. Measure thickness. Take the average of 5 areas.
    a. If thickness readings are inconsistent try different area or make a small scratch in the sample.
    b. Make note of thickness vs. where the sample was placed on the holder.

B.5 Atomic layer deposition (ALD) of Al_2O_3 (200nm)

1. Press vent on ALD program screen for the Cambridge ALD machine.
2. Open substrate chamber.
3. Load substrate by placing it face up on plate.
4. Close substrate chamber.
5. Press pump down on program screen.
6. Open up TMA valve located inside ALD (open door and find the green knob, turn to open it)
7. Set flow to 20 sccm.
8. Load program Binod 0.1nm with Temp.
9. The screen should look like this:
10. Change the value for step 12 to 2000
11. Press start.
12. Once deposition is finished, vent chamber, remove sample, pump down chamber, close TMA valve.
13. If using Si substrate, use multimeter to check if surface is conducting (resistance should be over 40 MΩ). Be sure to press range before checking resistance. If surface is conducting Al_2O_3 must be redeposited as the inner and outer terminals of the coax would short.

B.6 Etching of Al_2O_3 to open windows for Au layer macropads

1. To access bottom contacts, windows over the macropads need to be opened.
2. Set aside corresponding photomask
    a. Each pattern has an "Etch layer" mask. It's the one without any address lines
3. Follow photolithography steps previously detailed using the Etch layer mask as your photo mask.
    a. The mask is a positive mask so you should align the openings in the mask with the Au macro pads. Make sure you have the correct alignment and only the area over the Au pads are exposed
4. Once photolithography is finished, pour small amount of Transetch-N solution into a small cylindrical dish (same amount used for developer).
    a. The Transetch-N bottle is found in the Acids cabinet (In the Hydrogen peroxide section)
    b. Be very careful when using this product and properly label the container the solution is poured into
        i. Proper labeling: Solution Name, User Name, Date
5. Transetch-N has a 20nm/ hr etch rate. Therefore, leave sample in solution for a minimum of 10 hours. Do not leave sample in solution for more than 24 hours.
6. Once etching is finished, rinse sample with DI-H_2O and blow dry with N_2
7. Confirm etching amount with the profilometer.

B.7 Deposition (sputter) of Cr for outer metal layer

1. Pin wafer to substrate holder with **2** clips (try to cover as little of the wafer as possible) tape a piece of Si to holder to verify deposition thickness.
2. Load holder into AJA System main chamber (make sure holder is properly aligned).
3. Turn Rotation on, turn on Ar gas, open pressure valve (press pressure button on screen)
    a. Pressure valve should initially be set to 20 mTorr
    b. Ar gas flow should be set to 18 sccm (default setting)
4. Run substrate clean process:
    a. Set Gun 1 (Gun with no target) to 15 V, Turn the gun on
        i. You should get a plasma
    b. Run for 1 min, then set Gun 1 to 0 V
5. Cr layer deposition
    a. If Cr target is in Lesker AJA system:
        i. Turn on Au gun and set voltage to 50 with shutter closed
        ii. Set ramp time to 90

iii. Set voltage to 200
iv. Once voltage reaches 200 open shutter and zero deposition timer
v. Deposit for 4 minutes
1. After 4 minutes close shutter, set ramp time to 60 and set voltage to 50.
vi. Turn off gun once voltage reaches 50.

b. Set pressure valve to 20 mTorr
c. Wait for pressure valve to stabilize and reach 20 mTorr
d. Press open on the pressure valve section
e. If Cr target is not in AJA, Old sputter system can be used:

6. Lift off of metal
a. Fill small cylindrical dish with 1165 solution (similar amount as performed with developer solution)
b. Turn on small hot plate (metal surface) to between 70-75 C
c. Place substrate in dish and place dish on hot plate.
d. Lift off should take approximately 10 minutes (time varies)
e. It helps to swish (agitate) the solution.
f. When metal has lifted off and pattern remains take sample out and rinse with DI-H_2O and blow dry with N_2
i. This may take a few iterations to completely remove metal
ii. Check under microscope to make sure metal has completely lifted off.
g. DO NOT PLACE SAMPLE IN SONICATOR TO AID IN LIFTOFF. SONICATION WILL BREAK THE SHARP PILLARS

B.8 Extended core

[See Appendix A]

B.9 Electrical characterization of chip

1. Testing resistance for shorting:
a. If using the yellow multimeter: Turn to Ohmmeter setting, **press range** (changes to lower input current). Never press terminals to chip without pressing the range button! This has shorted the chip in the past due to the voltage being above the breakdown voltage of 150 nm of Al2O3. Press the two terminals to the inner (Au) and outer (Cr) pad of a coaxial region. The resistance should be above 25 MΩ. Ideally the screen will show “OL” meaning the resistance is above 40 MΩ.

B.10 Ebeam for Si pillars

This process was adapted from a process developed by Fan Ye:

1. The BC clean room has two molecular weights of PMMA: 495 and 950 kDa, both in an
   anisole solution, and the concentration by mass is 8% and 9%, respectively. The 495 is
   denoted 495 PMMA A8, for example. For this process, both are used as this is a bilayer process. The 495 layer should be at least twice the thickness of the total metal deposition.
    a. Find the MicroChem® PMMA data sheet. It has the spin-speed curves.
2. Set the hot-plate to 180 °C, bake-dry a clean substrate for 2 min in air
3. Spin 495 PMMA A4:
    a. Choose appropriate spin speed and acceleration/ time values according to the desired thickness of the PMMA
    b. Values typically used: 500 rpm, 5s ramp + 4000 rpm, 60s
    c. Bake on hot plate at 180 °C for 90 s
4. Spin 950 PMMA A4.5:
    a. Choose appropriate spin speed and acceleration/ time values according to the desired thickness of the PMMA
    b. Values typically used: 500 rpm, 5s ramp + 4000 rpm, 60s
    c. Bake on hot plate at 180 °C for 90 s
5. Perform a dosage test to determine doses for all diameters (3.5 μm to 300 nm)
    a. Typically, 200 $\mu C/cm^2$ was used for all diameters above 1 μm
    b. For diameters in the 300 – 900 nm range, doses varied between 250-400 $\mu C/cm^2$
6. Once dose values have been confirmed, run pattern "300-3500nm hole array"
    a. Ensure dose and probe current have been changed to appropriate values
7. Develop in MIBK/IPA 30% for 2 minutes then rinse in DI water
    a. Slightly agitate the solution during development and watch for pattern to emerge
    b. Once pattern can be seen clearly, develop for another 10 secs, then remove sample.
    c. Check pattern using Leica microscope. If underdeveloped, place back in developing solution for 10-15 seconds
8. Use ebeam to deposit 100-110 nm Al
    a. Do not use sputtering or thermal evaporation as they tend to coat the sidewalls of photoresist, therefore making lift off difficult, as well as enlarging the original pattern.
9. Lift-off with Microposit® 1165 resist stripper or acetone for at least 12 hr at room T.
10. After 12 hours, immerse a clean transfer pipette into the lift-off solution, and, while immersed, gently and slowly squirt off the remaining PMMA. Rinse the sample with IPA then DI.
11. Verify the pattern has been fully transferred.
12. Additional information:
    a. If you mix a PMMA dilution, let it sit for 2 days before you use it
    b. Always use fresh, disposable, plastic cups in all of the EBL processes

c. Once the substrate has been cleaned, only use IPA and DI as solvents. Other than for the lift-off step, stay away from acetone if possible, as it can leave behind a film.
d. Avoid carbon tape at all costs during the EBL process. That stuff is nasty.

B.11 Si nanowires

1. ICP RIE-8 in the Harvard clean room was used to etch the Si substrates.
    a. Recipes were provided by Ling Xie.
    b. Etch Rate varied throughout the 2-week period between subsequent cleanings with a higher etch rate (~ 0.5 μm/min) just after the RIE had been cleaned.
    c. It's important to be consistent when reserving the machine to ensure the etch rate/ conditions are similar to previous uses.
2. After RIE, bring sample(s) to BC Higgins Hall lab and use benchtop SEM to measure pillar height and diameter.
3. Next, take samples to lab with tube furnace.
4. Place sample(s) in quartz boat and use quartz rod to push boat to the middle of the tube furnace.
5. Set temperature to 1000 degrees.
6. After 6 hours, turn off tube furnace and let sample(s) cool before removing.
7. VERY CAREFULLY, pour 25 ml BOE into plastic container wide enough for sample to lay flat while being fully submerged.
8. One at a time, place sample(s) in BOE for 60 seconds.
9. After 60 s, rinse with DI water and dry with N_2 air.
10. Check pillar diameters on the bench top SEM, if the diameter of the smallest region is larger than 200 nm, repeat steps 6-8 for 2 hours (instead of 6) and placing sample in BOE for 30 seconds instead of 60.

Appendix C: Origin Code for Data Processing

Throughout the data processing, certain Origin functionalities were repeatedly being used. Instead of continuing to manually select these functions from the Origin GUI, scripts were developed and implemented in an effort to save time. Excluding trivial arithmetic scripts and loops, the scripts involving three procedures are listed below. They're included as a guide to anyone continuing the work presented in this thesis, however, it is left to the user to search the origin help book for a specific description of each parameter.

(1) Averaging multiple curves in a plot

```
// Count the number of data plots in the layer and save result in
variable "count"

layer -c;

// Get the name of this Graph page

string gname$ = %H;

// Create a new book named smooth (actual name is stored in bkname$)

newbook na:=Smoothed;

// Start with no columns

// Input Range refers to 'ii'th plot

// Output Range refers to two, new columns

// Adjacent averaging method shown below using 325 points

wks.ncols=0;

loop(ii,1,count) {

    range riy = [gname$]!$(ii);

    range roy = [bkname$]!($(ii*2-1),$(ii*2));

    smooth iy:=riy meth:=aav npts:=325 oy:=roy;

}
```

(2) Unstack, Extract, Average Curves:

```
//Unstack the data, irng2 refers to data which determines how it's
unstacked.

//This was used for data taken in multiple sweeps or trials

loop(ii, 1, 10) {

wunstackcol irng1:=col(ii) irng2:=col(1) ow:=Sheet$(ii)!;

}

//Extract the data

wextract iy:=col(c)

settings.Cols:=2

settings.stCondition.Condition:="col(c)>0"

settings.stRowRange.RowFrom:=0

settings.stRowRange.RowTo:=79999

settings.stMethod.Method:=3

settings.stMethod.ColFrom:=10

settings.stMethod.WksSpecified:=Sheet1!;


//Average the curves//

avecurves
iy:=[Book1]Sheet1!((K,A),(K,B),(K,C),(K,D),(K,E),(K,F),(K,G),(K,H),(K,I)
,(K,J))

method:=0 avex:=0 interp:=linear;


//For multiple data extractions//

wextract iy:=col(k)

settings.Cols:=10
```

```
settings.stCondition.Condition:="col(k)>0"

settngs.stRowRange.RowFrom:=0

settings.stRowRange.RowTo:=79999

settngs.stMethod.Method:=3

settings.stMethod.ColFrom:=10

settngs.stMethod.WksSpecified:=Sheet2!;
```

(3) Copy row, swapping columns, looping arithmetic

```
// Copying rows, iw = input ow = output r1 = start copy r2 = stop copy

wrcopy iw:=[Book Name]Sheet Name! ow:=[Book3]Sheet1! r1:=1671 r2:=1671
dr1:=12;

// For looping sequence//

loop (i,4,28) {wcol(i)= ((wcol(i)- wcol(2))/ (wcol(3)- wcol(2)));};

//for swapping columns//

colswap (2,10); colswap (3,9); colswap (4,8); colswap (5,7);
```